INFN - Laboratori Nazionali di Frascati

LNF-90/035(R)
9 Maggio 1990

# THE ARES SUPERCONDUCTING LINAC

*Printed and Published by*
*Servizio Documentazione dei*
*Laboratori Nazionali di Frascati*

*Technical Editor*
Luigina Invidia

*Cover*
Claudio Federici

# THE ARES SUPERCONDUCTING LINAC

Edited by : C.Pagani 8,2), S.Tazzari 7,5)

## The ARES Study Group

P.Amadei 1), A.Aragona 1), M.Barone 1), S.Bartalucci 1), M.Bassetti 1), M.E.Biagini1), C.Biscari 1), R.Boni 1), M.Castellano 1), A.Cattoni 1), N.Cavallo 3), F.Cevenini 3,9), V. Chimenti 1), S.De Simone 1), D.Di Gioacchino 1), G.Di Pirro 1), S.Faini 1), G.Felici1), M.Ferrario2), L.Ferrucci,2) S.Gallo 1), U.Gambardella 1), A.Ghigo 1), S.Guiducci1), S. Kulinski1), M.R.Masullo 3), P.Michelato 2), C.Milardi 1), M.Minestrini 1), G.Modestino1), C.Pagani8,2), L.Palumbo1,6), R.Parodi 4), P.Patteri 1), A.Peretti 2), M.Preger1), G.Raffone 1), C.Sanelli 1), L.Serafini 2), M.Serio 1), F.Sgamma 1), B.Spataro1), L.Trasatti 1), S.Tazzari 7,5), F.Tazzioli1), C.Vaccarezza 1), M.Vescovi 1), G.Vignola 1)

(1) INFN, Laboratori Nazionali di Frascati - CP13, 00040 FRASCATI
(2) INFN, Sezione di Milano
(3) INFN, Sezione di Napoli
(4) INFN, Sezione di Genova
(5) INFN, Sezione di Roma -Tor Vergata
(6) Università di Roma "La Sapienza", Dip. di Energetica
(7) Università di Roma "Tor Vergata", Dip. di Fisica
(8) Università di Milano, Dip. di Fisica
(9) Università di Napoli, Dip. di Sc. Fisiche

# TABLE OF CONTENTS

# THE ARES SUPERCONDUCTING LINAC

## 1 - GENERAL DESCRIPTION

### 1.1 - Introduction

In the ARES Design Study (LNF-90/005) a site-independent accelerator complex was presented that consisted of:

- A 510 MeV Superconducting Linac
- A two-ring Φ-Factory.

The Linac was intended to serve as an injector for the Φ-Factory storage rings, as a test facility for techniques and components to be used for the future VHE Linear Colliders (LC) - in particular fully-superconducting ones - and as a high-quality FEL driver.

It was the natural continuation of the R&D work in progress on LISA and on SC RF-cavity design and construction techniques in collaboration with the italian industry. The key to the realisation of HE superconducting LC's is in fact the achievement of high gradients with good quality factors in industrially-produceable structures, and the production and acceleration of very high peak-current, low emittance electron beams.

The scientific, economic and manpower availability aspects of Design Study have been the object of much discussion both within the Laboratory and in the INFN Management Board.

From the discussion an optimised time- and cost-effective strategy has emerged that foresees:

i) building the Φ-Factory storage rings as fast as possible, using the existing ADONE buildings and facility and a conventional (existing or new) injector.

ii) building the SC Linac on a slightly slower time-scale, by expanding the existing LISA buildings and facilities.

Consequently, we present here a revised version of the original ARES SC Linac design, stripped of all positron production equipment and facilities, that incorporates the following features :

a) minimum non-recirculated energy compatible with the achievement of the emittance and energy spread design goals and with a significant R&D program in the direction of high-field practical accelerating structures;

b) utilization of all existing LISA facilities;

c) moderate expansion of the existing LISA buildings to provide floor space for experiments and tests within the existing LISA main hall;

d) potential for energy upgrade by recirculation

e) revised time and expenditure scale.

A short description of the accelerator design, based on the ARES Design Study, is given in paragraph 1.3.

We only remark here that it consists of twenty 500 MHz, four-cell SC cavities, including the four LISA ones. The number is the minimum required to provide a reasonable chance of developing full field prototypes and a meaningful operability test. The energy is high enough that recirculation without too much deterioration of the beam quality can be envisaged for higher energy applications.

The accelerator nominal energy, at the nominal field value of 10 MV/m, is 240 MeV. However, it is foreseen that the actual average field of cavities produced in the course of an R&D project, will be somewhat lower. At an average field of 8 MV/m the energy, still adequate for recirculation, is 192 MeV.

An updated time-table is shown in Table 1.1 and updated cost and spending profile estimates for the Project are given in Tables 1.2 and 1.3. (paragraph 1.4.) .

## 1.2. - Goals

The goals of the project are - in compliance with the INFN five-year plan document - to develop the technology of SC RF cavities, linear accelerators, and electron colliders, and to build a high-field, high current, low emittance SC accelerator (1÷5).

It is our belief that SC Linacs are a necessary step in the strive towards energies much higher than those obtainable today. Already now they are being considered as possible power sources for warm Linear Colliders but, as soon as the SC RF cavity technology will permit fields in the order of 40÷50 MV/m to be reached with high Q's, fully SC Linear Colliders will become the most cost-effective way of achieving very high energies(6,7) because they will produce the very high pulse currents and very low emittances and energy spreads required by high luminosity, multi-TeV Linear Colliders much more easily and with much lower energy consumption than by using 'warm' structures. Concerning future colliders, the focal points of interest for ARES are the generation and acceleration of very low emittance beams with high peak currents.

A FEL program to produce high power laser beams in the region of wavelengths below 100 nm, not accessible to ordinary lasers, is also presented in the Appendix.

The project has two phases :

- The first phase, extending approximately to 1993 and to be carried out within the existing LISA buildings, includes the commissioning of LISA and its upgrading so that it becomes the test bench for all critical ARES components ( such as : high performance RF cavities with $E_{acc} \approx 10$ MV/m @ $Q \approx 3\ 10^9$ constituting a significant step towards collider-grade parameters, high current low emittance gun and associated equipment - steering, lenses, compressor, etc - and high level beam diagnostics ) that have to be developed during the first phase itself. It also includes exploitation of the facility by the infrared FEL experiment designed in collaboration with ENEA.

The detailed design of the SC Linac, ancillary equipment and buildings will be completed and building and operation permits secured.

- The second phase, starting approximately in 1994 will cover actual construction of the LISA building extension and of the full size machine. The extension leaves room for a possible energy upgrade by recirculation at present not included in the cost estimate.

## 1.3 - Description of the accelerator and of its location

The SC Linac has to provide electron beams at a nominal energy of 240 MeV. It must accelerate very low emittance beams without degradation and be capable of reaching a single-pass energy high enough to perform significant beam quality tests and FEL experiments.

A layout of the accelerator is shown in Fig. 1.1. It shows, schematically, the physical arrangement of the accelerator in the fully expanded configuration that includes the final RF gun, the bunch length compressor and the layout of a possible recirculation channel. As discussed in § 2.3, the LISA injector, including the capture and preacceleration sections will be installed beside the RF one, for preliminary tests. A short description of the rationale of the layout is given below.

Electrons are generated by the gun, passed through a matching section and accelerated by the first Linac Section, L1, consisting of four SC cavities each providing a nominal voltage gain of 12 MV.

The electron injector output energy is ≥ 4 MeV. At the output of L1 the nominal beam energy is therefore ≈ 52 MeV or slightly higher, the exact value depending on the type of gun that is being used.

Each four-cell SC cavity in section L1 has its own cryostat and forms a cryomodule, the smallest unit of the cryogenic structure that can be individually tested. The distance between focusing elements is minimised in the low energy region where space-charge forces are important.

The distance between adjacent cryostats is kept to the minimum value of one RF wavelength (0.6 m); focusing, diagnostics, control and vacuum components are integrated within this length.

Following Section L1, the electron beam is brought to the main Linac Section, L2, through an isochronous achromatic channel (TC12) that would include all splitter and combiner devices required to handle the primary and the recirculated electron beams.

Section L2 consists of 16 four-cell cavities, two to a cryostat to increase the Linac filling factor. The cryomodule therefore contains two cavities.

The overall nominal voltage provided by Section L2 is 192 MV. The electron beam nominal energy at the output of L2 is therefore ≈ 240 MeV.

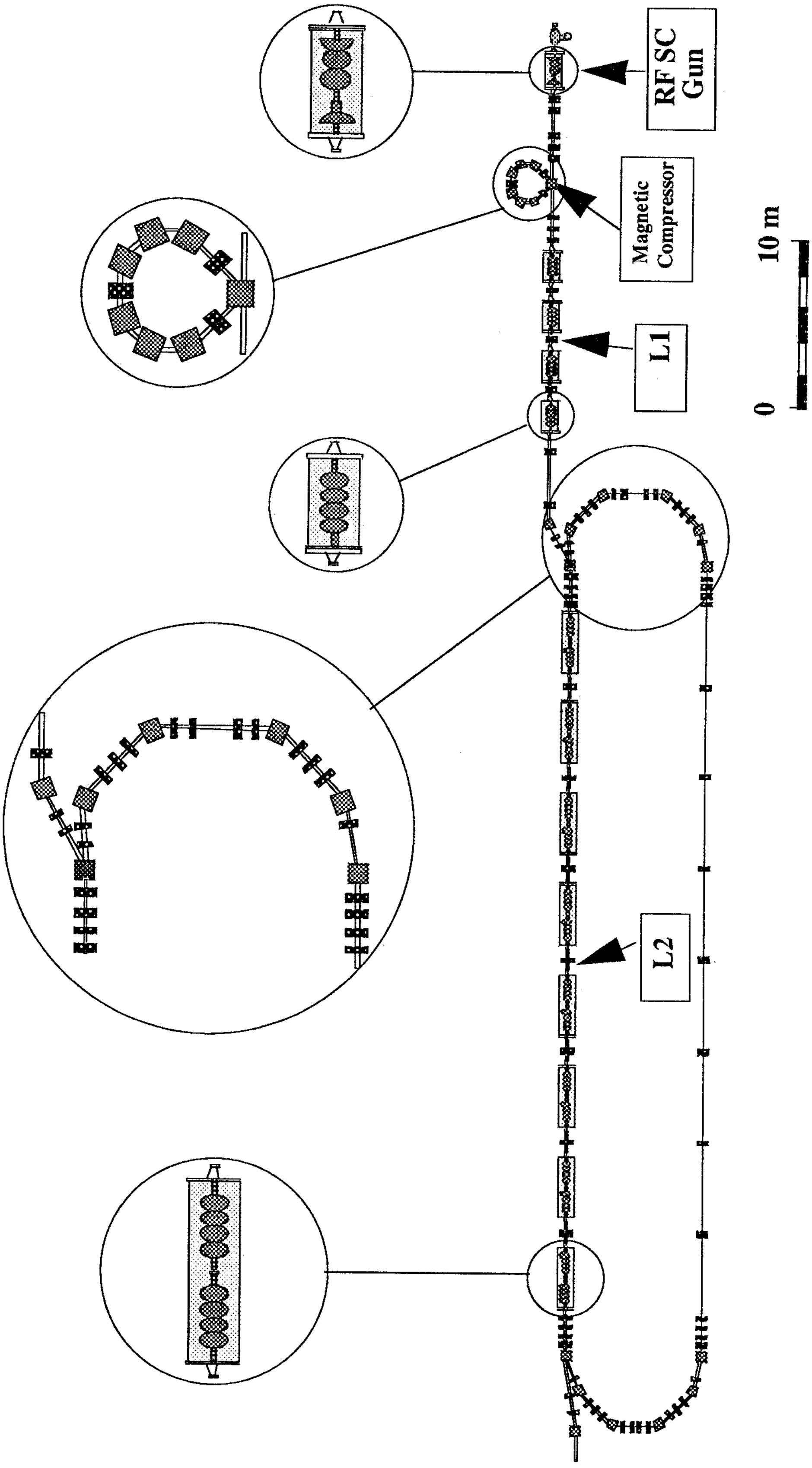

Fig. 1.1 - Schematic layout of the ARES SC LINAC

In the recirculation mode, electrons are brought back to the input of L2 through the isochronous, achromatic transport channel shown in Fig.1.1 and passed once more through L2. The electron beam final nominal energy at the output of the Linac then becomes ≈ 430 MeV.

The accelerator will be located in the LISA general area: Fig 1.2 shows its location on a map of LNF .

The proposed solution for the expansion of the existing LISA building satisfies the following criteria : lowest cost, good shielding, minimum interference between the construction work and the operation of LISA and of the equipment being developed in the existing halls, subsequent utilization of the existing halls for beam tests and experiments, possibility of a later energy upgrade by recirculation.

It consists of two parallel tunnels - the first approximately 4.5 m wide and 80 m long to house the accelerator proper, the second 3.5 m wide and 50 m long to house ancillary equipment and the recirculation channel - running at depths varying from approximately 4 to approximately 12 m and ending at floor level in the LISA main hall. The tunnels run below the hard lavic rock layer, in compact but easily excavated soil. They will be excavated using conventional tecniques, starting from a vertical shaft; the connection to the LISA hall can be realized at the very end of construction so that the activities taking place in the hall itself need not be interrupted but for a very short period. A detailed optimisation study, based on soundings, is underway.

A modest extension of the LISA ancillary buildings is also foreseen to house the main refrigerator and some additional service equipment.

The ground cofiguration and the proposed layout of the tunnels are shown in Fig. 1.3.

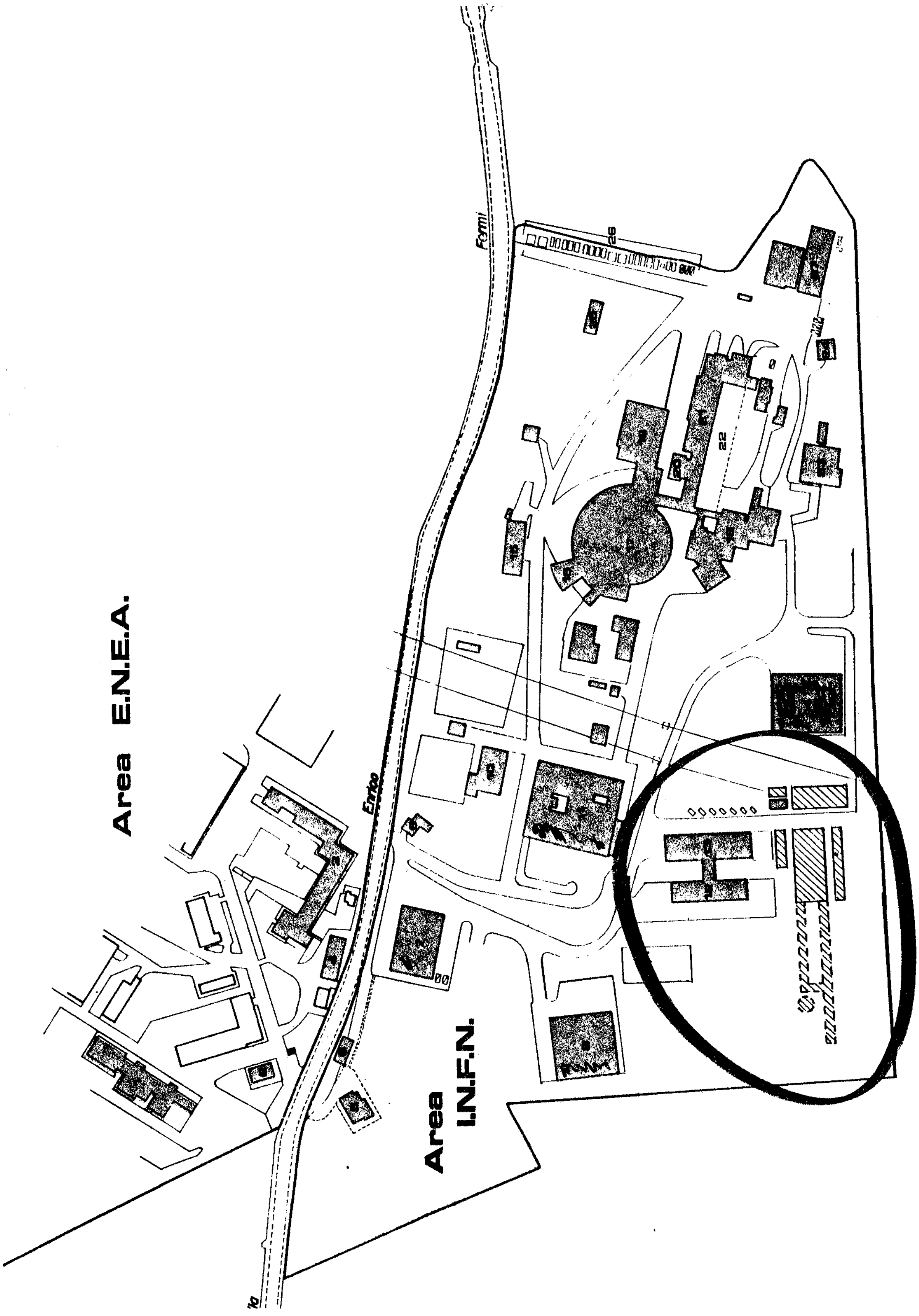

Fig. 1.2 - The new facility on the map of LNF

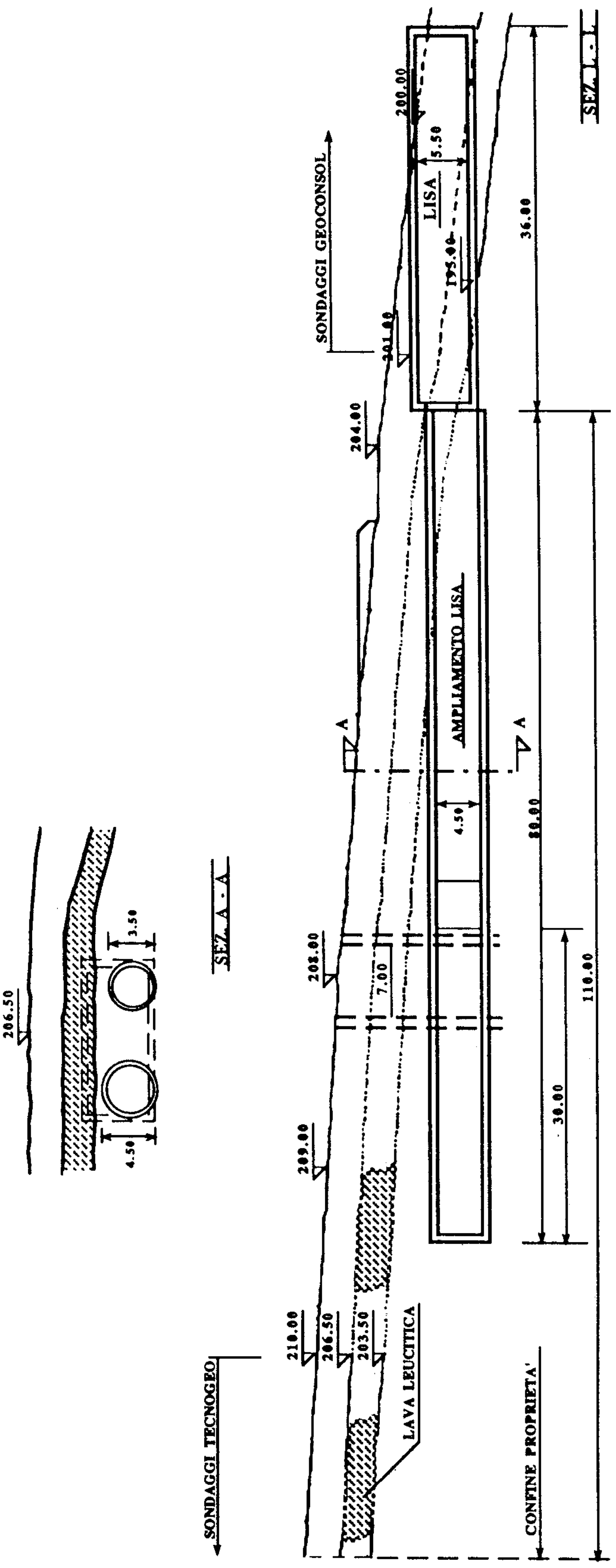

Fig. 1.3 - The ground configuration and the proposed layout of the tunnels.

## 1.4 - Time Schedule, Costs, Spendig Profile

**Table 1.1 - Provisional Time Schedule**

| | 1991 | 1992 | 1993 | 1994 | 1995 | 1966 |
|---|---|---|---|---|---|---|
| • **LISA** | | | | | | |
| - Commissioning and tests ----- | ---------- | ------- | | | | |
| - IR FEL (INFN/ENEA) | - | ---------- | ---------- | ---------- | --- | |
| • **Buildings & Conv.Plant** | | | | | | |
| - Design | ---------- | -------- | | | | |
| - Authorizations and contracting | --- | ---------- | ---------- | | | |
| - Construction | | | | ---------- | -------- | |
| • **SC Cavities** | | | | | | |
| - R&D and prototypes --- | ---------- | ---------- | ---------- | | | |
| - Fabrication & Test of fi. | | ---- | ---------- | ---------- | -------- | |
| - Installation | | | | | -------- | ---------- |
| • **Cryogenic Plant** | | | | | | |
| - Design | | ----- | ---------- | | | |
| - Fabrication | | | | ---------- | ---------- | -- |
| - Installation | | | | | ---------- | ---------- |
| • **Machine components** | | | | | | |
| - Design & prototypes | ---------- | ------ | | | | |
| - Fabrication & test | ------- | ---------- | ---------- | ---------- | -- | |
| - Installation | | | | | ---------- | ------- |
| • **Commissioning** | | | | | | ------- |

**TABLE 1.2** : Costs in GLit.

| | |
|---|---|
| • Low Emittance Injector | 2.5 |
| • SC Cavities | 7.0 |
| • RF System | 1.5 |
| • Cryogenic System | 6.0 |
| • Vacuum Components | 3.0 |
| • Magnets &DC Power Supplies | 1.5 |
| • Diagnostics &Computer Control | 1.0 |
| • Supports and Alignment | .8 |
| • Installation | .5 |
| • Buildings and Conventional Plants | 4.5 |
| Subtotal | 27.8 |
| • R&D + Funzionamento | 5.0 |
| TOTAL | 32.8 |
| • IVA + 15% Contingency | 7.0 |
| **Totale generale** | **39.8** |

**Table 1.3.** Expenditure Profile

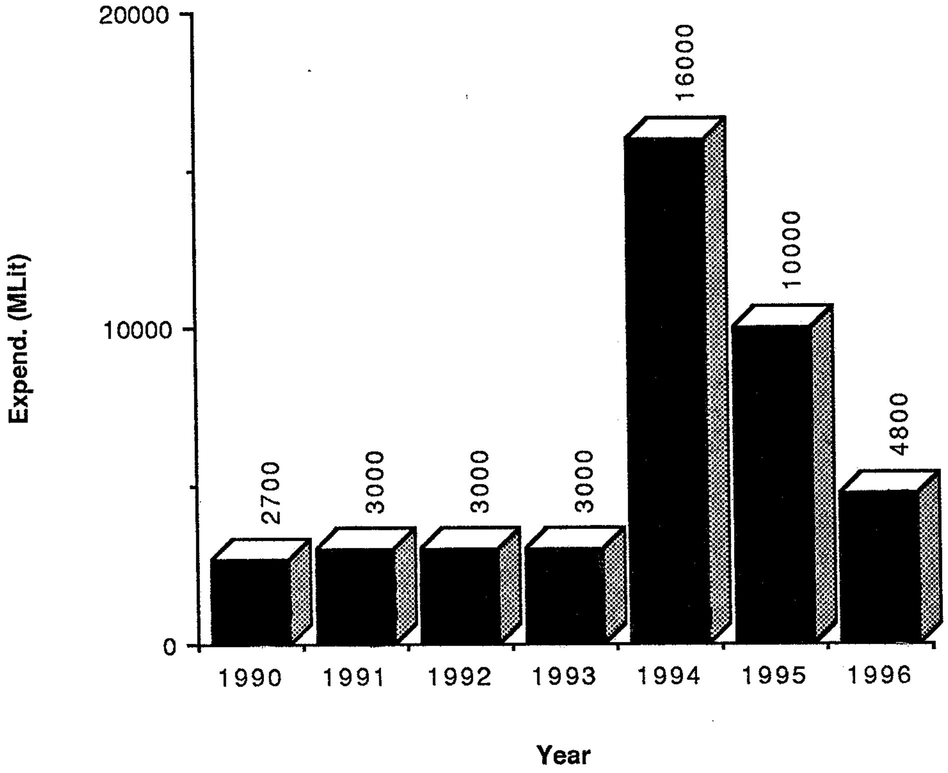

# 2 - OPTICS

## 2.1 - Introduction

As explained in § 1.3, the SC linear accelerator has two sections :

- Section L1 consisting of four SC cavities each providing an accelerating voltage of 1.2 g, being g the average accelerating gradient. The input energy is $E_{i1} = 8$ MeV and the output energy is $E_{f1} = (8 + 4.8\ g)$ MeV. Each four-cell SC cavity in section L1 has its own cryostat and constitutes a cryomodule.
- Section L2 consists of 16 four-cell cavities, with one cryostat to a pair of cavities to increase the Linac filling factor; the cryomodule is correspondingly longer. Its overall output energy is $E_{f2} = (E_{f1} + 19.2g)$ MeV: for g = 10 MV/m $E_{f1} = 56$ MeV, $E_{f2} = 248$ MeV. It can be recirculated to increase the beam energy to a maximum of 440 MeV.

## 2.2 - Linac focusing

Transverse focalization along the Linac is provided by a FODO sequence of 0.2 m long quadrupoles, one per cryogenic module.

The distance between quadrupoles is 3 m in L1 while the focalization can be made weaker on L2, and the half FODO cell is therefore lengthened to 5.4 m to fit the longer cryomodule. In the following we will assume g= 10 MV/m.

The first section, L1, needs a special treatment.
This because the effect of the RF field of an accelerating cavity on the beam transverse optical functions is negligible only insofar as the beam energy increase in the cavity is smaller than the input energy (16); else, the FODO lattice focusing is highly perturbed and a strong mismatch occurs and proper corrective action has to be taken.

The condition is not verified along the first part of L1 since the beam is injected at 8 MeV and accelerated by the first cavity to 20 MeV. Both the input betatron functions and the quadrupole strengths must therefore be modified to compensate for the RF cavity effects. The solution is to provide a FODO sequence that is not formed of identical cells, and is designed to guarantee that the optical functions at the end of the section match the following FODO cell eigenvalues and that the average beam sizes are almost constant along the section.

Section L2 has double length cryomodules and in case of recirculation the e$^-$ beams passes through it twice. In the first passage the beam is accelerated from ≈56 MeV to ≈248 MeV, in the second it is further accelerated to the final nominal energy of ≈440 MeV.

The focusing lattice must therefore cope not only with the varying beam energy in any one pass but also with the different input energy of the two passes.

The proposed lattice is still a standard 120° phase advance FODO in which some adjustment of the quadrupole field must be provided to match the betatron functions; the cell is lengthened to 10.8 m to fit the cryomodule length. The average quadrupole strength is reduced to 1.6 m$^{-2}$, corresponding to a maximum gradient of 1.5 T/m. The overall beam size is only slightly reduced with respect to that in L1, because even though the emittance has been adiabatically damped the greater length of the FODO cell makes the betatron functions larger.

A triplet between L1 and L2 matches the optical functions between the linacs. Figures 2.1 and 2.2 show the optical functions and the beam transverse dimensions along L1, the matching section and L2.

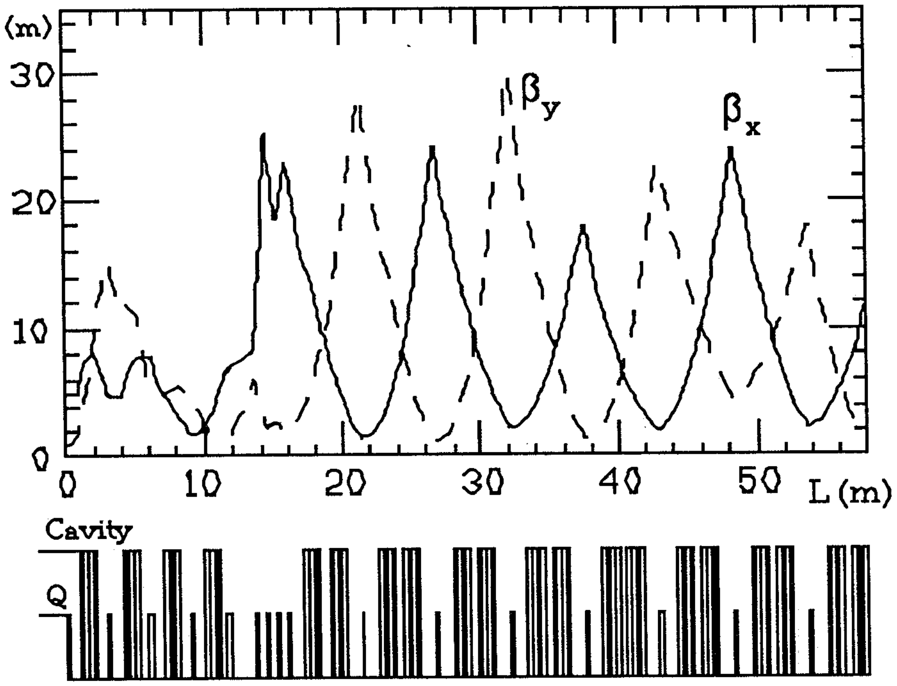

**Fig.2.1** - Betatron functions along linac L1, matching section and linac L2. Initial energy = 8 MeV; final energy = 248 MeV.

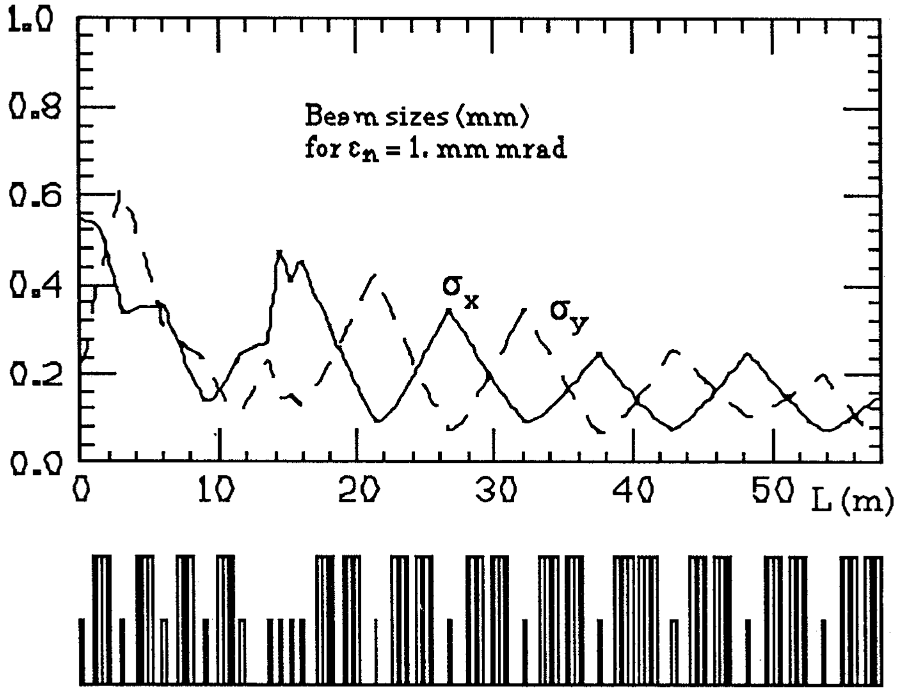

Fig.2.2 - Beam transverse sizes along linac L1, matching section and linac L2 for a normalized emittance of $1 \times 10^{-6}$ m rad. Initial energy = 8 MeV; final energy = 248 MeV.

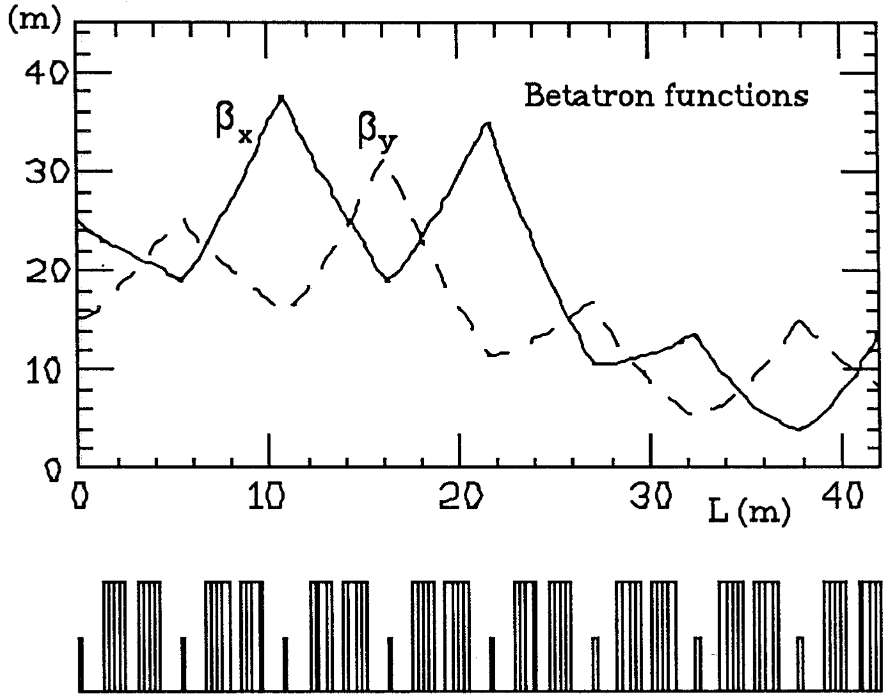

Fig.2.3 - Betatron functions along linac L2 on the second passage. Initial energy = 248 MeV; final energy = 440 MeV.

On its second passage through L2 the beam sees a weaker focusing structure, but the beam sizes are nevertheless kept smaller than 0.3 mm ( $\varepsilon_n \approx 1\mathrm{x}10^{-6}$ )

Figures 2.3 and 2.4 show the optical functions and the beam transverse dimensions on the second passage. The two transverse planes are of course interchangeable.

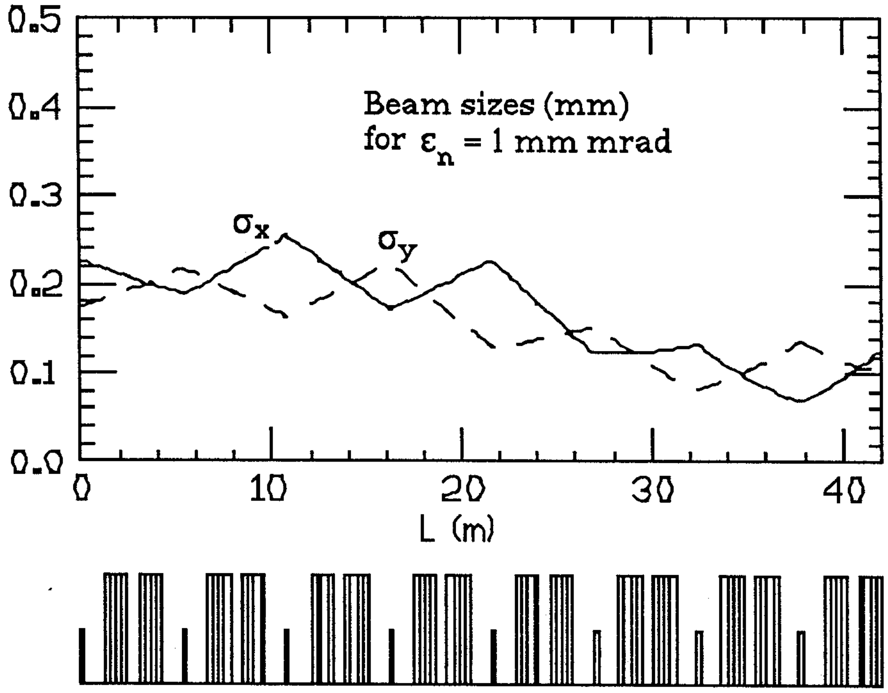

**Fig.2.4** - Beam transverse sizes along linac L2 on the second passage for a normalized emittance of $1\mathrm{x}10^{-6}$ m rad. Initial energy = 248 MeV; final energy = 440 MeV.

## 2.3 - Recirculation lattices

A possible recirculation arc lattice is here described for the 240 MeV electron beam. The recirculation line must fulfil two basic requirements: achromaticity and isochronism. Both depend on the trajectories inside the bending magnets and are therefore driven by the arcs.

We recall that, for ultrarelativistic particles, an isochronous line is also achromatic and that the condition of isochronism is fulfilled if the integral over the arc of the dispersion function normalized to the curvature radius vanishes.

To meet the above specification a symmetric configuration with four dipoles, each bending the beam through 45°, has been chosen. Negative dispersion is produced at the two inner dipoles, so as to compensate both the positive dispersion introduced by the two outer dipoles and that produced by the splitter.

The eigenvalues of the FODO lattice configuration along L2, described in § 2.2, provide the betatron function values at the output of L2; these are matched to those of the arc by a first matching section containing four quadrupoles. The matching conditions to be fulfilled by the other matching sections - at the other end of the first arc and at both ends of the second arc- are of course different and the sections will consequently be tuned differently.

The optical functions have been forced to be symmetric with respect to the center of the arc. Their maximum values are less than 20 m, and the maxima occur in the nondispersive region, where there is no momentum spread contribution to the beam size. In the region where the horizontal dispersion function, $D_x$, is non-zero the maximum value of dispersion is $D_x^{max} = 0.6$ m and $\beta_x$ is always less than 7 m.

The optical functions along the matching section and one-half arc are plotted in fig.2.5.

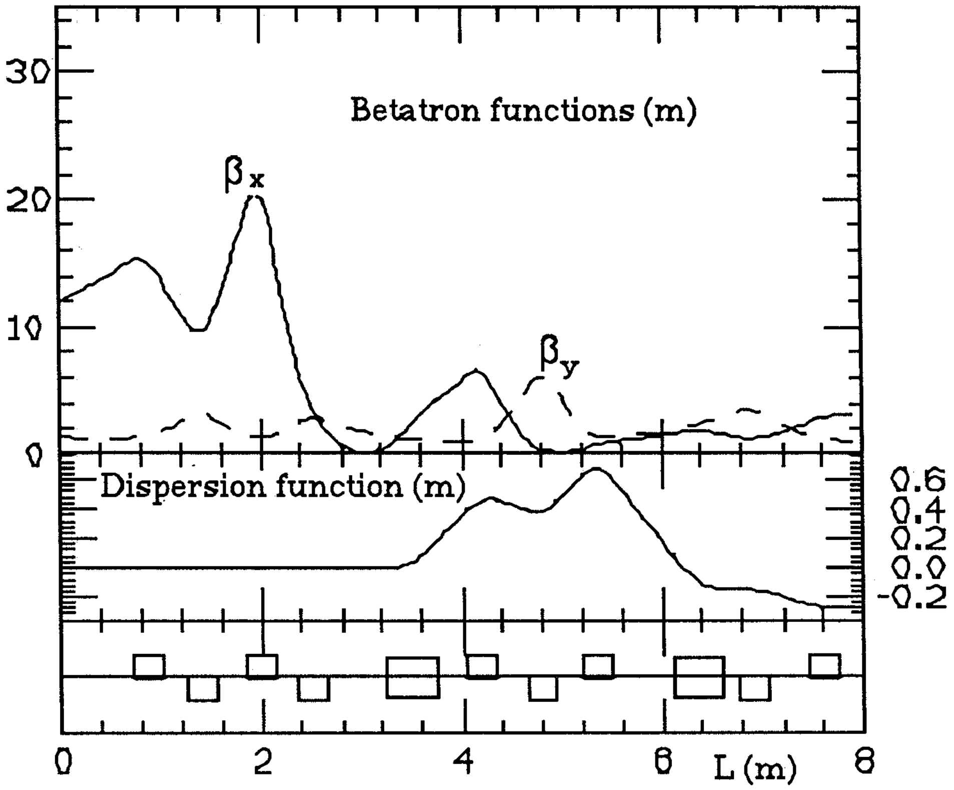

**Fig.2.5** - Optical functions in the matching section between L2 and the arc and along half recirculating arc .

The quadrupoles are 0.30 m long. The highest quadrupole field gradient is $G_{max} = 7$ T/m.

# 3 - BEAM DYNAMICS

## 3.1 - Introduction

The dynamics of an "ensemble" of charges in a linear accelerator is affected by the so called "collective forces". These forces are generated by the electromagnetic fields created by the interaction of the beam with the surrounding walls. They act back on the beam itself perturbing the dynamics of particles guided by the externally applied fields. The physical process is characterized by energy loss of the beam and, depending on the current intensity, by instability phenomena in both the longitudinal and the transverse dimensions.

Collective effects are analyzed in the time domain by means of the "wake-potentials", defined as the integrated field per unit charge experienced by a unit test particle travelling in the fields induced by the bunches accelerated in the linac, in both the longitudinal and the transverse dimension.

Single bunch dynamics is dominated by the intensity - over the length of the bunch - of the short range wakefield mainly originated by the interaction of the bunch current with sharp discontinuities in the vacuum envelope.

The dynamics of many bunches in a linear accelerator is instead affected by long-range wakefields mainly due to persistent (high-Q) parasitic resonant modes excited by the bunch current in the r.f. cavities or in other cavity-like objects.

## 3.2 - Induced Wake-fields

The longitudinal wake-potential is defined as the energy lost by a unit charge that travels in the e.m. field created by a point charge Q a distance τ away, in front:

$$w_z(\tau) = \frac{1}{Q}\int_d E_z\left(z, t = \frac{z}{c} - \tau\right) dz \qquad \text{[Volt / Coulomb]}$$

The above integral is relative to a point charge and defines the impulsive (Green function) wake-potential. The effective wake potential seen by a charge within a bunch depends on the bunch charge distribution $\rho(\tau)$ and can be calculated by means of the folding integral:

$$W_z(\tau) = \int_{-\infty}^{\tau} w_z\left(\tau - \tau'\right) r(\tau')\, d\tau' \qquad \text{[Volt / Coulomb]}$$

If the trailing charge is also subject to transverse forces, a transverse wake potential is introduced and defined as the transverse momentum kick per unit charge experienced by the test particle :

$$\mathbf{M}(\tau) = Q\int_{d} \left[\mathbf{E}(z,t) + \mathbf{v}\times \mathbf{B}(z,t)\right]_{\perp} dz \;\; ; \quad \text{with } t = \frac{z}{c} - \tau$$

$$w_{\perp}(\tau) = \frac{M(\tau)}{Q r_o}$$

By analogy with the longitudinal case we compute the effect on a real bunch, with a given space distribution, by applying the folding integral:

$$W_{\perp}(\tau) = \frac{M(\tau)}{q_1 q_2 r_o} = \int_{-\infty}^{\tau} w_{\perp}(\tau - \tau')\, \rho(\tau')\, d\tau'$$

The first step in the analysis of collective phenomena is to estimate the integrated longitudinal and transverse wakes. This can be done - more or less rigorously - by different methods.

For closed structures, both the longitudinal and the transverse impulsive wakes can be calculated as sums over the normal modes of the structure. This method is however in practice limited by the fact that r.f. cavities are not perfectly closed structures so that, above the iris cut-off frequency, some analytical correction is needed.

We estimated the impulsive wake potentials by applying general frequency-scaling laws to the SLAC and CEBAF wake-potentials. The approximated result has then been used to derive the bunch wakes and compare them with those calculated directly in the time domain by means of the TBCI computer code.

The code - severely limited by CPU time required for the huge number of mesh points - computes the wakefield induced by a gaussian bunch integrated over the bunch distribution that approaches the wake Green function for very short bunches . The scaled impulsive wakes are shown in Fig.3.1. The bunch wakes are compared to the TBCI results in Fig.3.2.

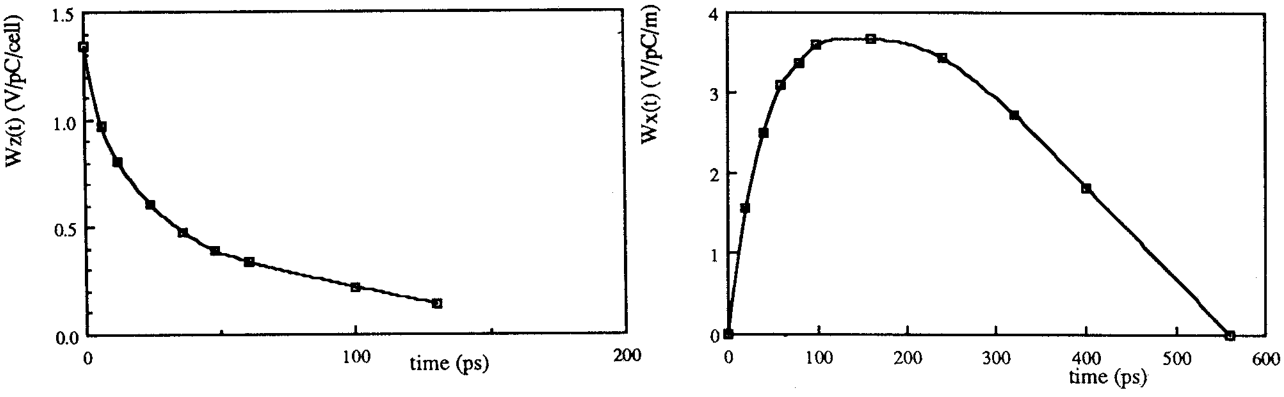

**Fig.3.1** - Scaled impulsive wakes.

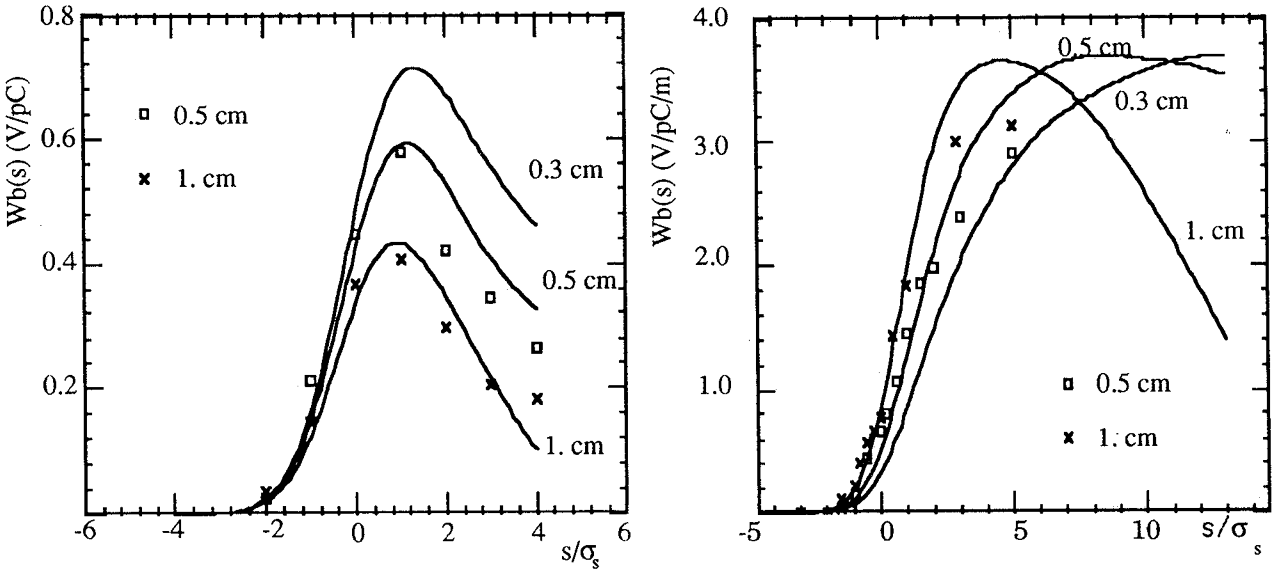

**Fig.3.2** - The bunch wakes compared to the TBCI results.

## 3.3 - Single bunch dynamics

### a) Longitudinal wake field

The short range longitudinal forces cause particles to lose an amount of energy that depends on their position in the bunch; the bunch therefore experiences an average energy loss and has an energy spread correlated to position along the bunch itself.

Using the longitudinal bunch wake-potential we can calculate the overall energy loss $\Delta U$ and the structure loss factor $k(\sigma_l)$ (energy lost per unit charge square) as:

$$\Delta U = Q^2 \int_{-\infty}^{\infty} W_z(\tau)\,\rho(\tau)\,d\tau$$

$$k(\sigma_l) = \frac{\Delta U}{Q^2}$$

The rms energy spread induced by wakefields in a monoenergetic bunch is calculated to be:

$$\sigma_E^2 = \int_{-\infty}^{\infty} [E - \langle E\rangle]^2 f(E)\,dE = \int_{-\infty}^{\infty} \left[W_z(\tau)\right]^2 \rho(\tau)\frac{d\tau}{Q} = \frac{\Delta U}{Q}$$

The resulting energy loss and energy spread for the case of the ARES Linac are given in Table 3.1, where the design values are also reported for comparison.

It must be remembered that, if required, the energy spread, because it is correlated to position, can be partly compensated by accelerating the beam off-crest, so as to make use of the slope of the external rf voltage.

Proper control of the energy spread to position correlation can also be used to produce NBS damping of the transverse motion.

### b) Transverse wake field

In the smooth focusing approximation the equation of motion for a test particle at longitudinal position z within the bunch and at position s along the linac is:

$$\frac{d}{ds}\left[\gamma(s,z)\frac{d}{ds}x(s,z)\right] + k^2(s,z)\,\gamma(s,z)\,x(s,z) = \frac{e}{mc^2}\int_z^{\infty} dz'\,\rho(z')\,w_\perp(z'-z)\;x(s,z')$$

Assuming a linear dipole wake $w_\perp(z) = w_\perp' \cdot z$ , this equation has been solved - by a perturbation method - for a rectangular charge distribution of length $l$. The result is :

$$x(s,z) = x_0\sqrt{\frac{E_0}{E(s)}}\,e^{iks}\sum_{n=0}^{\infty}\frac{1}{n!\,(2n)!}\left(\frac{\eta}{2i}\right)^n$$

where

$$\eta = \left(\frac{1}{2}-\frac{z}{l}\right)^2 \frac{eQw_\perp' \, l}{Kg}\ln\left(1+\frac{gs}{E_0}\right) = aQl\left(\frac{1}{2}-\frac{z}{l}\right)^2$$

being: g the energy gradient, K the integrated focalization and the front of the bunch at $z = l/2$

The term n=1 in the sum corresponds to the two-particle model; the model is applicable whenever the parameter $\eta$ is less than ~ 48, which is the case for all three SC linac sections.

If one imagines the bunch divided into thin slices, the amplitude of the n=1 term gives the maximum displacement of the center of the slice found at a distance z from the bunch head, namely.

$$\frac{\Delta x\,(z)}{x_o} = \frac{1}{4}\sqrt{\frac{E_o}{E_f}}\, a\,Q\,l\left(\frac{1}{2} - \frac{z}{l}\right)^2$$

It is clear that the model predicts a dilution in the (x,x') phase space. The new rms value of the particle x distribution is:

$$\sigma_x = \sqrt{\sigma_{xo}^2 + \sigma_{xw}^2}$$

with

$$\left(\frac{\sigma_{xw}}{x_o}\right)^2 = \frac{(a\,Q\,l)^2}{180}\frac{E_o}{E_f}$$

The corresponding emittance degradation is given by:

$$\frac{\Delta\varepsilon}{\varepsilon} = \sqrt{1 + \left(\frac{\sigma_{xw}}{\sigma_{xo}}\right)^2} - 1 \approx \frac{1}{2}\left(\frac{\sigma_{xw}}{\sigma_{xo}}\right)^2$$

For the worst-case parameters discussed in Paragraph 4. - Q = 15 nC and $l$ = 1cm - the computed emittance degradation is always less than 1% and is therefore negligible. The advantage of the low -frequency structure is here most evident.

**Table 3.1 - ARES Linac energy loss and energy spread**

| | | | | |
|---|---|---|---|---|
| Bunch Length, $\sigma_l$ | [mm] | 3 | 5 | 10 |
| Energy loss per cell | [keV] | .44 | .38<br>.41* | .29<br>.29* |
| Linac total energy loss | [keV] | 35. | 30.<br>33.* | 23.<br>23.* |
| Energy spread per cell | [keV] | .22 | .18 | .13 |
| Linac total energy spread | [keV] | 18. | 14. | 10. |

* TBCI calculations

# 4 - ELECTRON GENERATION

## 4.1 - Introduction

The general requirements for the generation and acceleration of electrons to be injected in the ARES LINAC have been discussed in References (14). The main requirements are the production of electron beams of very high quality as needed for single passage high gain FEL's and SC electron TeV colliders development.

The general layout of the linac is presented in Fig. 1.1. As shown in Fig. 1.1, the 48 MeV SC linac section L1, is fed by an electron injector, consisting of a SC RF gun, followed by a magnetic compressor. On the side of this high performance injector, the LISA injector, including the capture and preacceleration sections will be installed for preliminary tests.

## 4.2.- RF injector

As mentioned in the introduction, one of the most important design problems to solve for the design of TeV electron-positron colliders is the generation of intense, bright beams(6,7).

High current (some hundreds of Ampères) and low normalized emittance (some mm mrad) electron beams, accelerated to .5 ÷ 1 GeV, are also required for short wavelength (in the range from VUV to soft X rays ) high gain, high power, single-pass FEL's (8-12).

The accelerated beam brightness can not be higher than that generated at the gun and transmitted through the main accelerator injection system; the performance of the Linac injector is therefore a primary concern.

As extensively reported in a dedicated paper (16), it is foreseen to develop, for ARES, a state-of-the-art injector that could also produce the beams needed for possible tests of the LINAC against ring scheme, forseen as a promissing alternative for future Φ and B-Factories.

Preliminary results on the expected performance are reviewed in the following, together with the rationale of the choices that have been made. We remark here that the proposed SC laser-driven RF gun operating at 500 MHz (the ARES SC Linac frequency) and featuring a 30 MV/m electric field value at the photocathode, looks very promising; in particular, the low operating frequency guarantees that harmful RF and wake-field induced effects are much less severe than in other similar projects (17-19).

The use of superconducting cavities is mandatory for CW or high repetition rate operation with high electric field on the cathode surface. The clean environment, typical of a SC cavity, is also instrumental in lengthening the cathode lifetime (20).

A schematic drawing of the SC injector is presented in Fig.4.1. It consists of two, separately powered and phased SC cavities, the first one being equipped with a laser driven photocathode. The peak current delivered by the SC RF gun within a normalized emittance - at the injector output - of a few mm•mrad is of the order of a few tens of Ampères; a magnetic compressor is therefore needed to raise it to the level of some hundreds of Ampères. The second cavity, independently phased and powered, is needed to linearize the longitudinal phase space so that the magnetic compression can be fully exploited.

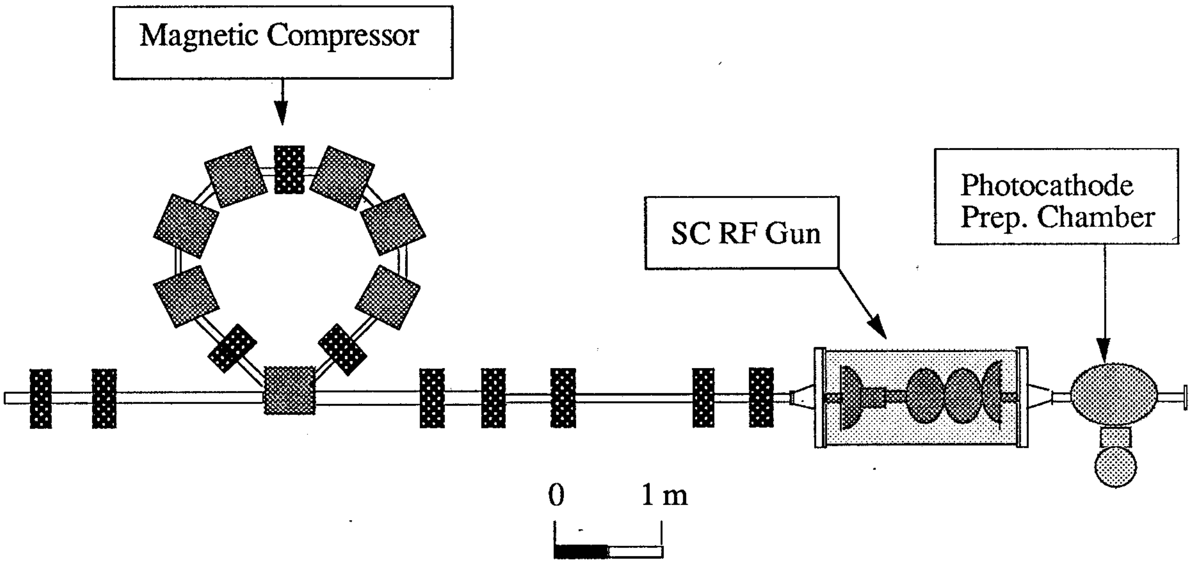

Fig. 4.1 - Schematic drawing of the superconducting RF injector. Magnetic compressor and photocathode preparation chamber are also sketched.

## a) Basic Theory

The geometry of the gun cavities and the cathode and laser pulse characteristics are dictated by the need to preserve beam quality throughout the injection system.

The main phenomena tending to raise the electron bunch transverse temperature and therefore to blow-up the normalized transverse emittance, $\varepsilon_n$, are:

- RF linear effects
- RF non linear effects
- Wake field effects

A detailed discussion of these effects is given in Reference (16).

Here we just recall, for a better understanding of the main design problems, the results of a first order estimate (16,21) of the transverse normalized emittance deterioration suffered by a bunch emitted and accelerated in the RF gun, based on the following approximations :

- the electric RF field on the axis is a pure sinusoid;
- off axis RF fields are derived through a linear expansion;
- wake field effects are neglected; the bunch charge density distribution can be either gaussian or uniform.
- the emitted bunch is mono-energetic and beam envelope variations through the gun are neglected (only transverse and longitudinal momentum transfers are considered).

We also note that our definition of the normalized emittance is the following (22,23):

$$\varepsilon_n = \sqrt{<x^2><p_x^2> - <x\,p_x>^2}$$

The results of the above approximations can be summarized in the following formula:

$$\Delta\varepsilon_{TOT}^2 = \Delta\varepsilon_{RF}^2 + \Delta\varepsilon_{sc}^2 + 2\,J_x\;\Delta\varepsilon_{RF}\,\Delta\varepsilon_{sc}$$

where $\Delta\varepsilon_{sc}$ is the emittance increase due to the space charge forces and $\Delta\varepsilon_{RF}$ is that due to RF linear effects, both computed at the injection phase $\phi_0$ that minimizes the emittance blow-up. $J_x$ is the transverse correlation factor(16). $\Delta\varepsilon_{SC}$, $\Delta\varepsilon_{RF}$ and $\phi_0$ are defined by the following equations:

$$\Delta\varepsilon_{sc}\,[\mathrm{m\ rad}] = \frac{5.7 \cdot 10^{-6} \cdot Q_b[\mathrm{nC}]}{\sin\phi_0 \cdot E_0[\mathrm{MV/m}] \cdot (3\sigma_r[\mathrm{m}] + 5\sigma_z[\mathrm{m}])} \qquad E = E_0 \sin(\omega_{RF}\,t + \phi_0)$$

$$\Delta\varepsilon_{RF}\,[\mathrm{m\ rad}] = .69 \cdot E_0[\mathrm{MV/m}] \cdot \sigma_r^2 \cdot (k_{RF} \cdot \sigma_z)^2$$

$$\left(\frac{\pi}{2} - \phi_0\right) \sin\phi_0 = 5.1 \cdot 10^{11} \cdot \frac{E_0[\mathrm{MV/m}]}{k_{RF}}$$

The normalized transverse emittance at the gun exit, $\varepsilon_{no}$, is given, in terms of the emittance at the cathode, $\varepsilon_{nc}$, and of the total emittance increase, by:

$$\varepsilon_{no} = \sqrt{\varepsilon_{nc}^2 + \Delta\varepsilon_{TOT}^2}$$

Under the approximation that all photo-electrons emerge from the cathode with the same energy (i.e. neglecting the straggling inside the cathode), assuming that this energy is given by the difference between the laser photon energy and the work function of the cathode material and considering a laser pulse with a double gaussian distribution in radius and time (with rms widths $\sigma_r$ and $\sigma_t$ ), the normalized emittance at the cathode surface, $\varepsilon_{nc}$, is given by :

$$\varepsilon_{nc}[\mathrm{m\ rad}] = \sqrt{\frac{W}{3m_0c^2}} \bullet \sigma_r[\mathrm{m}]$$

where: $W = h\nu_{laser} - W_l$ [eV] and $W_l$ is the $e^-$ work function

To minimize $\varepsilon_{nc}$ one can decrease the laser spot until the limit on the maximum cathode current density (typically 500 A/cm$^2$) is reached, giving a minimum laser spot radius of the order of 1 mm for some tens of Ampère of cathode current. All considered, typical values of $\varepsilon_{nc}$ range from ≈.8 to ≈ 2 mm•mrad.

Once the RF frequency and the peak value electric field on the cathode have been fixed, the value of the output emittance is a function only of the bunch charge, $\sigma_r$ and $\sigma_z$.

Figure 4.2 shows the iso-emittance lines as functions of the bunch spot radius and length for two different bunch charges, .5 nC and 10 nC. They are computed with the ARES parameters, namely an RF frequency of 500 MHz and a cathode peak field of 30 MV/m.

It can be easily seen that the emittance of short bunches is dominated by the space charge effect while that of long bunches is dominated by RF effects.

In defying the actual bunch shape the behaviour in the longitudinal phase space, not accounted for in the diagram, must also be considered. Too long bunches (≥ few tenths of RF degrees) come out curved in longitudinal phase space and the magnetic compressor can not operate efficiently. The emittance blow-up during bunch length compression has to be carefully evaluated to find the minimum compression energy at which it is still tolerable.

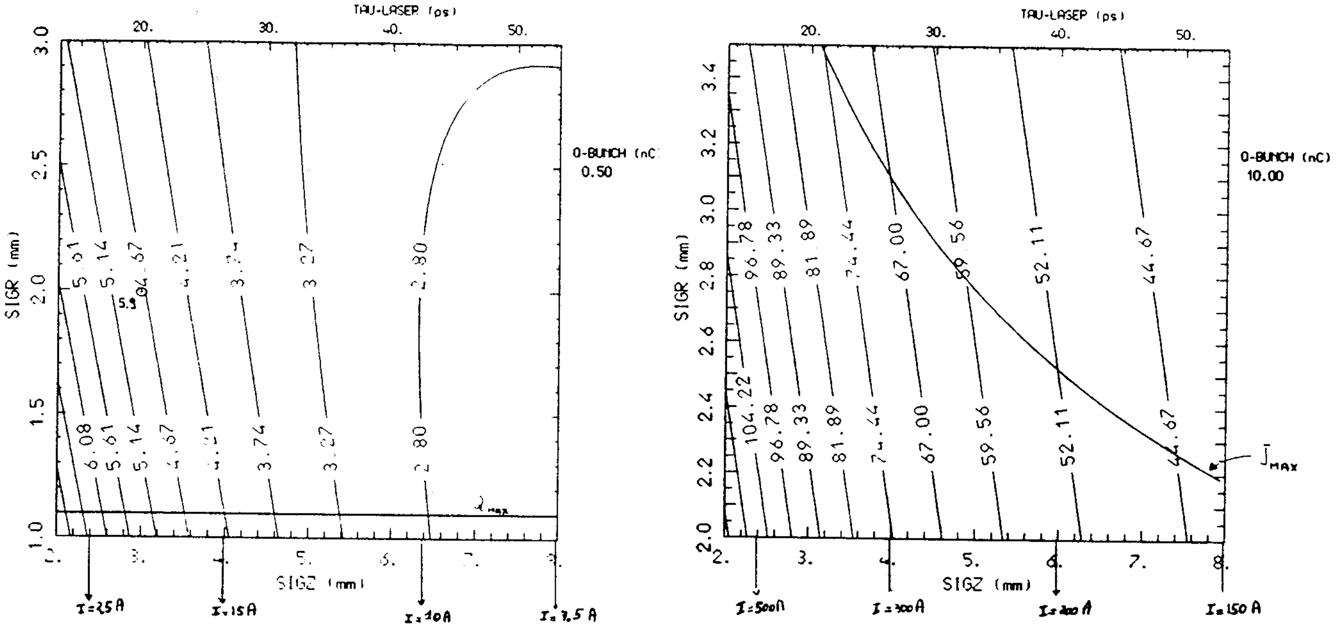

**Fig. 4.2** - Iso-emittance plot respectively for a 500 pC and a 10 nC bunch emitted and accelerated by a RF-gun: the RF frequency is 500 MHz, the peak field on the cathode 30 MV/m and the starting energy of the photo-electrons .2 eV, as typical for a semiconductor photocathode illuminated by a doubled Nd-YAG mode-locked laser. The plot shows the iso-emittance lines as functions of the bunch gaussian length ($s_z$) and radial width ($s_r$) in mm. The upper scale mark the values needed for the laser pulse time-length (FWHM) in ps, while the arrows show the current values expected at the gun exit. The values of the normalized transverse emittance that label the lines are in mm mrad. The dots show the value of the normalized transverse emittance computed by the PIC code ITACA.

## b) Computational tools

The behaviour of the transverse normalized emittance is dominated by the interaction of the bunch with its self-field, and of the self-field with the environment (i.e. the cavity surface) (16). That naturally claims for a numerical simulation procedure able to self-consistently describe both the self-field propagation inside the cavity and the electron beam dynamics in the presence of the RF field and of the self-field.

Numerical self-consistent procedures of the PIC (Particle In Cell) type have therefore been used to accurately estimate the behaviour of the emittance and of all other related beam dynamics quantities (energy spread, longitudinal emittance, etc.). Various codes, developed in the different laboratories have been available for quite some time, for instance MASK and PARMELA in Los Alamos (17,18) and Brookhaven(19) that take space-charge but not wake-field effects into account, in a manner that is not self-consistent, TBCI-SF (a self consistent PIC code of the MAFIA family) in Wuppertal(20).

A new PIC code, named ITACA(24,25), recently developed by some of the authors at the Milan University has been used to design the ARES RF gun. ITACA has been extensively checked against other codes, agrees well with other analytical and experimental results, and has novel features and distinctive advantages.

ITACA is an axi-symmetrical code which solves, self-consistently, a sub-system of the Maxwell + Newton Lorentz equations for cylindrical symmetric fields and sources. The bunch current is assumed to have radial and axial components and the self-field is assumed to be a monopole field ($TM_{0np}$-like). A specially developed charge assignment algorithm minimizes unphysical fluctuations in the driving term, and the equations of motion fourth-order integration algorithm can compute all quantities related to particle dynamics - notably transverse and longitudinal emittances, energy spread, rms divergence, etc - very accurately.

An eigenvector finder, that can compute the $TM_{0np}$ resonating modes of any axi-symmetrical structure, is included in the package to compute the accelerating RF field distribution inside the gun cavity.

The PARMELA-SUPERFISH code system, suitable for studying the bunch dynamics in the presence of the RF and the space-charge fields only, is operational both in Frascati and in Milan. It will be used to study the magnetic compressor.

### c) Results of the numerical simulations

The gun SC RF cavity design must not only comply with the requirements by beam dynamics, but also those needed for reliable operation beam dynamics at the maximum accelerating field.

Re-entrant cavities, that are more difficult to clean, were therefore 'a priori' discarded. A number of other constraints follow :

- Because enough space must be left free on the cut-off tubes for the main coupler and the HOM coupler, radius and length of the cut-off tubes must exceed certain minimum values. The proposed values are: 85 mm for the radius and 150 mm for the length.
- Because the cells must be coupled in the π-mode the coupling coefficient (usually a few percent) also has a minimum value determining the iris thickness and aperture.
- Because we are interested in maximum peak field on the cathode, the iris profile must such as to minimize the ratio between the maximum electric field on the iris and the field on the cathode

The trade off between beam dynamics and RF superconductivity requirements is not straightforward. Our first attack to the problem has been to check the beam dynamics performance of a well tested cavity geometry. One and a half cells terminated by a cut-off tube are needed: the photocathode is placed in the center of the flat end wall of the first first half cell and the next cell, tuned to the same frequency, provides two further free parameters. The main coupler and the HOM coupler are attached to the cut-off tube.

The selected geometry is that of the ARES 500 MHz cavity, with only one and half cells. The peak field on the cathode is 30 MV/m, corresponding to an average accelerating field of about 13 MV/m, approximately 30% higher than the ARES cavity nominal field. The value should not prove excessive considering that one deals with a single dedicated structure with only one and a half cells.

The $TM_{010-\pi}$ accelerating mode is computed using the RELCAV part of the ITACA package. The energy stored in the cavity is about 86 J, with an R/Q of about 210 Ohm.

The beam dynamics simulations have been carried out for three different values of the bunch charge (100 pC, .5 nC and 1 nC) each with a different pulse length, typical of the ARES foreseen modes of operation. The results are summarized in Table 4.2. Note that the different values of the optimum injection phase, due to the different time lengths of the laser pulse, cause slight variations of the gun output energy.

A complete analysis of the data is given elsewhere(16); it however worth pointing out once more that , because the head of the bunch enters the second cell too early, when the RF field sign has not yet reversed, and gets a slight deceleration, the longitudinal phase space at the cavity output is slightly curved, especially towards the bunch head ( see Fig. 4.3). The effect is more pronounced for longer bunches and limits strongly the performance of the magnetic compressor.

The latter, usually consisting of four dipoles, rotates the bunch in longitudinal phase space so as to decrease the bunch-length. The rotation, based on path length differences for particles of different momenta, exploits the strong correlation between energy and phase, clearly visible in Fig. 4.3. The path length difference versus momentum is represented in TRANSPORT notation by the R56 matrix element.

## Table 4.2 - SC Gun Parameters

| | | | | |
|---|---|---|---|---|
| Bunch charge | [nC] | .1 | .5 | 1. |
| RF injection phase | [Deg] | 56 | 60 | 48 |
| Laser spot ($s_r$) | [mm] | 2 | 2 | 2 |
| Laser length ($2s_t$) | [psec] | 40 | 20 | 47 |
| Output energy | [MeV] | 6.8 | 7.3 | 6.7 |
| Energy spread (rms) | [KeV] | ± 68 | ± 28 | ± 30 |
| Bunch radius (rms) | [mm] | 6.3 | 6.3 | 5.3 |
| Bunch length (rms) | [mm] | 12.1 | 5.9 | 14.2 |
| Bunch divergence (rms) | [mrad] | 6.0 | 5.9 | 6.2 |
| Bunch transv. norm. emitt. | [m rad] | $1.4 \cdot 10^{-6}$ | $5 \cdot 10^{-6}$ | $4.2 \cdot 10^{-6}$ |
| Bunch long. norm. emitt. | [m rad] | $\approx 10^{-5}$ | $2.6 \cdot 10^{-5}$ | $2.7 \cdot 10^{-5}$ |
| Peak curr. (no compression) | [A] | 4.8 | 20.2 | 16.3 |
| Peak current (with comp.) | [A] | 5.2 | > 200 | 25 |

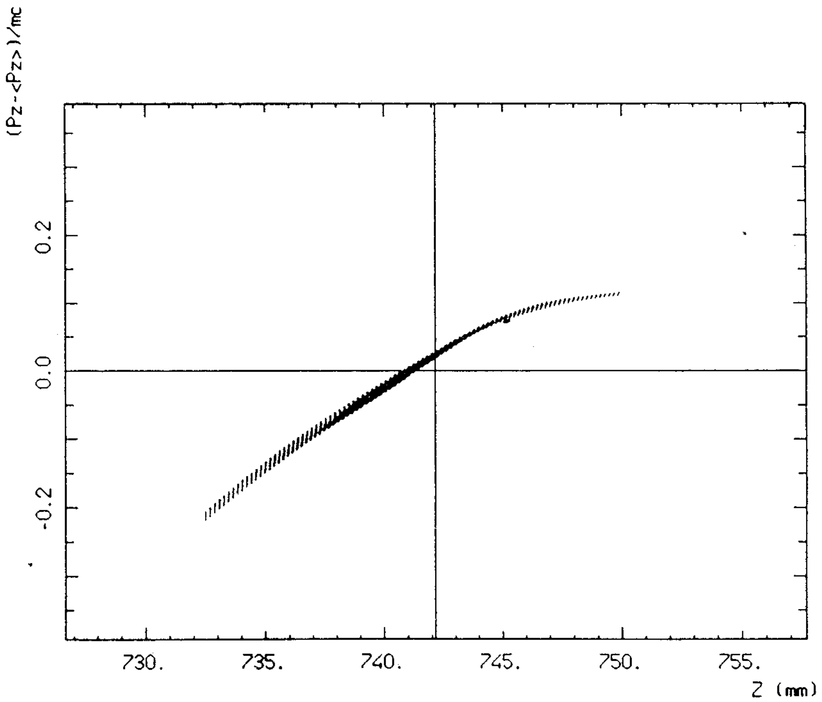

Fig. 4.3 - Longitudinal (z[mm], $\Delta p_z$) phase space at the exit of the gun for the case of the .5 nC bunch. The momentum deviation is in unit of $m_0c$. The peak current in the bunch is 20 A.

The case corresponding to R56 = -.73 cm/percent and .5 nC, one obtains at the compressor output the longitudinal phase ellipse shown in Fig. 4.4. The output current is about 200 A, with a rms bunch length of .8 mm. As evident from the figure, the more the correlation in phase space is linear the higher is the output current.

The behaviour of the bunch energy and energy spread are presented in Fig. 4.5 for the case of the .5 nC bunch. The other two cases (100 pC and 1 nC) are quite similar. The rms divergence and radius at the exit of the gun are fully compatible with the expected acceptance of the magnetic compressor.

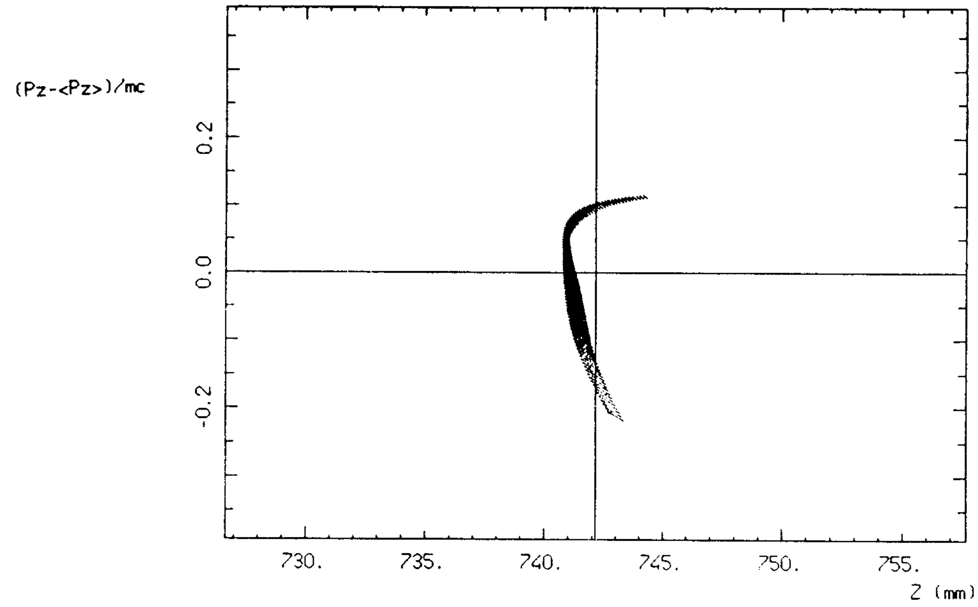

Fig. 4.4 - Longitudinal (z[mm], $Dp_z$) phase space after the magnetic compressor for the case of the .5 nC bunch. The magnetic compression is achieved applying in the transport matrix, representing the magnetic compressor, R56 = -.73 cm/percent. The peak current is 200 A.

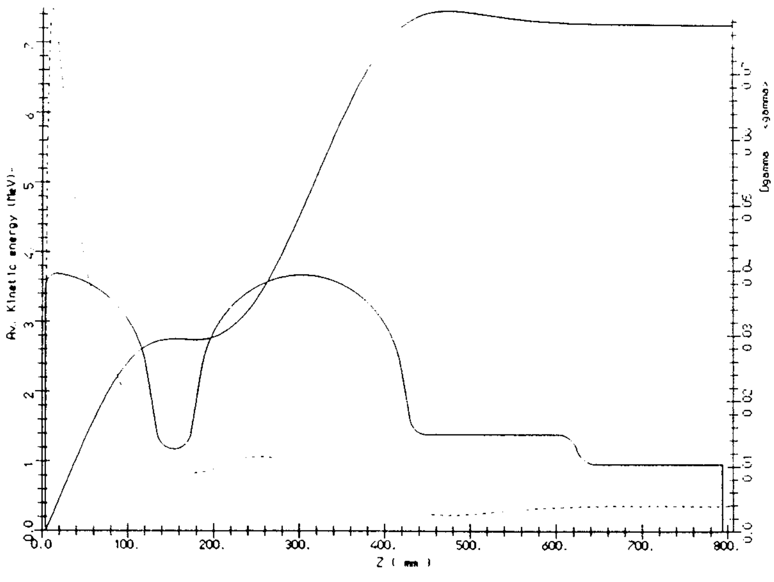

Fig. 4.5 - Bunch energy (left scale, solid line) and relative rms energy spread (right scale, dashed line) behaviours during the acceleration of a .5 nC bunch in a SC RF gun with a modified geometry. The final energy is 5. MeV and the final energy spread (rms) is ± 40 keV (.8 % of the final energy). On the diagram, the boundary profile of the gun cavity is also plotted.

For a fixed gun cavity geometry, higher injection phases give better longitudinal phase space distributions: since higher injection phases also reduce the transverse emittance blow up by space-charge forces, one is interested to push up the injection phase as much as possible. One solution that has been considered as a possible alternative is the addition of a third harmonic cell to flat-top the RF field. A preliminary study shows that the price paid is a severe degradation of the transverse phase space because of the effect of the smaller iris of the 1500 MHz cell.

A more promising idea, is to add a single, fully decoupled first-harmonic cell, as shown in Fig. 4.6. The extra free parameter - the injection phase into the extra cell - can be used to decouple the actions on longitudinal phase space from those on transverse phase space, to further optimize both (16). Work on the decoupled cell geometry is in progress.

The data given in Table 4.3 are a sample of what can be obtained - after only a preliminary optimization and for two typical bunch charges - including the first harmonic de-coupled cell. They are sufficient for significant experiments to be performed on both collider-grade beams and X-UV FEL's. The normalized transverse emittance could be in principle lowered by increasing the peak field on the cathode.

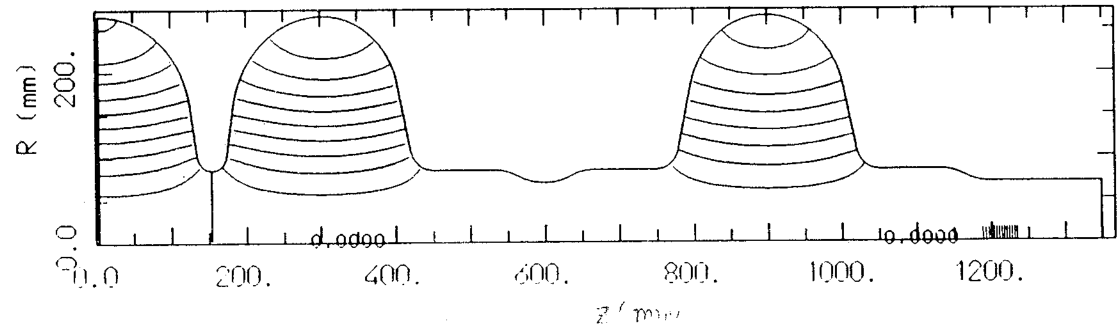

**Fig. 4.6** - Boundary profile of the SC RF gun attached to a single full-decoupled cell. See text for details.

**Table 4.3 - RF Injector Expected Performances**

| | | | |
|---|---|---|---|
| Bunch charge | [nC] | .5 | 10 |
| Output energy | [MeV] | 10 | 10 |
| Energy spread $\Delta\gamma/\gamma$ | [%] | ± .5 | ± 3 |
| Bunch transv. norm. emittance | [m rad] | $< 5 \cdot 10^{-6}$ | $< 4 \cdot 10^{-5}$ |
| Peak current; no compression | [A] | 20 | 200 |
| Peak current; with compression | [A] | 400 | 1000 |

### d) Photocathodes

Laser-driven photoemissive electron sources have the capability of emitting the high density, properly shaped, electron bunches required by the RF gun operation, to achieve the minimal emittance grow.

The specifications for the electron bunch from the cathode are listed in Table 4.4
A high quality electron emitter is needed in order to meet them. Standard thermionic dispenser cathodes have too low a current density and produce continuous beams ( at least at the ps level) that have then to be at low energy, where space charge effects dominate and blow the emittance up. Moreover the transverse component of the thermal motion of the emitted electrons gives a lower limit to the beam emittance that can not be overcome (17) .
The adoption of a photocathode is therefore mandatory.

**Table 4.4 - Electron bunch specifications**

| | | |
|---|---|---|
| Bunch charge | [nC] | .5 ÷ 20 |
| Pulse duration ($2\sigma_t$) | [ps] | 10 ÷ 40 |
| Spot radius ($\sigma_r$) | [mm] | 1.5 ÷ 3.5 |
| Current density | [A/cm$^2$] | 150 ÷ 700 |

The characteristics of the electron beams produced with various photocathodes in different laboratories, together with the photocathode material work function and quantum efficiency(26) are presented in Table 4.5.

We recall that the dependence of the current, I, delivered by a photocathode on the incident laser power, P, is given by :

$$I\,[A] = P\,[W] \bullet \eta \,/\, h\nu\,[eV]$$

where hν is the photon energy and η the photocathode quantum efficiency(14). As discussed above, the photon energy must be slightly higher than the work function of the photocathode material.

Photocathodes can be broadly classified into two categories: semiconductor photoemitters and metal photoemitters :

- Alkali semiconductor photoemitters ($Cs_3Sb$, $Na_2KCsSb$, etc.) are characterized by their high quantum efficiency and low work function. Current densities up to 600 A/cm$^2$ have been observed from a $Cs_3Sb$ photocathode, with laser pulse lenghts of 60 ps (27). Their drawback is extreme sensitivity to vacuum conditions (28).
- Metal photoemitters like Yttrium(29) and $LaB_6$(30) have relatively high quantum efficiency but still 2÷3 order of magnitude lower than semiconductor ones. They have some interesting properties : very long lifetime also in a relatively poor vacuum ($P \approx 10^{-6}$ mbar), very fast risetime (≈ ps) and easier preparation compared to alkali photoemitters.

Our specifications are best met by using cesiated semiconductor photoemitters - particularly $Cs_3Sb$ - and we expect that they can be placed inside the SC RF gun cavity (31).

The development of the preparation technology of cesiated photoemitters is in progress (20). In particular the photocathode preparation chamber developed at the Wuppertal University is shown in Fig. 4.7.

It should be added that other high quantum efficiency alkali photoemitters, like $Na_2KSb$, could also be used and that the laser system described in the next paragraph provides sufficient photon energy (3.5 eV) and enough pulse power (≈.2 mJ) to also operate metallic photoemitters A final decision on the type of cathode can therefore be taken later in the project.

**Table 4.5 - Photocathode Characteristics**

| Material | Work Function [eV] | Quantum Eff. | Current Dens. [A/cm$^2$] | Pulse Duration [ps] |
|---|---|---|---|---|
| $Cs_3Sb$ (K) | 1.6÷3 | $1 \div 3 \cdot 10^{-2}$ | 600 | 60 |
| GaAs (Cs) | 1.6÷2 | $4 \div 10 \cdot 10^{-2}$ | 180 | 70 |
| $LaB_6$ | 2.6 | $10^{-4}$ | 200 | $1 \cdot 10^4$ |
| Yttrium | 3.1 | $2 \cdot 10^{-4}$ | 500 | 2 |
| Magnesium | 3.6 | $10^{-4}$ | 20 | $3 \cdot 10^6$ |
| Copper | 4.5 | $6 \cdot 10^{-5}$ | 70 | $1 \cdot 10^4$ |
| Gold | 4.7 | $5 \cdot 10^{-6}$ | 500 | 10 |

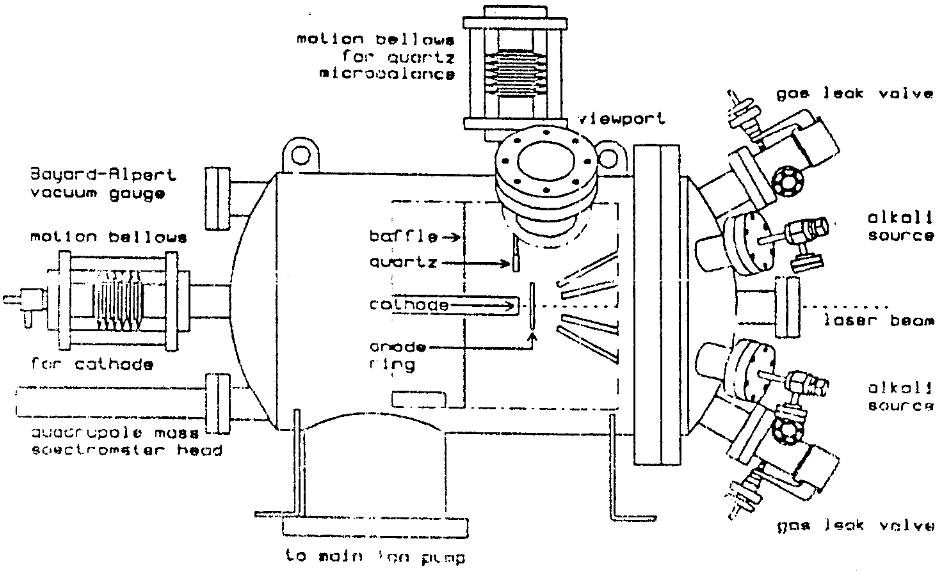

**Fig. 4.7** - Photocathode preparation chamber developed at the Wuppertal University.

### e) Laser system

SC TeV colliders ask for high charge and brightness electron bunches, while FEL operation asks for electron bunches having high peak current and brightness. For both applications the maximum possible repetition rate is forseen.

Even if the injection mode into the Φ-Factory is no longer envisaged(15), it is important to note that such an injector is also able to produce a continuous train of bunches at any sub-harmonic of the LINAC RF frequency. So that the beam of any ring having a bunch frequency which is a sub-harmonic of 500 MHz, could be used, together with the LINAC beam, for high disruption experiments in the LINAC-against-ring line.

The laser system proposed to meet all these requirement is a combination of a short pulse solid state laser and a dye lasers(32,33).

The main oscillator is a mode-locked CW Nd:YLF laser. It generates a continuous train of 35 picosecond long ($2\sigma_t$), low energy pulses. The output beam, which must have a sub-harmonic repetition rate (71.4 MHz in the proposed example), is locked to the 500 MHz RF master oscillator to keep the electron pulses in phase with the accelerating field; it is fed to different amplifier systems, depending on the machine mode of operation.

As shown in Fig. 4.8, line A, used for macropulses of high charge bunces, starts with a Pockel cell, that selects the right number of pulses. The two following Nd:YAG amplifier stages raise the pulse energy to the value required for extracting the desired electron bunch charge. A second and a third harmonic generator crystals then lower the infrared wavelength to visible and finally to near ultraviolet. The visible and the near ultraviolet pulses will be used alternatively, depending on the electron photoemission threshold of the photocathode.

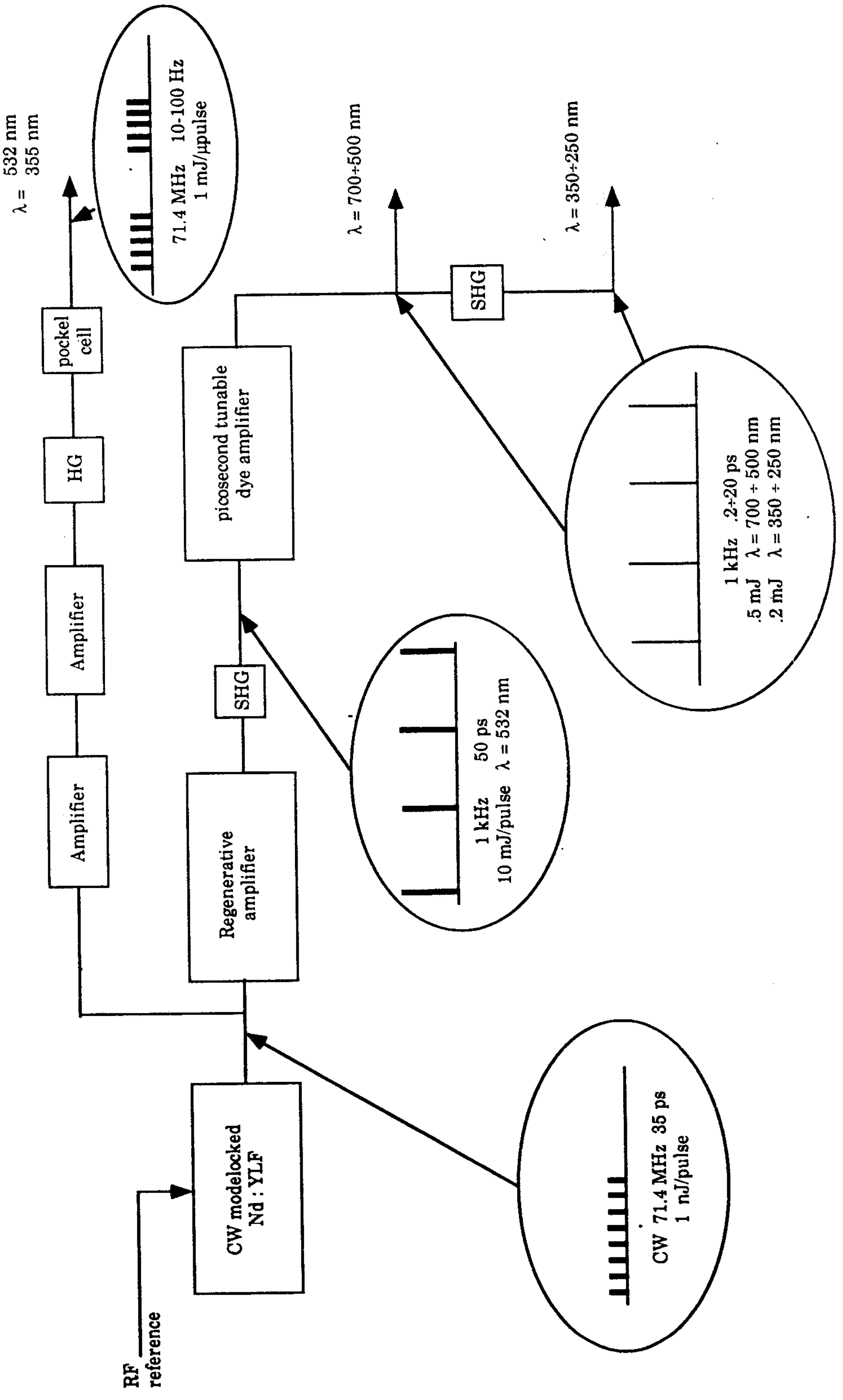

**Fig. 4.8** - Laser System main performances.

Line B, proposed for FEL operation and TeV collider injector development, contains a regenerative amplifier consisting of two Pockel cells and a large amplifier stage enclosed in an optical resonator. A single pulse is amplified in a multipass mode and delivered at 1 KHz repetition rate. After amplification, it is passed through a doubling crystal and then splitted in two:

- the first half is used to pump an ultrafast dye laser formed by two dye jets enclosed in an optical resonator, one being the active medium and the other the saturable absorber for pulse compression.
- the second half is used to synchronously pump three dye amplifier stages, through which the pulses coming from the ultrafast oscillator pass to be amplified.

The main characteristics of the system as presented are summarized in Table 4.6.

All laser components described and shown in Fig.4.8 are commercial and state-of-the-art. It should also be remarked that the field is in rapid evolution and that better performances, in particular higher repetition rates (>> 1 kHz), are to be expected in the near future .

**Table 4.6 - Laser System Characteristics**

| | |
|---|---|
| Tunability on a large wave length spectrum | 700 ÷ 250 nm |
| Variable micropulse length | 0.2 ÷ 20 ps |
| Continuous high energy pulse rep. rate | 1 kHz |
| High pulse energy | 0.2 ÷ 0.5 mJ |

### f) Diagnostics

A short list of the diagnostic tools that are an integral part of the RF Gun system is given below .

- A wall-current monitor, at the output of the last SC cavity, measures the beam current.
- The beam transverse emittance is measured by the pepper-pot method or using transition radiation.
- A streak-camera looking at the Cerenkov radiation from a quartz plate gives the bunch time profile.
- A magnetic spectrometer analyzes the beam momentum spread; an intercepting fluorescent screen, located at the position where the dispersion is largest, is looked-at by a TV camera.
- A Faraday-cup is used to measure the bunch charge.

## 4.3 LISA electron injector

As discussed above, the LISA injector(34) will be reassembeled lateral to the RF one. The major components are briefly presented in the following.

The injector consists of the following major parts:

- 100 keV thermoionic gun.
- Double chopping system..
- 500 MHz prebuncher.
- 1 MeV, 2.5 GHz capture section.
- Achromatic and isochronous transport line between the capture section and the SC Linac.

The other elements of the injector are: solenoidal focusing lenses, steering coils, collimators, current monitors, fluorescent screens.

All RF elements in the injector have been constructed and successfully tested.

The injector will be installed starting from next autumn.

### a) Injector Description

The block diagram of the 100 keV part of the injector is shown in Fig. 4.9.

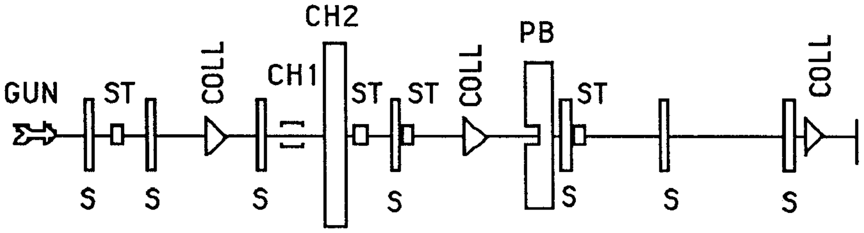

Fig. 4.9 - Sketch of the injector line at 100keV. S = Solenoidal lenses; ST = Steerings; COLL = Collimator; CH1 = Chopper 1 (50MHz); CH2 = Chopper 2 (500MHz); PB = Prebuncher (500MHz).

The gun(35) is a Pierce-geometry thermoionic triode which delivers a 1 ms macropulses beam at a repetition rate of 10Hz. The design parameters are: current I>200 mA, normalized emittance $e_n<10^{-5}$ m rad, energy W = 100 keV, energy dispersion $\Delta W/W = 10^{-3}$,.

A double chopping system has been chosen in order to operate with lower average current without diminishing the peak current, relaxing so the shielding requirements. The first chopper CH1 operates at the subharmonic frequency $f_1 = 50$ MHz and consists of a pair of deflecting electrodes. It selects 10% of the total current so that the beam afterwards is composed of a succession of micropulses at the frequency of 50 MHz. The second chopper CH2 is a RF copper cavity oscillating at f = 500 MHz in the deflecting $TE_{102}$ mode, with superimposed magnetic field on the beam axis. It selects a phase spread $\Delta\Phi_{ch}$ ranging between 36° and 60° over the wavelength according to the percentage of the total current that will be accelerated. Both choppers act deflecting vertically the beam; a pair of steerings corrects this deflection so that only the selected ~1% of the current passes through a collimator whose walls absorb the ~99% of the beam power.

The prebuncher is a klystron type microwave cavity oscillating in $TM_{010}$ mode at the same frequency of the superconducting cavities, followed by the corresponding drift (D=1.44m). The gap length is one tenth of the wavelength; the voltage is of the order of 10 kV; the bunching parameter is:

$$B_P = \pi\cdot D\cdot V_{PB}/V_g\cdot\lambda\cdot\beta_g = 1.4$$

where $V_g$ is the gun voltage, l the wavelength in the prebuncher, and $\beta_g$ the relative velocity corresponding to $V_g$.

The capture section is a normal conducting S-Band, standing wave, biperiodic $\pi/2$ graded $\beta$ accelerator, working at the fifth harmonic of the basic frequency, $f_{cs} = 2500$ MHz. It prepares the injection of the electron bunches into the SC Linac, which is a constant $\beta = 1$ structure, with sufficiently large $\beta$ ª 0.94, small phase bunch length $\Delta\phi$ n 1°-2° (@500MHz), and small energy dispersion $\Delta W/W$ n 1-2%. An axial magnetic field produced by superimposed solenoids counterbalances the radial defocusing forces due to either the space charge or to the radial component of the accelerating field.

The transport line between the capture section and the SC linac is achromatic to avoid dispersion in the horizontal phase plane and isochronous to avoid bunch lengthening. Since electrons are not fully relativistic at the injection energy, the spread in arrival time due to the energy spread has been taken into account and properly compensated with the trajectory length dependence on the dispersion function. The bending is obtained with three dipoles (45°, 90°, 45°) and two symmetric quadrupole doublets which adjust the dispersion function h to the isochronism condition which corresponds to :

$$\eta = \frac{L}{\sqrt{2}\gamma^{2}} - 2\sqrt{2}\,\rho\left(\frac{\pi}{4} - \frac{\sqrt{2}}{2}\right)$$

at the midpoint of the central dipole (L is the total line length, r the bending radius). Two triplets in front and after the arc take care of the matching between the linacs and the arc itself.

In the matching line between the capture section and the arc, a pulsed magnet deviates the beam to the spectrometer; the pulse timing is such that a single macropulse can be extracted, or the whole beam derived to the spectrometer arm. The spectrometer consists of two 60° sector bending magnets and two defocusing quadrupoles. The beam dimensions are analyzed on a fluorescent screen.

A bunch length measurement is foreseen exploting the spectrometer line: a vertically deflecting 2.5GHz cavity, positioned before the pulsed magnet, gives an angular kick to the electrons depending on their position along the bunch, causing a vertical widening of the beam spot on the screen proportional to the bunch length. To increase the sensitivity of the measurement a different set of quadrupole gradients will be used in this configuration which will give the optimum vertical phase advance between the cavity and the screen, so that while the energy measurement will be on-line this last diagnosic tool will be used only off-line.

All the magnets have been designed by means of the 3-D code Magnus; they are constructed with full Armco iron, except the two spectrometer laminated dipoles. The full iron magnets are home-made while the two laminated are built by a French firm. The characteristics of the magnetic elements are listed in Table 4.7 and the layout of the transport line is plotted in Fig. 4.10.

**Table 4.7 - 1.1 MeV Transport line element characteristics**

| Element type | Length [cm] | Gradient [gauss/cm] | Bending angle [degrees] |
|---|---|---|---|
| QUAD | 10.0 | -18.5000 | |
| QUAD | 10.0 | 17.0700 | |
| QUAD | 10.0 | -9.4570 | |
| BEND | 20.02765 | 1.1747 | 45. |
| QUAD | 10.0 | 13.2754 | |
| QUAD | 10.0 | -5.7083 | |
| BEND | 40.0553 | 1.1747 | 90. |
| QUAD | 10.0 | -5.7083 | |
| QUAD | 10.00 | 13.2754 | |
| BEND | 20.02765 | 1.1743 | 45. |
| QUAD | 10.0 | -10.7400 | |
| QUAD | 10.0 | 15.5000 | |
| QUAD | 10.0 | -8.7500 | |

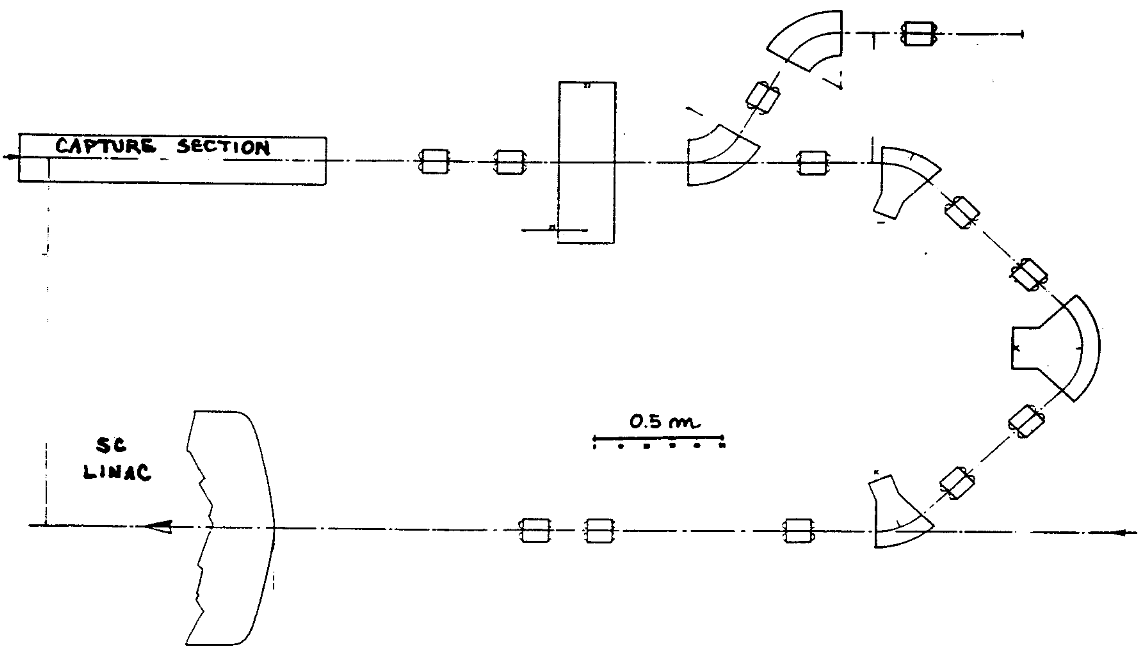

Fig. 4.10 - Layout of the transport line from capture section to SC Linac

### b) Particle dynamics

Tracking of particles along the injector has been carried out with a modified version of the program PARMELA simulating different currents, in order to determine the acceptance of the system in different working conditions.

The extremely high quality required for the beam asks for a careful adjustement of all the components of the line from the very beginning. In fact space charge problems influence the bunch transverse dimensions and the longitudinal phase space all along the transport. The maximum average current of 2mA in the Linac can be obtained using an extracted beam from the gun of 200mA and a chopping angle of CH2, $\Delta\phi_{ch}$ = 36°, or otherwise it is possible to decrease the initial current and to increase correspondingly $\Delta\phi_{ch}$. In fact the longitudinal space charge prevents the squeezing of the bunch to very short lengths at the input of the capture section. If the bunch length after the chopper system is longer the space charge effects are weaker for the same total current; furthermore decreasing the beam current intensity between the gun and the choppers the emittance growth due to transverse space charge can be avoided. So $I_{gun}$ = 120 mA and $\Delta\phi_{ch}$ = 60° have been chosen.

The increase of the beam emittance at low energies can be further reduced if the bunch length is not led to its possible minimum at the input of the capture section keeping the current density below critical values. The high peak current at higher energies can be obtained using the appropriate phase in the capture section, so that in the first cells of the section the beam is still under the bunching process. The longitudinal magnetic field produced by the solenoid around the section has been measured for different values of the current in the windings; the analytical expression obtained with a polynomial fit of the measured values has been introduced in the program PARMELA and used for particle tracking.

At the exit of the capture section the beam has circular symmetry and is highly focalized by the magnetic field of the capture section solenoid. The first two quadrupoles of the line are used to separate the two transverse planes and to recover the beam from a very small focus.

If the beam size inside a quadrupole is above a certain value (in our case with $\varepsilon_{x,y} = 5.6 \cdot 10^{-6}$ m rad, $e_{lim} \sim 0.9$ cm) the quadrupole field produces filamentation in the transverse phase space yielding to increase of the effective emittance value: the focusing kick given by the quadrupole is not linear with the distance from the axis, but distorted. This effect of course is significant only at energies up to the order of few MeVs and at low emittances. As the horizontal emittance conservation is more critical than the vertical one because of the presence of horizontal dispersion along the line, in the optical functions design special care has been put in keeping lower the horizontal betatron function inside the quadrupoles.

The achromaticity condition on the horizontal plane is satisfied only if the particle trajectories and their energies are not perturbed inside the dispersive region, so that the correlation is mantained between the particle energy and the displacement of the particle trajectory from the nominal trajectory. The space charge breaks this correlation, resulting in an increase of the horizontal emittance of about 20% along the dispersive zone. An increase of about 10% on the emittance occurs also for the direct action of the space charge forces while another 10% is due to the filamentation above described. The final vertical emittance results almost equal to the horizontal one. The beam emittances, $\varepsilon_u$ and $\varepsilon_u(\sigma)$, without and with space charge forces are plotted in Fig. 4.11. The bump of the horizontal emittance corresponds to the dispersive zone, because the momentum spread contribution to the beam size is included in the computation of the emittance. The envelopes are plotted in Fig. 4.12. The bunch length is plotted in Fig. 4.13. Table 4.8 gives the beam parameters in the principal points of the line.

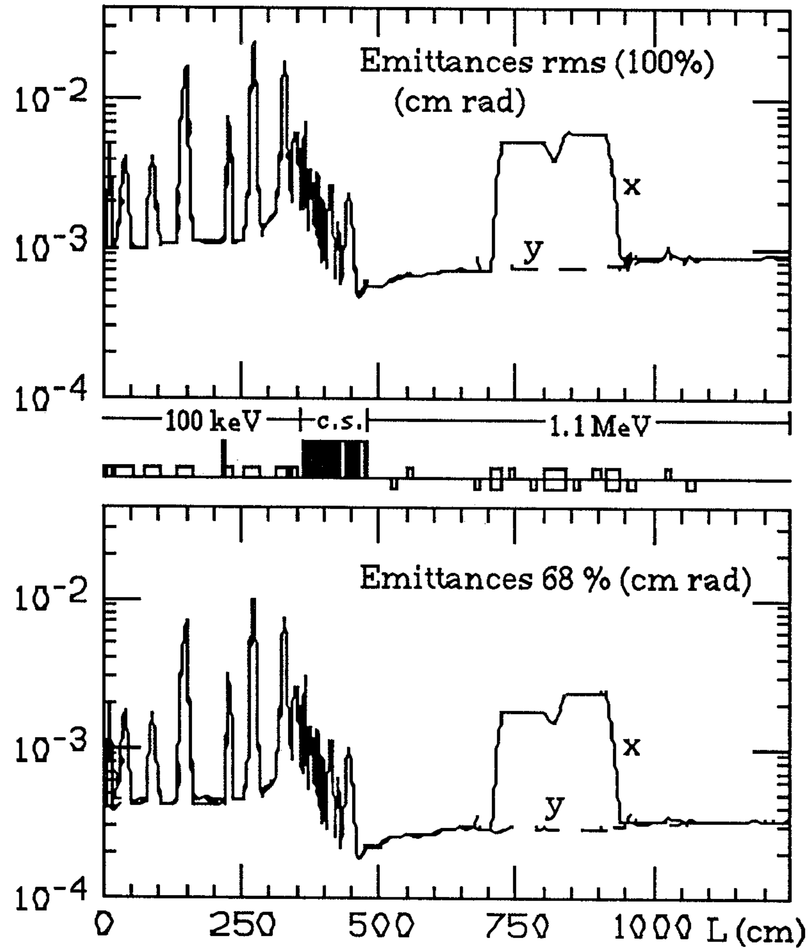

Fig. 4.11 - Beam emittances from gun to SC-Linac entrance

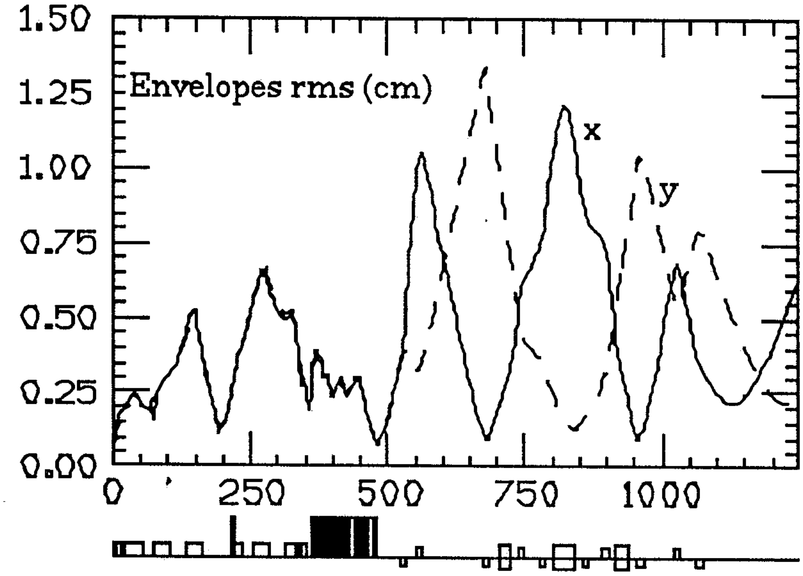

Fig. 4.12 - Beam transverse envelopes from gun to SC-Linac entrance

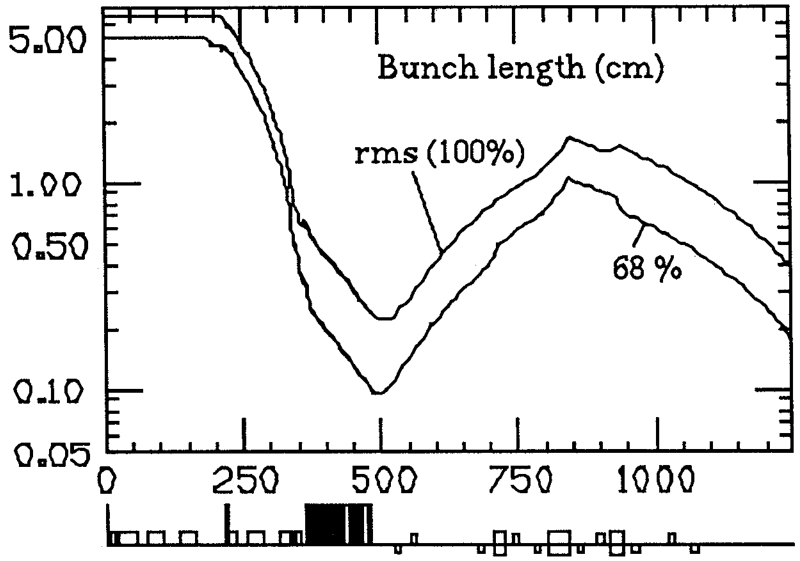

Fig. 4.13 - Bunch length from gun to SC-Linac entrance

**Table 4.8 - Beam parameters in the principal points of the line.**

| Beam Parameters | Gun output | Capture Section Input | Capture Section Output | SC Linac Input |
|---|---|---|---|---|
| $a_x$ | 0.0 | -6.0 | 0.66 | -3.8 |
| $\beta_x$ [m] | 0.025 | 0.5 | 0.24 | 4.4 |
| $\varepsilon_x$ [mm mrad] | 10.0 | 18.0 | 5.6 | 9.2 |
| $\varepsilon_x(\sigma)$ [mm mrad] | 4.3 | 7.2 | 2.3 | 3.4 |
| $e_x$ [mm] | 0.5 | 3.1 | 1.2 | 0.6 |
| $\alpha_y$ | 0.0 | -6.0 | 0.66 | -0.6 |
| $\beta_y$ [m] | 0.025 | 0.5 | 0.24 | 0.7 |
| $\varepsilon_y$ [mm mrad] | 10.0 | 18.0 | 5.6 | 8.4 |
| $\varepsilon_y(\sigma)$ [mm mrad] | 4.3 | 7.2 | 2.3 | 3.3 |
| $e_y$ [mm] | 0.5 | 3.1 | 1.2 | 0.3 |
| $E_0$ [MeV] | 0.10 | 0.098 | 1.17 | 1.17 |
| $\Delta E/E$ [%] | 0.01 | ±4.5 | ±1.5 | ±3.0 |
| $l_b$ (100%) [mm] | continuos | 7.0 | 3.1 | 3.8 |
| $l_b$ (68%) [mm] | continuos | 4.5 | 1.2 | 1.8 |
| $I_{av}$ [mA] | 120. | 2. | 2. | 2. |
| $I_p$ [A] | 0.12 | <1. | 6.4 | 4.3 |

# 5 - ACCELERATION SYSTEM

## 5.1 - Superconducting cavities

Superconducting cavities performances, compared to those of normal conducting cavities, outweigh the disadvantage of their very low operating temperature. In fact, their quality factor $Q_o$ being 4 ÷ 5 orders of magnitude higher than that of standard copper cavities, they can be operated CW - at low temperature - while the large amount of stored energy makes for a much reduced beam energy spread.

For the construction of high acceleration field cavities for ultrarelativistic particles, the use of bulk Niobium is favoured because of its relatively high critical temperature, $T_c = 9.2$ K, and its good mechanical properties compared to those of other superconducting metals.

At 500 MHz, theoretical upper limits can be derived for the corresponding accelerating field and Q values from the Nb upper critical field ($H_{c2}$ = 1600 Gauss) and from its surface resistance, $R_s$, at 4.2 K calculated from the BCS theory of superconductivity ; one obtains : $E_a \approx 40$ MV/m and $Q_o \approx 4 \times 10^9$ (36).

With present technology, fields in the range of $E_a \geq 10$ MV/m (at 4.2 K and 500 MHz) and low-field Q values ≈ $3.4 \times 10^9$ are routinely obtained in vertical tests of four-cell cavities. Degradation of $Q_o$ vs $E_a$ and of the maximum $E_a$ when cavities are horizontal, are topics under investigation. The field emission of Nb surface in SC cavities, a factor limiting the obtainable Q at high surface electric fields, is related to the surface cleaning: it has been ascertained that very clean Nb surfaces can support fields larger than 100 MV/m without electron emission.

To raise $Q_o$, SC cavities can be operated at lower temperatures; this does not however usually improve $E_a$ in the same way because $E_a$ is limited by the presence of non superconducting defects. These defects also produce the so called "residual" surface resistance, $R_{res}$. The value of $R_{res}$, that can not be computed from theory because it depends on the actual surface physical and chemical conditions, of course sets the lowest useful temperature of operation, below which no further benefit on $Q_o$ is obtained.

The presence of surface defects is considered unavoidable and the main effort over the past 10 years, has been devoted to reducing their size and number and to handle the local heating they generate. In fact better cryostabilization by using high thermal conductivity Nb, is the best techinque known to raise $E_a$.

The same idea underlies the technique of sputtering thin Nb films on copper cavities (37). In addition one saves the cost of the ultrapure bulk Nb, which can reach 20÷25 % of the overall cost of a fully equipped horizontal cavity. Finally, one hopes to be able to sputter different superconductive materials with higher critical temperatures and/or lower RF losses.

For ARES, the standard bulk Nb technology has been adopted as a first approach, with some mechanical improvement. developments in the field of copper coated cavities are also in progress (38). Experimental studies on the superconducting properties of Niobium alloys and compounds (NbN, NbTi, NbZr ) realized in form of thin films are also in progress. Some results on NbN films are reported in TAB 5.1.

**TABLE 5.1 - NbN superconducting thin films**

| | Ar [mbar] | $N_2$ [mbar] | $N_2$ flow [sccm] | Deposit. rate [Å/s] | Sputter power [W] | Measured thickness [Å] | $T_c$ [K] |
|---|---|---|---|---|---|---|---|
| NbN 1 | $1\ 10^{-2}$ | $2.0\ 10^{-3}$ | - | - | 609 | - | 0 |
| NbN 2 | $1\ 10^{-2}$ | $2.0\ 10^{-3}$ | - | - | 900 | - | 4.1 |
| NbN 3 | $5\ 10^{-3}$ | $3.4\ 10^{-4}$ | - | 10.5 | 598 | 2300 | 11.66 |
| NbN 4 (*) | $5\ 10^{-3}$ | $3.0\ 10^{-4}$ | - | 10.5 | 575 | 3500 | 14.5 |
| NbN 5 | $5\ 10^{-3}$ | $3.4\ 10^{-4}$ | 24 | 10.5 | 585 | - | 0 |
| NbN 6 | $5\ 10^{-3}$ | $1.2\ 10^{-4}$ | 10 | 10.5 | 432 | 2500 | 10.5 |
| NbN 7 (*) | $5\ 10^{-3}$ | $1.2\ 10^{-4}$ | 10 | 10.5 | 407 | 1200 | 11.25 |
| NbN 8 | $5\ 10^{-3}$ | $2.0\ 10^{-4}$ | 15 | 10.5 | 484 | - | 11.33 |
| NbN 9 (*) | $5\ 10^{-3}$ | $2.0\ 10^{-4}$ | 15 | 10.5 | 484 | 900 | 11.6 |
| NbN10(*) | $5\ 10^{-3}$ | $2.6\ 10^{-4}$ | 20 | 10.5 | 545 | 1200 | 12.3 |

*Deposited on sapphire substrate

In the following we discuss the design of the ARES superconducting cavity and the rationale behind the choice of its main parameters. A summary of the R&D program that has been started in collaboration with Italian industry is also presented, together with the expected milestones to reach the specified performance.

## a) Frequency

To guarantee the high quality of beam specified in paragraph 4.2.1, we are forced to select a SC Linac frequency on the low side of the .35 GHz ÷ 3 GHz range currently used for the acceleration of ultrarelativistic beams. In fact one can show (1) that to ensure the kind of single bunch performance required for linear colliders and FEL's, the frequency should lie below 1500 MHz.

If we further restrict the choice to most commonly used frequency values, we are left with only two frequencies : 350 MHz, developed and used at CERN, and 500 MHz, developed and used at DESY, KEK and on LISA in our own Laboratory.

From a purely technical point of view, the advantages of 500 MHz over 350 MHz are mainly three:

- 500 MHz is a sub-harmonic of other widely used frequencies: 1, 1.5 and 3 GHz ;
- standard power sources are easily found on the market ;
- the cavities and their ancillary equipment, being smaller, are easier to handle.

The last argument is of course important but the two others are more fundamental since they are linked to the positron capability required from our Linac and, we believe, to the development potential of the accelerator.

In fact, from the latter point of view, one of the goals of ARES is to produce a very low emittance beam, with high peak current and high repetition rate, so that the installation may become a test bench for future TeV colliders.

As shown by several authors (37) a fully superconducting linear accelerators may become advantageous for SC TeV Colliders if accelerating fields exceeding 30 MV/m can be achieved since the cost would then become competitive - for long (10÷20 cells) structures in the frequency range upwards of ≈ 3 GHz - with that of warm structures. The rate of increase of the useful field in SC cavities over the past 10 years, together with the number and quality of R&D programs in progress all over the world, make it reasonable to envisage that the goal will be reached in the not too distant future. In a 3 GHz Collider, however, the high peak current, high bunch charge, low emittance first part of the accelerator (below ≈ 1GeV) would presumably have to operate at much lower frequency. ARES could therefore be considered as a prototype of the injector for a TeV collider and, as such, it should be operated on a subharmonic of one of the higher standard frequencies.

A number of other minor advantages and disadvantages can be found for each of the two frequencies. Some the arguments that are usually given and that, in our opinion, balance out are:

- the 350 MHz cavity has a lower RF power loss per meter of active length. In fact the BCS part of the surface resistance, at a given temperature, scales like $\omega^2$.
- for a constant number of cells, 350 MHz requires less cavities and less associated equipment. For a given $E_{acc}$, the numbers scale like $\omega$.
- the 500 MHz cavity has a smaller surface (it scales like $\omega^{-2}$ ) and therefore, presumably, a smaller number of field emitters and defects that limit the maximum field holding capability and produce the negative slope in the measured Q versus $E_{acc}$ curves.
- the 500 MHz cavity smaller overall dimension, scaling like $\omega^{-3}$, give greater freedom to implement and test cleaning techniques.

It is our conclusion that with 500 MHz cavities the chance obtaining the high specified design value of $E_{acc}$ is greater.

Moreover, on an overall project basis, it has to be taken into account that the slight capital cost increase for cavities is almost exactly balanced by the lower cost of the RF power sources, which - at 500 MHz and for the ARES power level - are standard and available from stock.

### b) Cavity Geometry

Once the operation frequency has been fixed, the base cavity geometry has to be optimized to best meet the overall design specifications, and all the ancillary equipment has to be designed. In practice, as far as geometry is concerned, the only important parameter is the number of cells because, since 1979, all SC accelerating structures for ultrarelativistic particles are either spherical or elliptical. As a consequence, apart from the frequency scaling factor, they differ just on minor details (usually dictated by the fabrication procedure) that affect the overall cavity parameters only marginally .

The origin of this uniform design were the experimental results first obtained in Genova(39), and later confirmed by other Laboratories (40,41), showing that multipacting - at that time the foremost field limitation - was suppressed by giving the cavity a proper (spherical or elliptical) shape.

For ARES we choose four cells per cavity, a reasonable compromise between filling factor (which increases with the number of cells) and maximum field holding capability (which decreases with the number of cells).

As mentioned above, the technology used for cavity fabrication has some influence on the nominal cavity dimensions. Moreover the achievable mechanical tolerance and reproducibility, also dependent on the fabrication technique, are essential for the quality of the SC cavity.

To gain some insight on the problem of tolerances let us make some general consideration.

In this type of cavity the resonant mode used for acceleration is the $TM_{010\text{-}\pi}$, in which the accelerating field in two adjacent cells has the same amplitude but opposite sign.

A $TM_{010\text{-}\pi}$-like mode exists for any multicell cavity, but to have this mode at the nominal frequency, with almost the same field amplitude inside each cell (field flatness of few per cent), each cell - with its real boundary conditions determined by the adjacent cells and the cut-off tubes - must resonate at exactly the same, desired frequency. The sensitivity is of few kHz per percent of field flatness.

From a purely mechanical point of view this means that the shape of each cell should be identical to the ideal one to the order of a few hundredths of a millimetre; in practice however the resonant frequency is an integral property of the cell volume. The way the resonant frequency depends on the cell geometry can be better understood by looking at Fig. 5.1 that shows the sensitivity curves (for the $TM_{010\text{-}\pi}$ mode) for a 500 MHz half cell, scaled from the LEP design. The sensitivity is expressed as the frequency variation, in KHz, for a change of one $cm^2$ in the area of the cell axial cross section (42).

It can be seen that :

- standard mechanical tolerances are at least one order of magnitude too large: the sensitivity on the value of the equatorial diameter is of the order of 1MHz per millimetre when a frequency accuracy of less than $\approx$ 20 kHz is desired.
- using the degree of freedom afforded by the axial position of the actual profile, a volume compensation is possible, with respect to the $TM_{010\text{-}\pi}$ accelerating mode, which gives a good equivalence, between the real translated geometry and the theoretical one.

A technique to manufacture cells that are identical from the electromagnetic point of view, in spite of mechanical tolerances, has therefore been implemented in collaboration with an industrial firm. It consists essentially in measuring the profile of each half cell and then cutting it so that an equivalent shift of the cell profile in the axial direction - and a consequent electromagnetic compensation, according to the concept of volume equivalence mentioned above - are produced.

This technique has been successfully tested on a number of Cu and Nb half cells, produced by spinning under the supervision of ANSALDO CO. As a further improvement, it has been decided, for the ARES cavities, to change the fabrication technology, from spinning to deep-drawing. The reason is mainly that deep-drawing is intrinsically more reproducible, so that the need for costly compensation procedures is drastically reduced. Moreover, because cell obtained by deep drawing and electron beam welding, once tuned to the proper frequency, are mechanically almost identical to each other, the actual field distribution of higher order modes (HOM) is much better known and HOM couplers can be rendered much more efficient.

A comparison of the results obtained at KEK(43) , where deep-drawing is used, with those of DESY(44) and CERN(45) , where half-cells are spinned, confirms that the choice is correct.

A schematic drawing of the ARES cavity is presented in Fig. 5.2. The major modifications with respect to the CERN scaled cavity are the shape of the cut-off tubes, the position and dimension of the coupling ports and, finally, the cell diameter. Because each modification has a rationale dictated by experience or suggested by the specific ARES parameters, we will briefly discuss these choices in the following.

- All nominal dimensions have been rounded-off; the tuning of the cavity to the proper frequency and the field flatness are achieved by adjusting the central cell diameter, and the equatorial radius of curvature of the end half-cells. Both parameters are specified to within 0.1 mm, to be consistent with mechanical tolerances.

- Since deep-drawing nicely and consistently reproduces the nominal shape, dimensions are specified in such a way that the proper frequency at room temperature is reached after a total of 0.1 mm have been uniformly removed from the surface by electropolishing. The experimental (46) coefficient used to convert the room temperature frequency value to 4.3 K is 1.00138. A SUPERFISH(42) computation over one half cavity, with 32,000 mesh points, gives a theoretical field flatness of 0.4 %.
- The cut-off tube diameter has been slightly reduced and the chicane profile has been appreciably modified to reach a reasonable compromise between HOM out-coupling and wake field effects on the low energy beam.
- The dimension and position of the HOM and main coupler tubes has been modified to reduce the coupler induced field perturbation at the cost of a reduction in maximum coupling strength. The choice is consistent with the ARES beam parameters.

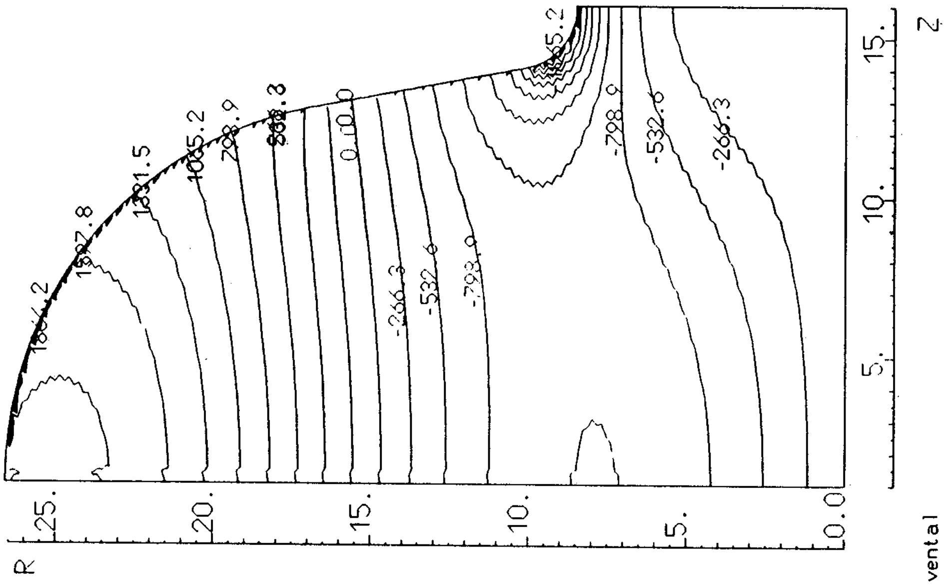

Fig. 5.1 - Sensitivity curves (for the $TM_{010}$-$\pi$ mode) for a 500 MHz half cell, scaled from the LEP design. The sensitivity is expressed as the frequency variation, in kHz, for a change of one $cm^2$ in the area of the cell axial cross section

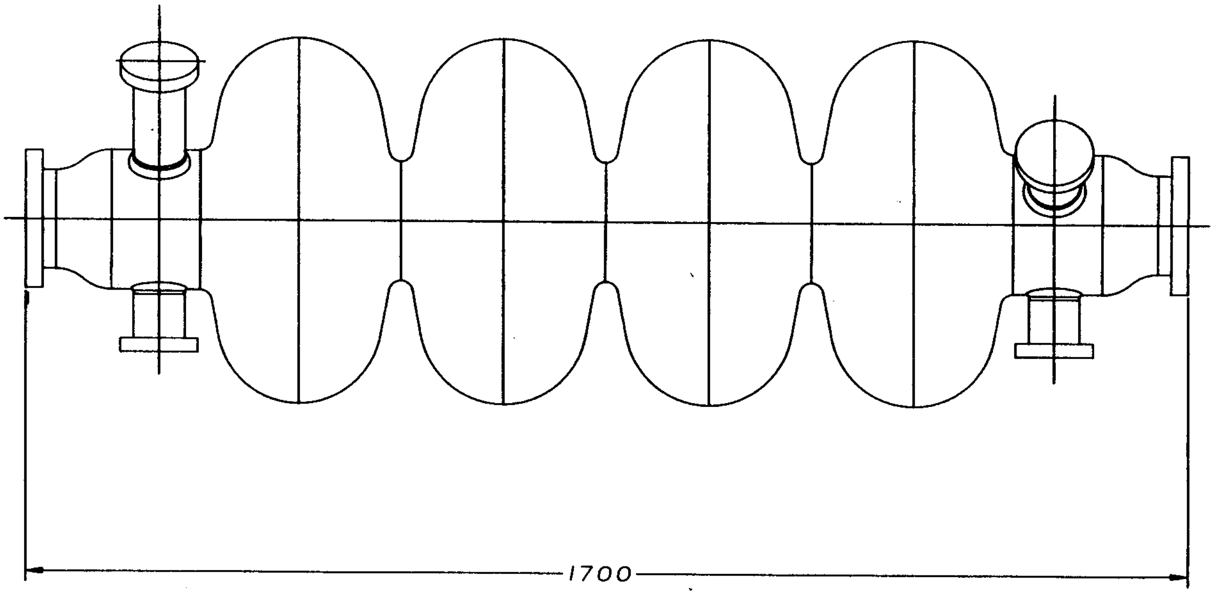

Fig. 5.2 - Schematic drawing of the ARES cavity

### c) HOM and Main Couplers

Each SC cavity is coupled to its RF driver via a coaxial line. A special device - the coupler - transforms the electromagnetic field configuration existing in the coaxial line into the configuration most suitable for exciting the fundamental ($TM_{010\text{-}\pi}$-like) accelerating mode in the resonator.

Usually the transition from the atmospheric pressure coaxial line to the cavity vacuum is through a cylindrical ceramic window. A straight cooled antenna couples to the electric field of the SC cavity in the region of the drift tube; the depth of its penetration inside the tube determines the coupling coefficient $\beta$ and hence $Q_{ext}$.

The SC cavity drift tube also carries higher order modes (HOM) couplers. Their function is to damp the HOM's by extracting the energy deposited by the bunched beam in the corresponding modes of oscillation of the e.m. field in the cavity. This is necessary because the interaction of the bunch with high order mode electromagnetic fields left in the cavity by preceding bunches can lead to instability or emittance blowup.

The HOM couplers are essentially high pass filters which do not couple to the fundamental mode but only to the higher frequency spurious fields. Connected to an external load they lower the HOM quality factor Q and field intensity. Each ARES cavity is equipped with two HOM couplers; the extracted RF power is dissipated in resistive loads located outside the cryostat.

The development of the couplers for the ARES cavities is in progress, taking into account the beam parameters. Particularly, due to the wide range of average beam current which are expected to be used, a main coupler with a variable coupling coefficient is foreseen.

A list of the monopole modes computed for the ARES cavity is presented in Table 5.1, together with their expected values of the R/Q parameter. The expected values of the average current density, $<j_s>$, and of the average radial electric field, $<E_r>$, at the coupler position are also given, for a proper design of the HOM couplers.

The frequency of the modes listed in table 5.1 are computed with the code OSCAR2D, while the electric field and the current density are obtained from the output of an implemented version of the code SUPERFISH, able to accept up to 32,000 mesh points(42). For a better resolution of the computed electric field on the cavity surface, a new routine has also been implemented.

Figure 5.3 shows the field pattern of few of the $TM_{0np}$ modes of the ARES cavity, as computed with the code OSCAR2D.

## Table 5.1 - ARES Cavity $TM_{0np}$ Modes

| Mode family | Frequency [MHz] | R/Q [Ω] | $\langle j_s \rangle$ [A/cm$^2$] | $\langle E_r \rangle$ [MV/m] |
|---|---|---|---|---|
| $TM_{010}$ | 491.9 | 0.0 | 0.2 | 0.1 |
| | 495.0 | 0.0 | 0.4 | 0.2 |
| | 498.0 | 0.0 | 0.5 | 0.2 |
| | 499.4 | 470.0 | 0.4 | 0.2 |
| $TM_{011}$ | 884.8 | 0.1 | 0.5 | 0.1 |
| | 893.7 | 8.1 | 1.0 | 0.2 |
| | 903.1 | 50.5 | 1.4 | 0.3 |
| | 906.7 | 109.0 | 1.2 | 0.3 |
| $TM_{020}$ | 1038.8 | 0.1 | 1.2 | 0.2 |
| | 1046.5 | 1.5 | 1.4 | 0.3 |
| | 1056.6 | 0.2 | 1.3 | 0.3 |
| | 1066.1 | 0.2 | 0.9 | 0.2 |
| $TM_{021}$ | 1318.2 | 1.1 | 2.7 | 0.4 |
| | 1341.5 | 0.8 | 5.6 | 0.8 |
| | 1367.0 | 0.4 | 8.4 | 1.2 |
| | 1392.5 | 2.4 | 8.2 | 1.2 |
| $TM_{012}$ | 1410.6 | 1.3 | 5.0 | 0.7 |
| | 1417.6 | 13.2 | 1.7 | 0.3 |
| | 1425.4 | 4.7 | 1.9 | 0.3 |
| | 1425.6 | 22.4 | 1.8 | 0.3 |

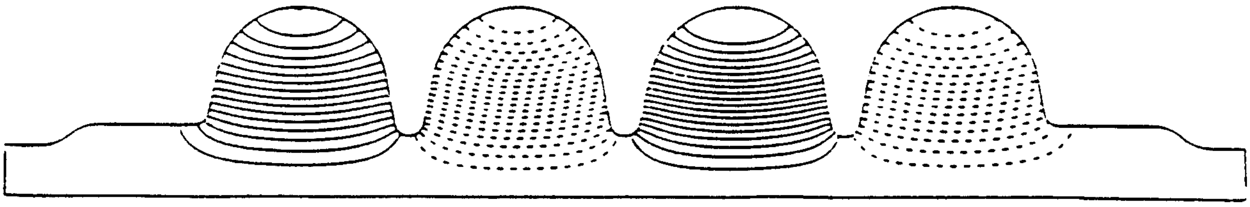

**$TM_{010\text{-}\pi}$ f = 499.4 MHz**

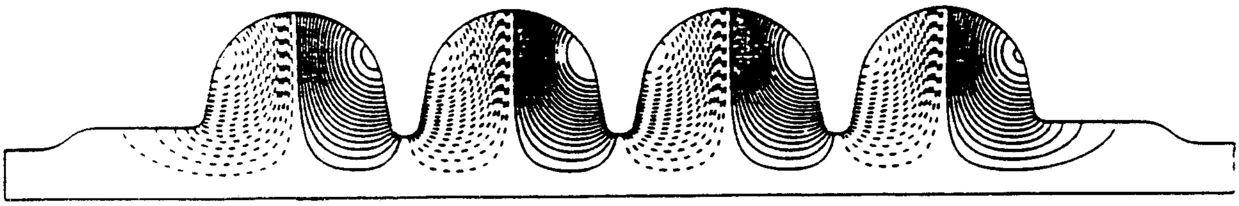

**$TM_{011}$ f = 907 MHz**

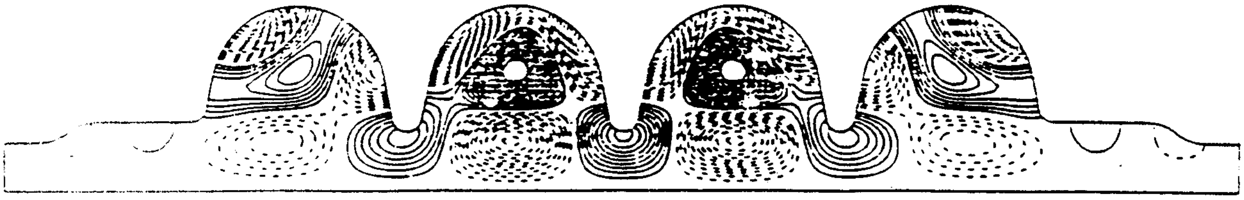

**$TM_{032}$ f = 1790 MHz**

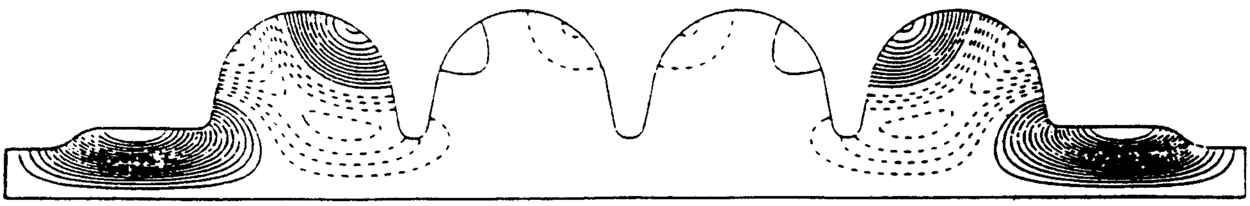

**"Tube mode" f = 1250 MHz**

**Fig. 2.4.3** - Field pattern of few of the $TM_{0np}$ modes of the ARES cavity, as computed with the code OSCAR2D.

## 5.2 - Radiofrequency

### a) General Design Criteria

The Superconducting LINAC consists of a total of twenty 4-cell cavity resonators. Section L1 has four cavities, and the main linac section - L2 - has sixteen cavities.

For a design maximum average current ($i_b$) of 0.2 mA, the maximum beam power per cavity ($P_b$) is:

$$P_b = V_A \langle i_b \rangle = 12\text{MV} \times 0.2\text{mA} = 2.4\text{kW}$$

and $P_d$, the power dissipated on the walls of the superconducting cavity at the nominal gradient of 10 MV/m, is given by :

$$P_d = \frac{V_A^2}{\left(\frac{R}{Q}\right) Q_0} = \frac{(12\text{MV})^2}{470\Omega \times 3\ 10^9} = 102\text{W}$$

The total required average RF power per SC cavity is thus 2.5 kW for an accelerating gradient of 10 MV/m and a cavity low field quality factor,$Q_o$, of $3{\cdot}10^9$.

Because of the maximum beam power is rather low, the external Q ($Q_{ext}$), given by the cavity coupling to the RF source, is rather high, even if the best coupling is chosen at $P_b$ .

In fact we have :

$$Q_{ext} = \frac{Q_0}{\beta} \approx 1.2 \bullet 10^8$$

where β is he coupling coefficient β given by :

$$\beta = \frac{P_b + P_d}{P_d} \approx 25$$

The bandwidth of the system,$B_L$ , given by :

$$B_L = \frac{F_0}{Q_{ext}} \approx 4\ \text{Hz}$$

is consequently very narrow.

Such a narrow bandwidth could create some problem in connection with the required accelerating field phase stability. In fact, the helium flow in the cryostat can induce mechanical vibrations in the accelerating structure (microphonic noise) that may be difficult to counteract with a mechanical tuning system. It is however at present believed that the problem can be solved using fast piezo-electric or magnetostricitve tuning devices. Furthermore, the topic will be further investigated experimentally on LISA before a final decision on the RF system is taken.

The presently envisaged and costed layout of the RF system relies on the fact that the phase stability problem will be solved and is based on the use of seven amplifier chains, each feeding four SC cavities via a coaxial distribution system, as shown in Fig 5.3 .

Because of the narrow bandwidth of the cavity-source system, an individual RF isolator (or circulator) is foreseen for each cavity. This provides the necessary isolation and avoids unwanted interactions between cavities. The installation of the isolators next to the resonators allows the system to operate under matched conditions. Small size, inexpensive, non-pressurised coaxial lines (i.e. the standard 3-1/8") can thus be used, so that part of the extra cost of circulators is actually recovered.

To adjust the phase of the accelerating field in each cavity within a group of four, a set of three coaxial phase shifters per group is provided. The phase adjustment between groups of four cavities is made at the low-power chain level.

A more complicated and costly solution than the one described, consisting of an independent power generator per cavity, that allows the phase of each cavity to be individually controlled at the low power electronics level, will be adopted should the microphonic noise prove to be a problem.

### b) Power Sources

The availability on the market of a large number of standard RF power generators for broadcasting applications - especially in the UHF band that contains the operating frequency of our SC cavities - makes the choice of the RF sources very easy. In particular, tetrodes cover the range of up to 1 GHz with powers up to 20 kW-cw.

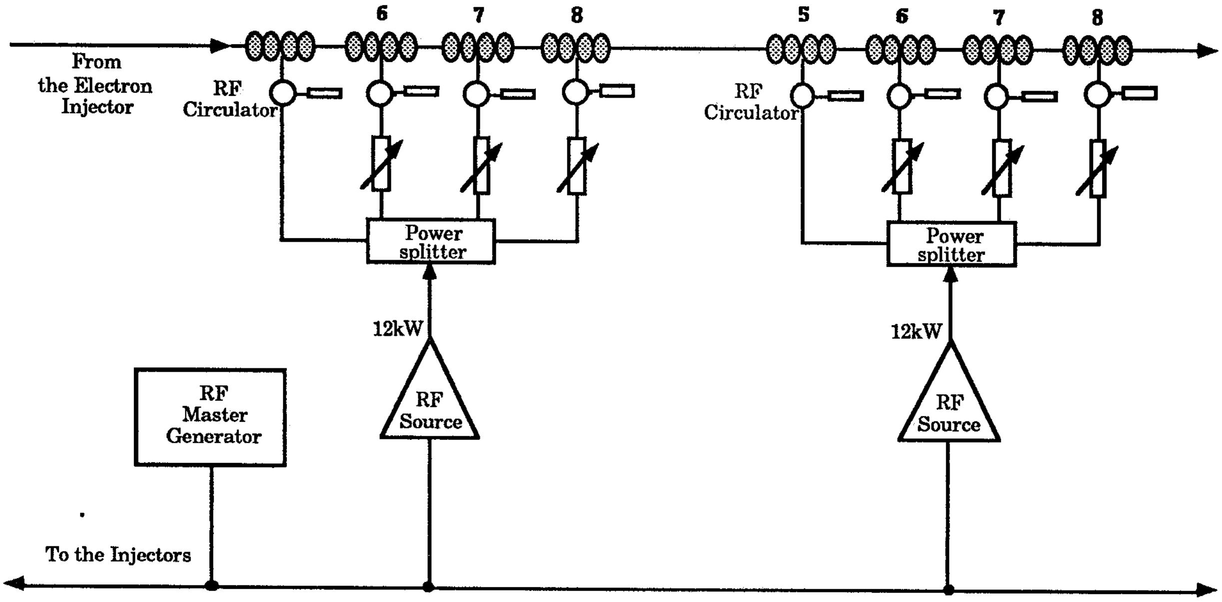

Fig. 5.3 - RF feeding system for two groups of four SC cavities.

With a maximum beam power rating of 2.4 kW per cavity, including the allowance for cavity and coaxial line losses, a 12 kW tetrode amplifier has been selected as the best candidate for powering one group of four SC cavities.

The amplification chains include a predriver stage, consisting of a 30÷40 W transistor amplifier, and two power stages, respectively rated 1 kW and 12 kW. The power is fed to the cavities via coaxial lines.

Alternate solutions such as klystron generators will also be considered; output powers of up to 20 kW for small size tubes are easily obtained.

Should it become necessary to power each cavity individually, 3 kW tetrode generators, easily found on the market, would be our preferred choice.

### c) The control system

To control both the beam energy and the beam size as particles travel through the accelerator, some of characteristic parameters of the SC cavities must be carefully controlled and continuously adjusted by means of dedicated circuitry and feedback loops.

The main parameters that have to be kept under control are: the amplitude of the cavity accelerating field, the phase of the cavity voltage with respect to that of the main RF driver and the cavity resonant frequency. These parameters, that all affect the beam energy spread, are not altogether independent from each other.

In the present design the specification for a beam energy spread of $\leq 10^{-3}$ requires the amplitude variation of the accelerating field in each cavity to be kept below $10^{-4}$.

This specifies the performance of the automatic gain control (AGC) system and of the RF chains phase and tuning control feedback loops. The design of the feedbacks also has to take into account the fact that the bandwidth of the coupled superconducting cavities is very narrow ( ≈ 4 Hz for ARES cavities). Obviously the phase control is effectve if an adequate power margin is available and phase fluctuations remain inside the cavity bandwidth.

Fig. 5.4 shows a block diagram of the proposed RF control system for ARES.

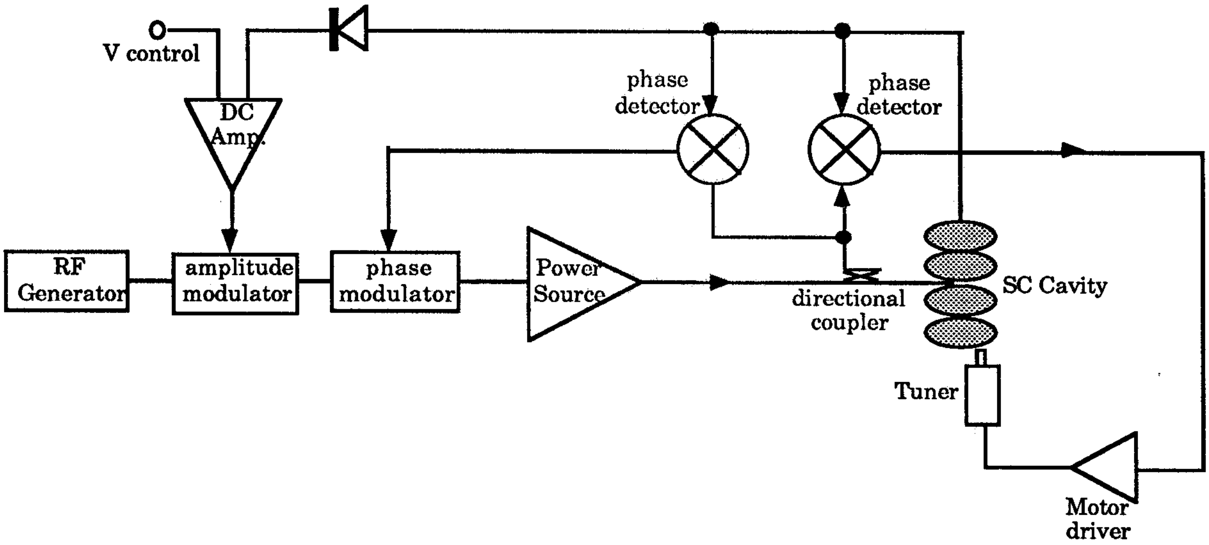

**Fig. 5.4** - Schematic layout of the RF controls in case of individual driving.

## 5.3 - Cryogenics

### a) Introduction

The cryogenic system is divided into four main sub-systems, each with its own function, namely :

- Cold Box (CB),
- Distribution System (transfer lines and connection U-tubes)
- Compressors and ancillary equipment (oil removal and the gas management systems)
- Cryostats.

The operating temperature of the cavities has to be as close as possible to the lowest LHe temperature attainable at normal pressure, that is between 4.24 K and 4.30 K when the unavoidable pressure drop along the lines and the heat exchangers is considered. This temperature is low enough to keep the surface resistance of superconducting Nb low at 500 MHz while avoiding the need for sub-atmospheric operation.

**Table 5.2 - Steady state operation parameters**

| | | | |
|---|---|---|---|
| Transfer line: | overall length | [m] | 120 |
| | Mass to cool | [kg] | 100 |
| N$^{er}$ single cavity cryostats | | | 4 |
| | Mass to cool | [kg] | 1600 |
| No. double cavity cryostat | | | 8 |
| | Mass to cool | [kg] | 6400 |
| Total RF dissipation @ 4.3 K,<br>(E$_a$ =10 MV/m, Q$_0$ = 3 x 10$^{9}$) | | [W] | 2040 |
| Static heat load @ 4.3 K<br>(on cryostats and distribution system) | | [W] | 250 |
| Heat load on radiation shields | | [W] | 2100 |
| | Mass to cool | [kg] | 2200 |
| TOTAL POWER: | @ 4.3 K | [W] | 2300 |
| | radiation shields | [W] | 2100 |

Moreover, to better control the cold flow he 4.3 K feeding line is operated in the He supercritical region, i.e. at 2.8 atm. Single phase Helium flow through the feeding lines is thus obtained and the cryogenic fluid is free to expand, producing a two phase stream, only just next to the cryostat. The main heat loads and the total power to be extracted at low temperature in the steady state operation regime are listed in Table 5.2.

### b) Cold Box

The CB specification has to include, in addition to the input design power, an appropriate allowance for all those extra low-temperature losses that must be manageable without needing to shut down the superconducting linac refrigeration.

The power specification for the CB is set at

2.800 W @ 4.3 K plus 4'000 W @ 60 K,

providing a low temperature heat load capability of 500 W above the nominal requirement. The safety factor is thus ≈ 1.2. The main features of the Cold Box are summarized in Table 5.3.

Since the coolant is the same He used to cool the cavities, care must be taken - to prevent plugging of the needle valves - to avoid all contamination of the Helium gas.

The upper pressure limit specification pressure will depend somewhat on the manufacturer, but should remain in the range of 12÷15 atm.

The thermodynamic efficiency, expressed as a percent of the efficiency of an ideal Carnot cycle operating between the same temperatures, implies an overall cryogenic plant plug-power requirement of 0.9 MW at room temperature

**Table 5.3 - Cold Box main features**

| | | |
|---|---|---|
| Operating temperature | [K] | 4.3 |
| Power @ 4.3 °K | [W] | 2800 |
| Additional power @ 60 °K | [W] | 4000 |
| Flow rate @ 4.3 °K | [g/s] | 140 |
| Room temp. pressure | [Atm a] | 12 |
| Pressurè @ 4.3 °K | [Atm a] | 2.8 |
| Return pressure | [Atm a] | 1.082 |
| Carnot efficiency | [%] | 21.4 |

Figure 5.5 shows a diagram of the gas flow path, while Figure 5.6 shows the corresponding temperature-entropy (T-S) thermodynamic cycle diagram.

The incoming stream, at 300 K and 12 atm, is cooled at constant pressure by means of counter flow heat exchangers in which the cold return gas produced by the two isoentropic expansion stages is heated-up to room temperature. The isoentropic expansions on the T-S diagram are intentionally drawn as "not ideal" to emphasise that the actual transformations are not completely reversible. A final stage of isoenthalpic expansion, obtained by means of a Joule-Thomson (J-T) valve, provide the necessary counter flow cooling at 4.3 K for the 2.8 atm (supercritical ) Helium stream.

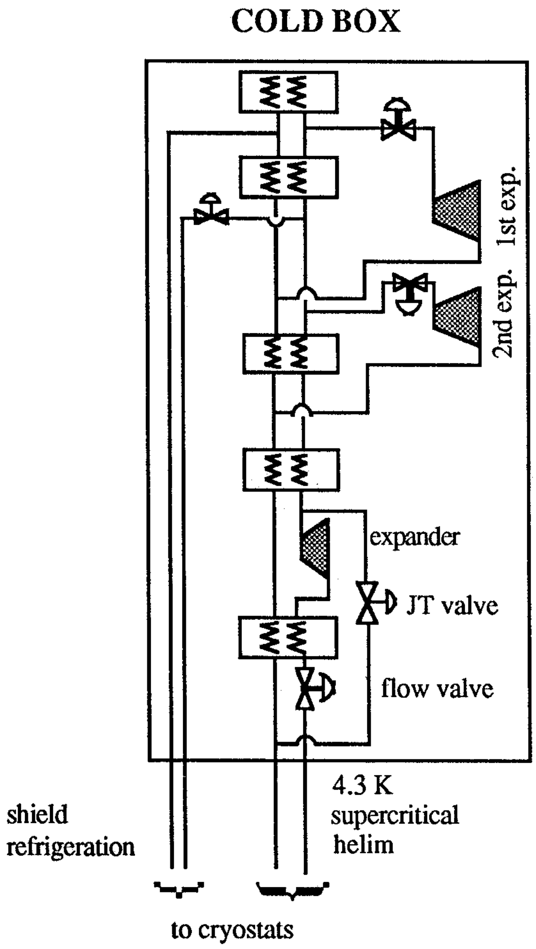

**Fig. 5.5** - Block diagram of a refrigerating machine

The final J-T expansion of the supercritical flow, which actually takes place just next to the cryostat, far from the CB, is also shown on T-S diagram. In fact the supercritical condition is maintained in the transfer line throughout, so that the single phase Helium flow can be better controlled.

The CB also provides the necessary intermediate temperature radiation-shield cooling, in the range 40 K÷ 80 K, for the whole cryogenic system. Closed-cycle intermediate temperature refrigeration is obtained using the same process He gas. This makes the plant operation simpler and cheaper and avoids the need for different cryogenic fluids; it will however not be possible to keep the cavities at $LN_2$ temperature for a long time unless the CB is in service.

To ensure maximum flexibility and reliability, all functions and parameters of the CB, such as pressures, temperatures, turbine speed, valve throttling, etc., are remotely controlled and monitored. An independent computer automatically controls the flow valves, the LHe level inside the cryostats, the shield temperatures and the alarm and safety procedures; the automatic control may be manually overridden whenever non-standard values of temperatures and pressures are required or during recovery from an emergency.

The CB control system provides the main control system with the refrigerator status data and takes care of all interlocks and links to other linac components (vacuum, RF, injector, etc.).

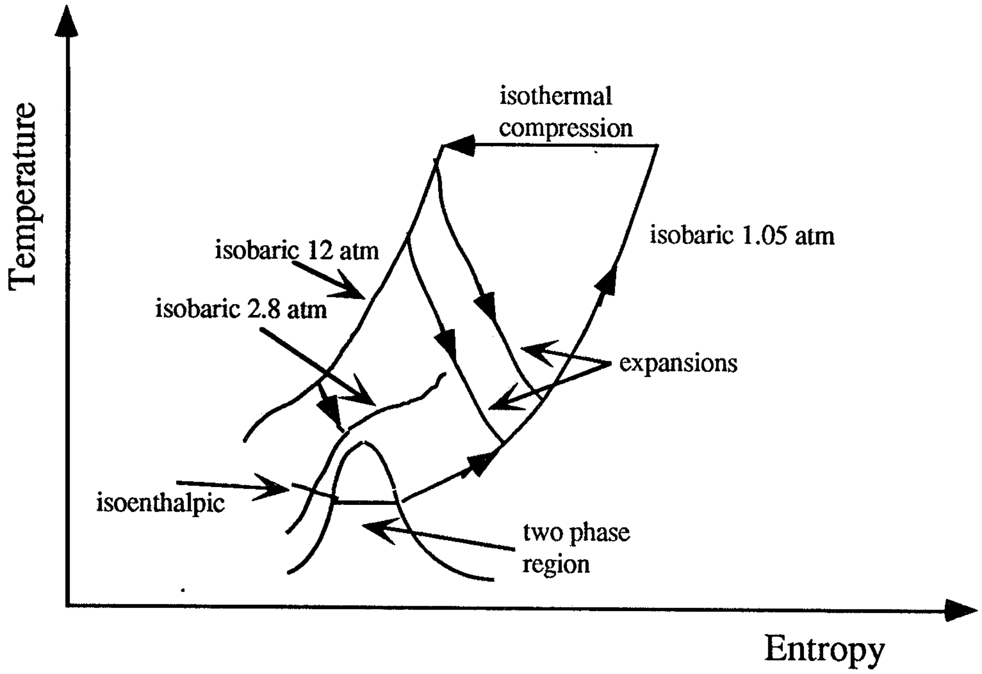

**Fig. 5.6** - Thermodynamic cycle on the T-S diagram

Many technical details of the CB that do not affect the basic performance of the system, such as the upper pressure limit, the use of serial instead of parallel turbine expanders, the use of a "wet" expander instead of a J-T expansion valve, etc., will need to be finalized in collaboration with the manufacturer.

### c) Distribution system

The distribution system function is to transport and distribute the 4.3 K and at 60 K cold streams to the cryostats with losses that must be negligible in comparison with the main heat loads.

As shown in Fig.5.7 all cryostats are connected to the CB via the main transfer line, and are fed in parallel. The distribution scheme is very simple and the task of regulating the cold flow as required by each cavity is left to the final J-T expansion valves.

In fact, the cavities will dissipate different amounts of energy depending on their quality factor $Q_0$, which, in addition, may vary during operation. A feedback on the liquid level inside the cryostats, acting independently on each final J-T valve, is therefore provided so as to keep the cavities always fully immersed in the LHe bath. The feedback is software-implemented in the CB controller.

The distribution system design also facilitates the maintenance of the cavities : individual cryomodules can be disconnected while the refrigerator stays in operation to keep the rest of the cryogenic complex cool. The technical solution uses fast connections (U-tubes) between the main transfer line and the cryostats, similar to those foreseen for CEBAF.

There are four U-tubes for each cryostat : two ( input and return) on the 4.3 K line and two on the 60 K line. Each fast connection is equipped with valve and purging port so that it can be mounted and dismounted without introducing contaminants that could freeze and plug the refrigerator.

**Table 5.4 - Transfer line main parameters**

| | | |
|---|---|---|
| Piping scheme | | 4 product streams;<br>cold shield; superinsulataion |
| Pressure of incoming 4.3 °K He | [Atm a] | 2.8 |
| Pressure of return 4.3 °K He gas | [Atm a] | 1.082 |
| Max. pressure drop on 4.3 °K return pipe | [Atm a] | 0.002 |
| Total heat loss @ 4.3 °K | [W] | 20 |
| No. of cryostat connections | | 12 |
| Type of connection | | U-tube for each stream |
| U-tube heat loss @ 4.3 K | [W] | 120 |
| Flow control | | 2.8 atm, 4.3 °K pipe : J-T valve<br>60 K pipe : needle valve |

A cross sectional view of the main transfer line is shown in the inset of Figure 5.7 . It is of the four-product-stream type with shield and superinsulation. The expected dynamic heat loss is less than 0.1 W/m @ 4.3 K. The main parameters are listed in Table 5.4.

As previously pointed out the pressure drop along the 4.3 K return line has to be kept as low as $210^{-3}$ atm in order to keep the LHe bath temperature inside the cryostat close to 4.3 K.

The pressure drop on the 4.3 K, 2.8 atm feed line is not as critical as that on the return line; it is only necessary to keep the end pressure higher than 2.245 atm, the critical pressure of He. It is also worth noting that no cooling occurs during the isoenthalpic expansion of He from 2.8 to 1.082 atm at 4.3 K.

As it can be seen from the data of Table 5.4 the largest heat load in the distribution system, 120 W @ 4.3 K, comes from the U-tube connections. The distribution system thermal losses add up to ≈ 5 % of the overall 4.3 K heat load.

### d) Compressors and ancillary equipment

An efficient compression system is vital to keep the cryogenic plant working. Figure 5.8 shows the block diagram of the CB together with the compressors, purifiers, and medium pressure storage tanks.

Two make the system more reliable two compressors are mounted in parallel so that one can be switched on if the other fails. This because, while in the event of a fault on the CB the compressor can keep the cavities cold for a long time, a compressor fault will cause the LHe evaporation to stop and the cavities to warm up very fast.

Unless the compressor is equipped with an oil removal system and downstream adsorbing filters, during compression the pure Helium will become contaminated with the compressor lubricant oil. As first approach we foresee only one heavy-duty purifier that can work continuously for one year; the filters can be replaced and/or purged while the purifier is in service.

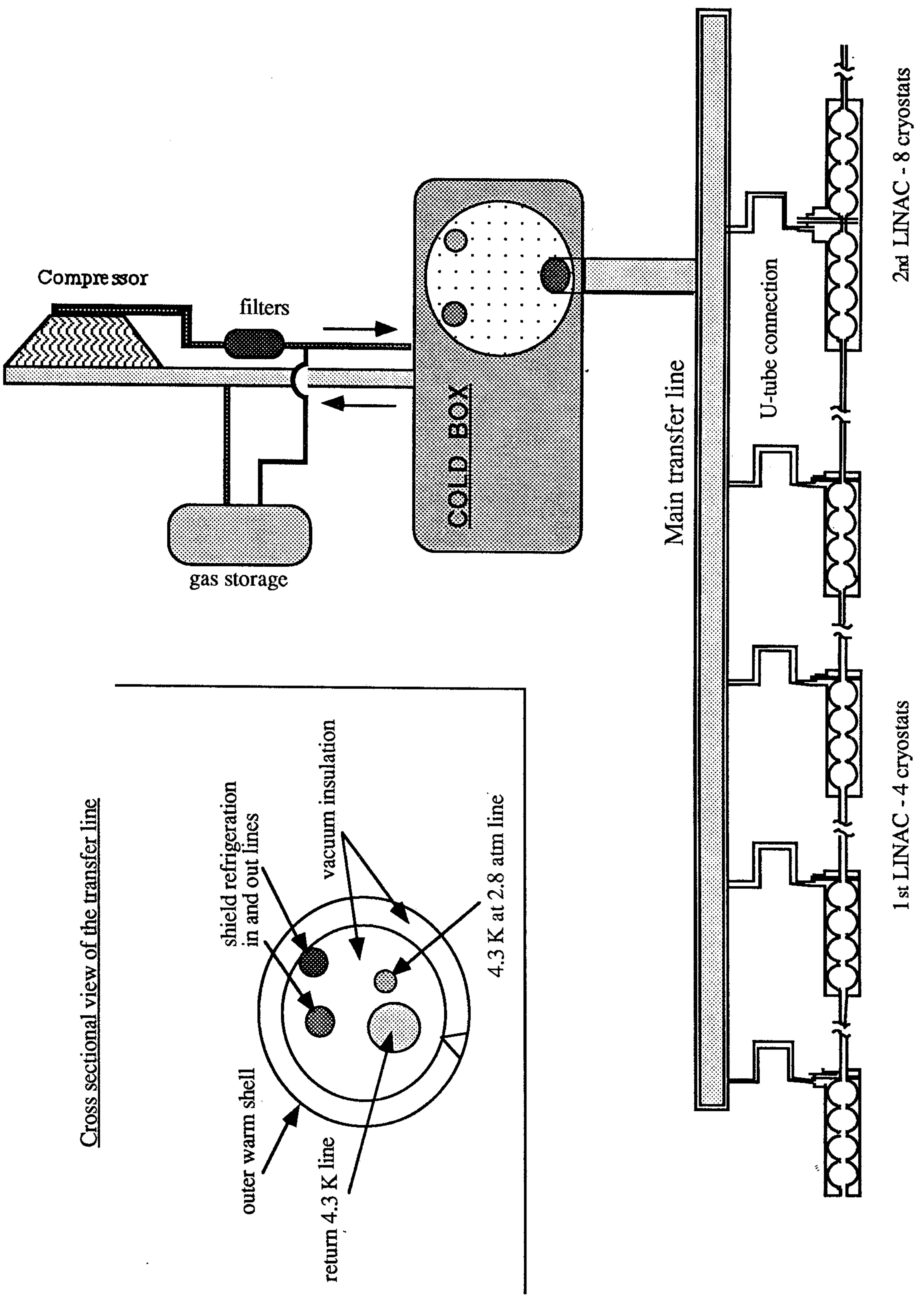

**Fig. 5.7** - Schematic layout of the cryogenic system. A cross sectional view of the main transfer line is shown in the inset.

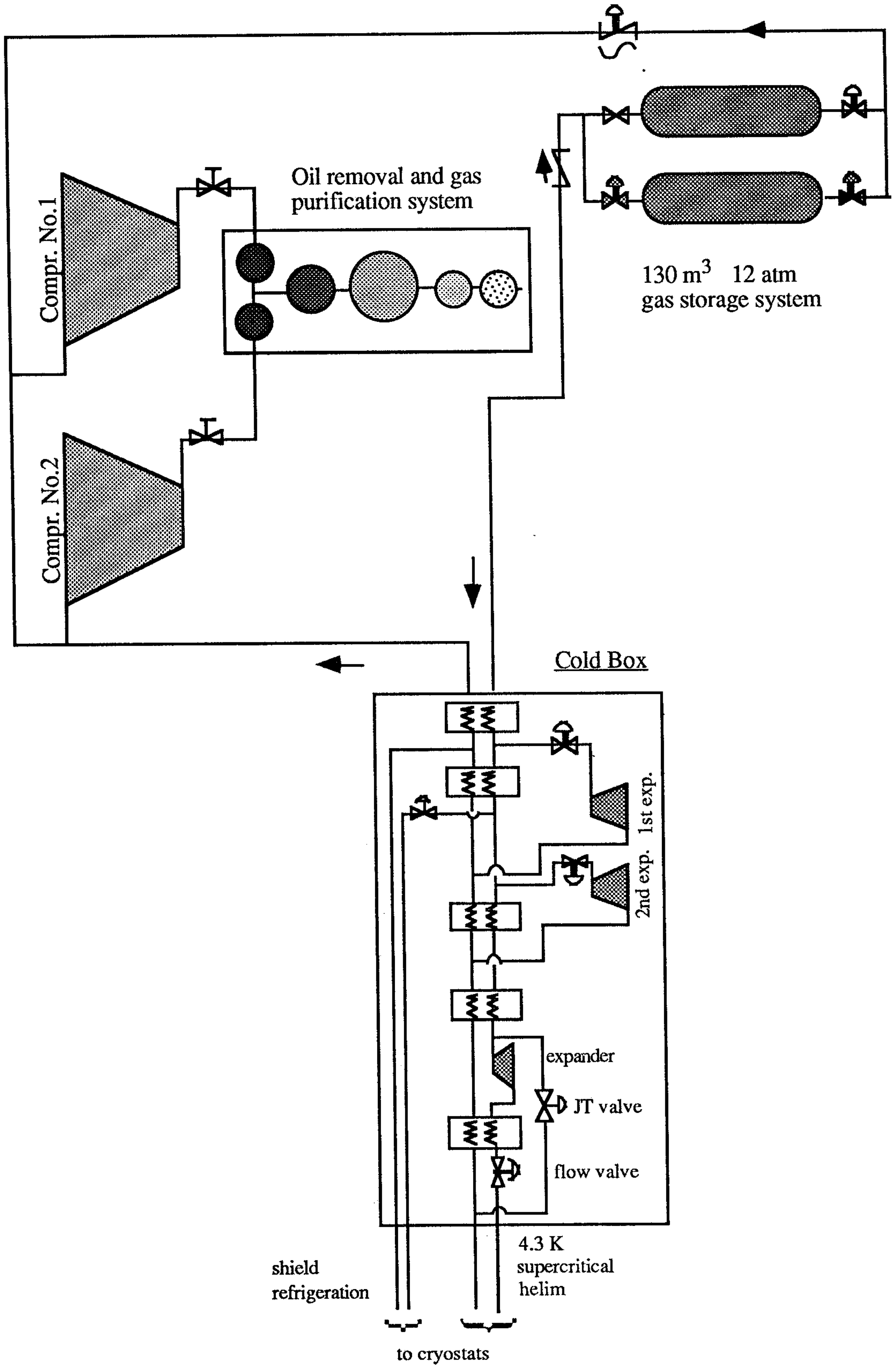

Fig. 5.8 - Block diagram of the cold box, together with the compressors, purifiers, and medium pressure storage tanks.

The system operates as follows: when the system is warm the pure Helium gas is stored in the pure gas storage tank and all the piping, cryostats, compressors and the CB, are filled with pure Helium gas.

The total gas inventory is about 1500 $m^3$ S.T.P., or 130 $m^3$ at room temperature and 12 atm.

For easier handling and purification the storage tank consists of two separate vessels of 65 $m^3$ each. After the compressors and the CB have been started the He starts to condense in the CB, the transfer lines and the cryostats, so that the return pressure lowers; this actuates a constant pressure make up valve that takes gas from the vessels and fills the return line at constant pressure. Once the steady state is reached, i.e. the cryostats are full of LHe, the CB starts operating in a closed cycle and the vessels can be closed.

When the cryostats have to be warmed up, the Helium can be recovered either by means of the CB compressors, in the form of pure He, and stored in the storage vessels or using a standard recovery system (gas bag and high pressure compressor, not included in the drawing). The latter system however leaves the He exposed to contaminants.

### e) Cryostats

From an engineering point of view, the cryostat must provide a proper environment for the SC cavities. Thermal insulation, shielding from magnetic fields, removal of the RF heat at constant temperature ($\approx$ 4.3 K), tuning, auxiliary equipment, clean conditions, UHV techniques, easy handling and mounting are the main features that have to be kept in mind in designing and manufacturing the cryostat.

At this stage no development has been attempted since SC cryostats have reached a satisfactory standard level of performance; the preliminary design and manufacture specifications are therefore based on existing designs, notably those for the CERN cavities (47).

The main components making up our cryostat are:

- outer vacuum vessel,
- GHe cooled radiation shield,
- magnetic shield,
- LHe vessel,
- thermal-magnetostrictive tuners (three).

Internal electrical cabling, waveguides, feedthrough tubes, support rods, niobium beam-pipe extensions, probes, etc., are also considered parts of the cryostat.

Two prototypes are under construction at ANSALDO CO.

### Vacuum vessel

A stainless-steel (AISI 316 LN) bar to which two rings of the same material are welded is the main support structure; aluminium-alloy staves are then bolted to the s.s. rings circumference. Two covering plates and a stainless-steel outer shell give the vacuum vessel the final required stiffness.

After assembly the vessel is He-leak pressure tested .

### GHe cooled radiation shield

The GHe cooled radiation shield is made of high conductivity, phosphorous free ETP or OF copper plates. The shield surface temperatures is kept approximatively constant by the GHe evaporated from the LHe bath; the cold gas flows inside copper pipes brazed on the copper sheets. The radiation shield is sorrounded by a multilayer, aluminized mylar (NRC-2) "superinsulation" blanket to decrease the radiant heat load on the shield; the blanket also provides a low thermal conductivity layer on the path of residual gas molecules.

### Magnetic shield

Any magnetic flux in the vicinity of the cavity is "captured" within the niobium during cool-down and produces a degradation of the SC cavity performance.

Beside avoiding the use of magnetic materials in the construction of the cryostat, the cavity has therefore to be shielded, during cool-down, from external magnetic fields; a µ-metal shield is therefore usually incorporated in the cryostat.

Other precautions must nevertheless be observed during the cool-down sequence of operations; for example the tuner may be switched on only when the cavity is already cold because magnetic fields may appear during tuner activation.

### LHe tank

The LHe tank is a low magnetic permeability stainless-steel (AISI 316 LN) container built from two half-shells; its shape follows approximatively the shape of the cavity in order to minimize the LHe volume.

The half-shells are formed by pressing and then welded together. The complete shell is finally TIG-welded to the cavity end-flanges.

The final weld is performed after mechanically tuning the cavity, an operation consisting in a plastic deformation of each individual cell. The deformation should produce the desired RF field flatness and at the same time preserve the elastic behaviour of the four-cell cavity necessary for the operation of the tuner. To facilitate tuning, the following mechanical arrangements are implemented:

- a single-corrugation bellow is inserted at both ends to decrease the tank longitudinal stiffness so that the tank is less rigid than the cavity along the direction of the tuner forces.
- the central cavity iris is fixed to the tank by a collar. Transverse oscillations of the cavity are thus reduced both because of the symmetry of the structure and because of the transverse stiffness of the large diameter tank.
- the resonance frequencies of longitudinal mechanical oscillations are made as high as possible by connecting the cavity to the tuners by means of very stiff arms .

<u>Thermal magneto-strictive tuners</u>

Beam current changes, vibrations induced by vacuum pumps, LHe bath pressure changes induced by the liquid level control valves, drifts in the support temperatures reflecting on their length, may all lead to undesirable resonant frequency variations that have to be controlled by the tuner mechanism.

The cavity is "tuned" by changing its total length since individual cells are mechanically similar and their own frequency changes proportional to the overall length. Three equally spaced tuning bars are attached to both ends of the cavity by means stiff arms in order to obtain a circumferential symmetry. Because of the symmetry, the structure ends should remain parallel to each other and normal to the structure axis; any transverse mechanical resonance frequency should be higher than the relevant excitation frequencies.

Mechanical resonances of the cavity must also be taken into account to optimize the tuner response.

The selected thermal-magnetostrictive tuning system also complies with all the following general requirements:

- high precision in the presence of large forces;
- absence of rotating equipment that may scuff;
- tolerance of compression, tension and torque (which may appear during cavity cooldown, evacuation and thermal transients);
- mechanical stability;
- possibility to handle fast and slow responses separately.

The tuner bars consist of insulated, rectangular excitation coils wound around both ends of a copper tube. The copper tube is inserted in a coaxial nickel tube that provides the fast magneto-strictive elongation and kept in place by three low thermal conductivity spacers; the spacers also provide good thermal insulation so as to reduce the heat flux related to the Joule effect in the coils. Nickel is chosen because, even though it needs high exciting fields, it is less brittle than other magnetostrictive materials.

The tuner slow action is thermal and is obtained by inserting a heater inside the Ni tube, next to its midpoint. Cold GHe flowing through a labyrinth path (as in a counter flow exchanger) removes the generated heat. Radiation shields around the tuner are also provided to further improve its thermal insulation.

Note that the GHe mass flow rate must be carefully determined as a function of the current in the heater; improper heat exchange coefficients may lead to undesirable temperature gradients along the whole tuner.

A schematic drawing of the cavity inside the cryostat is presented in Fig.5.9, while Fig. 5.10 shows the magnetostrictive tuning system.

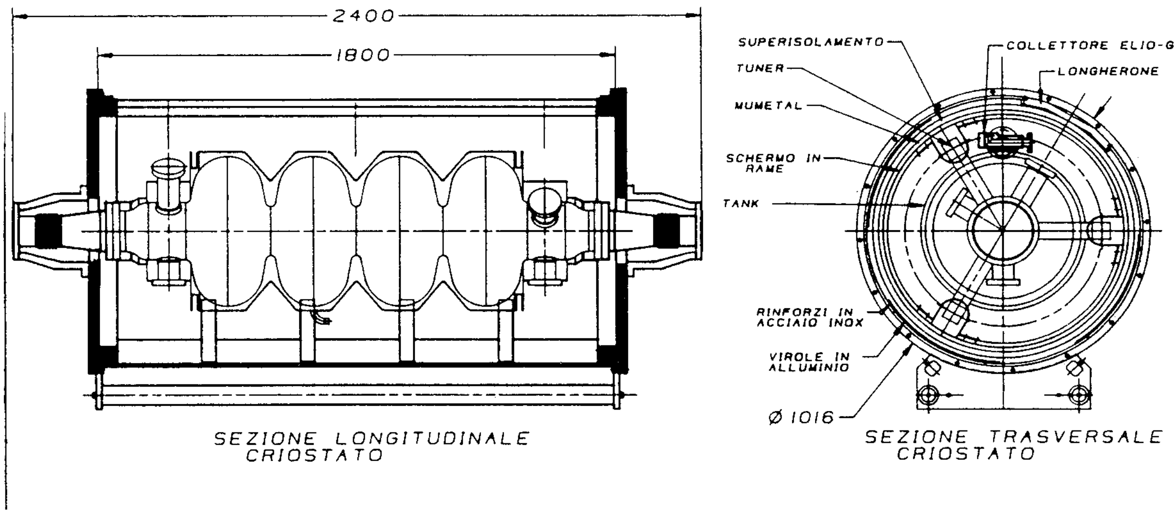

**Fig. 5.9** - Schematic drawing of the ARES cavity inside the cryostat.

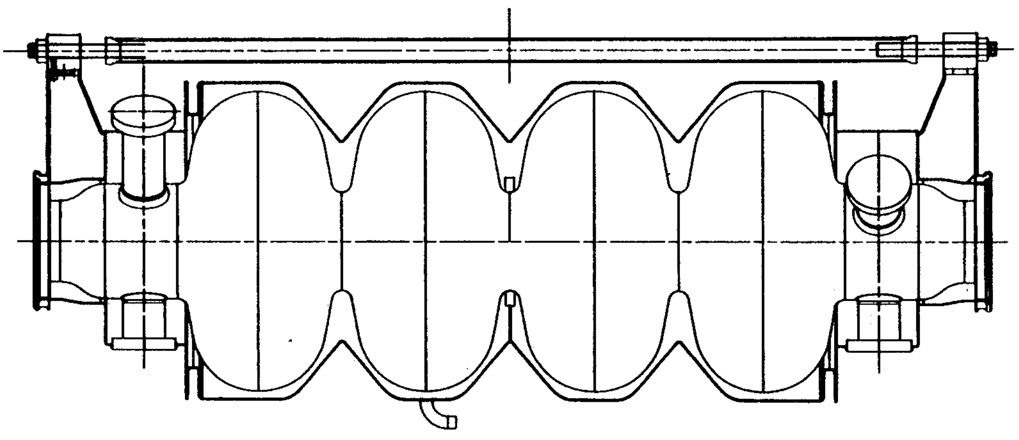

**Fig. 5.10** - Schematic drawing of the magnetostrictive tuning system.

# 6 - VACUUM SYSTEM

## 6.1 - Introduction

In superconducting accelerator systems very high vacuum is mainly required to protect the superconducting RF cavities from the condensation of molecules of the residual gases on the low temperature superconducting surface: the condensation of few hundreds of monolayers on the superconducting niobium surface would seriously degrade the RF cavity performance, in particular lowering its Q value.

In fact, for a SC linear accelerator this is the dominant phenomenon that sets the most severe requirements on the vacuum system ; interaction with the residual gas is a comparatively minor effect because the beam covers only a few hundreds of meters within the accelerator.

The pressure in the beam pipe and the SC cavities must be in in the $10^{-8}$ mbar range before cavity cooldown can be started in order to guarantee operation of the RF cavity for at least 2 years at a Q value not lower than 90 % of its initial value.

Very clean vacuum condition (no oil, no dust and no hydrocarbons) are imperative but no titanium sublimation pump can be used because titanium can easily form unwanted alloys with niobium.

It should also be recalled that SC cavity cryostats have to be evacuated to provide the necessary thermal insulation between room temperature and the liquid helium container.

From the point of view of vacuum the ARES linac complex consists of 3 superconducting Sections - that total 18 cryomodules - and about 200 meters of beam lines.

## 6.2 - The cryomodule

The cryomodule is the smallest unit of the superconducting accelerator structure that can be individually tested. Each cryomodule consists of either 4 or 8 RF cells, assembled in a single cryostat.

A gate valve is mounted at each end of a cryomodule to make it easier to test it and to prevent any contamination of the cavities after the initial testing by keeping them under good vacuum conditions at all subsequent times.

Moreover, thanks to the valves, each cryomodule can be separated from the accelerating structure, for instance to replace a defective cryomodule, without breaking the vacuum in the adjacent modules .

The all-metal, bakeable gate valves have a 100 mm inside diameter.

No elastomer sealing is acceptable because the outgassing rate would be too high. Moreover, all-metal gate valves can be supplied with RF contacts that perform a direct electrical connection between the two valve flanges, thereby shielding the inner valve mechanism from the beam.

A bake-out jacket is permanently assembled around the valve; it allows to perform a moderate temperature (200 ∞C) bake-out.

A total of 36 all-metal valves are needed for the three superconducting linac sections.

The pumping of the cryostat vacuum chamber is ensured, on each cryomodule, by a 50 l/s turbomolecular pump, connected to a valved port. After leak testing, if the chamber is He-tight, the valve can be closed and the pump can be switched off after the cryomodule has been cooled down. Should a leak be detected, the turbomolecular pump can be kept in continuous operation to keep the pressure in the insulation chamber below $10^{-4}$ mbar until the leak has been repaired.

## 6.3 - The cryomodule pumping system

As explained above, each cryomodule is terminated at each end by a valve.

In normal operation the valves are opened only when the pressure in the beam pipe has become lower then $10^{-9}$ mbar, to reduce the amount of condensable gases entering the cryomodule.

A room temperature stainless steel beam pipe connects two adjacent cryomodules; the UHV pumping system is connected to the pipe through a bellow.

The UHV pump is 230 l/s Starcell ion pump that maintains the pressure in the beam pipe at less than $10^{-7}$ mbar when the RF cavity is at room temperature.

Two other bellows are mounted at the pipe ends - on the beam line - to compensate for manufacturing tolerances and to simplify the beam pipe alignment easier. A proper shielding sleeve with sliding contacts must be provided inside all bellows to keep the vacuum chamber impedance seen by the beam low (48,49).

The beam pipe connecting two cryomodules contains all beam monitors. A focusing quadrupole also fits around it.

Figure 6.1 shows the layout of a cryomodule connection assembly.

The total niobium surface exposed to vacuum is about 4 $m^2$; the overall surface of the stainless steel parts is instead less than 1 $m^2$. In order to reduce the outgassing a moderate in-situ bake-out (≈ 150 °C) of the beam pipe is foreseen. Thin kapton heaters are mounted on the chamber and fit in the space between the beam pipe and the quadrupole pole faces.

A total of 15 ion pumps are used along the SC linac sections.

Rough pumping of the system and pumping during bake-out operations will be ensured by a mobile station that can be connected to the beam pipe, close to the ion pump, by means of an all metal corner valve. After bake-out, at the start of normal operation of the ion pump the roughing

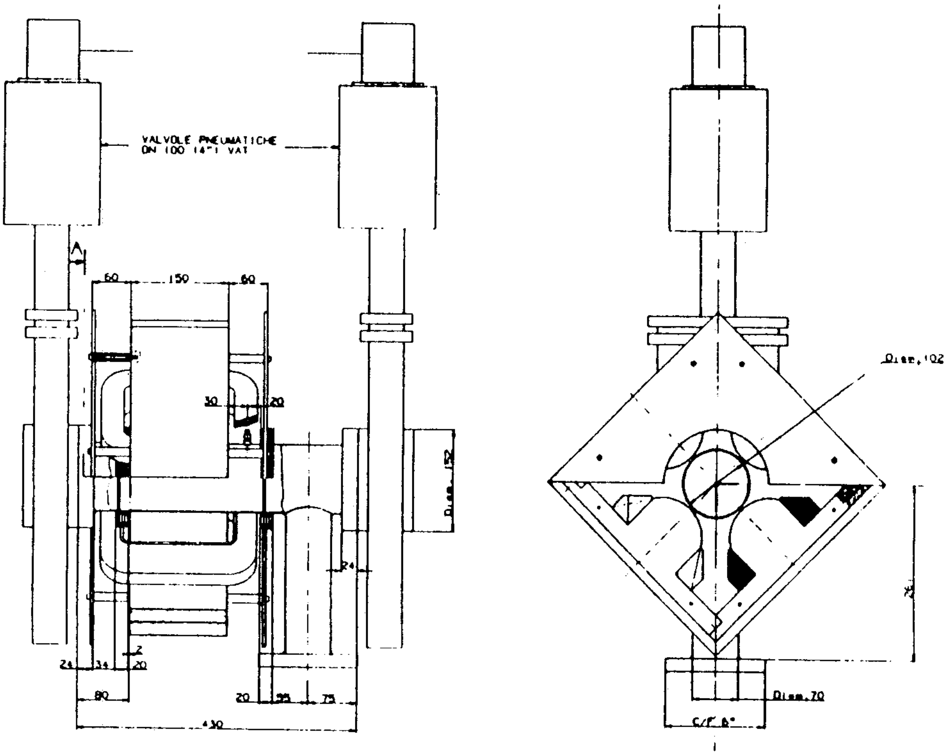

Fig. 6.1 - Layout of the connection assembly between two cryomodules of the sections L1 and L2.

system is detached from the beam tube.

In all, three roughing stations are foreseen for all Linac vacuum systems.

The solution is obviously cheaper than providing a fixed roughing pump station at each of the 22 forevacuum ports.

The roughing system must be absolutely free from hydrocarbons to avoid contamination. It consists of a magnetic-bearings turbomolecular pump with dry forevacuum pump or - alternatively - of a refrigerator-cooled cryopump backed by a dry pump.

An ionization gauge is mounted close to the beam tube and connected to the control system, to provide information on the total pressure in the beam line.

### Table 6.1 - SC Linac Vacuum Components

| | Ion pumps | Gate valves | RGA | Ion gauge | Forevacuum ports |
|---|---|---|---|---|---|
| **Section L1**<br>**Section L2** | 3<br>7 | 8<br>16 | 3<br>7 | 3<br>7 | 3<br>7 |
| **Total** | 10 | 24 | 10 | 10 | 10 |

A residual gas analyzer (RGA) is also mounted close to each high vacuum pumping port, between pairs of cryomodules, and provides on-line information on the composition of the residual gas in the beam pipe.

A total of 19 RGAs, controlled through a multiplexed system, are mounted on the SC linac. The information on the residual gas composition is used to diagnose the presence of a leak or of a pump malfunctioning before a permanent degradation of the RF cavity performances can occur.

Table 6.1 shows the inventory of the SC linac vacuum components.

## 6.4 - Recirculation beam lines vacuum system

From the point of view of vacuum the eventual recirculation beam line consists mainly of ≈100 m of a 100 mm inner diameter stainless steel tube, vacuum pumps, valves, gauges and forevacuum ports.

Vacuum requirements in the recirculation line, as previously explained, are less stringent than on the SC linac because the line contains no superconducting exposed surface.

To pump-down the recirculation lines, only 10 ion pumps - identical to the ones used in SC linac, ≈10 m away from each other - are therefore sufficient. The estimated mean pressure will be in the $10^{-8}$ mbar range.

Usual UHV surface cleaning treatments are used in order to reduce stainless steel outgassing (49). Medium temperature in-situ bake-out (≈ 300 °C) is foreseen.

Forepumping is normally done by connecting one of the mobile pumping stations to one of the 5 valved ports. The presence of 4 all-metal gate valves on the beam line makes it easier to service the vacuum system and to deal with abnormal situations.

12 ionization gauges and 5 RGA's are used for vacuum monitoring and diagnostics.

Table 6.2 summarizes the main vacuum components of the whole Linac system.

**Table 6.2 - Vacuum Component Overall Inventory**

| | Ion pumps | Gate valves | RGA | Ion gauge | Forevacuum ports |
|---|---|---|---|---|---|
| **Beam lines** | 10 | 4 | 5 | 12 | 5 |
| **SC Linacs** | 10 | 24 | 10 | 10 | 10 |
| **Total** | 20 | 28 | 15 | 22 | 15 |

# 7 - MAGNETS AND POWER SUPPLIES

## 7.1 - Linac Quadrupoles

The quadrupoles in between the s.c. cavities are fully symmetric quadrupoles with an aperture radius of 55 mm. The pole shape is, at this design stage assumed to be circular. The required quadrupolar constants and field gradients depend on the maximum energy of the particles along the Linac; they are given below for two energies.

| **Emax** [GeV] | **Length** [m] | $K^2$ [$m^{-2}$] | **Gradient** [T/m] |
|---|---|---|---|
| 0.1 | 0.2 | 2.9 | 1.0 |
| 0.3 | 0.2 | 1.6 | 1.6 |

The quadrupoles have been optimized for the maximum gradient of 1.6 T/m by means of the 3-D code Magnus. The gradient has been determined by analyzing the field harmonic content over a cylindrical region of radius $R_N$ around the quadrupole axis, inside the aperture. The gradient function along the radius can be expressed in cylindrical coordinates as :

$$G(x) = \Sigma_{n=1,\infty} ( n\, r^{n-1}) / (R_N)^n \bullet b_n$$

where n is the harmonic number (n=1, quadrupole; n = 5, dodecapole and so on) of the field component, $b_n$ the corresponding expansion coefficient and r the radial cylindrical coordinate.

The coefficients $b_n$ found by Magnus with $R_N = 50$ mm are the following:

| n | 1 | 5 | 9 | 13 | 17 | 21 |
|---|---|---|---|---|---|---|
| $b_n$ | 760 | -10.5 | 2.6 | 8.3 | -10.1 | -8.2 |

Better accuracy will be obtained by proper shaping of the pole tips in the course of the more detailed work still in progress.

Figure 7.1 shows the gradient along the radius in the median plane of the quadrupole. Magnus predicts a gradient variation of -0.1 % for x > 17 mm and of -1 % for x > 32 mm.

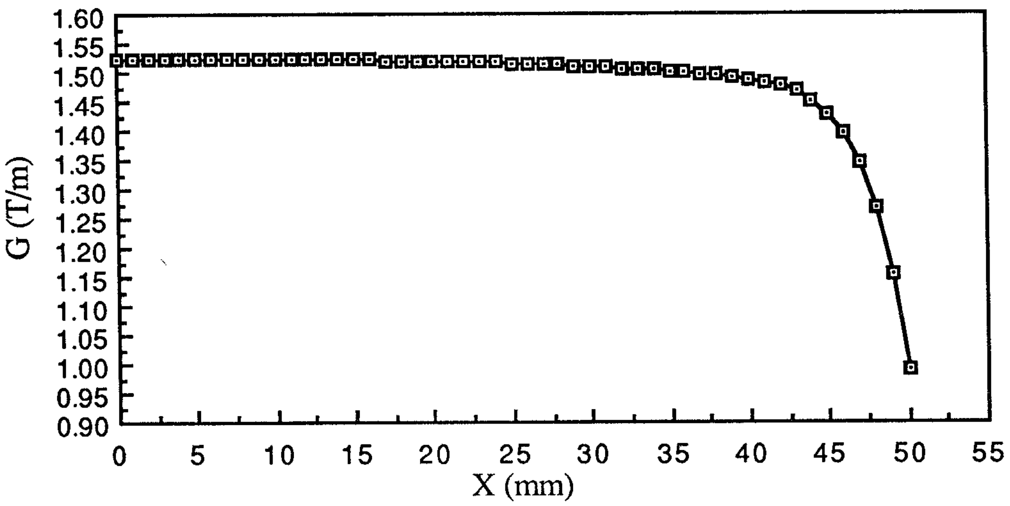

**Fig. 7.1** - Quadrupole gradient as a function of radial distance from axis.

The magnetic length of the half quadrupole defined as :

$$L_{mag} = \int [ \, G(s)/Go \, ] \cdot ds \, .$$

has been calculated by integrating over an axis parallel to the quadrupole axis, through a point 5 mm away from the quadrupole center.

Figure 7.2 shows the normalized value of G(s) with respect to the value on the central plane.

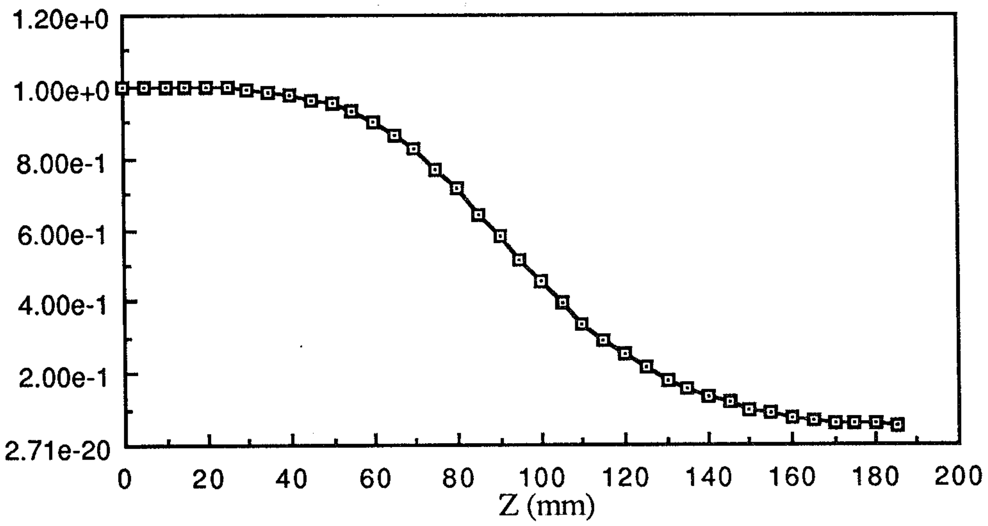

**Fig. 7.2** - Normalized value of G(s) with respect to the value on the central plane.

The value for $(L_{mag}/2)$ obtained by integrating the curve of Fig. 7.2 (half length) is 103.6 mm, this means that the mechanical length of the quadrupole must be 142.8 mm instead of the nominal 150 mm to obtain the desired magnetic length of 200 mm.

The same cross-section has been adopted for the two kinds of quadrupole. Corrector windings are provided for dipolar correction of the beam orbit. The quadrupole will be shielded so that the fringe fields can not get to the SC cavities.

The mechanical lay-out of the quadrupole is shown in Fig. 7.3.

Table 7.1 lists the basic parameters.

**Table 7.1 - Quadrupole basic parameters**

| | | |
|---|---|---|
| Gradient(maximum) | [T/m] | 1.6 |
| Inscribed radius | [mm] | 55 |
| Pole field | [T] | 0.09 |
| Pole shape | | circular |
| Ampere-turns per pole | | 2000 |
| Current | [A] | 40.8 |
| Current density | [A/mm2] | 3.14 |
| Turns per pole | | 49 |
| Copper conductor | | 4.5*4.5 Ø 3 |
| Magnetic length | [m] | 0.2 |
| Magnet resistance | [mΩ] | 200 |
| Power | [W] | 341 |
| Voltage | [V] | 8.2 |
| Iron weight | [Kg] | 73 |
| Copper weight | [Kg] | 15,5 |

The main characteristics of power supplies needed to individually power each quadrupole are the following:

| | | |
|---|---|---|
| Voltage | [V] | 12.5 |
| Current | [A] | 50 |
| Stability | | $\leq 1 * 10^{-4}$ |
| Ripple (rms) | | $\leq 1 * 10^{-4}$ |
| Resolution | | $\approx 5 * 10^{-5}$ |

The reserve voltage necessary to account for voltage drops on connections is included.

Further optimization of the system should include arrangements where magnets can be powered in series so as to simplify the power supplies and the corresponding control circuitry.

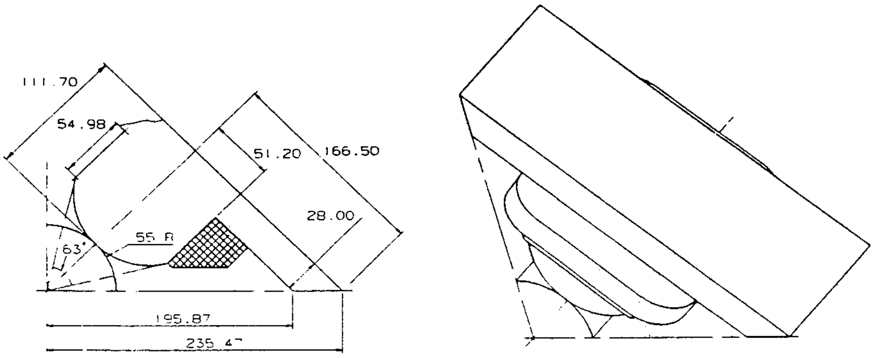

Fig. 7.3 - Mechanical layout of the Linac Quadrupole.

## 7.2 - Recirculation arc dipole magnets

With a nominal field of 1.13 T (@ 0.34 GeV) and a maximum field of 1.3 T, the dipoles can be regarded as conventional magnets.

The magnetic circuit has been designed so as not to exceed 1.8 T anywhere in the iron when the gap field is 1.3 T.

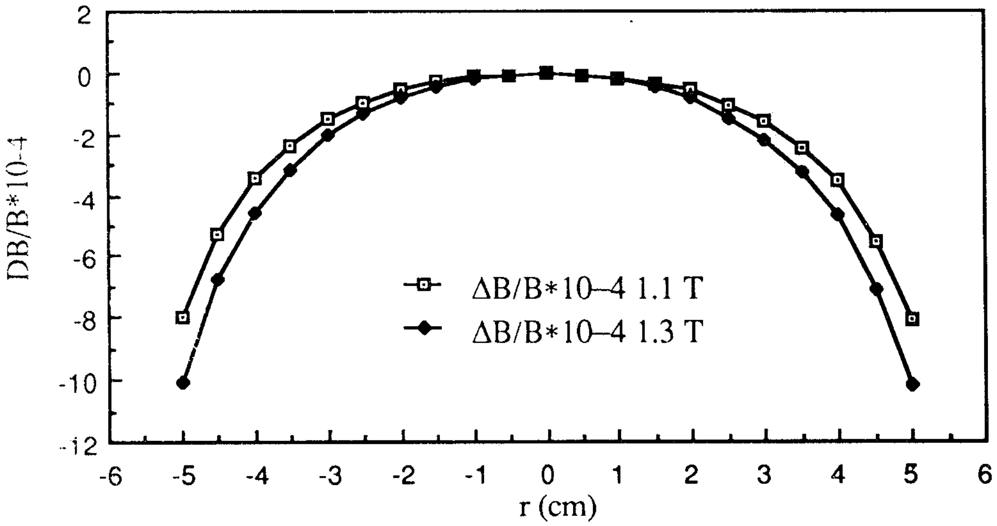

**Fig. 7.4** - Field profile of the recirculation arc dipoles.

The field profile has been studied by means of POISSON. At the moment the final shimming has not been taken into account. The field quality is already satisfactory at both the nominal and the maximum energy, as can be seen from Fig.7.4. and from the following Table 7.2.

The laminated magnet yoke is curved to follows the beam radius of curvature and has parallel end faces. A possible technical assembly is shown in Fig. 7.5.

**Table 7.2 - Dipole field quality**

| | @ x=20 mm | @ x=30 mm |
|---|---|---|
| (DB/B) $*$ $10^{-4}$ @ 1.13 T<br>(DB/B) $*$ $10^{-4}$ @ 1.3 T | -0.57<br>0.80 | -1.50<br>-2.06 |

The design current density is very close to the one that minimizes the sum of capital and running costs. It is 3.4 A/mm$^2$ at the nominal field and reaches 3.85 A/mm$^2$ at 1.3 T.

With the chosen steel dimensions, at maximum field value the iron absorbs about 8.5 % of the applied Ampere-turns.

The dipole main parameters are listed in Table 7.3.

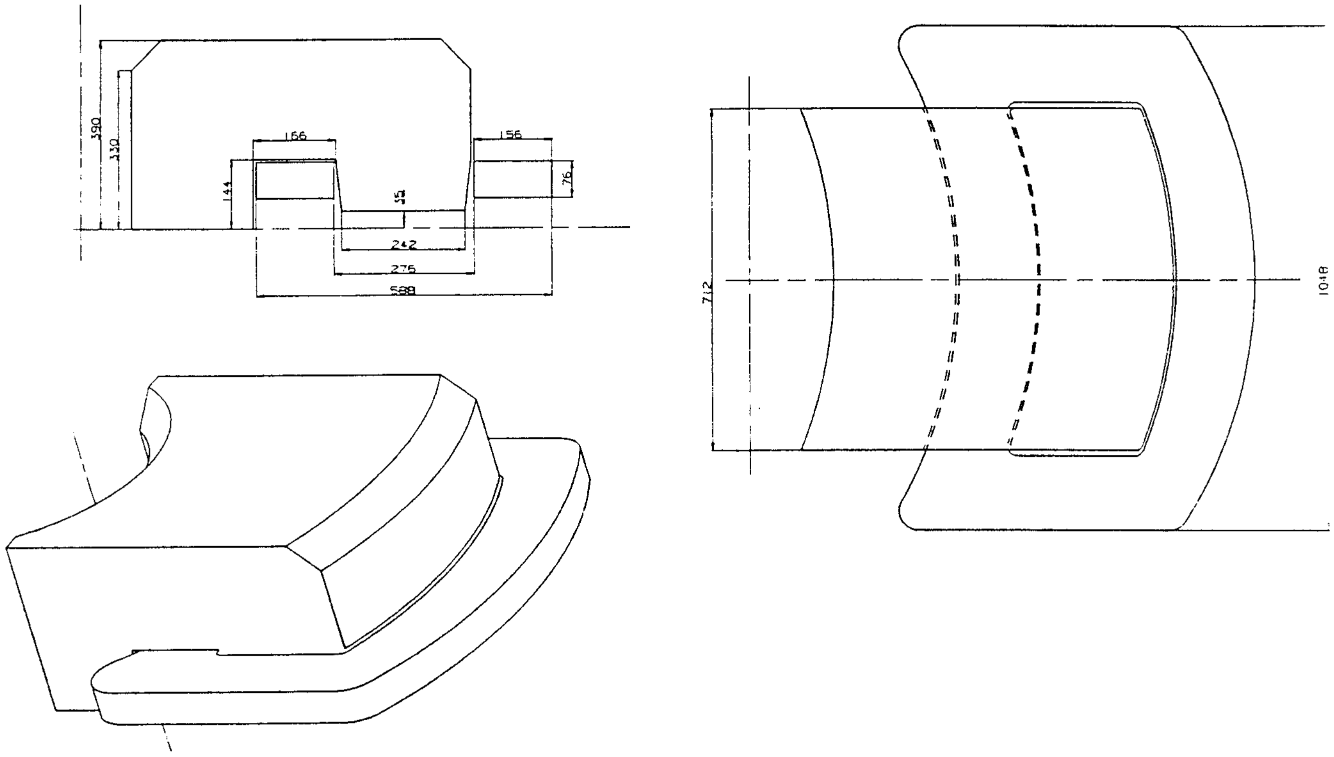

**Fig. 7.5** - Possible mechanical layout of the Recirculation Arc Dipoles.

### Table 7.3 - Recirc. Arc Dipole parameter list

| | | |
|---|---|---|
| Energy | [GeV] | 0.34 |
| Bending radius | [m] | 1.0 |
| Magnetic length | [m] | 0.785 |
| Nominal field | [T] | 1.133 |
| Pole/gap ratio | | 3.8 |
| Return leg/gap ratio | | 0.92 |
| Gap | [mm] | 70 |
| Pole width | [mm] | 266/244 |
| Amp.-turns per coil | | 34,000 |
| Current | [A] | 354 |
| Current density | [A/mm$^2$] | 3.4 |
| Turns per pole | | 96 |
| Conductor : Copper | | 12*12 Ø7 |
| Coil resistance (@ 60° C) | [Ω] | 0.051 |
| Coil inductance | 0.115 | H |
| Power per dipole | [kW] | 12.8 |
| Voltage per dipole | [V] | 36 |
| Iron weight | [kg] | 2586 |
| Copper weight | [kg] | 506 |
| Total weight | [kg] | 3092 |

No attention has been at the moment paid to the longitudinal effective field profile. Work with the three dimensional code Magnus is in progress to determine the mechanical length that will give the required magnetic length.

As concerns power supplies for the dipoles, each recirculation arc (180°) contains four 45° dipoles that can be series connected. The resulting circuit has the following electrical characteristics :

- Circuit resistance (@ 60° C) : 0.204 Ω
- Static circuit inductance : 0.92 H.

and the output voltage and current required of a classical twelve-phase bridge converter, with a 10% allowance for voltage drops on connecting cables, are :

- d.c. Voltage : 160 V
- d.c. Current : 360 A

The main transformer power is ≈ 62 kVA, with a secondary voltage of 115 V and a line current of 170 A.

The current ripple at full current is about $6 * 10^{-5}$ . Additional filtering is however foreseen to guarantee a current ripple of less than $1 * 10^{-4}$ down to current levels of ≈ 10% of the maximum value.

The power supply resolution is better than $1 * 10^{-4}$. A long term stability of the same order or better can easily be reached by means of a high stability ( $1 * 10^{-6}$) commercial transducer .

## 7.3 - Recirculation arc quadrupoles

The recirculation arc lattice contains quadrupoles whose characteristics are summarised in Table 7.3..

The magnetic length, 0.3 m, is the same for all quadrupoles. The values of $k^2$ (and of the gradient G) are very different, ranging from a minimum of 1.08 $m^{-2}$ (G= 1.22 T/m) to a maximum of 13.32 $m^{-2}$ (15.1 T/m).

The quadrupole has been optimized for the average value of $k^2$, i.e. 6.68 $m^{-2}$ ; the currents are then scaled so as to reach the other gradient values with the same geometry. A single type of quadrupole is thus foreseen at this first-order optimization stage and, consequently, no attempt to simplify the powering scheme has made; these points will have to be reconsidered in the course of further study.

The electromagnetic design has been made using the bi-dimensional code Poisson; two possible solutions, both with hyperbolic pole profiles have been studied. The first fits around a rectangular vacuum chamber with a cross-section of 11(horizontal) * 7 (vertical) $cm^2$, the second fits around an elliptical vacuum chamber inscribed in the above rectangle. In both cases the pole profile is hyperbolic.

Because of the eight-fold symmetry of the magnet only one-half pole, has been studied.

The magnetic field can be expressed in complex form as :

$$(B_x - i\,B_y) = i * \Sigma\, n *(A_n + i\,B_n)/R * (z/R)^{(n-1)}$$

where $B_x$ and $B_y$ are the horizontal and vertical components of the field respectively, n is the harmonic number ( 2 for quadrupole, 6 for 12-pole and so on), $A_n$ and $B_n$ are the coefficients of the expansion, R is a normalization radius and z is the complex variable. The normalization radius is 60 mm for the rectangular vacuum chamber case and 40 mm for the other case.

The field along the x axis can be obtained by simply replacing z by x and taking the first derivative to obtain the field gradient.

In our approximation $B_n$ is identically zero for all n's and $A_n$ takes on the values shown in Table 7.4 for the optimized quadrupole at the average gradient. At maximum gradient the scaling factors are 2.3 for the rectangular chamber and 2.37 for the elliptical vacuum chamber. At the lowest gradient the scaling factors become (1/ 5.40) and (1/ 5.43) respectively.

The gradient uniformity for the two quadrupole apertures is shown in Fig. 7.6.

## Table 7.4 - Quadrupole gradient uniformity

| n | **Rectangular V.Ch**<br>$n(A_n)/R$ | **Elliptical V.Ch.**<br>$n(A_n)/R$ |
|---|---|---|
| 2 | 3955.3 | 2661.2 |
| 6 | -136.09 | -78.40 |
| 10 | -88.39 | -3.188 |
| 14 | -19.956 | -20.765 |
| 18 | 31.174 | 8.020 |

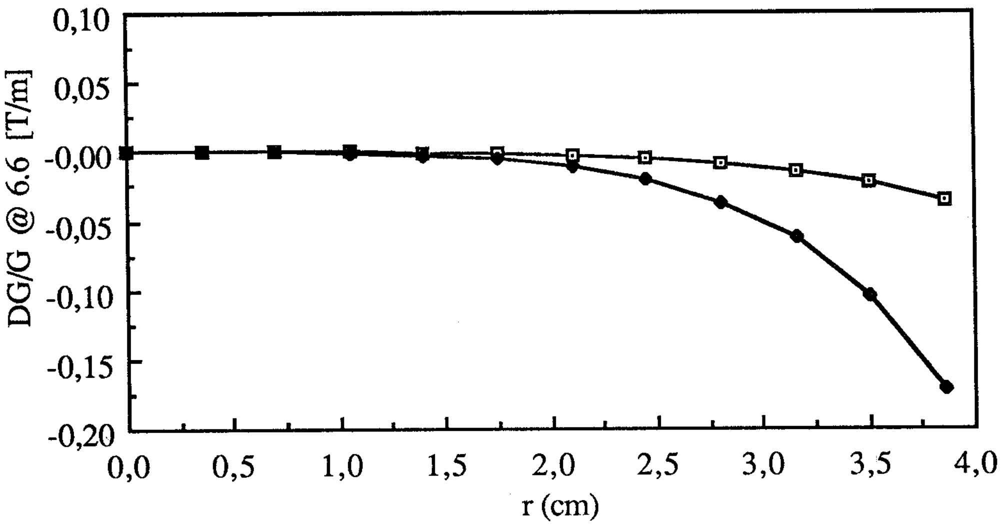

**Fig. 7.6** - Gradient uniformity of the two quadrupoles

The predicted gradient variation is : -0.1 % @ r=16.3 mm and @ r=11.2 mm respectively and -1% @ r=27.3 mm and r = 20.4 mm respectively.

The maximum value of the field in the iron is always lower than 1.8 T at the highest gradient, well away from saturation.

Correction windings are included in the main coils. They can produce about 10 % of the total Ampere-turns and can be used to generate dipolar fields in both planes.

Table 7.5 lists the main parameters of the two kind of the quadrupoles.

Figure 7.7 shows the mechanical lay-out of one of the two optimized quadrupoles.

**Table 7.5 - Main parameters of the two quadrupoles**

| Elliptical v.c. | | | Rectangular v.c. |
|---|---|---|---|
| Gradient (nominal) | [T/m] | 6.6 | 6.6 |
| Inscribed radius | [mm] | 62 | 44 |
| Pole field | [T] | 0.435 | 0.29 |
| Pole shape | | Hyperbolic | Hyperbolic |
| Ampere-turns per pole | | 10250 | 5160 |
| Current | [A] | 157.5 | 151.8 |
| Maximum current | | 454 | 368 |
| Nominal current density | [A/mm2] | 3.55 | 3.42 |
| Max. current density | [A/mm2] | 10.23 | 8.29 |
| Min. current density | [A/mm2] | 0.66 | 0.63 |
| Turns per pole | | 65 | 34 |
| Copper conductor | | 8*8 Ø 5 | 8*8 Ø 5 |
| Magnetic length | [m] | 0.3 | 0.3 |
| Magnet resistance | [mΩ] | 132 | 60. |
| Nominal voltage | [V] | 20.8 | 9. |
| Maximum voltage | [V] | 60 | 22. |
| Nominal power | [W] | 3300 | 139 |
| Maximum power | [W] | 27240 | 8170 |
| Iron weight | [Kg] | 193 | 94 |
| Copper weight | [Kg] | 116 | 53 |

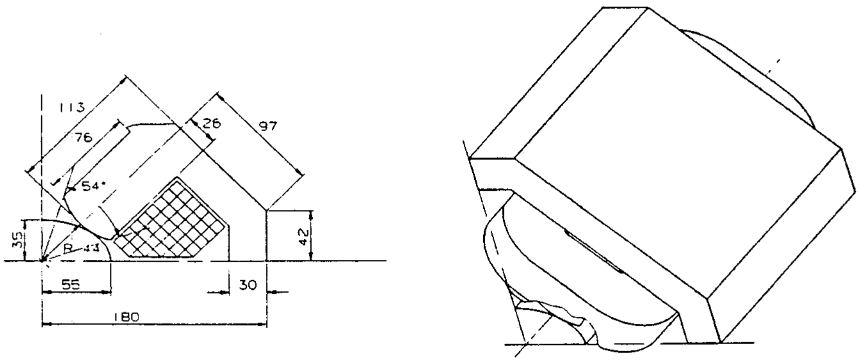

Fig. 7.7 - Mechanical layout of one of the two optimized quadrupoles.

# 8 - BEAM INSTRUMENTATION AND CONTROL SYSTEM

## 8.1 - Basic Requirements

The Beam Instrumentation and Control system should allow the ARES performance and hardware to be monitored and controlled from a single Main Control Room. All monitoring and control components and systems , such as Diagnostics elements, Magnets, RF, Beam and Machine timing, Cryogenics, Vacuum, etc., must be under full computer control. To be more specific, the Beam Instrumenrtation and Control system should fulfill the following basic requirements :

- to present meaningful yet concise information or alarms about the operational status of the hardware and the performance of components;
- to automatically reset to a wanted condition a given sub-component, component or a combination thereof in a consistent and safe way;
- to decode complex commands (e.g. set-up of a particular Linac beam) into a sequence of separate, synchronized, interdependent actions. A machine timing system is thus necessary to synchronize the various states of the accelerators. A fast analogic beam timing system is also necessary to tag the various beams;
- to let the machine physicist interact with the Instrumentation & Control system in a transparent way in terms of accelerator physics quantities;
- to simulate, in real time, the effect of commands on performance;
- to simulate the beam behaviour according to analytical or empirical models of the various components in order to avoid or reduce to a minimum, already in the commissioning stage, the trial and error time-consuming practice;
- to be extremely reliable and capable of fast response times.

The requirements listed above are rather crucial especially in view of the experimental nature of the machine that will require maximum operating flexibility. In particular the last one is essential for a safe handling of high power beams in a superconducting environment.

Moreover, as extensive use of modeling is to be implemented since the very beginning, the full integration of the diagnostic system into the computer control system is a major design constraint.

The ultimate goal of the diagnostic and control system is the capability for the operator to set the requested value of a given beam characteristics (e.g. emittance, current intensity, time structure) and let the computer system act so that the measured beam characteristic matches within reasonable limits the requested value.

Tuning and maintaining the optimal conditions of a beam may eventually require the implementation of real-time feedback loops acting on different systems, on a time scale that can range from minutes down to seconds, sometimes on a pulse-to-pulse basis; these loops could be computer-mediated. The need for within-the-pulse feedback is at this stage excluded.

The features of the ARES LINAC most relevant for establishing the number and type of beam diagnostics and control components and instruments are:

- high power beams may permanently damage the accelerator and/or create inacceptable radiation levels if mis-steered. We recall that the SC RF cavities can be quenched by few Joules of incident energy, to be compared with a beam power in the order of tens of kWatts.
- very low emittance beams;
- the intention of using the accelerator as a test-bench for collider and FEL grade beams. This calls for extensive and redundant general-purpose beam instrumentation. Moreover, the implementation of special instrumentation and of sections devoted to some particular beam measurement may be occasionally required.

A list of the main accelerator complex component systems is given in Table 8.1.

**Table 8.1 - ARES Main Components**

| | | |
|---|---|---|
| **INJ** | RF SC Injector | > 4 MeV |
| **IBAS** | Injector Beam Analysis Station | output of INJ |
| **TCI1** | Transport line from injector to Linac 1 | |
| **L1** | SC Linac, Section 1 | 48 MeV |
| **LBAS** | L1: Beam Analysis Station | output of L1 |
| **TC12** | Transport channel from L1 to L2 | |
| **L2** | SC Linac, Section 2 | 196 MeV |
| **TC1** | Recirculation Channel 1 | |
| **TC2** | Recirculation Channel 2 | |

## 8.2 - Beam Diagnostics

The full complement of beam instrumentation is summarized in Table 8.2.

Wall current monitors with a bandwidth up to ~ 2 GHz are used for the monitoring of tightly bunched beams.

The total beam current is monitored by toroidal current transformers having a bandwidth in the range from a few Hz to ~ 20 MHz. An auxiliary winding, carrying pulses of known charge provides a calibration signal to be injected in between successive beam pulses. Current transformers are placed at the beginning and at the end of each Linac section and of each transport line, to monitor the accelerated beam current. Whenever a significant beam loss is detected, a beam stopper is automatically inserted upstream and the gun current is lowered.

**Table 8.2 - Summary of Diagnostic Devices**

| TYPE OF DIAGNOSTICS | INJ | IBAS LBAS | L1 | L2 | Transport Channels |
|---|---|---|---|---|---|
| Wall current monitor | 1 | 1+1 | 2 | 2 | 8 |
| Toroidal current monitor | 1 | 1+1 | 2 | 2 | 8 |
| Beam dump/Faraday cup | 1 | 1+1 | 1 | 1 | |
| Energy defining slit | | 2+2 | | | 4 |
| DC Current transformer | 1 | | | | |
| Beam position monitor | | 3+3 | 7 | 7 | ~ 50 |
| Emittance monitor | | 1+1 | | | |
| SEM grid/rotating wire | 1 | 1+1 | | | 10 |
| Fluoresc. screen + TV | 1 | 1+1 | | | 10 |

Each Linac section is protected by a retractable beam dump incorporating a Faraday cup for precision current measurement. The Faraday cup structure is coaxial so that it can also be used to measure the incoming beam fast time structure. When the upstream Linac section or transport channel are being set-up or optimized, the input beam stopper of the next section is kept inserted until the incoming beam characteristics are acceptable.

Computer controlled moveable slits are used along transport lines to scrape away any beam halo outside the channel acceptance limit and to prevent distributed beam spills.

At the exit of the injector a measurement station (IBAS) is provided to fully characterize the beam in the longitudinal and transverse phase-space. The measurement station includes a spectrometer magnet to measure the beam energy and energy spread and a transverse RF cavity to measure bunch length.The basic arrangement is similar to that implemented on Lisa (50).

The measurement of a low emittance beam is best done at low energy, at the injector output, in two steps. The beam transverse size is first measured, at a given location, by scraping it with a motorized blade, measuring the transmitted current to a Faraday cup as a function of the scraper position and computing the transverse charge distribution by differentiation. The opening angle is then measured by passing the beam through a narrow slit and measuring the transverse dimensions by means of a fluorescent screen and a TV camera, located downstream the slit after a sufficiently long drift space.

An emittance measurement station (LBAS) is provided at the the end of the first superconducting Linac section, L1.

Energy measurements are done in the non-zero dispersion regions of the transport lines and of the recirculation arcs by means of fluorescent screens and TV cameras or secondary emission devices such as rotating wires or retractable wire grids. No beam intercepting devices are foreseen on the SC Linac.

The beam emittance is measured at the output of the Linac section L2, in order to dinamically match the optical functions of the following transport channels and to optimize beam steering; this minimises the emittance degradation. The transverse emittance is determined by measuring the beam transverse dimensions with a fluorescent screen as a function of the orientation of the phase-space ellipse corresponding, i.e. of the strength of an upstream quadrupole. Since the transport matrix from quadrupole to screen is known, the beam emittance can be determined by a quadratic fit of the beam size vs. quadrupole strength curve (51).

## 8.3 - Beam Position Monitors

Beam position monitors (BPM) are used to measure and steer the beam trajectory in the Linacs, transport channels and arcs.

Longitudinal and transverse wake fields in the RF cavities, that may blow up the beam longitudinal and transverse emittances, have to be reduced to a minimum; the beam must therefore be made to enter the Linac section as exactly as possible on axis and be kept there. Preliminary calculations (52) show that, because of the relatively low Linac frequency, the absolute accuracy required of the beam position monitors is ~ 0.1 mm, comparable to the standard quadrupole position alignment tolerance. The resolution should be better than the minimum rms beam transverse size, i.e. ~ 50 μm.

One BPM per quadrupole is foreseen. The BPM's are designed to fit inside quadrupoles and are installed on all Linac, transport channel and recirculation arc quadrupoles . The mechanical center of the monitor is precisely referenced to the quadrupole axis. Shielded bellows at both ends mechanically decouple it from the rest of the vacuum chamber (see Fig. 8.1).

To fully exploit the potentials of the Superconducting Linac, the BPM and the associated electronic detector are designed to work with any number of bunches and any time structure of the beam. They consist of four 50 Ω strip-line electrodes (53) short circuited at one end, inside the vacuum chamber. The four strips are everywhere arranged in the horizontal and vertical plane for direct X and Y position readout, except in the vicinity of the spectrometer magnets and in high dispersion regions (51) where they are mounted at 45 degrees.

The strips are 0.15 m long, to produce a broadly resonant response at around 500 MHz, the Linac drive frequency.

The strip-line monitor voltage response is a doublet of opposite polarity pulses, separated by a time interval of 1 nsec, in coincidence with each bunch. Since the waveguide cutoff frequency associated with the vacuum chamber radius is ~ 2.2 GHz, no RF feed-through is expected at the monitor location.

A schematic view of the beam position electronics is shown in Fig. 8.2. The narrow pulses are smoothed by the filtering action of the cables connecting to the detector head and are fed to band-pass filters resonating at 500 MHz. The pass-band shape is such as to let the ringing response decay within approximately 50 nsec (quality factor ~ 20), in order to discriminate between the electron bursts. In the proposed scheme the 500 MHz pseudo-sinusoids are down-converted to 71.4 MHz by means of mixers with a local oscillator frequency of 6 • 71.4 MHz, amplified and fed to the detector. The position detector is based on the phase modulation-demodulation technique, whereby the amplitude ratio of two opposing strips, carrying the position information, is converted by means of a quadrature hybrid junction into a phase difference between two pseudo-sinusoidal signals (54). The advantage of such type of detector is that it is self-normalizing: i.e. the position information is independent of the current intensity. The output of a phase detector gives the position information.

A gate signal provided by the beam timing system allows to select any one beam pulse (electron, positron, first or second passage). The detector operates at any bunch configuration in the range from single bunch to continous beam. Detectors operate in a multiplexing mode to sample the position of groups of 10 BPM's.

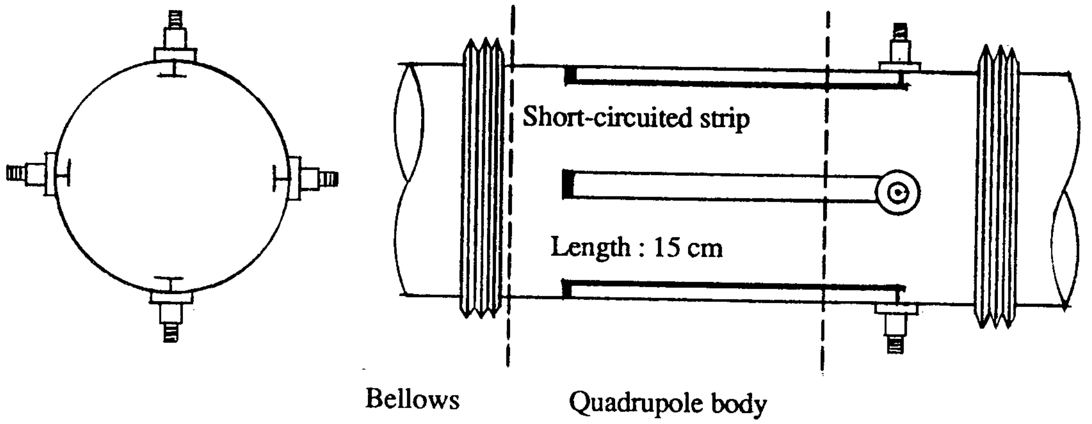

Fig. 8.1 - Schematic view of a strip-line Beam Position Monitor of the section L3 quadrupole.

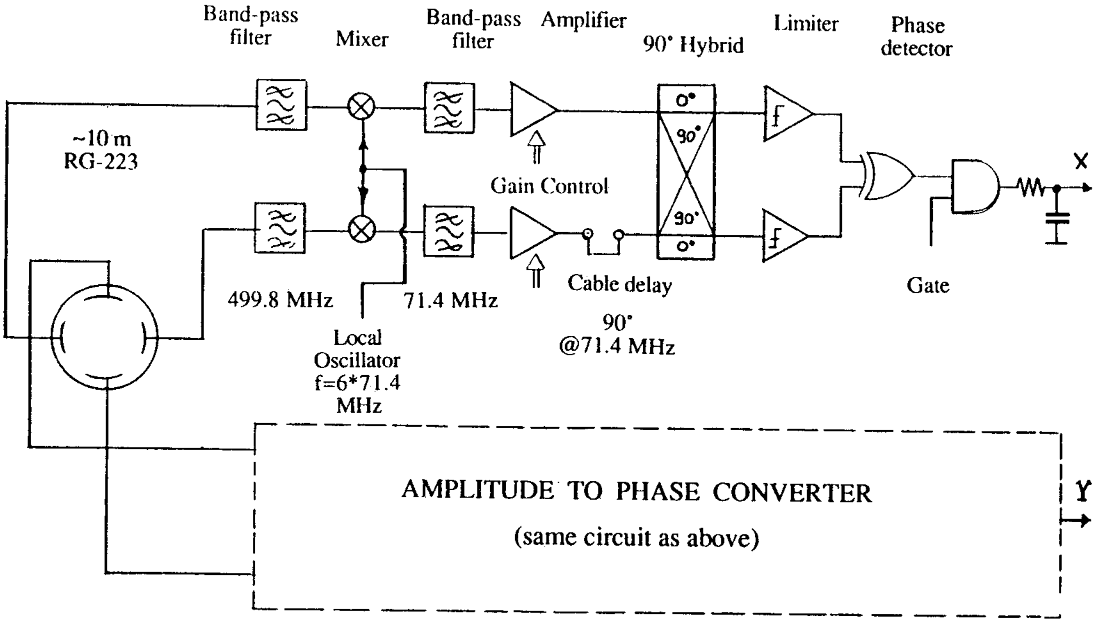

Fig. 8.2 - Schematic diagram of the beam position monitor detector.

## 8.4 - Control System

### a) Introduction

The Control System is a very critical point for an accelerator complex, especially if tight constraints are posed on beam quality and or on the performance of the machines, the last being heavily dependent on the availability of a good and reliable hardware and software environment.

The Control System has therefore to be part of the machine design itself and must develop in parallel with it. It can be thought of as having two main parts:

- the "real machine" part consisting of the control hardware and software used to interface equipment and instrumentation; its design must take into account the accelerator topological and functional distribution and avoid data flow bottle-necks.
- the "virtual machine" part consisting of the control, modeling, simulation and optimization software; its design and commissioning is determined by accelerator physics and is, therefore, closely related to the machine type and the specified overall performance.

The initial design of a new accelerator control system is always complicated by the accelerator components and parameters to be controlled not usually being completely specified at the beginning of a project and also by the fact that performance as well as cost of components and tools that come on the market evolve very fast on the time scale of the average project.

The vertical growth of hardware capabilities in the computer field (computing power and memory capacity keep doubling every 2-3 years, and the growth curve shows no signs of a plateaux) creates an environment where whatever is functioning is definitely old. Moreover, the corresponding development in the software field keeps delivering new tools which are not only powerful, but also easy to learn and to use. The situation is thus definitely unstable but, on the other hand, an ever increasing number of powerful tools, which become reliable very soon because the number of users is also growing fast, are thrown on the market. The involvement of industry in the electronic standards also provides the user with always new and more reliable instruments. A classical example is the amazing speed at which the VME standard has diffused, as compared to CAMAC.

On the other hand the lifetime of an accelerator is comparatively long and during its span the machines are usually partially or even totally reconfigured. Hardware and software products used in the system should therefore be standard, possibly non proprietary, with large diffusion, so that they may be expected to receive strong support from the manufacturer over many years.

We have here tried to lay down some basic scenarios, based on current philosophies about hardware and software architectures(55) so as to be able to derive reasonably reliable cost and manpower estimates. A definite detailed solution has not however being singled out as yet and a final committment will be made only at the very last moment compatible with the time scale of the project.

It is worth recalling here that, from the point of view of the control system, the general features of the ARES accelerator complex are:

- Linac sections are separate but must operate synchronously and in very strict correlation.
- The physical dimensions of the site are of the order of a hundred meters.
- The accelerator is to be used as a test bench for accelerator development. This means that the control system must be particularly flexible and friendly towards both professional operators and machine physicists.

Two different lines of approach to the problem of designing the system are being investigated, based on what has or is being done on similar projects such as LEP(56), ESRF, ELETTRA(57), and our own LISA(58).

One is a 'conventional' distributed system, along the lines of those installed and tested on LEP or being implemented at ESRF and ELETTRA, the other is a less conventional centralized system based on the one being implemented for LISA.

Both have advantages and disadvantages that will be briefly discussed in the following. From the point of view of capital cost there are no substantial differences and a final decision on which to adopt can be taken later.

Both are based on the use of VME as a peripheral interface.It is the most modern, practical and widespreaded modular electronics interface standard and distributed processing system. Because many of multi-vendor products based on the 68K family are available, specific choices are not critical.

### b) Distributed system

From the machine component point of view several sub-systems can be identified such as magnet power supplies, RF, vacuum and refrigeration equipment, beam diagnostics sensors, alarm monitoring and access control. A structure capable of coping separately with all procedures and functionalities along the machine - a flexible, modular and open scheme, implemented using intelligent and hierarchical levels - is the answer to the problem.

It includes a local area network (i. e. ETHERNET), workstations with high processing speed and very powerful graphics to serve as consoles for the human interface, one of the several software tools able to generate windows, menus, etc., and finally an operating system for the peripheral CPU's which has already been used and debugged.

The whole system is distributed, so to ensure local processing power to set, monitor and diagnose the hardware. Topological and/or functional criteria are taken into account. A modular approach, provides the required flexibility.

Based on the above concepts, the four logical level architecture briefly described in the following is proposed(59); its block-diagram is shown in Fig. 8.4.1. Note that although not each box in the diagram has been named at this stage, real products have been considered for the various blocks.

### First level

A few workstation consoles and one server provide the man interface to operate the accelerator. The powerful graphics capabilities can be used to increase the "bandwidth" of the operator comprehension and the processing power provides adequate support for modeling and/or simulation.

The server provides the general Data-Base, the normal spooling and log file management, other service programs and the link to the external network. Sub-systems and low level instrumentations can be deep-accessed through personal computers, with unsophisticated tools. A special personal computer is completely dedicated to the continuous monitoring of alarm messages incoming from the lower levels.

### Second level

It consists of several supervisor processors that manage all procedures needed to operate different machine sub-systems and provide general control functions for all main accelerator parameters. To limit the need for throughput to the first level, they also filter-out insignificant messages and are thus able to manage the sector they supervise without overloading the consoles.

The processors are connected to an appropriate network so that they can be physically placed where they are most useful.

### Third level

The third level consists of several additional processors, sharing the VME bus, that manage smaller accelerator parts or sub-systems. They mainly provide setting and readout functions for all linked modules. A continuous monitoring procedure informs the second level supervisor on the status of the hardware. A distributed Data-Base can thus be up-dated.

Fourth level

The lowest level is the interface to the accelerator hardware proper (such as magnet power supplies, RF, vacuum and diagnostics components etc.). Many of the interfaces have only a limited number of channels (typically ADC, DAC and I/O bits) and can be served by a same, simple, general purpose module. General purpose instrumentation interfaces, typically IEEE-488 and the new VXI, are also foreseen.

The physical size and the topology of the accelerator complex and the need to provide distributed power, require a network system that can serve different kind of processors.

In principle each processor (console, server, sub-system supervisor and lower level distributed CPU) could have a different operating environment (a general or special purpose operating system or simply a real-time kernel). Standardization is however a must, in order to reduce the amount of software development and improve the message-exchange performance in a non homogeneous environment.

Careful analysis of the requirements in terms of message size, necessary speed and transmission rate, indicates that three different types of links are required:

- link between consoles, server and supervisor processors. Because of the small number of nodes (<20) an IEEE 802.3 Ethernet CSMA/CD link with TCP/IP protocol is the most suitable. Non deterministic behaviour can be minimised by leaving most of the machine management to the sub-system supervisor so that the number and size of messages are drastically decreased.
- link, connecting each supervisor to the lower level CPU's ( both in VME crates). It consists of a fast parallel bus, like VICbus (formerly VMV bus), and of a slower serial multi-drop, such as MIL-1553-B. Depending on the particular demand, both can provide optimal links among several crates, a feature not foreseen by the VME standard.
- link between end-level VME crates and specific equipment. As earlier mentioned, a very simple special module can be implemented to interface to several types of power supplies. A multi-drop highway based on a simple command-response protocol is a very cost-effective solution.

As concerns software, one notes that while hardware costs are falling and high performance products are continuosly coming on the market, overall software charges - including development - are on the rise. As a consequence a multitude of soft/hardware integrated solutions, are offered on the multi-vendor market as turnkey solutions.

In line with the general scheme outlined above, we choose the UNIX operating system,with C and FORTRAN, for the console level. As a data-base we will adopt Oracle, the most diffused and supported. General modeling programs (such as MAD and PARMELA) will be implemented to serve as tools for the "virtual machine" control system programs. Lower levels will use the OS-9 operating system, C, FORTRAN and Assembler.

To make the system as user-friendly and possible all modern tools such as X Windows, Dataviews, DV-Draw and DV-Tools are being investigated.

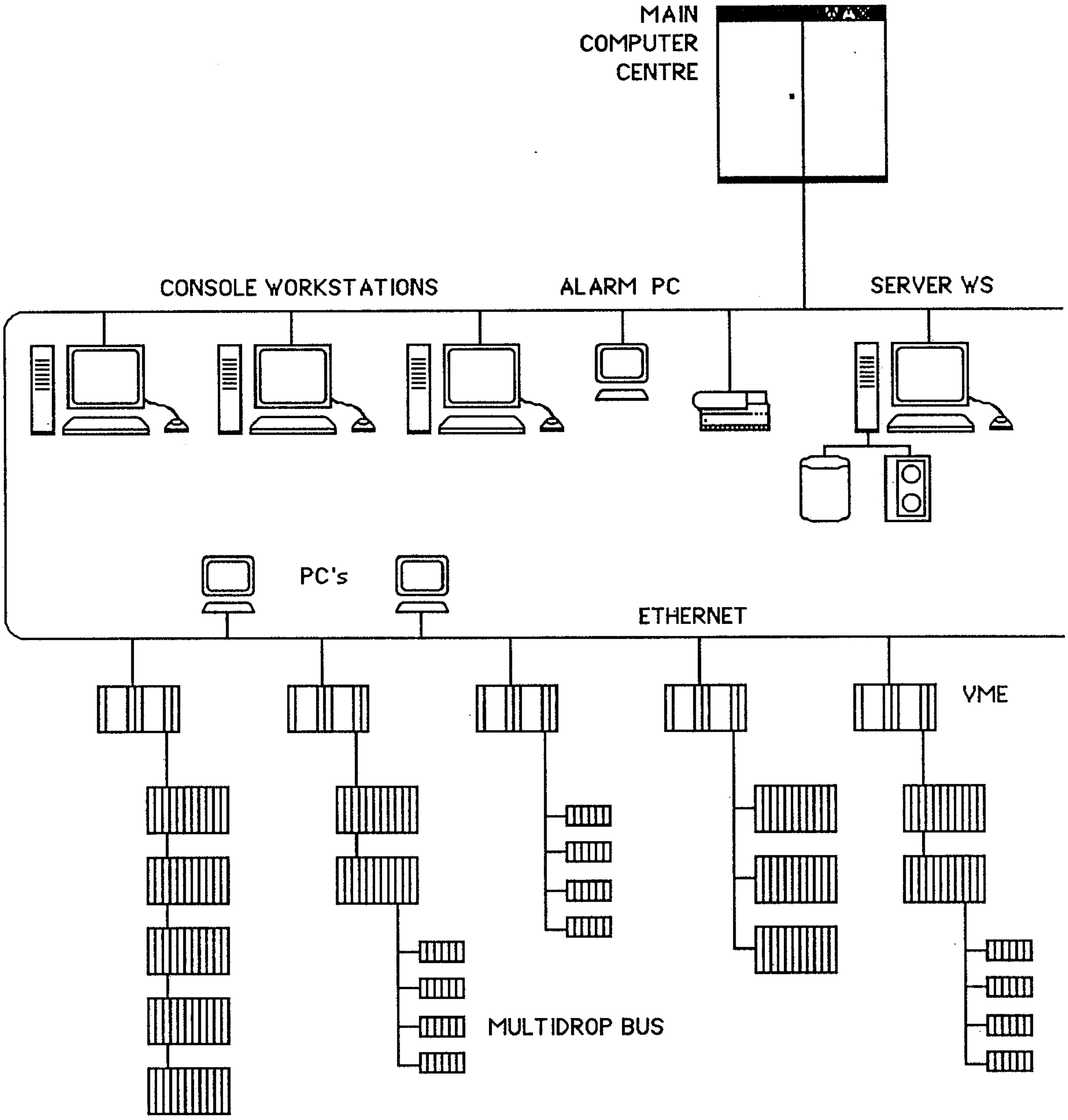

Fig. 8.3 - Block diagram of the Distributed System Configuration

The main advantage of the system is mainly that of requiring very little development and of being able of readily making use of the hardware and software tools, developed for instance in the course of the joint program between ESRF, Elettra, CERN, et al. that has resulted in a marked improvement in standardization.

### c) Centralized system

The controls for LISA (50) were (and are being) developed in an attempt to develop a new approach to an integrated accelerator control system and to use the fact that increasingly powerful tools are continuously being marketed.

As an example it will become possible to use FDDI instead of ETHERNET, with a net increase in speed of a factor of ten. Copper cables will be replaced by fiber-optics cables, allowing larger distances to be covered without repeaters and increasing the connection reliability, at least as long as low radiation environments are considered. OS-9 will be probably replaced by the Motorola VMEexex, which supports not only multitasking but also multiprocessor systems.

During the development of the LISA control system, quite a few new ideas have been implemented and more are being tested.

The basic idea is to concentrate and centralize the communication system because a centralized system is more simple to handle and also more reliable, since attention can be paid to only a small number of easily replaceable units.

This is contrary to what is generally claimed about the reliability of a distributed system, but it has to be noted that there is a conceptual difference between an accelerator control system and a system which has to meet military standards: reliability considerations can change dramatically when a network which has to be able to continue functioning, even partially, in case of intentional damage is considered instead of a control system - limited to a few buildings - for an experimental physics setup.

The implementation of a centralized system is made possible by the availability of very fast parallel buses (51).

The LISA system is built around a central VME processor which coordinates all the communications between different parts of the entire setup and keeps updated a central memory which constitutes the prototype of the system database.

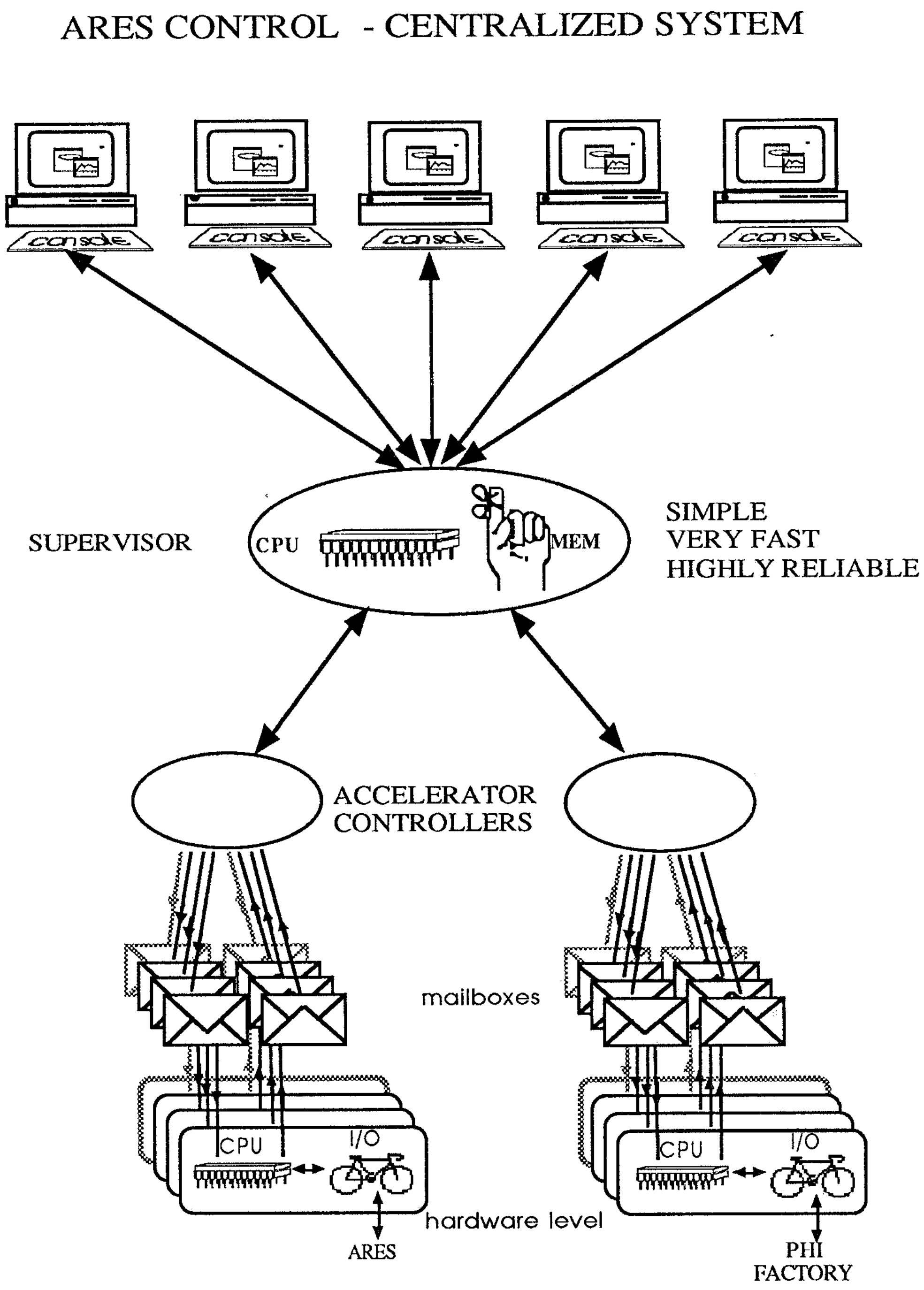

**Fig. 8.4** - Block diagram of the Centralized System Configuration.

In a multiple accelerator environment it would be very easy to extend this scheme using a tree configuration. You would have more than one central processor, possibly one for each machine, and an additional upper level coordinating the local supervisors. The different roots of the tree would act as filtering bridges, transmitting to the upper levels only the necessary information and shielding the main supervisor from local traffic. A possible block diagram is shown in Figure 8.4.2.

The high speed local buses used in LISA suffer from distance problems: it is very difficult to operate them at distances over 100 meters. Fortunately, several fiber optic connections are appearing on the market to replace our 60 conductor cables. Although the optical fibers are sensitive to radiation damage, it is easy to implement a mixed system where large distances are covered by fiber optics trunks, while local cables could cover the high radiation level sections.As far as software aspects are concerned, new and powerful tools are being developed for the easy implementation of the human interface, which has been a gigantic problem up to now. Hypercard is a first example of this kind of software.

For the peripheral CPU software the usual solution of a multitasking system is nowadays strongly under objection. A multitasking system for a peripheral CPU which only has to look at a few memory locations every now and then looks very much like trying to kill a fly with a cannon. The opposite point of view is represented by the famous statement "One task, one processor". This is an optimal way to look at things, although, as with every beautiful theoretical construction, it sometimes suffers from implementation problems, like having to buy a new CPU to perform some really trivial task. The intrinsic soundness of the principle however lies in its extreme simplicity.

The main advantages of the centralized system configuration is the large bandwidth afforded by the direct memory access mechanism. For example, the LISA system allows the exchange of 1700 messages per second in between (the three) levels, while comparable systems built around ETHERNET have a capacity of only a few tens of messages per second.

An additional advantage of such a hierarchical system is the centralized database. A single location for all machine status data means no problems of memory consistency and very easy maintenance.

Although some authors find the 'centralized' software a difficulty, the central argument for this kind of solution is that new, powerful tools are becoming available and should be used and that the statement "old is more reliable" does not apply to software.

## 9 - POWER INVENTORY

Usual the most power demanding systems are the magnets and the radio frequency,but here the use of superconducting components requires a significant part of the whole power to be devoted to cryogenics.The numbers listed in the power inventory are a first order estimate done for the purpose of cost evaluation; for minor details, still missing, concerning mostly conventional electrical services, the forecast is based on estimates derived from similar installations.

In particular, conventional plants include heating, air conditioning, lighting, compressed air plants, alarm & fire protections, etc. The power devoted to helium compressors depends on the liquefaction rate needed by the s.c. cavities. Finally, it must be noted that the listed power - except ,of course, that for the general building services - is intended as maximum requirement, with the SC LINAC in operation at maximum energy.

The total power inventory is detailed in the following Table 9.2.1 and adds up to about 1.9 MW.

**Table 9.2.1 - Power Inventory [kW]**

| | |
|---|---|
| **LINAC** | |
| Injector | 250 |
| Conventional & s. c. linac Quadrupoles | 30 |
| Recirculation Arcs Dipoles | 80 |
| Recirculation Arcs Quadrupoles | 60 |
| Helium compressors | 900 |
| Radiofrequency | 180 |
| **Subtotal** | **1500** |
| **GENERAL SERVICES** | |
| Cooling water system | |
| Primary circuits with forced ventilation cooling towers | 150 |
| Secondary circuits for purified water | 100 |
| General building services | |
| 7 % of the operating power | 150 |
| **Subtotal** | **400** |
| **TOTAL** | **1900** |

## REFERENCES

(1) Proc. Discussion Meeting on SC Linear Accelerators; Frascati, Oct. 1986

(2) Proc. Discussion Meeting on Physics possibilities of a high luminosity e+e- facility of up to 12 GeV; Frascati, Apr. 1987

(3) Proc. Workshop on Heavy-Quark Factory and Nuclear Physics Facility with Superconducting Linacs, Courmayeur, 14-18 December 1987, E. De Santis, M. Greco, M. Piccolo and S. Tazzari Eds., Italian Physical Society, Conf. Proc. Vol 9, 1988.

(4) U. Amaldi, G. Ciognet, Nucl. Instr. and Methods, A260 (1987), 7.

(5) U. Amaldi, Proc. of the Topical Seminar on Heavy Flavours, S. Miniato, 1987, F.L. Navarria Ed., Nuclear Physics B (Proc. Suppl.) 1B (1988), 237.

(6) R.Sundelin, "Fully Superconducting Linear Colliders", Proc. Capri Workshop on Linear Colliders, Capri, 13-17 June 1988.

(7) D.L. Rubin et al., Superconducting RF Linear Collider, Proc. of the 1989 Particle Accelerator Conference, March 20-23, 1989. Chicago, IEEE 89CH2669-0, p.721.

(8) W.A.Barletta, A.M.Sessler, Radiation from fine, intense, self focussed beams at high energy, Proc. of INFN Int. School of Electromagnetic Radiation and Particle Beam Acceleration, Varenna, Italy, June 20-25, 1988, p. 211-220.

(9) G.Vignola, et al., A new method for pumping an optical klystron, Proc. of International Workshop on Coherent and Collective Properties in the Interaction of Relativistic Electrons and Electromagnetic Radiation, Villa Olmo (Co), Italy, September 13-16, 1984, p. 43-46.

(10) J.C.Goldstein, Electron beam requirement for soft X-ray/XUV free electron laser, Proc. of the ICFA workshop on low emittance e-e+ beams, Brookhaven National Laboratory, March 20-25,1987, p. 180-196.

(11) J.M.Peterson, et al., Summary of the working group on design of an a FEL/storage ring for L<1000 A, Proc. of Int. Workshop on Coherent and Collective Properties in the Interaction of Relativistic Electrons and Electromagnetic Radiation, Villa Olmo (Co), Italy, September 13-16, 1984, p. 43-46.

(12) L. Serafini et al. Rep. LNF-90/016(R), March 1990.

(13) S.Bartalucci, L.Palumbo, M.Bassetti - Int.Report- LNF-89/051(R)

(14) ARES Design, Study, The Machine, Rep. LNF-90/005(R), Frascati, Jenuary 1990.
C. Pagani, S. Tazzari - "ARES: Configurazione del Linac SC" - MEMO ARES 12, Frascati October 1989.

(15) Proposal for a Φ-Factory, Rep. LNF-90/031(R), Frascati, April 1990.

(16) L. Serafini et al., Rep. INFN/TC-90/10, Milano, May 1990
L. Serafini et al., LNF Internal Memos, ARES 2, 14.
L. Serafini et al., Design of the SC Laser Driven Injector for ARES, Presented at the 2nd EPAC Conference, Nice, June 1990.

(17) J.S.Fraser, R.L.Sheffield, High-brightness injectors for RF-driven Free-electron lasers, Los Alamos 1987, IEEE Jour. Quan. Electr. Vol. QE-23 No. 9 Sept. 1987 p. 1489/1496.

(18) R.L.Sheffield, High-brightness electron injectors, Proc. of the ICFA workshop on low emittance e-e+ beams, Brookhaven National Laboratory, March 20-25,1987, p. 141-152.

(19) K.T.McDonald, Design of the laser driven Radio-Frequency electron gun for the Brookhaven accelerator test facility, Princeton University, January 17, 1988.

(20) H. Chaloupka, H. Heinrichs, H. Piel, et al, A Proposed Superconducting Photoemission Source of High Brightness, Proc. 1st EPAC, Rome, June 7-11, 1988.

(21) K.J.KIM, Rf and space charge effects in laser-driven electrons guns, Berkeley 1988, Nucl.Instr. and Meth. A275 (1989) 201-218.

(22) P.M.Lapostolle, Possible emittance increase through filamentation due to the space charge in continuous beams, IEEE Trans. Nucl. Sci. vol. NS-18, no. 3, p. 1101-1104, 1971.

(23) J.D.Lawson, The physics of charged-particles beams, Oxford University Press 1977.

(24) Serafini et al., Proc. first EPAC, Rome, Italy, June 1988.

(25) Serafini et al., Proc. of INFN Int. School of Electromagnetic Radiation and Particle Beam Acceleration, Varenna, Italy, June 20-25, 1988, p. 211-220.

(26) P.E.Oettinger, A selections of high-brightness laser driven cathodes for electron accelerators and FEL's, Proc. of the ICFA workshop on low emittance e-e+ beams, Brookhaven National Laboratory, March 20-25,1987, p. 153-163.

(27) T.Weiland, CERN/ISR-TH/80-07, 1980

(28) J. S. Fraser et al., Proc. 1987 Part. Accel. Conf., Washington. DC, March 16-19, 1987.

(29) C. H. Lee et al, Practical Laser Activated Photo-emissive Electron Source, Rev. Sci. Instrum, 56, (4), 1985.

(30) K.Batchelor et al., Development of high brightness electron gun for the ATF at BNL, Proc. 1st EPAC, Rome, June 7-11, 1988.

(31) M. Boussoukaya et al, Pulsed Photocurrents from Lanthanum Hexaboride Cathodes in the ns Regime, Nucl. Instr. and Methods, a 264, 1988.

(32) H.E.Koechner, Solid State Laser Engineering, Springer-Verlag, New York, 1976.

(33) S.L.Shapiro, Ultrashort Light Pulses: Picosecond Techniques and Applications, Springer-Verlag, New York, 1977.

(34) C. Biscari et al., "An Injector for LISA" - Rep. LNF-88/08(R) Frascati 1988.
C. Biscari et al., LISA Injector, Presented at the 2nd EPAC Conference, Nice, June 1990.

(35) S. Kulinski, M.Vescovi - "A Gun For LISA" - Rep LNF 87/98(R) Frascati Nov. 1987.

(36) H. Piel, Wuppertal University note WUB 87-13, (1987).

(37) C. Benvenuti, N. Cirelli, M. Hauer, W. Weingarten, Proc. 2nd Workshop on RF Superconductivity, H. Lengeler Ed., Geneva, July 23-27, 1984

(38) D. Di Gioacchino, U. Gambardella, P. Gislon, G. Paterno', C. Vaccarezza, INFN note LNF 89/064 (R), (1989)

(39) V.Lagomarsino, G.Manuzio, R.Parodi, R.Vaccarone, IEEE Trans. MAG-15, 25 (1979).

(40) C.M.Lyneis, H.A.Schwettman, J.P.Turneaure, Appl. Phys. Lett. 31, 541 (1977).

(41) U.Klein and D.Proch, Proc. of the Conf. on Future Possibilities for Electron Acc., Charlottesville (Virginia), 1979.

(42) L.Serafini, S.Gustafsson, C.Pagani, Proc. 11th Int. Conf. on Cyclotrons and Their Appl., Tokyo, October 1986, Ionics Pub., Tokyo, 370 (1987).

(43) T.Tajima, T.Furuya, T.Suzuki and Y.Iino, "Pre-tuning of TRISTAN Superconducting RF Cavities", Proc. 4th Workshop on RF Soperconduc., KEK, Japan, August 1989.

(44) B.Dwersteg et al. "Superconducting Cavities for HERA", Proc. 3st Workshop on RF Soperconductivity, ANL, Argonne, Illinois, September 1987.

(45) Ph.Bernard et al., "Superconducting RF Cavities for LEP", Proc. 1st European Particle Acc. Conf., Rome, Italy, June 1988.

(46) D.Boussard et al., CERN/EF/RF 88-3, 12 October 1988.

(47) Ph.Bernard et al.,Test of a 352 MHz Superconducting Cavity in the CERN SPS, Proc. European Particle Accelerator Conference, Rome, June 1988, p. 988. World Scientific, Singapore.

(48) "The Vacuum Bellows and the Optimization of their Shielding", LEP Note 568, Sept.1986.

(49) A.G. Mathewson, "The effect of cleaning and other treatments on the vacuum properties of technological materials used in ultra-high vacuum." Proc. 10th Italian Nat. Conf.on Vacuum Science and Technology, Stresa, Italy, Oct. 1987, Il Vuoto.

(50) B. Spataro, LNF Internal Memo LIS-30 (1988)
M. Bassetti, B. Spataro, LNF Internal Memo LIS-42 (1989)
M. Castellano, LNF Internal Memo LIS-53 (1989)
R. Boni, A. Gallo, LNF Internal Memo LIS-68 (1990)

(51) J. Rees, L. Rivkin, SLAC-PUB-3305 (1984)
K.T. Mc Donald, D.P. Russel, Lecture Notes in Physics-343, M. Month and S. Turner eds., pp. 162-132. Springer-Verlag 1989.

(52) S. Bartalucci, C. Biscari, L. Palumbo, LNF Internal Memo ARES-20 (1989)

(53) R. E. Shafer, IEEE Transactions on Nuclear Science, Vol NS-32, No 5, p. 1933 (1985).

(54) E. F. Higgings, J. E. Griffin, IEEE Transactions on Nuclear Science, Vol NS-22, No 3, p. 1574 (1975). J. Borer, R. Jung, CERN 84-15, p. 416 (1984).

(55) Int. Conf. on Accelerator and Large Experimental Physics Control Systems, Vancouver, October 1989.

(56) P.G.Innocenti, "The LEP Control System: Architecture, feature and performance", CERN-SPS/89-35 (ACC) (1989).

(57) M.Mignacco, Int. Conf on Accelerator and Large Experimental Physics Control Systems, Vancouver, October 1989.

(58) M.Castellano et al., IEEE Trans, on Nucl. Sci. <u>36</u>, 1619 (89).

(59) N.Cavallo, LNF Internal Memo ARES-29 (1989)

# APPENDIX

# X-VUV POSSIBLE FEL EXPERIMENTS

L.Serafini, M.Ferrario, C.Pagani, A.Ghigo*, P.Michelato, A.Peretti

INFN and Università di Milano - Via Celoria 16 - 20133 Milano
*INFN Laboratori Nazionali di Frascati - P.O. BOX 13 - 00044 Frascati

## 1 - Introduction

The availability of intense electron beams of high quality makes the ARES SC LINAC complex a unique facility to perform several experiments in the X-ray VUV FEL mainstream. In this chapter we present a feasibility study of a device able to generate coherent radiation of high brightness in the soft X-ray VUV spectral region (photon energies in the 10-120 eV range), together with a tentative list of the possible FEL experiments.

Detailed, but still preliminary, numerical simulations will be extensively reported: they anticipate the FEL performances and support the enclosed lists of parameters concerning the beam quality requirements and the wiggler characteristics. These simulations have been carried out taking into account a new recently proposed technique: the "ion focussing" of the beam, achieved with a pre-ionized plasma channel added inside the beam pipe in the wiggler(5).

Some new applications of old ideas are also presented here for the first time, in the last two sections: they deal with the subject of coherent spontaneous emission. Inside our range of radiation wavelengths such new schemes will open the possibility to obtain coherent radiation wavelength of ≈ 50 Å, in the so called "water window". The new experimental physics field which may be explored with such a radiation source is, in our opinion, as wide as needed to justify the big effort to build such a device.

Indeed, it is well known that the shorter is the radiation wavelength, the higher must be the beam quality needed to operate a single pass high-gain FEL in the SASE (Self Amplified from Spontaneous Emission) mode. As shown elsewhere(1), the choice of a low frequency and a superconducting structure for the beam acceleration plays a crucial role in minimizing the beam quality degradation through the LINAC. In this respect, the injection system turns out to be one of the most important part of the whole complex.

It is worthwhile to mention that the SC LINAC will also constitute an experimental tool to study the beam-beam and the beam-radiation field interactions: such effects are of great relevance in the design of all future $e^+ e^-$ TeV colliders. A better understanding of the beamstrahlung processes will surely allow to improve the feasibility and the performances of such machines.

## 2 - One Dimensional Model Predictions.

As elsewhere presented in more detail(1), the expected beam characteristics at the LINAC output, for FEL experiments, can be summarized as shown in Table 1. Having available beams with a relativistic factor, $\gamma$, in the range 600÷1200, one can easily observe that the resonant radiation wavelength, given by the usual FEL resonance relationship, lies in the range 200-20 nm (for the first harmonic) when wigglers with typical periods of a few centimetres are considered. In fact the FEL resonance equation is:

$$\lambda_r = \frac{\lambda_w (1 + a_w^2)}{2\gamma^2 n}$$

where: $\lambda_w$ is the wiggler period, $\lambda_r$ the n-th harmonic radiation wavelength and $a_w$ is the dimensionless vector potential of the wiggler. In a planar wiggler $a_w$ is related to the peak magnetic field, $B_w$, by the formula: $a_w \approx .66\, \lambda_w\,[\mathrm{cm}]\, B_w\,[\mathrm{T}]$.

### Table 1 - Expected Beam Characteristics

| | | | |
|---|---|---|---|
| Beam energy | [MeV] | 300 ÷ 580 (820*) | |
| Peak current | [A] | 400 | 1000 |
| Norm. transv. emitt. | [m rad] | $4 \div 8 \cdot 10^{-6}$ | $4 \div 5 \cdot 10^{-5}$ |
| Relative energy spread | | $.5 \div 1 \cdot 10^{-3}$ | $2 \div 5 \cdot 10^{-3}$ |

* Eventually obtainable with a second recirculation.

Unfortunately, the scaling law for the exponential growth of the radiation field is quite unfavourable in the very short wavelength domain. The gain length, $L_g$, i.e. the length over which the radiation field intensity grows by a factor e, scales indeed like the beam energy divided by the cubic root of the wiggler period, as in the following formula, which holds in the cold-beam limit and before saturation(2):

$$L_g \approx \frac{\gamma}{\sqrt[3]{J\,\lambda_w B_w^2}}$$

where J is the beam current density.

To reach the VUV to soft X-ray domain (radiation wavelength between 10 and 100 nm) high $\gamma$ and short wiggler periods are both needed, $B_w$ being dependent on $\lambda_w$ as will be shown later. That implies that fine and intense beams must be used in order to overcome by the increase in current density the corresponding increase of the gain length.

It is well known that in an untapered wiggler, because of the exponential growth of the radiation field, once the high gain regime is achieved, intensity reaches saturation after a typical length of the order of $4\pi L_g$: at that point the radiation power, $P_r$, is roughly given by the beam power, $P_b$, times the Pearce parameter, $\rho$, ($\rho = \lambda_w/4\pi L_g$), that is $P_r = \rho\ P_b$(2). Then, the saturated radiation power comes out invariant with respect to the beam energy.

A more important scaling law sets a threshold for the radiated power, which must be high enough to ensure that the quantum fluctuations in the photon beam do not destroy the coherence properties of the radiated field: the condition is given by

$$P_r\,[\mathrm{MW}] > \frac{5.9\ 10^{-6}}{\lambda_r^2\, q_f^2}$$

where $q_f$ is the maximum quantum fluctuation compatible with the radiated field coherence; $q_f$ should actually be of the same order of magnitude as the ratio between the incoherent radiated power and the coherent one, so as to ensure that the incoherent quantum noise does not significantly perturb the coherence of the radiated field. The previous relationship comes from the scaling of the quantum fluctuation with the inverse square root of the number of photons per wavelength(3).

The requirement of a radiated power scaling like the square of the frequency (i.e. the square of the photon energy) actually sets one of the major limits in going towards the X-ray domain.

The transverse size, $r_b$, of the electron beam in a wiggler with appropriate shaping of the pole face is given by(4):

$$r_b = \sqrt{\frac{\varepsilon_n \lambda_\beta}{2\pi\gamma}} \qquad \text{being:} \qquad \lambda_\beta = \frac{\sqrt{2}\,\gamma\lambda_w}{a_w} H \tag{1}$$

Where $\varepsilon_n$ is the transverse normalized emittance of the beam and the parameter H represents the effect of the ion focussing in decreasing the betatron wavelength $\lambda_\beta$. In absence of ion focussing $H = 1$; the ion focussing effect makes $H < 1$ (5).

The relevance of producing low emittance beams and to increase the focussing strength of the wiggler optics is then straightforward. The ion focussing scheme consists essentially in producing, inside the beam pipe along the wiggler, a tenuous ion channel: this is generated by injecting an intense leading low energy (≈ 300 MeV) electron beam into a low pressure helium column. The beam ionizes the helium gas and the space charge field of the beam ejects the detached plasma electrons from the beam vicinity. The charge of the second injected electron beam is partially, or totally (depending on the helium pressure) compensated in passing through the ion channel. The pinch field acting on the beam increases the focussing strength, decreases the beam transverse size and produces a substantial gain length contraction. Finally, it is worthwhile noting that the gain length scales with the cubic root of H.

Two major constraints on the quality of the electron beam injected into the wiggler must be taken into account when the cold beam limit approximation is abandoned. The transverse and the longitudinal phase spaces of the electron and of the photon beams must be matched if the interaction between the two beams has to be ensured all along the wiggler, in order to set up the energy exchange which is the basic condition to achieve an exponential gain in the radiated field power. For the transverse phase space one must match the emittance of the electron beam with the emittance of a diffraction limited radiation beam; this means that(6):

$$\varepsilon_n = \frac{\lambda_r \gamma}{2\pi} f_1 \tag{2}$$

where $f_1$ must be kept below 1 (as discussed later).

Since the line-width of the radiated field at saturation is of the order of $\rho$, the energy spread of the injected beam must be less than this quantity: in practice it has been found from simulations(7) that the proper condition is given by:

$$\frac{\Delta\gamma}{\gamma} < \frac{\rho}{4}$$

A last condition comes from the requirement that diffraction does not remove radiation from the edge of the electron beam over a length shorter than the gain length; this requires the Rayleigh length, $Z_r$, to be larger than the gain length, $L_g$(8):

$$L_g = Z_r f_3 \quad \text{being} \quad f_3 \leq 1 \qquad \text{and} \qquad Z_r = \frac{\pi r_b^2}{\lambda_r}$$

In some sense this condition sets a limit to the extent to which the ion focussing can be pushed: a reduction of the beam radius causes a decrease of the gain length, scaling like the square of the cubic root of the radius, but unfortunately also the Rayleigh length decreases scaling like the square of the radius. The best compromise on the effectiveness of the ion focussing technique is reached when $f_3 \approx 1$, that is when the diffracted power is not higher then the power increase due to the exponential gain. A further ion focussing increase, making $f_3 > 1$, no longer improves the FEL performance, as will be shown later.

Taking into account what could be a typical step-by-step upgrading of the SC LINAC facility, especially in terms of beam current and output emittance, we listed in Table 2 the corresponding envisageable FEL experiments: the table has been divided into four sections, to list the quantities related to the beam requirements, to the wiggler characteristics, to the FEL radiated power and to the above mentioned parameter $f_i$, that control the validity of the one-dimensional evaluation. The quantity $f_2 \equiv f_1^2 \cdot f_3$ must be less than 1(5). The two parameters S and K measure the slippage effect and the superradiance behaviour of the FEL, as defined in ref.(9).

Moving from left to right on Table 2 the difficulty of the FEL experiment grows, both because of the tighter beam quality requirements and of the difficulties in manufacturing the required wiggler.

A few comments on the beam parameters are in order:

- the first anticipated beam will be produced by the LINAC without any recirculation, with a peak current of 200 A and a transverse normalized emittance (rms value of $1 \cdot 10^{-5}$) fully consistent with the preliminary design of the injection system(1).

- the energy spread shown in the Table takes into accounts the effect of the longitudinal wake-field excited inside the RF cavities: here it must be remarked that such low values for the energy spread are made possible only by the low RF frequency selected for the LINAC.

## Table 2 - Possible FEL Experiments

| | | | | | | |
|---|---|---|---|---|---|---|
| Beam energy, T | [MeV] | 292 | 500 | 580 | 580 | B |
| Peak current, $I_{peak}$ | [A] | 200 | 400 | 400 | 400 | E |
| Bunch length, $\sigma_b$ | [mm] | .3 | .3 | .2 | .2 | A |
| Norm emittance, $\varepsilon_n$ | [m rad] | $1\cdot10^{-5}$ | $8\cdot10^{-6}$ | $1.5\cdot10^{-6}$ | $4\cdot10^{-6}$ | M |
| Energy spread, rms | [keV] | ±100 | ±150 | ±200 | ±200 | |
| Wiggler period, $\lambda_w$ | [cm] | 3 | 3 | 2 | 2 | W |
| Peak mag. field, $B_w$ | [T] | .75 | .75 | 1. | 1. | I |
| Wiggler parameter, $a_w$ | | 1.49 | 1.49 | 1.32 | 1.32 | G |
| Wiggler pole gap | [cm] | .9 | .9 | .45 | .45 | G |
| Max. field for SmCo | [T] | .8 | .8 | 1.1 | 1.1 | L |
| Ion focussing param, H | | 1 | 1 | 1 | .38 | E |
| Beam radius, $R_b$ | [μm] | 210 | 190 | 67 | 67 | R |
| Rad. Wavelength, $\lambda_r$ | [nm] | 133 | 50 | 21 | 21 | |
| Pierce parameter, $\rho$ | | $2.1\cdot10^{-3}$ | $1.7\cdot10^{-3}$ | $2.0\cdot10^{-3}$ | $2.0\cdot10^{-3}$ | F |
| Photon energy | [eV] | 9 | 25 | 58 | 58 | E |
| Saturation power, $P_{sat}$ | [MW] | 190 | 380(40*) | 550(320*) | 550 | L |
| Gain length, $L_g$ | [m] | .66 | .81(1.36*) | .46(.62*) | 8.2 | |
| Intensity at saturation | [W/cm$^2$] | $4.2\cdot10^{10}$ | $1.0\cdot10^{11}$ | $1.2\cdot10^{12}$ | $1.2\cdot10^{12}$ | |
| $(\Delta\gamma/\gamma)/(\rho/4)$ | | 1.06 | 1.4 | 1.15 | 1.15 | |
| Quantum fluctuation param., $q_f$ | | $4\cdot10^{-6}$ | $8\cdot10^{-6}$ | $1.6\cdot10^{-5}$ | $1.6\cdot10^{-5}$ | C |
| $f_1 \equiv 2\pi\varepsilon_n/(\lambda_r\gamma)$ | | .79 | 1.02 | .34 | 1.04 | H |
| $f_2 \equiv f_1^2 f_3$ | | .59 | .65 | .11 | .97 | E |
| $f_3 \equiv L_g/Z_r$ | | .95 | .62 | .99 | .9 | C |
| S | | .15 | .056 | .053 | .053 | K |
| K | | .007 | .003 | .002 | .002 | |

* FRED-3D calculations.

Therefore the first FEL experiment will be just a standard single pass FEL amplifier at a resonance radiation wavelength of ≈ 133 nm, where an input signal is available by a Nd-YLF laser multiplied in frequency at the eighth harmonic by a passage through a triple BBO crystal(10). A few MW of peak power can be delivered in 50 ps pulses at a repetition rate of 1 kHz. The wiggler parameters are consistent with the Halbach scaling law for hybrid magnet wigglers(11): with a gap of 9 mm the maximum allowed peak field is .8 T, versus the selected .75 T.

Integrating numerically the standard Compton-FEL equations for the one-dimensional model, we observe a saturated power of 190 MW after 8 meters of wiggler, when a 1 MW of input power has been injected into the wiggler: the value of $\rho$ is in this case $\approx 2 \cdot 10^{-3}$. As shown in Table 2, the test quantities are all under control, especially the $f_1$ parameter, while the slippage and the superradiance parameters, being very small, indicate that the steady state regime is adequate to describe the exponential growth of the FEL radiation field.

The other three columns of Table 2 show the parameters required to operate a FEL amplifier starting from spontaneous emission, at radiation wavelengths of 50 and 21 nm, respectively. The beam must be recirculated once in the second stage of the LINAC to raise the energy to roughly .5 GeV ; the peak current increases up to 400 A, as anticipated(1). The input signal is in this case the incoherent spontaneous synchrotron emission, $P_{inc}$, which reaches a few tens of kW per meter of wiggler, as estimated by the formula(12)

$$P_{inc}\,[\mathrm{kW/m}] = 1.9\,\frac{a_w^2\,(1 + a_w^2)\,I\,[\mathrm{A}]}{\lambda_w\,[\mathrm{cm}]\ \lambda_r\,[\mathrm{nm}]}$$

The fourth column deals with a particular application of the ion focussing technique: since the required emittance, as shown in the third column, is too small, a slight amount of ion focussing (H = .38) allows to increase the maximum emittance by a factor of three, keeping $\rho$ constant. Further comments on this case will be given in the next section, where the 3-D simulation results are presented.

## 3 - Numerical Simulations of the High Gain FEL

The computer code FRED-3D has been used(20) to simulate the behaviour of the coupling between the electron beam and the radiation field induced by the wiggler field, for a 3-D beams (i.e. taking into account the transverse phase space evolution for both the particles and the field). Slippage effects are in this frequency-domain and, for millimetre long electron bunches, quite negligible; the steady state approximation used by FRED-3D is then completely adequate.

The input electron beam is actually mono-energetic, but it is well known that for energy spreads below the value given by the Pellegrini's rule(6) no serious deterioration of the FEL performance is to be expected. The field power growth is shown on a logarithmic scale, in Fig. 1, for the case of the parameters presented in column 2 of Table 1, i.e. for a radiation wavelength of 50 nm.

After three meters of lethargy, the signal grows exponentially up to 30 MW; the latter value is reached at the end of a 20 m long wiggler. Since the gain is about 3.2 dB/m, as shown in Fig. 2, a further 3.5 meters of wiggler length would be needed to reach the 1-D estimated saturation power at 380 MW.

The observed gain length, $L_g$, is therefore 1.36 m, which must be compared to the value of .81 m, predicted by the 1-D model. The discrepancy can be understood taking into account that the Rayleigh length, $Z_r$, for this case is slightly above the gain length. Since the 1-D model is valid in the limit $Z_r >> L_g$ (i.e. $f_3 << 1$), the gain decrease due to diffraction effects cannot be accounted for by the 1-D model. The same holds for the transverse phase space effects: since the emittance is just above threshold, ($f_1 = 1.02$), one must expect the 1-D calculation to predict a higher gain than the 3-D one.

We want to point out that a coherent input signal of 100 W has been used to start the FEL, even though no coherent signal is available at this wavelength (50 nm). In particular, since FRED-3D is not able to simulate the start up from the Schottky noise or from the incoherent spontaneous emission, 100 W has to be taken just as a reference value, to be compared to the incoherent synchrotron radiation power, which is in this case 36 kW/m. Harmonic switching (see below) or other exotic ideas like the SHOK scheme(13) could overcome the input signal problem.

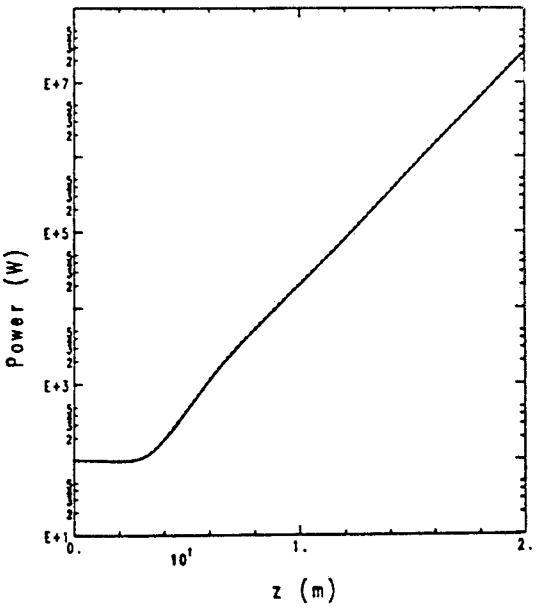

**Fig. 1** - Field power growth, on a log scale, with the parameters presented in column 2 of Table 1.

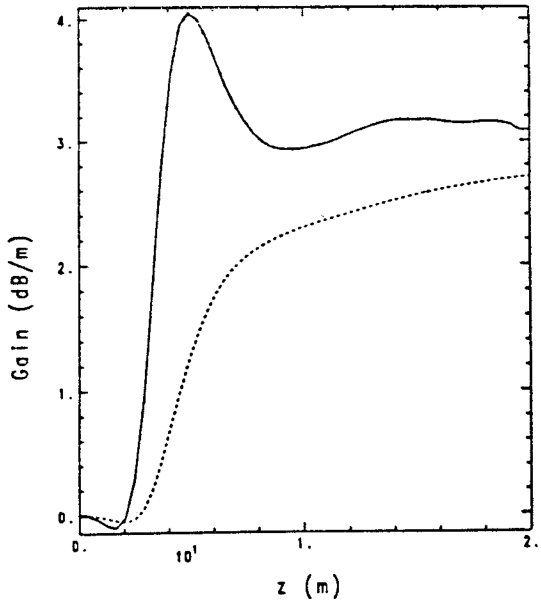

**Fig. 2** - Incremental (solid line) and average (dashed line) gain along the wiggler for the case of Fig. 1.

The full exploitation of the ion focussing technique has been carefully studied for the case of the 21 nm radiation wavelength, with a 580 MeV beam at 400 A (third column of Table 2). The field power computed by FRED-3D along the wiggler is shown in Fig. 3 and 4 on logarithmic and linear scales, respectively. The input signal is still a 100 W coherent field. The incoherent synchrotron radiation power is in this case 85 kW per meter of wiggler, or, equivalently, 1.7 kW per wiggler period.

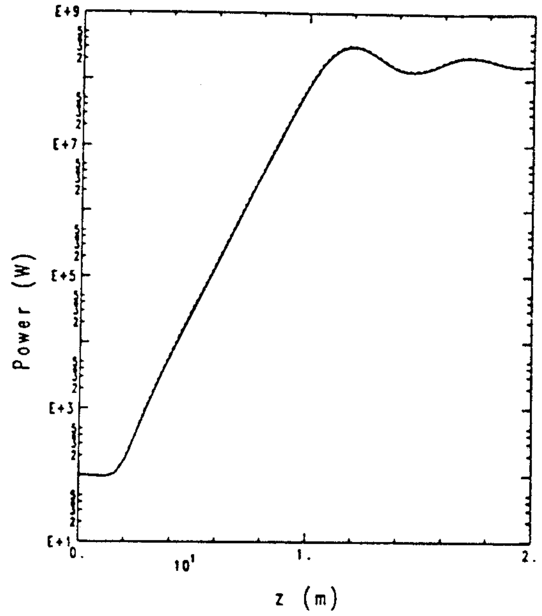

**Fig. 3** - Field power growth, on a log scale, with the parameters presented in column 3 of Table 2.

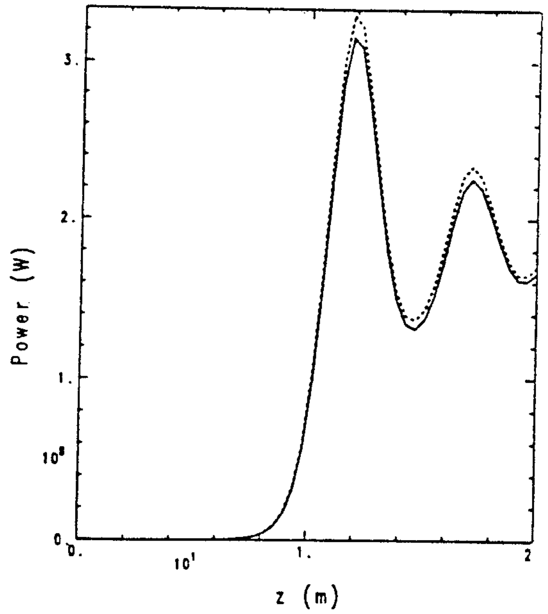

**Fig. 4** - Same as Fig. 3, but on a linear scale. The power is in units of $10^8$ W.

After 2 meters of lethargy the exponential gain sets in and the radiation field reaches the 320 MW saturation power level at z = 12 m: the corresponding intensity is $1.2 \cdot 10^{12}$ W/cm$^2$, confined in a narrow cone of about .1 mm rms radius and $1.1 \cdot 10^{-5}$ rad rms angular width. In Figs. 5 and 6 the intensity profiles are plotted as functions of the transverse coordinate x of the wiggler, at the entrance (z = 0) and at the exit of the wiggler (z = 20 m) respectively.

The input field is a gaussian laser beam focussed at z = 0. At the wiggler exit the intensity profile, due to diffraction effect, shows that some radiation escapes from the electron beam: the gaussian fit (dashed curve in Fig. 6) reveals that the optical guiding and the diffraction along the wiggler produce a distortion of the intensity profile, which is no longer gaussian. It should be noted that the peak value of Fig. 6 ($5 \cdot 10^{11}$) is lower than the peak value ($1.2 \cdot 10^{12}$) at saturation (z = 12 m).

Moreover, the phase profile of the radiation field at z = 20 m, shown in Fig. 7, indicates that the radiation beam is de-focussed, since the phase increases off-axis.

The "natural" betatron wavelength, $\lambda_\beta$, for this case is 24.5 m, which gives an rms beam radius in the wiggler of about 53 microns with a normalized rms emittance of 1.5 mm mrad. The incremental gain is shown (solid line) in Fig. 8: with an average value of 7 dB/m during the exponential growth, the gain length is approximately .62 m, slightly above the 1-D predicted one.

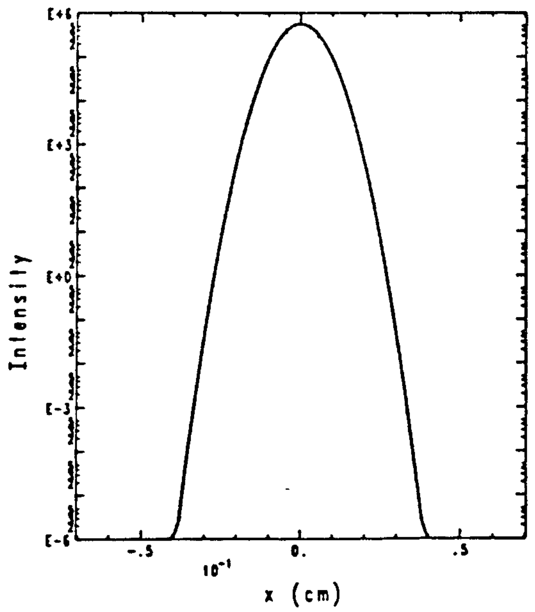

**Fig. 5** - Intensity profile as a function of the transverse coordinate x of the wiggler at the start-up (z = 0 m), for the case of the parameters presented in column 3 of Table 2.

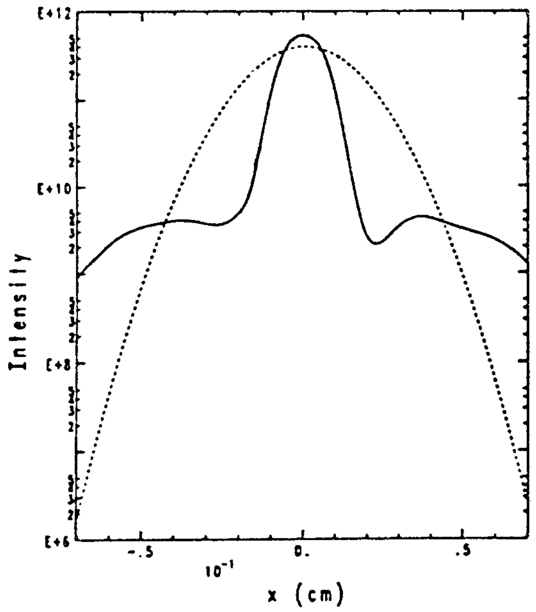

**Fig. 6** - As Fig. 5 at the end of the wiggler (z = 20 m). Actual intensity (solid line) and gaussian fit (dashed line).

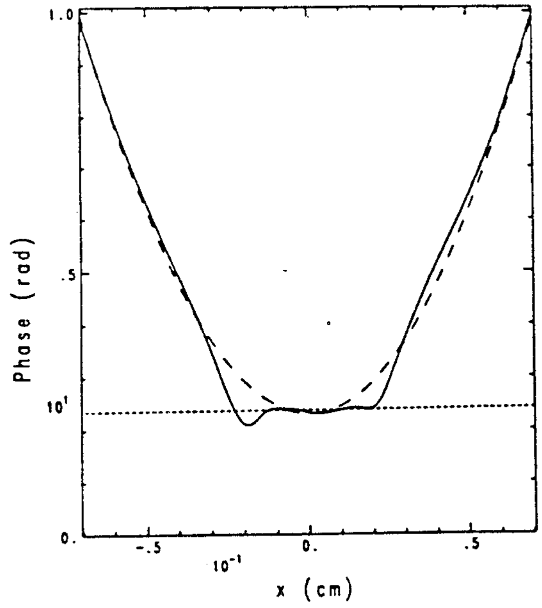

**Fig. 7** - Radiation field phase profile (solid line) and its gaussian fit (dashed line) at z = 20 m.

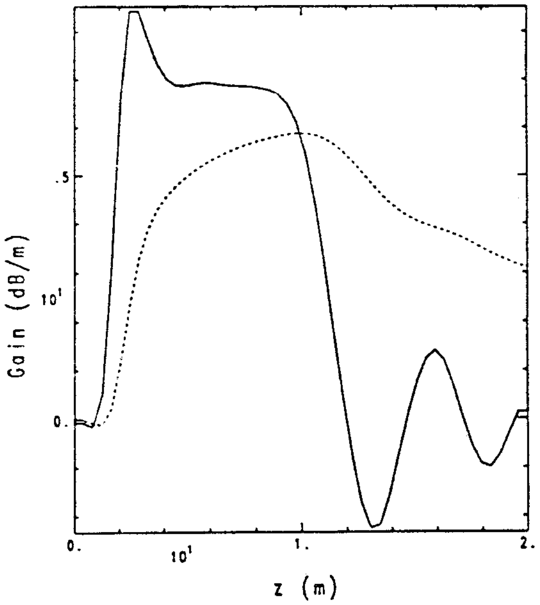

**Fig. 8** - Incremental gain (solid line) and average gain (dashed line).

The total gain is about 65 dB after 12 metres of wiggler. Since the Rayleigh length is .41 m, the diffraction effects are probably responsible for such a decrease in the gain.

Introducing some amount of ion focussing one can decrease the betatron wavelength and squeeze the electron beam. In Fig. 9 is presented the radiated field power produced by reducing by a factor ten the betatron wavelength, i.e. by setting H = 0.1. The saturation is reached at z = 8 m, with a wiggler much shorter than the previous one (H = 1, no ion focussing), but the saturation level is slightly lower: 250 MW versus 320 MW of the no-ion focussing case.

The peak field intensity at saturation, $I_{sat}$, is about $4.4 \cdot 10^{12}$ W/cm$^2$, with a spot radius of .6 mm and an rms angular divergence of $1 \cdot 10^{-5}$ rad. The incremental gain has now a plateau at 10 dB/m, with a total gain of 64 dB along the 8 meter wiggler.

The intensity profile is plotted in Fig. 10, at the wiggler exit. The exit profile exhibits very clearly the substantial fraction of field escaped from the electron beam, which has a maximum radius of about 50 microns.

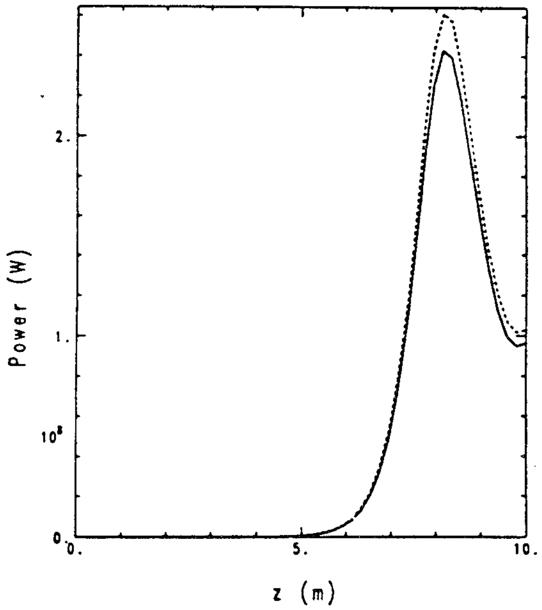

**Fig. 9** - Radiated field power produced by reducing the betatron wavelength by a factor ten, i.e. setting H = 0.1.

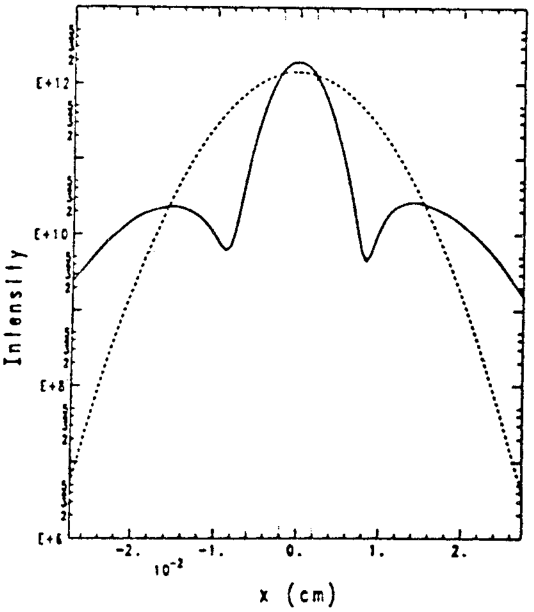

**Fig. 10** - Intensity profile at the wiggler exit. The exit profile exhibits very clearly the substantial fraction of field escaped from the electron beam.

The optical guiding applied by the electron beam on the laser field is however better evidenced by the phase profile of the laser field, plotted in Fig. 11 at the wiggler exit: inside the electron beam, i.e. for x < 60 microns, the field phase decreases with the transverse coordinate, then the optical beam is converging. Outside the electron beam the field phase is instead strongly increasing, showing that the optical beam is defocussed in that region. The electron beam acts on the laser field as an optical fiber with a high refractive index. The optical guiding, already observed elsewhere (21), is stronger during the exponential gain than after saturation. That is clearly shown in Fig. 12, where the iso-intensity curves are plotted in the (x,z) plane for the case without the ion focussing: the laser beam is squeezed and focussed whenever the field is growing, i.e. the gain is positive.

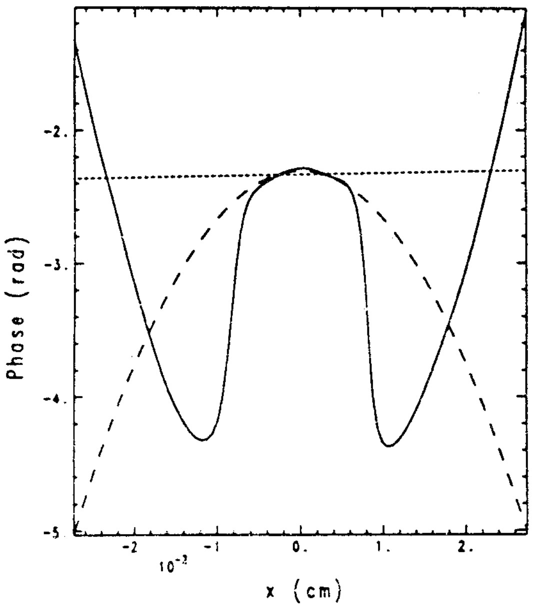

**Fig. 11** - Phase profile of the laser field at the wiggler exit (solid line) and its gaussian fit (dashed line).

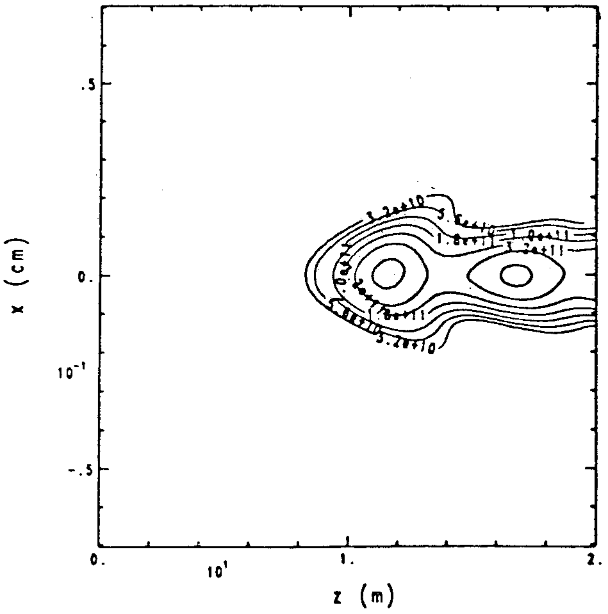

**Fig. 12** -Iso-intensity curves, plotted in the (x,z) plane for the case without ion focussing.

The effect of ion focussing in decreasing the gain length has been explored performing FEL simulations with FRED-3D also at H = .75 and at H = .2. The results are summarized in Fig. 13, where the gain length observed in the FRED-3D calculations is plotted (dashed line) versus the betatron wavelength (H = 1 corresponds to $\lambda_\beta$ = 24.5 m). The solid line in the same figure represents the gain length scaling as $H^{1/3}$, as predicted by the 1-D model: the gain length observed in the 3-D calculations then indicates that the FEL performance is enhanced by the ion focussing technique, but not as much as one would expect from the 1-D model considerations. That can be explained observing the dashed line plotted in Fig. 13, showing the $f_3$ coefficient, which gives the ratio between the gain length and the Rayleigh length: this ratio grows quickly above 1, indicating that diffraction effects become more and more relevant for the FEL performance.

It can be therefore concluded that the maximum benefit from the ion focussing technique can be obtained not by increasing the FEL performance, keeping constant the beam parameters, but relaxing the beam quality requirements keeping unaltered the gain length. It can be easily seen from equation (1) that the emittance can be scaled like the inverse of the amount H of ion focussing applied, keeping constant the beam radius, hence the gain length. One can therefore reduce the tight requirement on the beam emittance shown in the third column of Table 2 and list a new set of parameters in the fourth column, by simply scaling the emittance by a factor 2.7 and taking H = .38. In this way the gain length should stay constant since the Rayleigh length is not changed (the beam radius is not varied) and the FEL performances are unaltered but achieved with a beam which is now consistent with the ones of Table 1. The $f_l$ parameter is still within the safety range $f_l \approx 1$, the quantum fluctuations parameter being very low, $q_f = 1 \cdot 10^{-5}$.

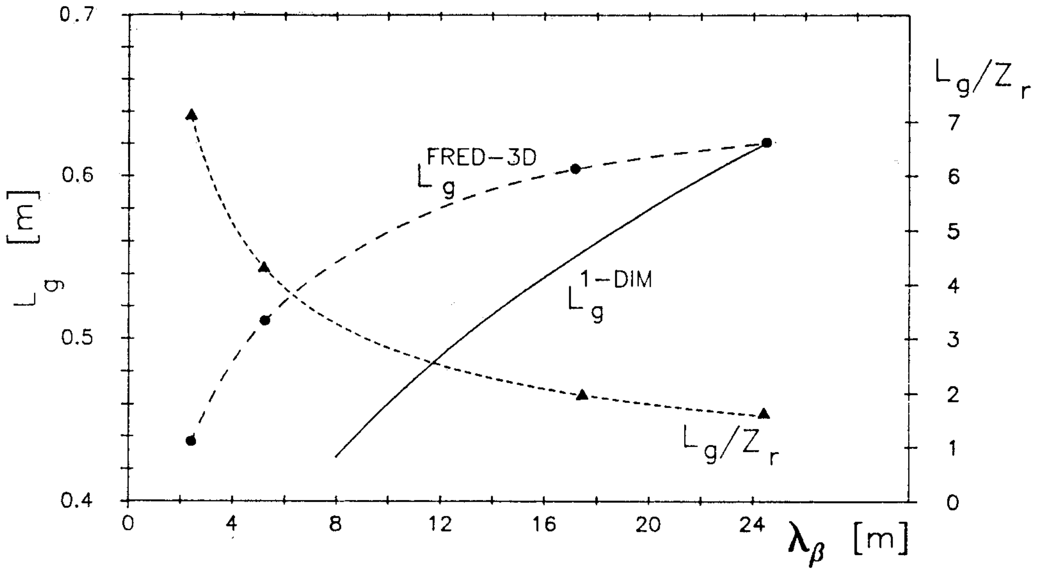

Fig. 13 - Effect of the ion focussing in decreasing the gain length (see text for details).

At 250 MW of peak power the number of photons per bunch is $3 \cdot 10^{13}$. With a bunch length of 1.2 ps the number of wavelengths contained in the laser pulse will be of the order of $2 \cdot 10^4$ with about $1 \cdot 10^5$ electrons per wavelength.

Since the maximum electron beam wiggle amplitude is in the range of 5 microns, very small with respect to the beam size, no serious problems are envisaged for the production of a uniform ion channel over the ±100 microns of the beam transverse size.

## 4 - High Gain Optical Klystron and the Coherent VUV

The Self Amplified Spontaneous Emission (SASE) regime of an FEL allows to produce coherent VUV and soft-X-ray radiation starting from the incoherent spontaneous emission in the wiggler. In such a regime, the incoherent radiation, having an optical power proportional to the number of the electrons, is amplified by the electron beam in a single pass through the wiggler. The stimulated radiation grows exponentially to a saturation level which is proportional to $N^{4/3}$, N being the number of electrons in the bunch.

Beside the problems arising from the wiggler length needed to achieve saturation starting from the incoherent spontaneous emission (they will be discussed in the next section), one of the major points is that the coherence of the output signal is lower than that obtainable from an FEL amplifier with a coherent input signal.

The coherence length of the output signal produced in the SASE regime is indeed given roughly by the slippage length: since the electrons interact with one another via the common radiation field, the interaction length is equal to the slippage length, hence the photons separated by more than the slippage length are of course decoupled. Therefore, the start up of the field amplification process from photon and electron populations which are both randomly distributed in phase cannot assure a narrow bandwidth and a coherent output signal.

Since the availability of coherent input signals (i.e. of a photon population peaked around a given phase) in the UV region decreases strongly with the wavelength, one could try to start with a "coherent" beam instead of a coherent input signal, i.e. with a bunched beam. The start up from a pre-bunched beam ensures a higher coherence of the radiation since the spontaneous emitted photon population is no longer randomly distributed in phase, but is peaked in phase around the electron beam bunching phase(14).

In Figs. 14 a and b the longitudinal phase-space for the electron beam of the FRED-3D simulation previously discussed is shown at two different positions along the wiggler:

- at z = 4 m, where the field power is still a few orders of magnitude lower than the saturation level, the beam has achieved an energy spread from the input signal but is still distributed fairly uniformly in phase. Since the wiggler field is dispersive, the energy spread will be transformed, along the wiggler, into a phase spread
- at z = 8 m, near saturation, the phase space appears like in Fig. 14 b, where the beam has achieved a substantial bunching, being well known that the bunching in the exponential regime grows exponentially too (the bunching parameter b is defined, as usual, $b=<e^{i\theta}>$, where the average <> is performed over the $\theta$ electron phase distribution).

Integrating numerically the 1-D FEL equations(9) in the Compton limit ($\rho$<<1) one finds that, starting with a signal six orders of magnitude lower than the saturation level (in the present case 100 W), the field power saturates at 550 MW after 10.5 meters of wiggler length, and the bunching grows up to ≈.7 just before saturation, as shown in Fig. 15, according to the sets of parameters presented in Table 2, column 3.

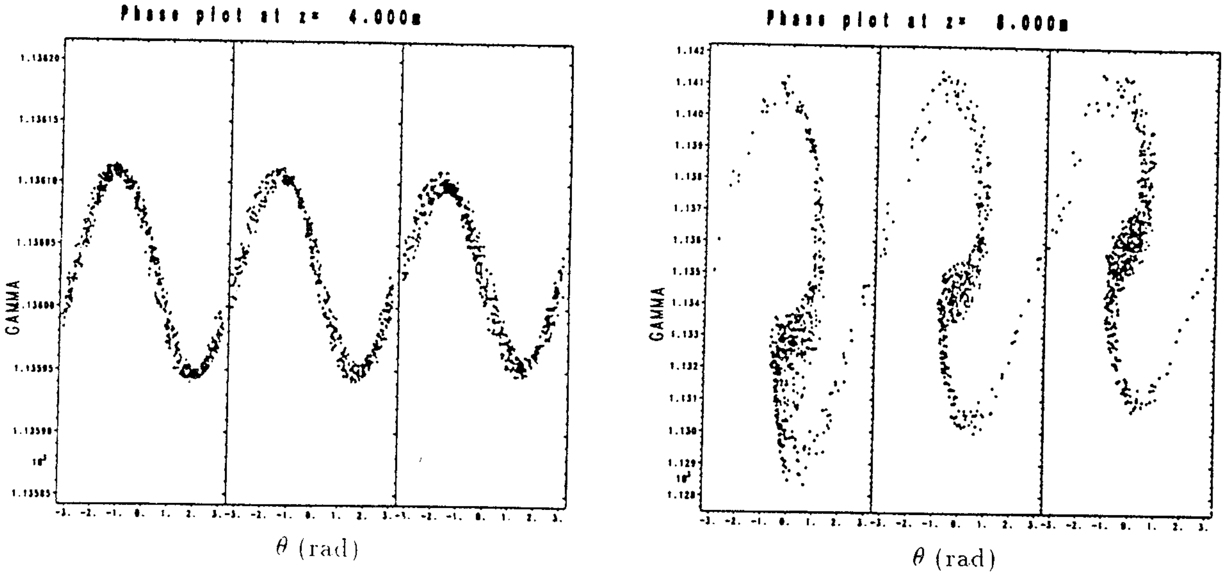

**Figs. 14 a & b** - Longitudinal phase spaces for the electron beam of the FRED-3D simulation at two different positions along the wiggler:

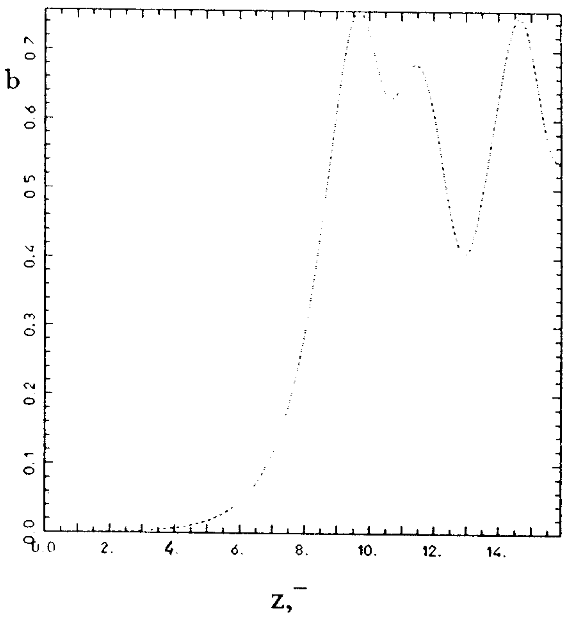

**Fig. 15** - Beam bunching along the wiggler for the sets of parameters presented in Table 2, column 3.

Starting from these considerations and following the scheme of the optical klystron(15), we propose to separate the wiggler into two parts: the first one acts as a buncher and the second one as a radiator. If the two parts are decoupled, that is the radiation generated in the buncher is discarded, the radiator works as a generator of coherent spontaneous radiation at its proper resonant wavelength. In other words, truncating the exponential gain at a suitable point close to saturation and discarding the radiated field generated so far (which is scarcely coherent), one can get a bunched beam able to radiate coherent synchrotron radiation, in a transient "superradiant" regime involving the overall beam.

The separation of the electron and the radiation beam can be achieved via a small magnetic deflection at the end of the first wiggler: such a deflection must of course ensure that the debunching effect on the beam is negligible with respect to the radiation wavelength scale. Since to the first order, the path length difference, $\Delta L$, for a beam with energy spread $\Delta\gamma/\gamma$ deflected by a magnet of angle $\theta$ (assumed small) and radius of curvature $\rho_b$ is given by:

$$\Delta L \approx \rho_b \frac{\Delta\gamma\,\theta^3}{6\gamma}$$

setting $\rho_b = 2$ m (B = .96 T at 580 MeV) and $\theta = 5$ mrad, $\Delta L$ is less than 1 nm for $\Delta\gamma/\gamma$ of the order of 1 %, as typical near the saturation. Over 1 m, which could be the separation of the two wigglers (in order to achieve a shift of a few mm between the beam and the radiation) the path length difference due to the emittance, given by:

$$\Delta L \approx \frac{L\,\Delta\theta^2}{2} \qquad \text{where } \Delta\theta \text{ is the rms beam divergence}$$

is of the order of 1 nm. Therefore the debunching effect at the entrance of the radiator can be kept small with respect to the radiation wavelength (20 nm).

Other possibilities to achieve the beam-field separation such as thin radiation absorbers or wiggler truncations (no half period at the wiggler end) must be investigated, but could in principle be exploited.

In order to evaluate the field power generated in the radiator we apply a cut to the numerical integration of the FEL-Compton equation(9), which corresponds to the first wiggler exit. At the cut (working actually as a variable threshold) we simply reduce the field intensity to zero, we keep the particle phase space unaltered (assuming zero debunching in the transport between the two wigglers) and we insert the new resonance condition (proper of the radiator) by zeroing the detuning. This is simply achieved by keeping <p> = 0, i.e. by summing the quantity <p> at the threshold to all the particles, where <p> is the normalized detuning, given by:

$$<p> = \frac{<\gamma-\gamma_r>}{\rho\gamma_r} .$$

That is equivalent to shift the resonant wavelength to the new value - proper of the radiator - which is determined by the beam energy at the end of the first wiggler.

In the present case the beam energy loss in the first wiggler, $\delta\gamma$, is always small - .04% ÷.15% of its initial energy - hence the wavelength increase, $\delta\lambda_r$, of the radiation emitted in the radiator is very small with respect to the resonant wavelength, $\lambda_r$, of the first "bunching" wiggler, according to the equation:

$$\frac{\delta\lambda_r}{\lambda_r} = -2\frac{\delta\gamma}{\gamma} \leq .3\,\%$$

The field power generated in the radiator is plotted in Fig. 16 versus the cumulative length of the system buncher wiggler - radiator, for three different threshold positions. The crosses show the standard steady state behaviour of the field power (i.e. for a buncher wiggler extending without any threshold) with a saturation level of 550 MW at z = 10.5 m: the curve is plotted just for reference. The solid line, the dashed line and the dotted one mark the field growth in the radiator when the length of the buncher wiggler is 8 m, 8.8 m and 9.6 m respectively. When the threshold is located at z = 8.8 m one gets 100 MW of field power from the first wiggler, then with two meters of radiator length (from z = 8.8 m to z = 10.8 m) the coherent spontaneous emission grows to 700 MW and then saturates again. Shifting the threshold towards larger z's causes the radiation to saturate in a shorter length (from z = 9.6 m to z = 10.9 m ) lowering at the same time the power level (260 MW).

Since the threshold variation requires a variable length of the buncher wiggler (which can cause serious technological problems), the same effect can be achieved by varying the input signal power and taking a fixed buncher wiggler length, as shown in Fig. 17. Here the buncher wiggler length is assumed to be 8 m and the radiator starts at z = 8 m. The effect on the longitudinal phase of the beam transport from the wiggler to the radiator is neglected. As in Fig. 16, the crossed line shows the standard steady state exponential growth, while the other lines show the field power in the radiator for three different input powers at the entrance of the buncher wiggler: the solid line is referred to 100 W, the dashed to 400 W and the dotted one to 1000 W.

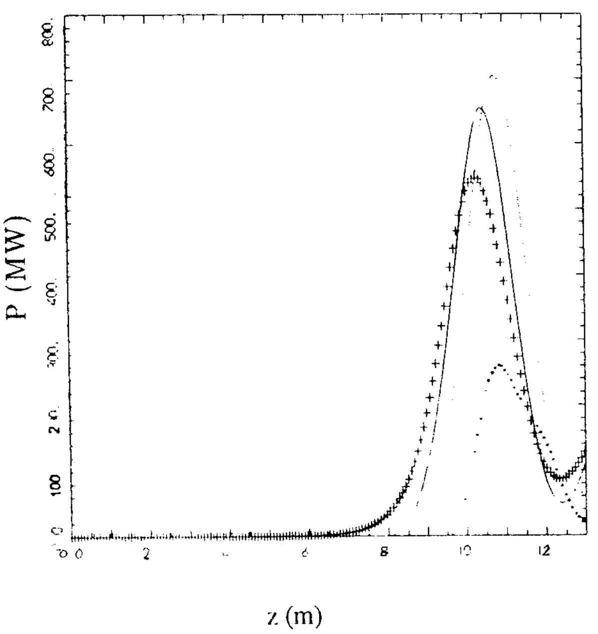

**Fig. 16** - Field power generated in the radiator versus the cumulative length of the system buncher wiggler - radiator for three different threshold positions: the crossed line shows the standard steady state behaviour, whereas the solid line, the dashed line and the dotted one mark the field growth in the radiator when the length of the buncher wiggler is 8 m, 8.8 m and 9.6 m respectively.

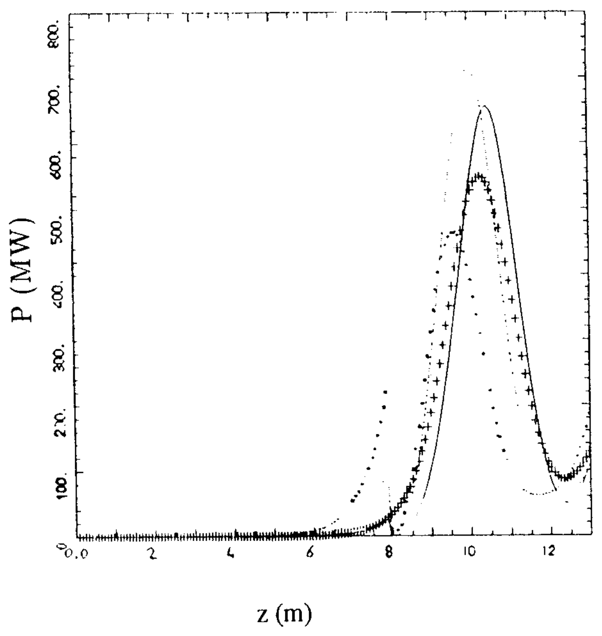

**Fig. 17** - As Fig. 16, but varying the input signal power at the buncher wiggler entrance and taking a fixed buncher wiggler length (z = 8 m). The crosses show the standard steady state exponential growth (no threshold on the buncher wiggler, 100 W of input power), while the other lines show the field power in the radiator for three different input power signals: the solid line refers to 100 W, the dashed to 400 W and the dotted one to 1000 W.

In Fig. 18 the bunching factor, b, is plotted for the same cases versus the cumulative length of the buncher wiggler-radiator system. It is clearly visible that the dashed line, corresponding to the 400 W input signal case which has the maximum field power generated in the radiator, has also the higher bunching level, fairly constant between z = 8 m and z = 10 m, where the saturation is reached in the radiator.

Moreover the solid line clearly exhibits a departure from the exponential law, also typical of the bunching in the steady state high gain regime: the field power is not growing exponentially in the radiator, as shown in Fig. 19, where the logarithm of the field power is plotted for the steady state and for the three different threshold positions.

We can interpret the emission in the radiator in the following way: the bunched beam, once injected into the radiator is initially superradiant since it does no longer interact with the radiation field that caused the bunching. The coherent radiation generated has an intensity (before saturation) scaling with $b^2 \cdot N^2$ (N is the electron number) and grows very rapidly, as shown in Fig. 20, where a peak gain of 60-70 dB/m is reached in the first part of the radiator. This value is one order of magnitude higher with respect to the 8 dB/m of the steady state exponential gain.

It is interesting to notice that the radiated field still reaches saturation. This is due again to the potential well produced by the radiation, in which the electrons are trapped: when the electron oscillation period in the potential well is fairly equal to the exponential growth rate the electron beam starts to absorb energy from the radiated field. The OK experiments at Orsay are very similar to this scheme, with the exception that they operate in the low gain domain, where saturation cannot be reached, and the bunching can be assumed constant(16).

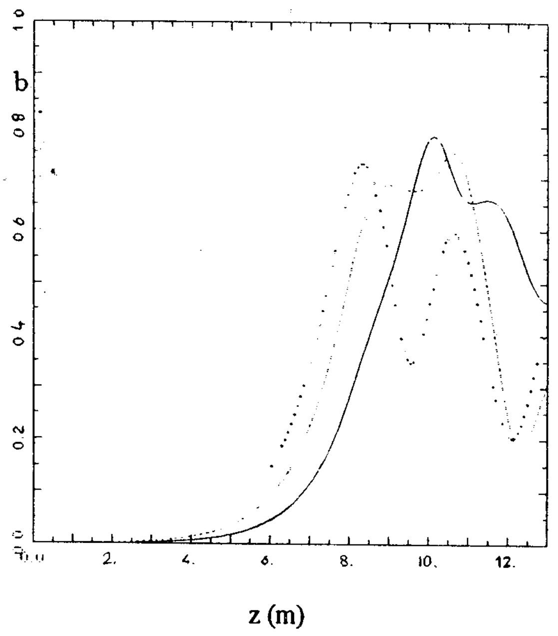

**Fig. 18** - The bunching amplitude, b, plotted for the same cases of Fig. 17 versus the cumulative length of the buncher wiggler-radiator system.

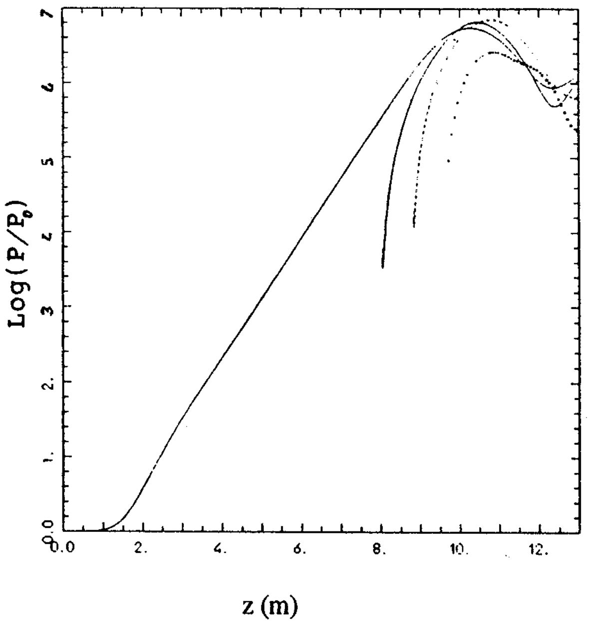

**Fig. 19** - The logarithm of the field power in the radiator plotted for the steady state and for the three different threshold positions, specified in Fig. 16.

In some sense the first part of the radiator shows a transient superradiant behaviour, involving all the electrons in the bunch: the observed superradiance is only transient since the slippage effects are, in our case, negligible, hence the field is always "sitting" on the electrons of the beam, interacting with them. The transient superradiance is therefore switched off when the field intensity grows and the bunching is no longer constant. To evaluate the coherence quality of the radiated field we can assume a constant bunching and use the formula(15):

$$\frac{dP_{coh}/d\Omega}{dP_{inc}/d\Omega} \approx |b|^2 \zeta$$

which gives the ratio between the coherent power radiated per unit solid angle and the incoherent one. $\zeta$ is the number of electrons in the coherence length $N_w \lambda_r$ of the radiation, $N_w$ being the number of the radiator periods.

Assuming in our case: $|b|^2 \approx .35$, $N_w = 100$ and $\zeta \approx 10^7$, the ratio between the coherent power and the incoherent one is in the order of $10^6$.

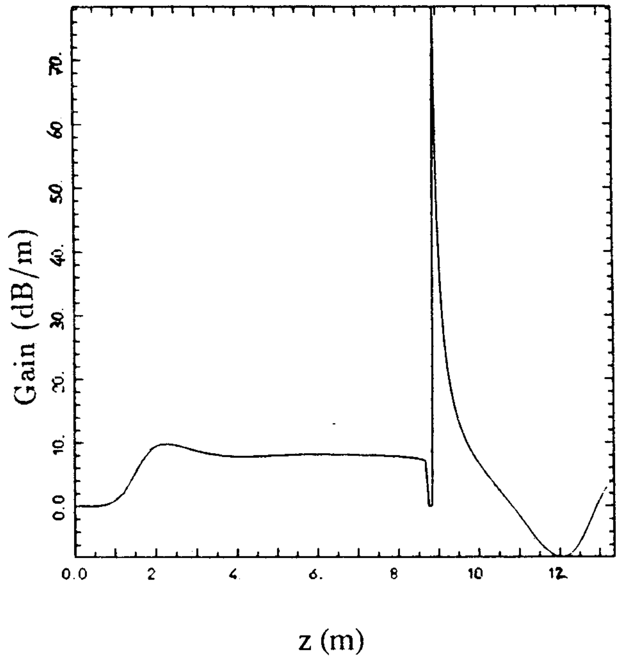

Fig. 20 - Coherent radiation growing in the wiggler-radiator system. A peak gain of 60-70 dB/m is reached in the first part of the radiator. This value is one order of magnitude higher with respect to the 8 dB/m of the steady state exponential gain.

## 5 - HASW: Harmonic Switching and Far Future Experiments

In the first wiggler, the buncher wiggler, the beam is bunched not only on the fundamental but also on higher harmonics. It is well known that in a planar wiggler only the odd harmonics are present on axis. The dimensionless field intensity $|A|^2$ and the bunching on the fundamental harmonic are plotted in Fig. 21 as a function of the dimensionless wiggler length $z,^{-} = 4\pi\rho z/\lambda_w$ for a typical case with $a_w = 1.48$, while the bunching on the higher harmonics is plotted in Fig. 22. The third and fifth harmonic bunchings are quite pronounced (.3 and .5 respectively) just before saturation: that clearly indicates the possibility to use a radiator tuned not on the fundamental but on a higher harmonic.

This idea has already been exploited by the OK experiments in Orsay(16,17,18) and has recently been proposed in the high gain domain with a varied scheme(19). Nevertheless, the novelty of our wiggler+radiator scheme is that we do not take the radiation from the first wiggler into the radiator, but we transfer only the bunched beam. The rational for this, in this range of wavelengths, is to avoid any phase slips between the beam and the radiation field generated in the passage from the buncher wiggler to the radiator wiggler. In fact, at the entrance of the radiator, a change in the relative phase can cause a shift in the beam-field coupling from an emission regime to an absorption one. It must be stressed that a difference of only 1 nm between the path lengths of the electron beam and of the radiation field produces, with a radiation wavelength of 5 nm, a significant change in the relative phase. In this case the electron beam, at the radiator entrance, is no longer in-phase with the radiation field, fact that causes a dramatic decrease of the radiation field and, eventually, of the beam bunching all along the first part of the radiator wiggler. In this respect, the relevance to cut out the beam-field interaction, avoiding to inject the radiation field into the radiator, is straightforward.

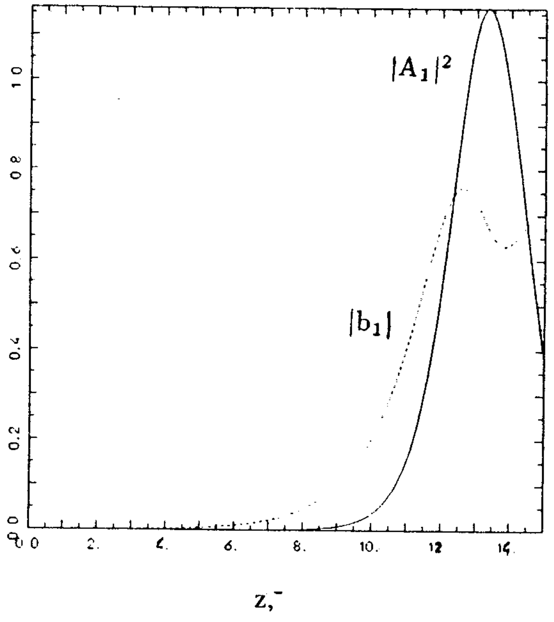

**Fig. 21** - Dimensionless field intensity and bunching on the fundamental first harmonic along a wiggler with $a_w$ = 1.48 (see text for details)

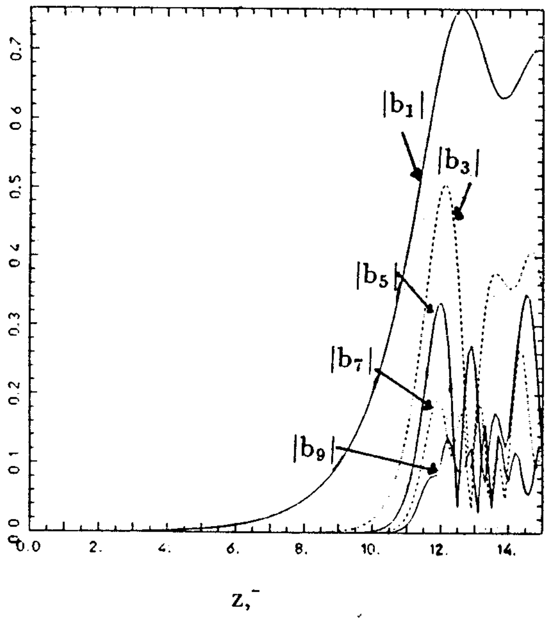

**Fig. 22** - Higher harmonic bunching parameters for the same wiggler as in Fig. 21

Since the previously illustrated possible experiments are foreseen with a radiation wavelength in the range of 20÷50 nm, it is a natural choice to consider a jump in frequency of a factor 5 in order to point directly towards ≈ 5 nm, i.e. towards the so called "water window". The experiment described in the following will therefore deal with a fifth harmonic switching, but the scheme is in principle completely general and applicable to other harmonics.

The main parameters of the foreseen experiment are listed in Table 3. Recirculating the beam twice in the L3 section of the ARES Linac, its energy can be boosted to 820 MeV: in the first wiggler the beam radiates at a fundamental wavelength of 25 nm plus the higher odd harmonics.

### Table 3 - HASW Experiment Main Parameters

| | T [MeV] | I [A] | $\varepsilon_n$ [m rad] | $\Delta\gamma/\gamma$ [keV] |
|---|---|---|---|---|
| **Beam Parameters** | 820 | 400 | $3 \cdot 10^{-6}$ | ± 250 |

| | $\lambda_w$[cm] | $\lambda_r$[nm] | $B_w$[T] | H | $R_b$[$\mu$m] | $\rho$ | $f_3$ | $f_1$ |
|---|---|---|---|---|---|---|---|---|
| **Buncher wiggler** | 4 | 25 | .56 | .5 | 92 | $2 \cdot 10^{-3}$ | .82 | |
| **5th Harm. Radiator** | 2 | 5 | .41 | .1 | 50 | $1 \cdot 10^{-3}$ | | 2.35 |

| | $P_{sat}$[MW] | $I_{sat}$[W/cm$^2$] | Photon Num. | $q_f$ |
|---|---|---|---|---|
| **Radiation parameters for $\lambda_r$ = 5 nm** | 140 | $1.8 \cdot 10^{12}$ | $6.5 \cdot 10^{12}$ | $4 \cdot 10^{-5}$ |

Adding a slight ion focussing, one can achieve $\rho = 2 \cdot 10^{-3}$ and reach, after a 14 m wiggler, a fifth harmonic bunching, $b_5$, of the order of 0.05. The added ion focussing must be kept low in order to avoid too short Rayleigh lengths: at this wavelength the beam is very fine and the diffraction effects can dominate. In our case we choose a safe value for the parameter $f_3$, i.e. $f_3$=.82.

Injecting now the beam into the radiator, whose fundamental is tuned at 5 nm (the fifth harmonic of the previous wiggler), we achieve coherent emission at 5 nm with a quasi-exponential growth of the radiation.

The dimensionless field intensity and the bunching on the fundamental in the buncher wiggler, i.e. $\lambda_r$ = 25 nm, are plotted in Fig. 23 up to the dimensionless $\bar{z}$ = 10.5: thereafter the bunching and the dimensionless field intensity are referred to the fundamental of the radiator wiggler, i.e. $\lambda_r$ = 5 nm, plotted up to $\bar{z}$ = 20 .

The corresponding field power is shown by the dashed line plotted in Fig. 24, where 50 MW at $\lambda_r$ = 25 nm are generated in the buncher wiggler (14 m long). The saturated power level in the radiator wiggler (10 m long, from z = 14 m to z = 24 m) is 160 MW at $\lambda_r = 5$ nm. The logarithm of the field power, plotted in Fig. 25, clearly shows that the field growth in the radiator has an initial very rapid but non-exponential behaviour, followed by a quasi-exponential one (i.e. quasi linear on a log. scale) up to the saturation.

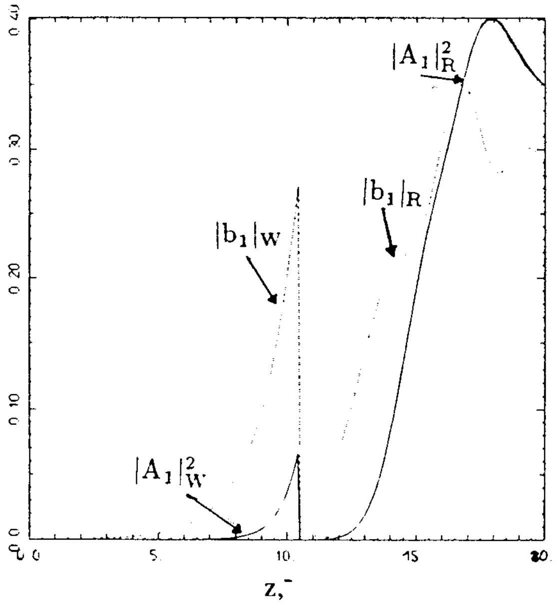

**Fig. 23** - Dimensionless field intensity (solid line) and bunching (dashed line) for the $\lambda_r = 25$ nm (z,¯ < 10.5) in the buncher wiggler and for $\lambda_r = 5$ nm (z,¯ > 10.5) in the radiator. (see text for details).

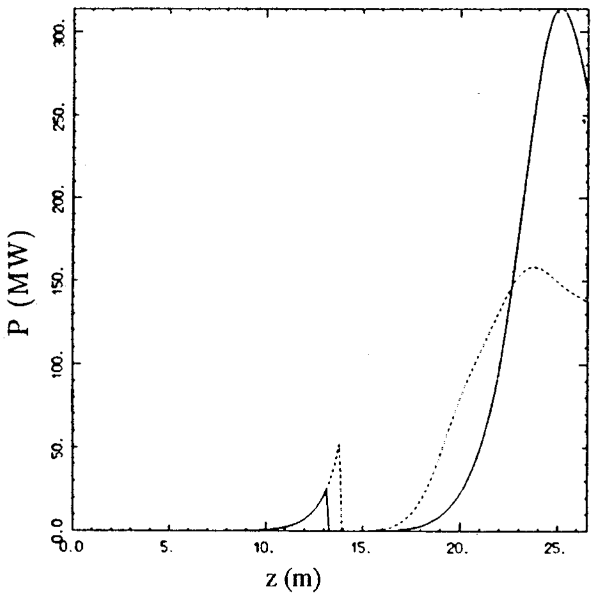

**Fig. 24** - Field power growth at $\lambda_r = 5$ nm for two different lengths of the buncher wiggler (see text for details).

The bunching on the fundamental harmonic of the radiator (i.e. on the fifth harmonic of the buncher wiggler) is indeed low at the radiator entrance, around 0.05, hence the radiation emission is no longer a pure coherent spontaneous emission as in the case of the previous section, where the bunching was 0.5. In this case the bunching and the field grow together in a way more similar to the standard steady state regime. Cutting the buncher wiggler at z = 13 m the fifth harmonic bunching is now lower: $|b_5| = .001$ . The evolution of the field power and of the bunching in the radiator, shown by the solid line of Fig. 25 and 26 respectively, are more similar to the exponential gain regime, with a saturated power level at 320 MW. This larger value is due to the lower energy spread achieved by the beam at the end of the buncher wiggler. Such a spread, which is modulated on the scale of the fundamental radiation wavelength $\lambda_r = 25$ nm, grows in the buncher wiggler together with the bunching $b_1$ . At the entrance of the radiator the spread on $\lambda_r = 25$ nm acts as an incoherent beam spread since the radiator is tuned at the lower wavelength $\lambda_r = 5$ nm . We can conclude that higher is the value of $|b_5|$ at the radiator entrance, more is the incoherent energy spread of the beam and lower is the gain in the radiator. Since the emittance condition relationship (2) is violated inside the radiator ($f_1 = 2.35$), one would like to have the highest possible $|b_5|$ at the radiator entrance in order to overcome the emittance condition, which is strictly true for an unbunched beam. Hence a trade off between the two opposite requirements must be found: 3-D simulations are needed to evaluate what is the maximum value of $f_1$ (as a function of the bunching $|b_5|$ at the entrance) which ensures an acceptable gain deterioration.

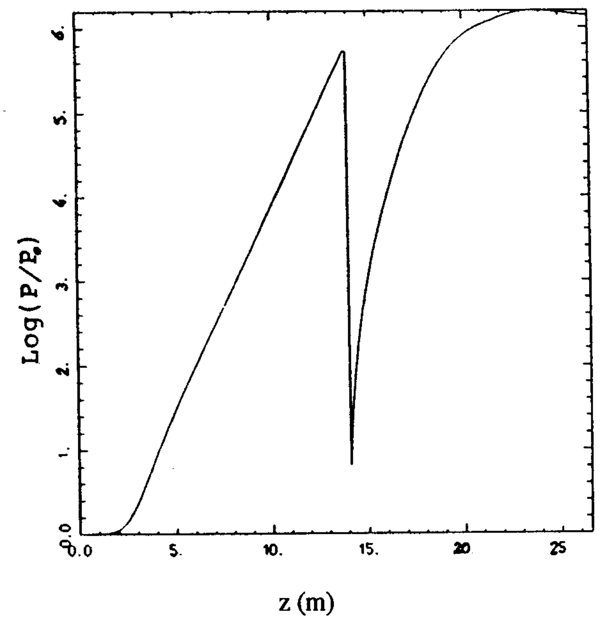

**Fig. 25** - Logarithm of the field power on $\lambda_r = 25$ nm (for z<14 m) in the buncher wiggler and on $\lambda_r = 5$ nm (for z>14 m) in the radiator (see text for details).

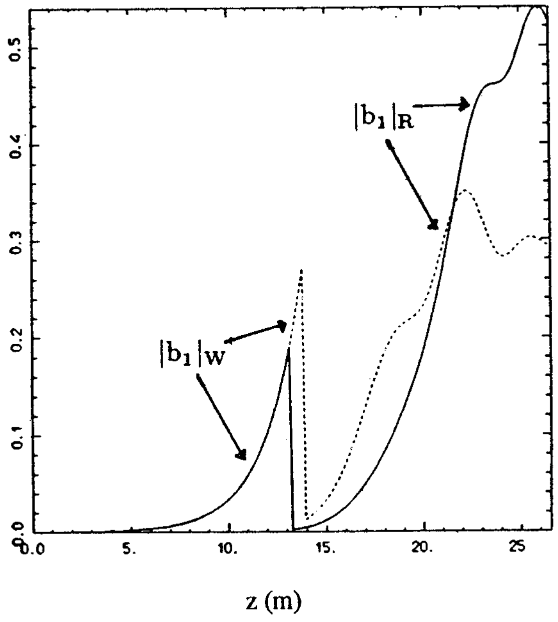

**Fig. 26** - Bunching parameter amplitude in the buncher wiggler and in the radiator for two different buncher wiggler length (see text for details).

The electron longitudinal phase spaces along the radiator are shown in Fig. 27a to 27d . The phase space, extending in the buncher wiggler over $2\pi$ radians of the radiation $\lambda_r = 25$ nm, is scaled at the radiator entrance over the corresponding $10\pi$ radians of the $\lambda_r = 5$ nm. The energy spread on the scale of the wavelength $\lambda_r = 25$ nm is clearly visible (the spread is normalized to the parameter $\rho = 1\cdot10^{-3}$). Since the radiation at 25 nm is no more resonant in the radiator, the onset of the radiation at 5 nm stimulates the bunching over the five buckets contained between 0 and $10\pi$ of the phase space. At z = 18 m, slightly before saturation, the bunching on the radiation at 5 nm is clearly visible. The initial energy spread has been taken as the expected spread of the beam, $\Delta\gamma/\gamma = \pm3\cdot10^{-4}$

The coherence of the radiated field can be estimated assuming a constant $b_5 \approx 0.1$: the ratio between coherent and incoherent power per unit solid angle comes out to be $1.7\cdot10^{-5}$, which is just consistent with the quantum fluctuation parameter, $q_f \approx 4\cdot10^{-5}$.

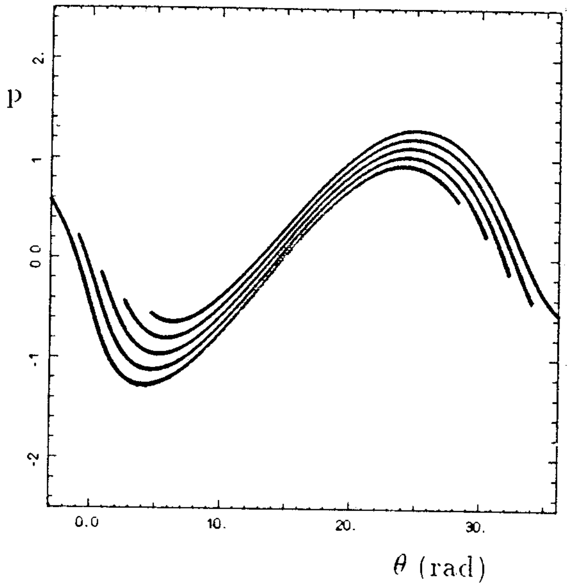

**Fig. 27a** - Longitudinal phase space at the buncher wiggler exit (z = 14 m).

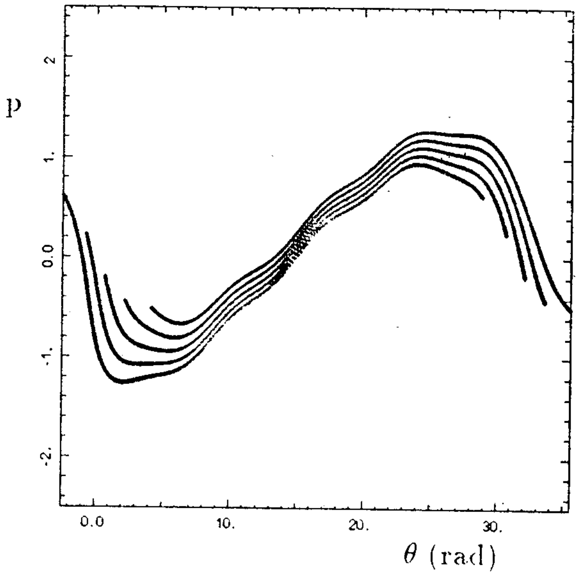

**Fig. 27b** - Longitudinal phase space at z = 15.3 m (1.3 m far from the radiator entrance)

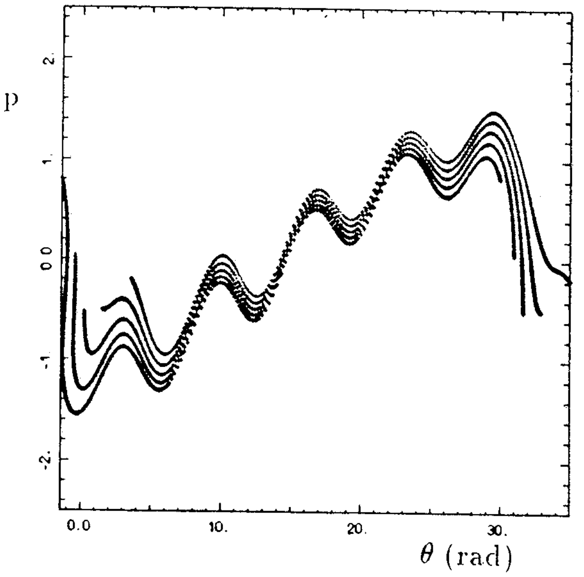

**Fig. 27c** - Longitudinal phase space at z = 16.7 m (2.7 m far from the radiator entrance)

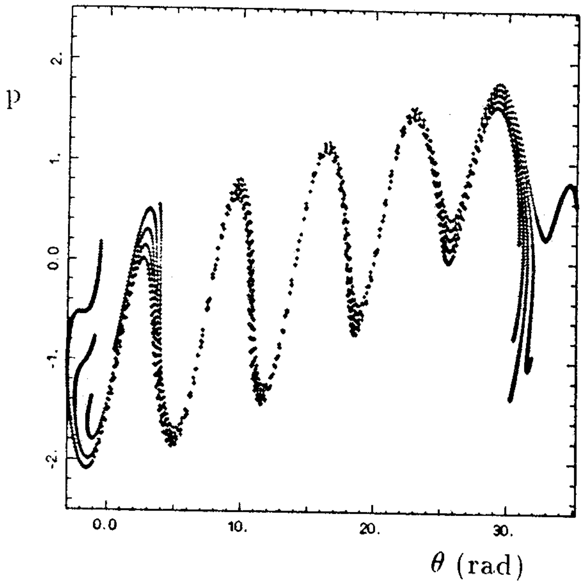

**Fig. 27d** - Longitudinal phase space at z = 18.8 m (4 m far from the radiator entrance)

## 6 - Conclusion

The high energy particle accelerator community agrees that one of the most relevant topic, on the way of the TeV electron-positron collider realization, is the capability to generate electron beams with high peak current and very low normalized emittance. The construction of an intermediate energy LINAC able to produce high quality beams seems to be a necessary step towards the TeV collider. In this respect, a soft X-ray FEL must be viewed as a test bench of the beam quality achieved. We have shown that with the ARES SC Linac facility several experiments in this context are envisageable: the link X-ray FEL's - SC LINAC's will hopefully be a marriage of convenience.

## Acknowledgments

We are indebted to W.A.Barletta and A.M.Sessler for their support and encouragement in proposing the X-VUV FEL experiments in the ARES project context. We thank especially W.A.Barletta for the numerical simulations made with FRED-3D and we are also grateful to G.Vignola and M.Castellano for helpful and valuable discussions.

## References

(1) "Ares Design Study (The Machine)" - Report LNF-90/005(R), January 17th 1990, Frascati.

(2) R.Bonifacio, C.Pellegrini and L.M.Narducci - Optics Comm 50 (1084) 373.

(3) G.Preparata - QFT of the FEL- Phys. Rev. A38, 233 (1988)

(4) E.T.Scharlemann - "Wiggle plane focussing in a linear wiggler" - LLNL Report UCRL-92429.

(5) W.A.Barletta and A.M.Sessler - Proc. of the INFN Int. School on Electromagnetic Radiation and Particle Beams Acceleration - Varenna (Italy), June 1988, p. 211-220.

(6) C.Pellegrini - NIM A227 (1980) 177.

(7) J.B.Murphy, C.Pellegrini and R.Bonifacio - Optics Comm. 53 (1985) 197.

(8) E.T.Scharlemann, A.M.Sessler and J.S.Wurtele - NIM A239 (1985) 29.

(9) R.Bonifacio et al. - Proc. of the INFN Int. School on Electromagnetic Radiation and Particle Beams Acceleration - Varenna (Italy), June 1988, p. 35.

(10) A.Ghigo, Int. Rep. LNF-Ares, 35 (1990)

(11) K.Halbach - Proc. of "Undulator Magnets for SR and FEL" - Trieste (Italy), June 1987.

(12) N. Cavallo - Ph.D. Thesis - University of Salerno, 1985.

(13) L.Serafini et al. - To be published.

(14) D.F.Alferov and E.G.Bessonov - Sov. Phys. Tech. Phys. 24 (4) 1979, 450.

(15) R.Coisson - Part. Accelerators, 11 (1981) 245.

(16) J.M.Ortega et al. - NIM A237 (1985) 268.

(17) R.Prazeres and J.M.Ortega - IEEE Journal of Q. El. 25 (1989) 2316.

(18) M.Billardon, R.Coisson and Y.Lapierre - Appl. Phys. B39 (1986) 9.

(19) R.Bonifacio et al. - Proc. Int. FEL Conference 1989.

(20) W.A.Barletta, private communication.

(21) E.T.Scharlemann, A.M.Sessler and J.S.Wurtele, Proc. of Int. Work. on Coherent and Collective Prop. in the Int. of rel. electr.and e.m.Rad., Como, Italy, Sept. 1984, p.29.

# SHOK: SUB-HARMONIC HIGH-GAIN OPTICAL KLYSTRON

L. Serafini, M. Ferrario, C. Pagani, A. Peretti

INFN and Università di Milano - Via Celoria 16 - 20133 Milano

## Abstract

A new method for pumping a single passage high gain FEL is presented, based on the exploitation of a sub-harmonic input signal which drives the start up of the exponential gain on the fundamental harmonic of the wiggler. Significant gain enhancements can be obtained: furthemore, the advantage of the SHOK scheme is very pronounced in the VUV soft X-ray domain, where no coherent input signal is available at such short radiation wavelengths, since it allows to employ the comon available UV laser beams as input signal for a XUV FEL.

## 1 - Introduction

One of the main open problem in the operation of FEL-s and Optical Klystrons within the short wavelength domain is the difficulty to find a suitable coherent signal (i.e. a laser beam) to be used as the input radiation field for the FEL amplifier(1). Being straightforward that a VUV X-ray FEL must be a single passage amplifier(2) (due to the lacking of efficient mirrors in this frequency range), an input signal is needed to be injected into the wiggler and amplified via the high gain FEL mechanism, based on a strong coupling between the wiggle electron beam motion and the radiation field. The best results, in term of coherence and output power of the radiation field, are obtained with a coherent input signal with same radiation wavelength as the fundamental resonating wavelength of the selected wiggler-beam system (3).

In the SASE (Self Amplified Spontaneous Emission) mode of operation the input signal is directly the incoherent spontaneous emission produced by the beam because of its transverse motion in the wiggler. The field power of the spontaneous emission radiation scales with the beam current I and with the square of the beam energy $\gamma^2$: it can easily reach some tens of kW per meter of wiggler(7), for wiggler-beam systems tuned to radiate in the X-VUV range. Whenever the high gain conditions are satisfied by the beam-wiggler system, the exponential growth of the self-amplified radiation sets up and the field power (at saturation) comes out to scale(4) like $I^{4/3}$ (whenever the superradian effects(5) are negligible). The advantage of the SASE mode is that no input signal is required: however the coherence of the output signal is lower. The coherence length of the output signal produced in the SASE regime is indeed given roughly by the slippage length: since the electrons interact with one another via the common radiation field, the interaction length is equal to the slippage length, hence the photons separated by more than the slippage length are of course decoupled. Therefore, the start up of the field amplification process from photon and electron populations which are both randomly distributed in phase cannot assure a narrow bandwidth and a coherent output signal.

Some frequency multiplication scheme have been recently proposed to avoid this difficulty (6,7): they essentially consist of a double (planar) wiggler cascade in which the fundamental harmonic of the second wiggler is tuned at the same frequency as one of the higher (odd) harmonics of the first wiggler. At the passage between the two wigglers a jump in frequency is obtained by a factor 3 or 5: the advantage is clearly that the coherent input signal injected at the entrance of the first wiggler is lower in frequency than the radiated field at the output of the whole system. Hence, laser beams available in the UV range can be converted in the X-VUV range and amplified up to high peak powers level(7) (some hundrets of MW). However, such schemes have the disadvantage to require two different (and in some cases separate) wigglers, fact that strongly increases the un-reliability of the whole system and all the problems related to beam-radiation phase mis-matching, beam transport, wiggler tolerances, etc. Moreover, high frequency multiplication factors cause a relevant gain decrease in the second wiggler because of the induced energy spread by the first wiggler on its fundamental harmonic, which is seen as an incoherent energy spread by the fundamental harmonic of the second wiggler(8): theefore the frequency multiplication cannot be higher than a factor 3 or 5 if the FEL performances need to be saved.

In this paper we present a scheme of frequency multiplication operating with only one wiggler, requiring no input signal nor on the fundamental neither on higher hamonics and an unbunched beam at the wiggler entrance, i.e. a device capable to start up the exponential gain process on the fundamental harmonic just from the equilibrium condition of zero field and zero bunching. This device is based simply on a sub-harmonic signal injection: under proper conditions, the subharmonic coherent input signal is capable to induce a modulation in the beam energy (i.e. a coherent energy spread) which is converted into a bunching by the wiggler dispersive action.

The first section is devoted to illustrate the extension of the FEL Compton equations to the presence of a sub-harmonic field wave and to present some general results obtained by the numerical integration.

The second section presents a first possible application of the SHOK scheme to drive a FEL in the VUV range, to obtain coherent radiation at a wavelength of 40 nm with a peak power of some hundrets of MW.

The last section presents the possibility to reach the so-called "water window" at 5 nm of radiation wavelength via the exploitation of an extended SHOK scheme.

Both the experiments should be feasible within the context of the ARES(17) project - as presented in the "ARES Design Study" -, which anticipates the design and construction of a SC LINAC able to produce high brightness electron beams in the 400-800 MeV range.

## 2 - The SHOK scheme

The break up of the equilibrium condition of zero field and unbunched beam, which is a stable fixed point for the FEL equations, is achieved via the injection of a sub-harmonic input signal, matched to the electron beam, into the wiggler. This signal can be a laser beam at a suitable frequency being a sub-multiple of the fundamental resonant wavelength of the wiggler-beam system. We called such a device, which is simply a sub-harmonic assisted wiggler, Sub-Harmonic Optical Klystron, because, as in the standard optical klystron configuration(9), an input laser beam is employed to stimulate a bunching of the injected beam on the scale of the resonant radiation wavelength. Once a small but finite bunching is achieved, if the proper conditions are met to operate the FEL in the high gain regime, the exponential growth of the radiated field naturally sets up according to the standard steady state behaviour of the FEL amplification process.

The driving effect of the sub-harmonic input signal, which has a wavelength $\lambda_s = s \cdot \lambda_r$ (s is the sub-harmonic index and $\lambda_r$ is the fundamental resonant wavelength of the wiggler), consists essentially in inducing a coherent energy modulation onto the electron beam: such an energy spread is transformed by the wiggler, which can be viewed as a dispersive medium, into a phase modulation, i.e. a density modulation. Therefore the beam comes out to be bunched on the scale of the sub-harmonic wavelength $\lambda_s$ and on all the higher harmonics: in particular the harmonic of wavelength $\lambda_r$ is just the bunching component of interest to start up the FEL amplification process on the resonant wavelength $\lambda_r$.

Let us examine now how a sub-harmonic signal of wavelength $\lambda_s$, injected into a wiggler of period $\lambda_w$ at the same time of an electron beam of energy $\gamma$, can induce a modulation in energy of the beam on the scale of its wavelength $\lambda_s$. The resonant wavelength $\lambda_r$ is given by the usual FEL resonance relationship:

$$\lambda_r = \frac{\lambda_w (1 + a_w^2)}{2 \gamma^2 n}$$

where n is an odd integer number (n=1 gives the fundamental first harmonic radiated by the beam while n>1 gives the higher resonating harmonics) and $a_w$ is the dimensionless vector potential of the wiggler. In a planar wiggler $a_w$ is related to the peak magnetic field, $B_w$, by the formula: $a_w \approx .66\ \lambda_w\ [\mathrm{cm}]\ B_w\ [\mathrm{T}]$.

We define an electromagnetic field for the sub-harmonic laser beam in a similar way as for the higher harmonics:

$$\vec{E}_s(z,t) = \frac{mc^2}{e}\frac{\hat{x}}{\sqrt{2}}\left(\tilde{e}_s(z,t)\, e^{i(kz-\omega t)/s} + \mathrm{c.c.}\right) \qquad 1)$$

where $\tilde{e}_s$ is a slowly varying complex amplitude that, using the SVEA approximation, can be derived from a vector potential $\tilde{a}_s = a_s\, e^{i\phi_s}$, such that $|\tilde{e}_s| = k\cdot a_s$, using $E=-(1/c)\partial/\partial t(mc^2\tilde{a}_s/e)$.

The normalized transverse velocity of an electron injected in a planar wiggler is given, neglecting the effects due to the electromagnetic wave and to the betatron motion, by(10):

$$\vec{\beta}_\perp = \sqrt{2}\,\frac{a_w}{\gamma}\cos(k_w z)\,\hat{x} \qquad 2)$$

where $k_w = 2\pi/\lambda_w$ and $\hat{x}$ gives the transverse horizontal direction of a planar wiggler extending longitudinally along z.

The work done by the sub-harmonic field on the wiggling electron, on the basis of the Lorentz energy equation, comes out to be(*):

$$\left(\frac{d\gamma}{dz}\right)_s = -2\,\frac{k a_w a_s}{\gamma}\cos\left(\frac{kz-\omega t}{s}+\phi_s\right)\cos(k_w z) \qquad 3)$$

The complete energy equation, including the radiative harmonics contribution, becomes:

$$\frac{d\gamma}{dz} = -2\sum_h^{h\,\mathrm{odd}}\frac{k a_w a_h}{\gamma}\cos[h(kz-\omega t)+\phi_h]\cos(k_w z) + \left(\frac{d\gamma}{dz}\right)_s \qquad 3\text{-b)}$$

where $a_h$ is the vector potential amplitude of the h-th harmonic.

In order to satisfy the SVEA approximation(11) it is usual to average over a wiggler period the fast oscillations induced in the energy equation by the planar magnetostatic field structure. In presence of a sub-harmonic field the averaging must be performed over $s\cdot\lambda_w$, i.e. over a number of wiggler periods equal to the sub-harmonic order s. Defining $\theta = (k_w+k)z - \omega\bar{t}$ as the average electron phase over a wiggler period (or, equivalently, over s wiggler periods), where $\bar{t} = (z/c)\cdot(1+(1+a_w^2/2\gamma^2))$ is the averaged arrival time, the actual electron phase, which takes into account the fast oscillations, comes out to be given by $\theta_f = \theta - \xi\sin(2k_w z)$, where the parameter $\xi$

---

(*) The contribution due to the betatron motion can be neglected whenever the betatron wavelength $\lambda_b$ is much larger than the wiggler period $\lambda_w$. Since $\lambda_b/\lambda_w = \sqrt{2}\cdot\gamma\cdot H/a_w$, for the case of X-VUV FEL's this ratio is >>1.

is defined as $\xi = ka_w^2/(4k_w\gamma^2)$ and, if the electron $\gamma$ is close to the resonant $\gamma_r$, it depends only on the wiggler potential $a_w$, i.e. $\xi = a_w^2/2(1+ a_w^2)$.

The averaged energy equation can then be written as

$$\overline{\left(\frac{d\gamma}{dz}\right)}_s = -2\frac{ka_w}{\gamma s\lambda_w}\int_{z-s\lambda_w}^{z} a_s \cos\left[\frac{\theta}{s} - \frac{k_w z'}{s} - \frac{\xi}{s}\sin(2k_w z') + \phi_s\right]\cos(k_w z')\, dz' \qquad 4)$$

Assuming that the electron phase $\theta$ remains constant over the averaging period $s\cdot\lambda_w$, it is easy to see that the integral in 4) is vanishing whenever the amplitude $a_s$ of the sub-harmonic field is constant over $s\cdot\lambda_w$: no energy spread can be induced with a sub-harmonic field whose intensity stays constant along the wiggler. In fact, the energy spread contributions produced at each half of a wiggler period are summed along s wiggler periods to give exactly zero. Taking as an example the sub-harmonic of order two (s=2), it is easy to figure out that the electron beam sweeps away one sub-harmonic wavelength, with respect to the sub-harmonic optical field wave, every two wiggler periods: therefore, each electron of the beam, independently of its phase, experiences, at each wiggler period, two opposite, but equal in amplitude, momentum transfers (corresponding to the two halves wiggler period). The total momentum transfer on the electron will be therefore exactly zero.

There is, however, a possibility to avoid such an exact compensation and get a not-vanishing total momentum transfer, as sketched in Fig.1: if the sub-harmonic field is given by a single mode laser beam of wavelength $\lambda_s$ injected into the wiggler from an external source, the optical field amplitude on axis will be given by

$$|\vec{E}| = \frac{|\vec{E_0}|}{\sqrt{1 + \frac{z^2}{Z_0^2}}} \qquad 5)$$

where $w_0$ is the spot at the beam waist and $Z_0$ is the Rayleigh range $Z_0 = \pi w_0^2/\lambda_s$. Since the transverse distribution of the optical field amplitude is gaussian ( $|E(r)| = |E(r=0)|\cdot e^{-(r/w)^2}$), the overlap between the electron beam (with transverse gaussian distribution of width $\sigma$) and the laser beam requires $w_0 = \sqrt{2}\sigma$ (**), fixing the Rayleigh range at $Z_0 = 2\pi\sigma^2/\lambda_s$. The integral on the r.h.s. in 4) is not vanishing if the variation of the sub-harmonic field is significant over one wiggler period $\lambda_w$: the Rayleigh range $Z_0$ must be therefore not too large with respect to $\lambda_w$.

---

(**) The wiggle motion of the electron beam can perturb the overlap with the sub-harmonic laser beam: the ratio between the amplitude of the wiggle motion and the rms beam radius can be extimated to be given by $(x_{max}/\sigma)=.01.B_w^{3/2}[T]/(\sqrt{\varepsilon_n H}.\gamma)$. In our case this ratio is always « 1, indicating that the overlap can be considered complete.

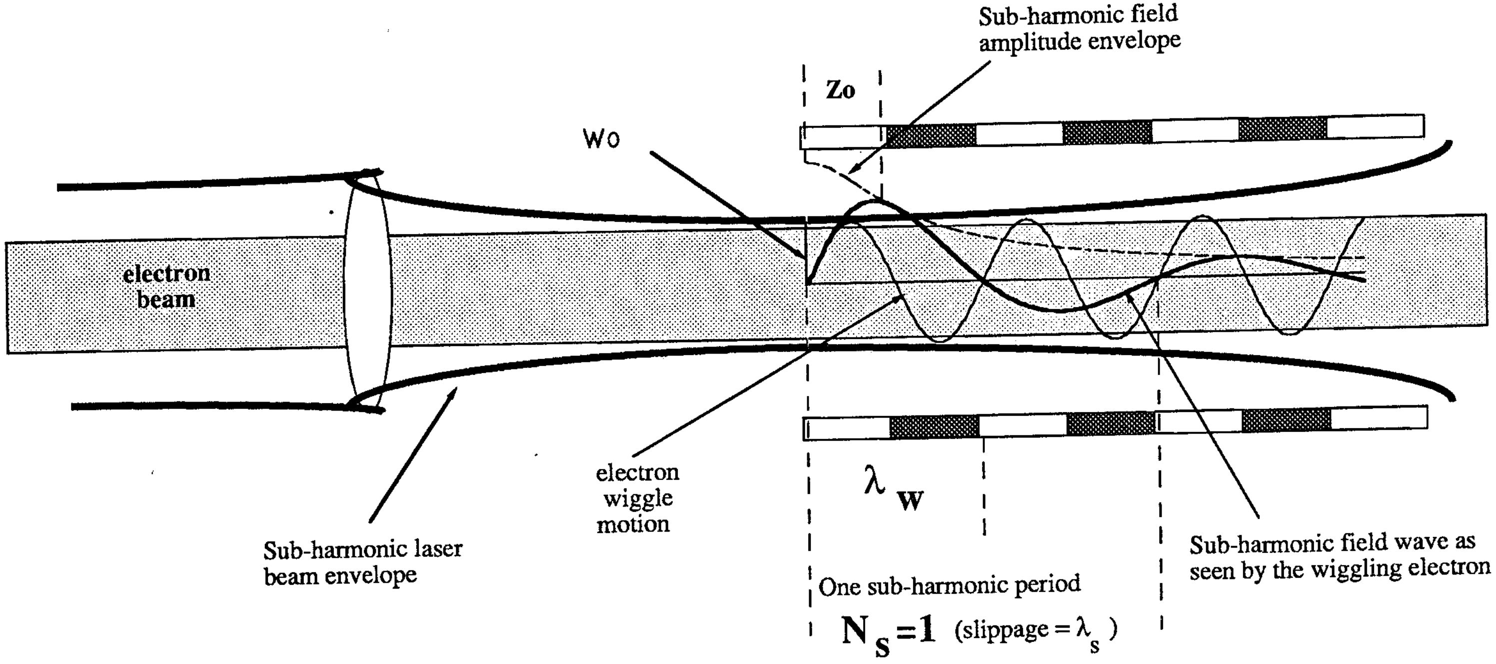

Fig.1 - Schematics of a second order s=2 sub-harmonic beam-field coupling

Taking the usual scaling low for the beam radius in a wiggler with appropriate shaping of the pole face(12) one can compute that the ratio $Z_0/\lambda_w$ is given by:

$$\frac{Z_0}{\lambda_w} = \frac{\gamma}{\sqrt{2}\,\pi\, s}\,\frac{H}{a_w} \qquad 6)$$

where H is the fractional reduction of the betatron wavelength due to the amount of ion focussing applied(13) (H=1 no ion focussing). For electron beams of some hundrets of MeV and a sub-harmonic index s in the range 3-5 a ratio $Z_0/\lambda_w$ in the order of some tens can be achieved: that implies a not-vanishing integral on the r.h.s. of eq. 4), i.e. the possibility to induce an energy spread in the electron beam using a sub-harmonic input signal.

We will examine later on the efficiency of such a process, after the insertion of the sub-harmonic field action in the FEL Compton equations(14), as described in the following.

The complex vector potential $\tilde{a}_s$ of the sub-harmonic field can be redefined and set in a dimensionless form introducing the new variables(11,15):

$$A_s = \frac{\omega}{\omega_p\sqrt{\rho\gamma_r}}\,\tilde{a}_s$$

$$p_j = \frac{\gamma_j - \gamma_r}{\rho\gamma_r} \qquad 7)$$

$$\bar{z} = 2\,k_w \rho\, z$$

where $\rho$ is the Pierce parameter $\rho=(1/\gamma)(a_w\omega_p/4ck_w)^{2/3}$, $\omega_p$ is the beam plasma frequency $\omega_p = \sqrt{4\pi e^2 n/m_0}$ (n is the electron beam density), $\gamma_j$ is the gamma of the j-th electron and $\gamma_r$ the resonant gamma. We recall that the complex dimensionless field amplitude $A_s$ is expressed as $A_s = |A_s|e^{i\phi_s}$, where $\rho|A_s|^2$ gives the ratio between the energy density of the sub-harmonic laser beam and the electron beam energy density. Assuming, at the wiggler entrance, a perfect overlap between the electron beam and the sub-harmonic laser beam, the initial value of $|A_s|^2$ at z=0 will be given by $|A_s^0|^2 = P_s/(\rho P_b)$, where $P_s$ is the sub-harmonic laser beam power and $P_b$ the electron beam power.

Expressed in the dimensionless units the momentum equation 3), which accounts for the energy spread induced by the sub-harmonic field, becomes:

$$\left(\frac{dp_j}{d\bar{z}}\right)_s = \dot{p}_j^{\,s} \equiv -\chi(\bar{z}) \frac{\left|A_s^0\right|}{\sqrt{1+\frac{\bar{z}^2}{\bar{Z}_0^2}}} \cos\left[\frac{\theta_j}{s} - \frac{\bar{z}}{2\rho s} - \frac{\xi}{s}\sin\left(\frac{\bar{z}}{\rho}\right) + \phi_s\right] \cos\left(\frac{\bar{z}}{2\rho}\right) \qquad 8)$$

$$\text{with} \quad \chi(\bar{z}) = \left\{\begin{matrix} 0 & \bar{z}<0 \\ 1 & \bar{z}\geq 0 \end{matrix}\right\}$$

where we recall that $\theta_j$ is the electron phase averaged over a wiggler period. The function $\chi(\bar{z})$ is needed to take into account a semi-infinite wiggler starting from $\bar{z}=0$: the sub-harmonic field action given in eq.3) starts indeed at the wiggler entrance, $\bar{z}=0$.

Since the coupling between the electron beam and the sub-harmonic field is very low, as will be shown later on, we will assume the sub-harmonic field as an external driving force whose variation in time and space is specified by the optical behaviour of the sub-harmonic laser beam, as given in eq.1), with an optical field amplitude as specified in eq.5).

Inserting the contribution to the energy spread coming from the sub-harmonic field into the FEL Compton equations we get:

$$\begin{aligned} &\frac{dp_j}{d\bar{z}} = -\sum_{h\ \mathrm{odd}} F_h(\xi)(A_h e^{ih\theta_j} + \mathrm{c.c.}) + \dot{p}_j^{\,s} \\ &\frac{d\theta_j}{d\bar{z}} = p_j \qquad\qquad j=1,N \qquad\qquad 9) \\ &\frac{dA_h}{d\bar{z}} = F_h(\xi) <e^{-ih\theta_j}> \qquad \text{where } < > \equiv \frac{1}{N}\sum_{j=1}^{N} \end{aligned}$$

where the term $b_h = <e^{-ih\theta_j}>$ is usually called the bunching parameter on the h-th harmonic. The coupling coefficients $F_h(\xi)$ are given by$^{(14)}$ $F_h(\xi) = J_{(h-1)/2}(h\xi) - J_{(h+1)/2}(h\xi)$.

Averaging the first of the eqs. 9) over the N electrons, using also the third one, we get:

$$\frac{d}{d\bar{z}}\left(<p> + \sum_{h}^{h\ \mathrm{odd}} \left|A_h\right|^2\right) = <\dot{p}^{\,s}> \qquad 10)$$

which states that the total momentum associated to the electron beam and to the odd radiative harmonics (on the r.h.s. of eq.10), which, in absence of the sub-harmonic field, is a well known constant of the motion, varies along the wiggler until the sub-harmonic field is able to exchange momentum to the electron beam, i.e. until $<\dot{p}^s>\neq 0$.

Looking at eq.8), it comes out that the work done by the sub-armonic field onto the beam electrons becomes vanishing for $\bar{z} \gg \bar{Z}_0$, implying that the momentum exchange $\langle p^s \rangle$ from the sub-armonic field to the electron beam reaches, after an initial transient regime, a constant value, given by

$$\langle p \rangle + \sum_{h}^{h\ \mathrm{odd}} |A_h|^2 = \langle p^s \rangle \equiv \int_0^{\bar{z}} \langle \dot{p}^s \rangle d\overline{z'} \qquad 11)$$

The new constant of the motion becomes $\langle p \rangle + \Sigma_h |A_h|^2 - \langle p^s \rangle = 0$, in the case of zero detuning and zero field amplitude at the wiggler entrance. It will be shown later that the final momentum exchange between the electron beam and the sub-harmonic field, i.e. the quantity $\langle p^s \rangle$ evaluated at $\bar{z} \gg \bar{Z}_0$, is negligible with respect to the final value of $\langle p \rangle$ at saturation, which is of the order of 1.

Therefore, we can explain the effect of the sub-harmonic field on the system formed by the beam and the radiative harmonics in terms of a driven shift of the system away from the equilibrium condition $b_h=0$ and $A_h=0$, applied during a transient regime which lasts a few units of $\bar{Z}_0$. It can be seen at a glance that the codition $b_h=0$ and $A_h=0$ is no more a fixed stable point for the system of eq. 9): if the term $p_j$ is modulated over the phase space with a non-zero first harmonic component, i.e. if $\langle p_j \cdot e^{i\theta_j} \rangle \neq 0$, a uniform beam ($b_h=0$) in absence of any starting signal ($A_h=0$) will get a phase modulation, i.e. a bunching, as given by: $\dot{b} = i \langle p_j \cdot e^{i\theta_j} \rangle$, which can be deduced by the 2nd of eq. 9). It comes out that the action of the sub-harmonic field is the breaking of the stable equilibrium condition of zero field and zero bunching. The new stable equilibrium condition becomes, for the eq. 9), $b_h=0$, $A_h=0$ and $A_s^0=0$ (or $Z_0 \rightarrow \infty$, i.e. a parallel laser beam).

In order to study the excitation of the exponential regime on the first and the higher harmonics of the wiggler, starting with a uniform beam and zero first harmonic signal ($A_1 = 0$), we integrated numerically the system of equations 9) using some hundrets (tipically 720) of macroparticles to simulate the electron beam. The macroparticles are initially distributed with $p_j=0$ and with phases $\theta_j$ uniformly distributed over $2\pi s$ radians in the phase space: the bucket of the sub-harmonic field is indeed extending over s buckets of the first harmonic, hence the phase space will have a periodicity of order $2\pi s$.

As a first test we pointed out our attention to the lowest sub-harmonic index, s=2, the second order sub-harmonic. The free parameters are in our case the amplitude of the sub-harmonic field at the wiggler entrance, $|A_s^0|$, the Rayleigh range of the sub-harmonic laser beam $Z_0$ and the wiggler potential $a_w$. We chose a typical value for $a_w = 1.5$, corresponding to a wiggler period $\lambda_w = 2$ cm and B = 1.1 T, a ratio $Z_0/\lambda_w = 10$ and an initial sub-harmonic field amplitude $|A_s^0| = 0.15$. The quantity $\bar{Z}_0$ is defined as $\bar{Z}_0 = 4\pi\rho \cdot (Z_0/\lambda_w)$. Taking for $\rho$ a typical value $\rho=.002$, we have $\bar{Z}_0 = .25$.

The phase variation for a particle started at ($\theta$=.035 rad, p=0 ) is plotted in Fig.2 versus $\bar{z}$ from $\bar{z}$=0. to $\bar{z}$=1., which corresponds to 40 wiggler periods. The small oscillations (of the order of $1\cdot10^{-5}$ rad) of the electron phase $\theta$ confirm that this is slowly varying along the wiggler and represents just the average electron phase over one wiggler period. Note that the fast electron phase $\theta_f$ exhibits fast oscillations over one wiggler period with amplitude $\xi$ (which is of the order of 1). The phase space trajectory is shown, for the same particle, by the solid line plotted in Fig.3: the scalloped shape of the trajectory clearly shows that the electron undergoes relevant oscillations in momentum accompanied by small oscillations in phase (note the enlarged scale in abscissa). The dashed line in the same figure connects the points of the trajectory corresponding to the end of each wiggler period: the fast oscillations induced by the sub-harmonic field are washed out and only a slowly varying phase shift is left. It must be noted that in the numerical integration the step has been taken small with respect to the wiggler period ( i.e. $\delta\bar{z} \ll 4\pi\rho$ ) in order to take into account the fast oscillations in p.

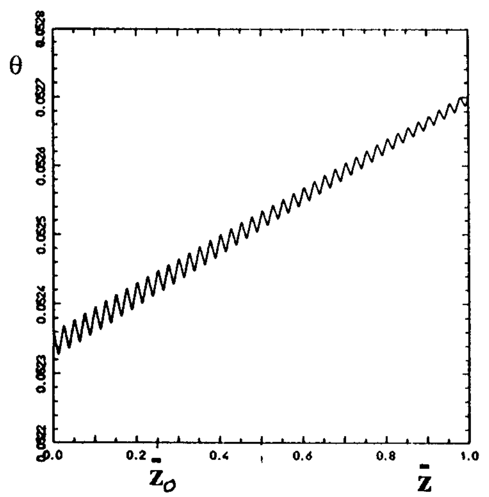

**Fig.2** - Behaviour of the average electron phase $\theta$ plotted as a function of $\bar{z}$, for a test particle.

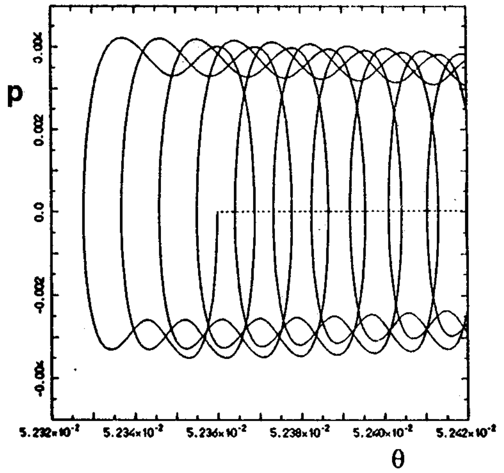

**Fig.3** - Phase space trajectory of the same particle of Fig.2, starting at $\bar{z}$=0 from $\theta$=.05236 rad, p=0.

The maximum value of p over the phase space $p_{max}$ (i.e. the amplitude of the beam energy modulation over a sub-harmonic wavelength, recalling that p is the normalized energy spread) is plotted in Fig.4 (solid line) as a function of $N_s = \bar{z}/(4\pi\rho s)$. Since at each wiggler period $\lambda_w$ the electrons shift by one first harmonic wavelength $\lambda_r$ with respect to the first harmonic field wave, a number s of wiggler periods are needed to produce a slippage of one sub-harmonic wavelength $\lambda_s=s\lambda_r$ with respect to the sub-harmonic field wave. Then, the quantity $N_s$ gives the number of sub-harmonic wavelengths seen by the beam, or, equivalently, the slippage in units of $\lambda_s$. The position of $Z_0$ on this scale is also shown in abscissa at $N_s(Z_0) = Z_0/s\lambda_w = 5$. The phase space is shown in Fig.5 after one half of the first wiggler period (dotted line) and after two wiggler periods (bolded line), i.e. at $N_s$=1. The phase space range is $2s\pi$ = 12.57 rad.

In Fig.4 the action of the sub-harmonic field is clearly visible: recalling that the number of wiggler periods are, for this case of s=2, just doubled with respect to $N_s$, it can be seen that the maxima in the energy modulation amplitude are reached at half of each wiggler period, with an envelope following just the laser beam intensity behaviour. The minima are initially positioned at the end of each wiggler period: for a constant average electron phase θ the integral in 4) gives always a minimum at $z=n\lambda_w$, and the minimum value is exactly zero if the sub-harmonic laser beam envelope is parallel, i.e. the optical field on axis is constant. The value of the minima is instead growing along the wiggler and their position shifts slowly just after the end of each wiggler period, due to the slow variation of the average electron phase θ, as shown by the dashed line plotted in Fig.4, which connects the values of the energy modulation amplitude at the end of each wiggler period: the asympthotic value of this curve, which is quickly reached at some $Z_0$ units, gives just the final amplitude of the energy modulation induced by the sub-harmonic laser beam. At that point the sub-harmonic intensity can be considered really negligible and no more active on the electron beam.

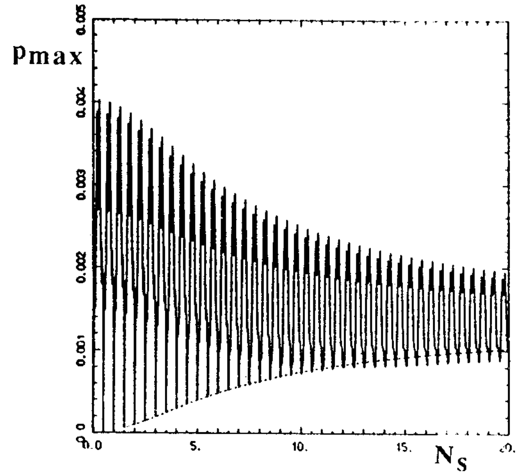

**Fig.4** - Maximum p over the phase space (i.e. amplitude of the energy modulation) plotted (solid line) along 40 wiggler periods, i.e. $N_S=20$. The dashed line connects the values assumed at the end of each wiggler period. See text for details.

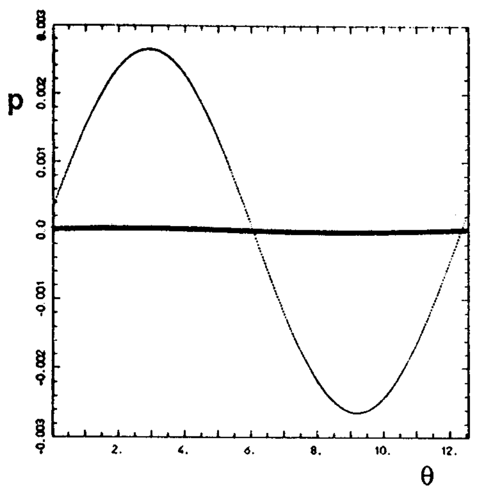

**Fig.5** - Phase spaces of the 720 simulating particles traced at the end of the first wiggler period (dotted line) and at the end of the second wiggler period (bolded line), where $N_S=1$. See text for details.

It is not so surprising that the asymptotic value of the final amplitude of the energy modulation does not depend (to the first order) on the value of $Z_0/\lambda_w$. Indeed, neglecting the slow variation of θ over a few units of $Z_0$, the total momentum transfer can be derived by an integral similar to that in eq.4) extended from z=0 up to $z=nZ_0$ (n small): the maximum over the phase space (θ=0-2π) scales linearly with $|A_s^0|$ (i.e. with the initial amplitude of the sub-harmonic optical field ) and scales invariant with $Z_0$. That is confirmed by the curves plotted in Fig.6: the solid line shows the maximum value of p over the phase space at the end of each wiggler period, from $N_s=0$ up to $N_s=160$ (i.e. along 320 wiggler periods), obtained with a value of $Z_0/\lambda_w = 10$, while the dashed line is given by a value of $Z_0/\lambda_w = 20$ and the dotted line by $Z_0/\lambda_w = 80$. The asympthotic value reached by the two curves is substantially the same.

The total momentum transfer $<p_s>$ between the sub-harmonic field and the electron beam is plotted (for the case $Z_0/\lambda_w=20$) in Fig.7 as a function of $\bar{z}$ from the wiggler entrance up to $\bar{z}=6.$, which corresponds to 240 wiggler periods. The momentum transfer is negative, implying that the electron beam looses energy, but its value is very small ($\approx -2 \cdot 10^{-9}$), hence the coupling between the sub-harmonic field and the electron beam is very weak. The momentum transfer from the electron beam to the sub-harmonic field (which should gain energy) is therefore negligible when compared to the sub-harmonic field intensity variation caused by the optical laser beam behaviour.

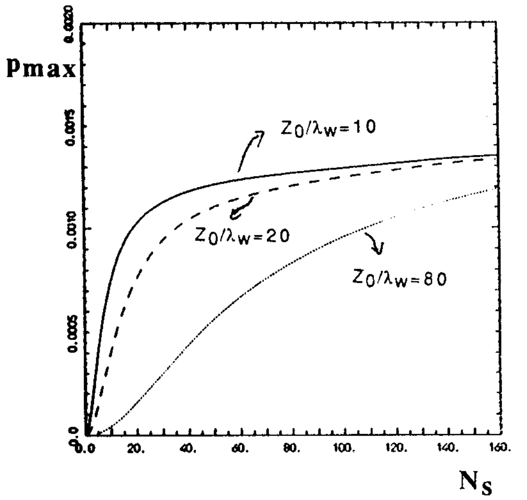

**Fig.6** - Maximum p over the phase space plotted at the end of each wiggler period, over 320 wiggler periods (i.e. $N_S$=160), for three different values of $Z_0/\lambda_w$, as indicated. See text for details.

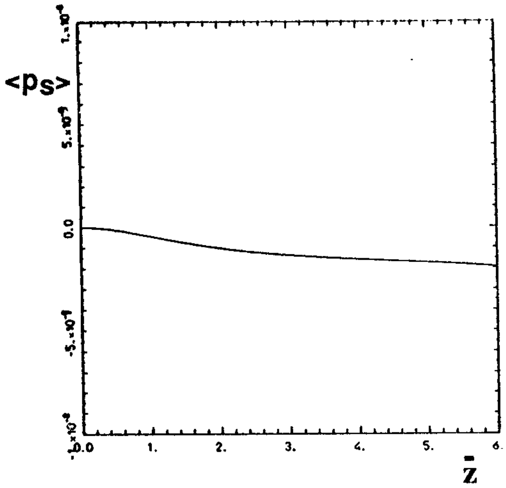

**Fig.7** - Momentum transfer $<p_S>$ between the sub-harmonic field wave and the electron beam, plotted as a function of z̄. See text for details.

To summarize, we list the following main results:

- the sub-harmonic field can induce a coherent energy spread whenever the intensity of the sub-harmonic signal is varying monotonically along the wiggler: the final energy spread scales linearly with the difference between the initial amplitude of the sub-harmonic signal (at the wiggler entrance) and its final amplitude (which is nearly zero for a defocussing optical laser beam matched with the electron beam at the wiggler entrance). Other type of sub-harmonic signals can be considered, within different spectral region: for instance, guided microwave pulses within linearly tapered wave-guides could be used as sub-harmonic signals for FEL's in the microwave region.

- the evolution of the sub-harmonic field along the wiggler is mainly determined by the optical properties of the laser beam, since the coupling with the electron beam is very weak: the sub-harmonic field produces essentially an energy modulation with a very low energy absorption from the electron beam ( $<p_S>$ negative and very small, like in a very low gain regime).

- the quantity $<p> + \Sigma_h|A_h|^2$, which is the usual constant of the motion in absence of the external driving force due the sub-harmonic field, is still constant just after an initial transient regime: the energy exchange between the electron beam and the radiative harmonics is not perturbed by the presence of the sub-harmonic field inducing the energy modulation since the total momentum transfer between the electron beam and the sub-harmonic field is negligible with respect to the coupling between the electron beam and the radiative harmonics.

- the average electron phase $\theta$ is still a slowly varying quantity, with very low residual oscillations over a wiggler period
- the final amplitude of the coherent energy spread induced by the sub-harmonic field does not depend (to a good approximation) from the Rayleigh range $Z_0$, i.e. from the actual shape of the laser beam envelope ( this seems to be valid for $Z_0$ not so much high with respect to the wiggler period).

The perfomances of the SHOK scheme can be deduced from the evolution of the first harmonic field intensity along the wiggler starting from a condition of zero field ($|A_1|^2=0$). Fixing the input parameters at the values indicated above we continued the integration of eq. 9) versus $\bar{z}$ varying the initial amplitude of the sub-harmonic field, namely with the three different values $|A_s^0|^2$ = .2, .02, .002.

We used an integration step equal to one hundreth of a wiggler period, i.e. $\delta\bar{z} = 4\pi\rho/100$, and a double precision calculation, i.e. a machine epsilon $\varepsilon_m$ around $1\cdot10^{-15}$: that implies a noise level on the initial bunching of the same order, since the "uniform" distribution of the particles in the initial phase space (at $\bar{z} = 0$) suffers for a straggling in the $\theta$ position of each particle which is equal to the machine epsilon. Therefore, the start up of the exponential regime in the first harmonic is unavoidable, as can be seen in Fig.8, where the bolded line mark the growth of the first harmonic normalized field intensity (the logarithm $\log|A_1|^2$ is plotted) versus $\bar{z}$.

The numerical noise in the phase space drives initially the field intensity which grows very fast, until the bunching, caused by the noise, reaches an equilibrium regime with the radiated field intensity (at $\bar{z}\approx2$): at that point the standard exponential behaviour sets in and the field continues to grow exponentially till the saturation is reached at $\bar{z}\approx50$, with a field intensity $|A_1|^2 \approx 1$. The behaviour of the bunching amplitude $|b_1|$ is plotted in Fig.9, where the dashed line marks the quantity $\log|b_1|$ as a function of $\bar{z}$. The bunching stays fairly constant at the initial value up to the point where the radiated field has grown enough to create a potential well in which the particles are trapped in: at that point also the bunching starts to grow exponentially (its log increases linearly).

The evolution of the logarithm of the field intensity $\log|A_1|^2$ in presence of an injected sub-harmonic signal is plotted in Fig.8: the dotted line is given by an initial $|A_s^0|^2 = 0.002$, the dashed line corresponds to $|A_s^0|^2 = 0.02$ and the solid line to $|A_s^0|^2 = 0.2$, while the behavior of the quantity $\log|b_1|$ is plotted in Fig.9 (solid line) just for the case $|A_s^0|^2 = 0.2$.The strong driving effect applied to the bunching by the sub-harmonic field is clearly evident: the energy spread induced by the sub-harmonic field is converted by the wiggler into a phase modulation, hence in a bunching, as specified by the phase equation for $\theta_i$ in the system 9). The first harmonic field reaches the saturation after $\bar{z}\approx20$ starting from a zero initial amplitude. The first plotted value, which specifies the lowest level of the scale at -38, is just the value of $\log|A_1|^2$ after the first integration step: this value $|A_1|^2 \approx 3.10^{-38}$ is given just by the numerical noise in the phase space, i.e. by the initial bunching, and is indeed the same for all the lines plotted in Fig.8.

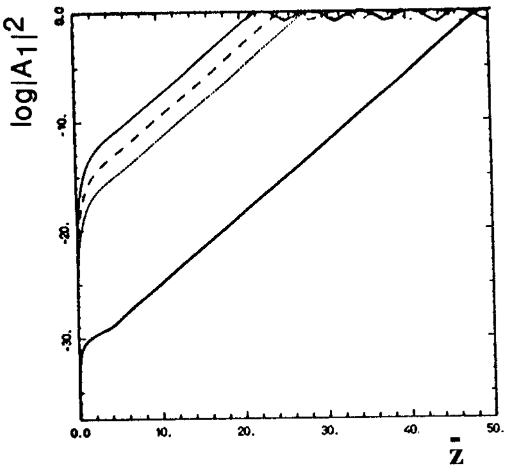

**Fig.8** - Logarithm of the normalized first harmonic field intensity, plotted as a function of $\bar{z}$, for three different values of the initial sub-harmonic field intensity. See text for details.

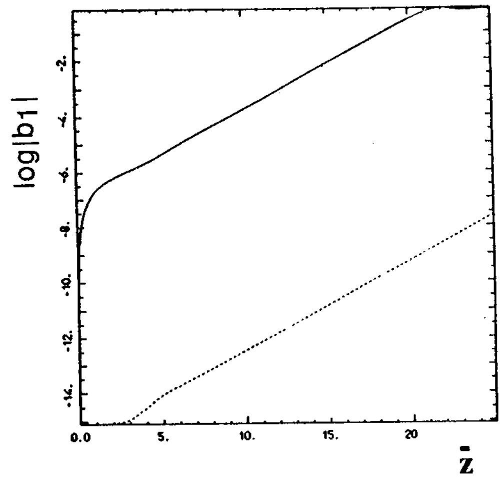

**Fig.9** - Logarithm of the bunching amplitude $|b_1|$, plotted as a function of $\bar{z}$, for the two cases: with the sub-harmonic field (solid line) and without (dashed line). See text for details.

The incremental gain g, defined as $g = d\ln|A_1|^2/d\bar{z}$ (nepers), is plotted in Fig.10 versus z,- along the first part of the wiggler (40 wiggler periods): the dashed line gives the gain behaviour for the case of the start up from the numerical noise, i.e. without any sub-harmonic field, while the solid line corresponds to the three sub-harmonic input signals listed above. While the dashed line approaches quickly the standard value assumed during the exponential growth, given by $g=\sqrt{3}\cdot F_1^{2/3}(\xi)$, whose value is, for the present case, g=1.6 nepers, the incremental gain of the sub-harmonic driven case stays much more at higher values up to $\bar{z}\approx 6$, where the driving effect of the sub-harmonic field on the first harmonic radiated field becomes negligible with respect to the natural exponential growth of the latter.

In order to check that the SVEA approximation is satisfied, the first harmonic field phase $\phi_1$ (we recall that $A_1=|A_1|e^{i\phi_1}$) must comes out to be a slowly varying function of $\bar{z}$: that is confirmed by the behaviour shown in Fig.11, where the solid line gives the phase $\phi_1(\bar{z})$ (modulus $2\pi$) along the wiggler up to saturation, for the case of $|A_s^0|^2 = 0.2$. The dashed line gives the behaviour of $\phi_1(\bar{z})$ in absence of the sub-harmonic field ($|A_s^0|^2 = 0.$).

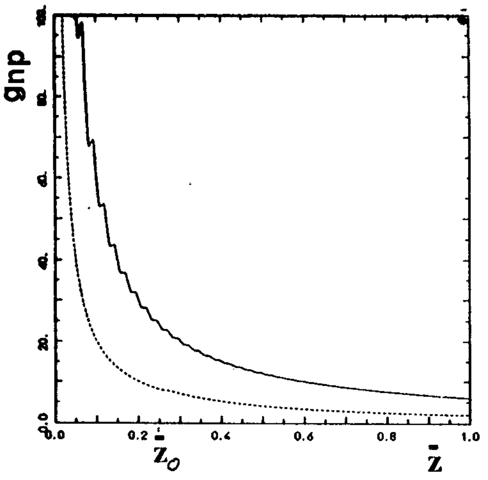

Fig.10 - Incremental gain (in nepers), plotted as a function of $\bar{z}$, for the two cases: with the sub-harmonic field (solid line) and without (dashed line).

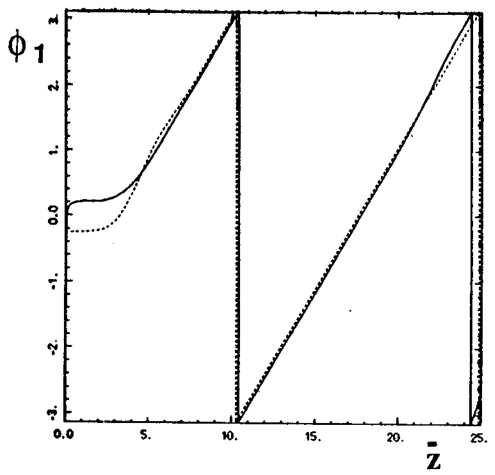

Fig.11 - First harmonic field phase $\phi_1$, plotted as a function of $\bar{z}$, for the two cases: with the sub-harmonic field (solid line) and without (dashed line).

The phase space is plotted at $\bar{z}$=15 in Fig.12-a and at $\bar{z}$=20 (just before saturation, that occurs at $\bar{z}$=23) in Fig.12-b. It is interesting to note that in Fig.12-a the first harmonic field has already produced an energy modulation on the scale of its wavelength which is comparable to the spread induced by the sub-harmonic s=2: the atter stays fairly unaltered along the wiggler and superposed to the two buckets generated by the first harmonic.

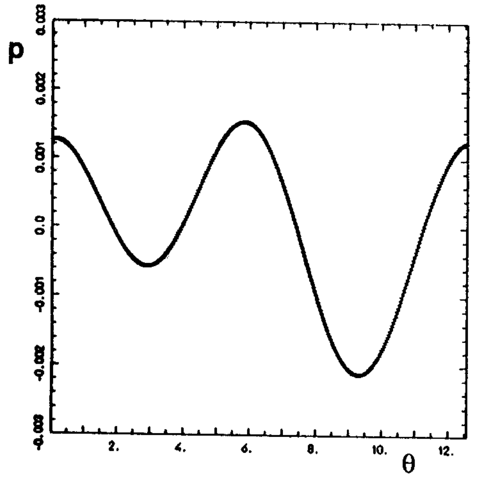

Fig.12-a - Phase space traced at $\bar{z}$=15 for the case of an initial sub-harmonic field intensity $|A_s^0|^2 = 0.2$.

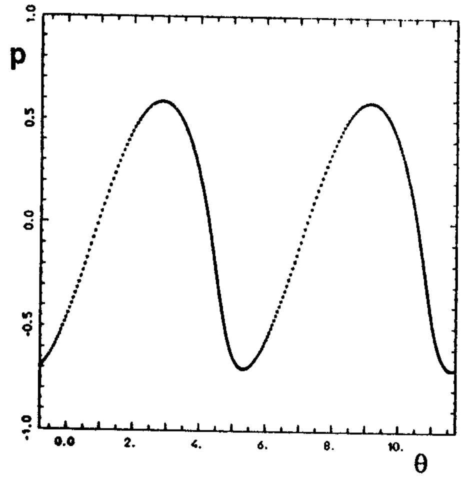

Fig.12-b - Phase space traced at $\bar{z}$=20 for the case of an initial sub-harmonic field intensity $|A_s^0|^2 = 0.2$.

Such an energy modulation on the scale of $\lambda_s$ is seen as an incoherent beam spread by the first harmonic field, but its amplitude comes out to be quite negligible if compared to the coherent spread produced by the first harmonic field when the saturation is approached: that can be clearly seen in Fig.12-b (note the rescaling by a factor 300 of the p-scale), where the incoherent sub-harmonic spread is no more visible over the phase space. The intensity at saturation does not suffer, therefore, for the action of the sub-harmonic field and its value at saturation is, as usual in the cold-beam limit of the steady state regime, $|A_1|^2 \approx 1.2$ (i.e. $P_1 \approx \rho P_{beam}$).

As a last test, we analyzed the sensitivity of the FEL performances, within the SHOK scheme, against the presence of a first harmonic field signal in input and against the variation of the numerical noise generating the initial bunching (which, to some exent, can be considered as a physical Schottky noise).

The logarithm of the normalized first harmonic field intensity ($\log|A_1|^2$) is plotted versus $\bar{z}$ in Fig.13 (solid line), for the case of $|A_s^0|^2 = .2$ and no first harmonic field in input ($|A_1|^2=0$): the first harmonic intensity, starting at 38 orders of magnitude below the saturation level, reaches after 3 units of $\bar{z}$ the level $10^{-20}$. When a signal on the first harmonic is injected in addition to the sub-harmonic field, at the levels $|A_1|^2=1\cdot10^{-29}$ and $|A_1|^2=1\cdot10^{-25}$, the behaviour of the first harmonic intensity is as shown by the dotted and the dashed lines, respectively: it comes out therefore that the driving action of the sub-harmonic field is unsensitive from a possible noise present on the first harmonic.

A similar conclusion can be reached about the sensitivity on the numerical noise: changing the machine espilon from (fairly indicative values) $\varepsilon_m \approx 1\cdot10^{-15}$ to $\varepsilon_m \approx 5\cdot10^{-8}$ (shifting from a 8 bytes floating point operation to a 4 bytes one), the initial bunching, present in the phase space because of the intrinsical straggling of the particle distribution, grows by the same quantity.

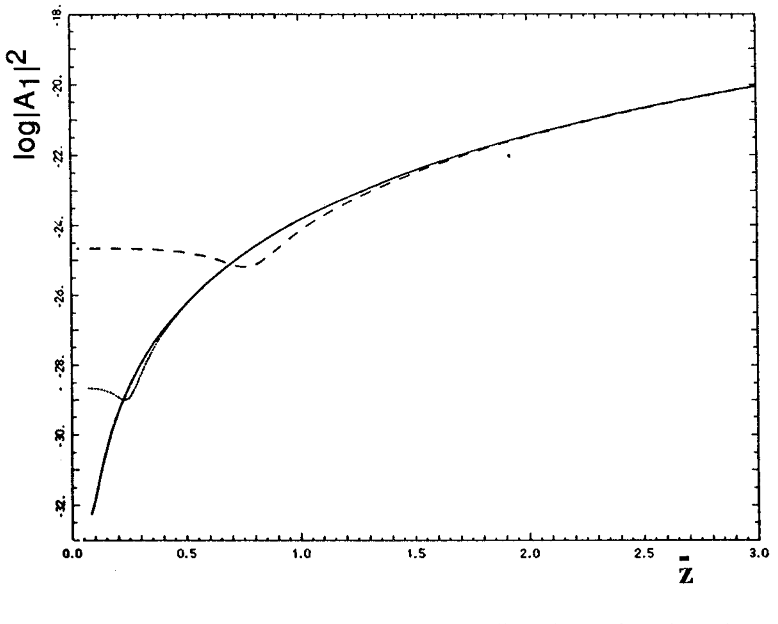

**Fig.13** - Logarithm of the normalized first harmonic field intensity.plotted as a function of $\bar{z}$ for three different values of the initial first harmonic intensity.See text for details.

The first harmonic field intensity starts therefore from a higher value, whose order of magnitude can be easily computed using eq. 9-c) at the first order of approximation by: $|A_1|(\bar{z}=\delta\bar{z}) \approx F_1(\xi)\cdot|b_1^0|\cdot\delta\bar{z}$, where $|b_1^0|$ is the initial bunching amplitude. Recalling that in the present case the integration step $\delta\bar{z}=4\pi\rho/100=2.5\cdot10^{-4}$ and $F_1(\xi)=.8$ we obtain $|A_1|^2(\bar{z}=\delta\bar{z}) \approx 4\cdot10^{-38}$ for the lower $\varepsilon_m$ and $|A_1|^2(\bar{z}=\delta\bar{z}) \approx 1\cdot10^{-22}$ for the higher one. However, the evolution of the first harmonic field intensity is scarcely dependent on the starting bunching amplitude, as can be deduced from the lines plotted in Fig.14, where the solid line gives the behaviour corresponding to the lower $|b_1^0|$ value and the dotted one corresponds to the higher $|b_1^0|$. The difference of 15 orders of magnitude in the starting field intensity values is strongly reduced, after a few units of $\bar{z}$, down to two orders of magnitude. The corresponding incremental gain behaviours are plotted in Fig.15 for the two cases.

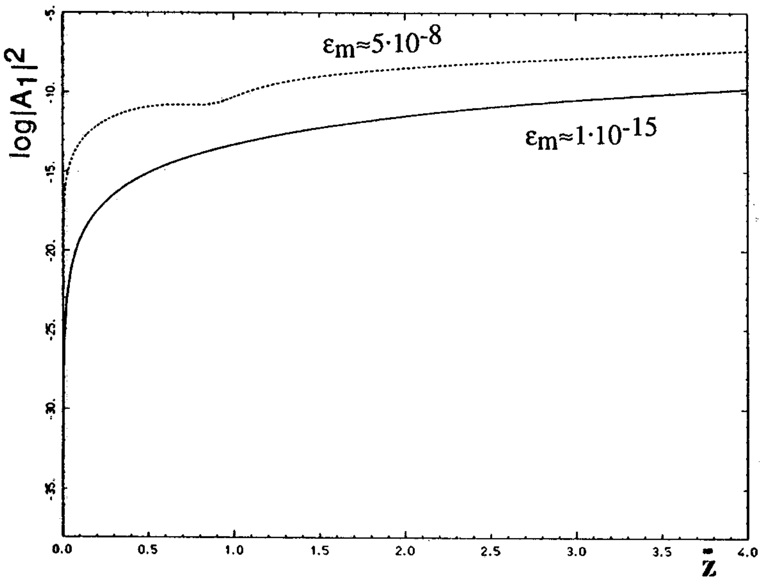

**Fig.14** - Logarithm of the normalized first harmonic field intensity.plotted as a function of $\bar{z}$ for two different values of the machine epsilon.$\varepsilon_m$ See text for details.

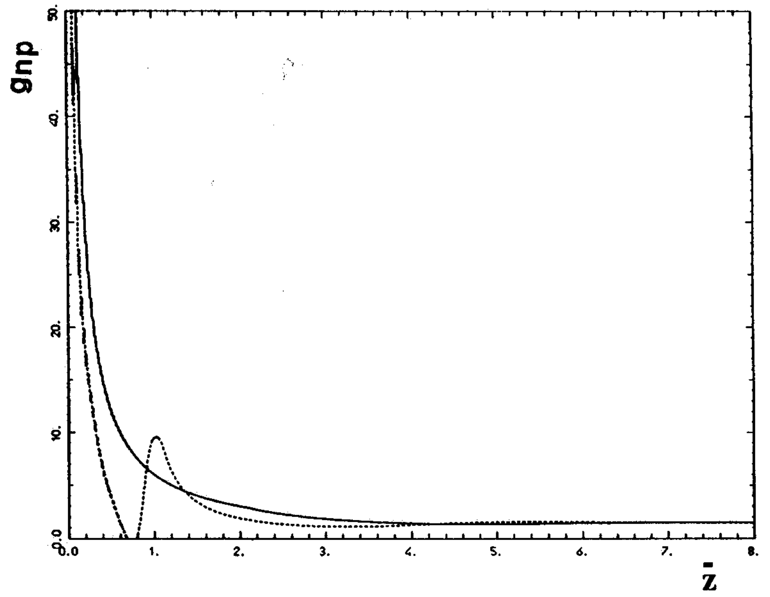

**Fig.15** - Incremental gain (in nepers) corresponding to the two curves plotted in Fig.14

Other sub-harmonic orders have been considered. In principle it can be shown that the index s can be given by the ratio of any pair of integer numbers, s = n/m: the periodicity will be given anyway by n wiggler periods. In fact, the electrons slippage m sub-harmonic wavelengths $\lambda_s$ (with respect to the sub-harmonic field) every n wiggler periods. N first harmonic buckets will still be needed to simulate one sub-harmonic bucket.

However, we analyzed still only the third sub-harmonic case, i.e. s=3. An experimental application of the fifth sub-harmonic will be treated later on in the last section.

We used again the same values for the wiggler-beam parameters as the ones listed above for the case of the second s=2 sub-harmonic.

The trajectory in the phase space of an electron started from the point ($\theta$=.05236 rad, p=0) is plotted in Fig.16, for the case of $|A_s^0|^2 = .2$: the trajectory still exhibits, as the s=2 case, a slow drift in the phase $\theta$, with large oscillations in p and small oscillations ($1 \cdot 10^{-5}$ rad) in phase. Now the macro-periodicity of the sub-harmonic action is no more (as in the case s=2) one wiggler period, but 3 wiggler period, i.e. one unit of $N_s$, as can be observed by the dotted and the dashed lines plotted in the figure, which show the particle position in the phase space at the end of each wiggler period (the dotted one) and every three wiggler periods (the dashed one).

The same effect can be observed looking at the behaviour of $p_{max}$, the maximum p value over the phase space, which is plotted (solid line) in Fig.17 along 30 wiggler periods ($N_s$=10): here again the dotted line connects the values assumed by $p_{max}$ at the end of each wiggler period, while the dashed line connects the values of $p_{max}$ at the end of each group of three wiggler periods (i.e. every unit of $N_s$).

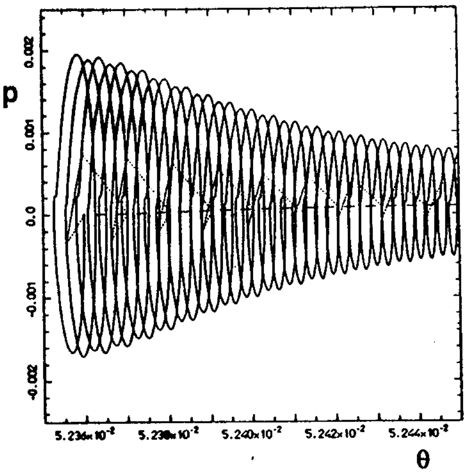

**Fig.16** - Phase space trajectory for a test particle starting at $\tilde{z}$=0 from the point ($\theta$=.05236 rad, p=0.), in the third s=3 sub-harmonic mode of operation. See text for details.

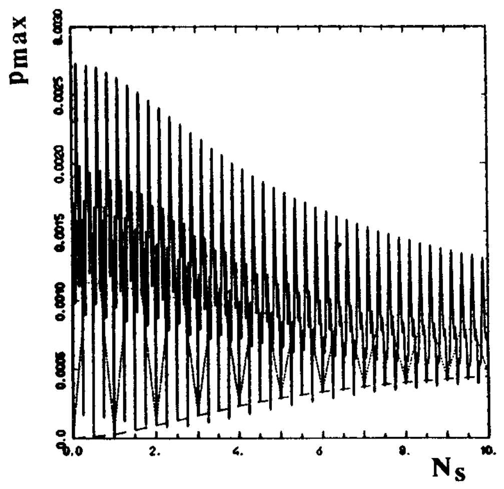

**Fig.17** - Maximum value of p over the phase space plotted (solid line) along 30 wiggler periods, i.e. $N_s$=10., for the third s=3 sub-harmonic case. See text for details.

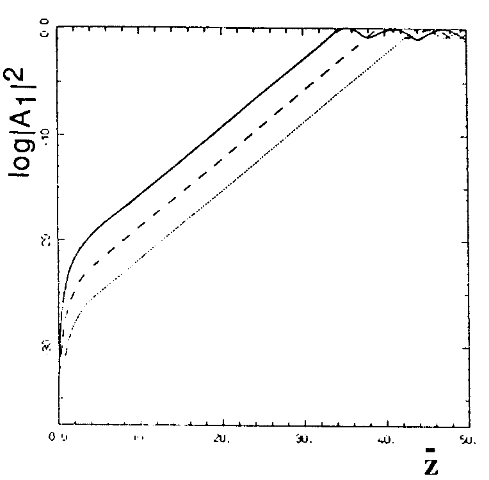

Fig.18 - Logarithm of the normalized first harmonic field intensity, plotted as a function of $\bar{z}$, for three different values of the initial sub-harmonic field intensity., for the third s=3 sub-harmonic case. See text for details.

The behaviour of the normalized intensity $|A_1|^2$ of the first harmonic field is shown in Fig.18, where the quantity $\log|A_1|^2$ is plotted for three different initial values of the sub-harmonic normalized field intensity: $|A_s^0|^2 = .2$ the solid line, $|A_s^0|^2 = .02$ the dashed line and $|A_s^0|^2 = .002$ the dotted one. The first harmonic field reaches saturation after $\bar{z}\approx 35$ starting from zero. The corresponding incremental gain g is plotted up to $\bar{z}=2.5$ in Fig.19. The crossed line shows the incremental gain of the first harmonic field growing from the numerical noise (i.e. without any sub-harmonic input signal): after a first "numerical" spike it reaches quickly the standard steady state value g=1.6 nepers (as reported above). On the contrary, the lines corresponding to the presence of a sub-harmonic field show, after the first unavoidable "numerical" spike which is common for all the lines, a large peak due to the driving effect of the sub-harmonic field: for the case $|A_s^0|^2 = .2$, the peak reaches the relevant value of 100 nepers!

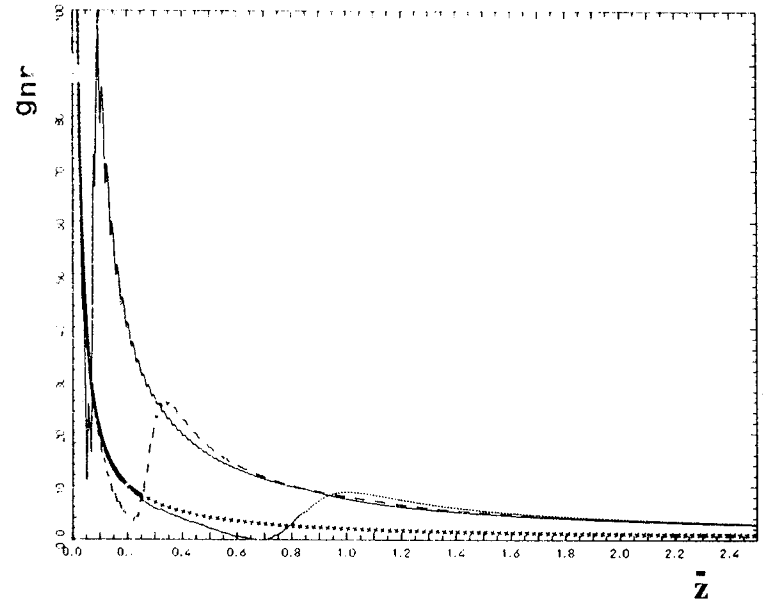

Fig.19 - Incremental gain (in nepers), plotted as a function of $\bar{z}$, for the two cases: with the sub-harmonic field (solid line) and without (dashed line). See text for details.

The evolution of the corresponding phase space is shown in Fig.20-a to 20-e for the case of $|A_s^0|^2 = .02$: the phase space are traced at the end of the first wiggler period (Fig.20-a), at the end of the third wiggler period when $N_S=1$ (Fig.20-b) and at the points $\bar{z}$= 30, 34 and 38 (Fig.20-c-d-e respectivley), just before saturation. It is clearly visible the progressive onset of the energy modulation produced by the first harmonic field which is driven by the energy modulation induced by the sub-harmonic field: the single initial sub-harmonic bucket splits up into three first harmonic buckets, whose energy modulation amplitude continously grows (note the renormalization applied on the p scale) and finally is transformed into a phase modulation, i.e. into a bunching (Fig.20-e).

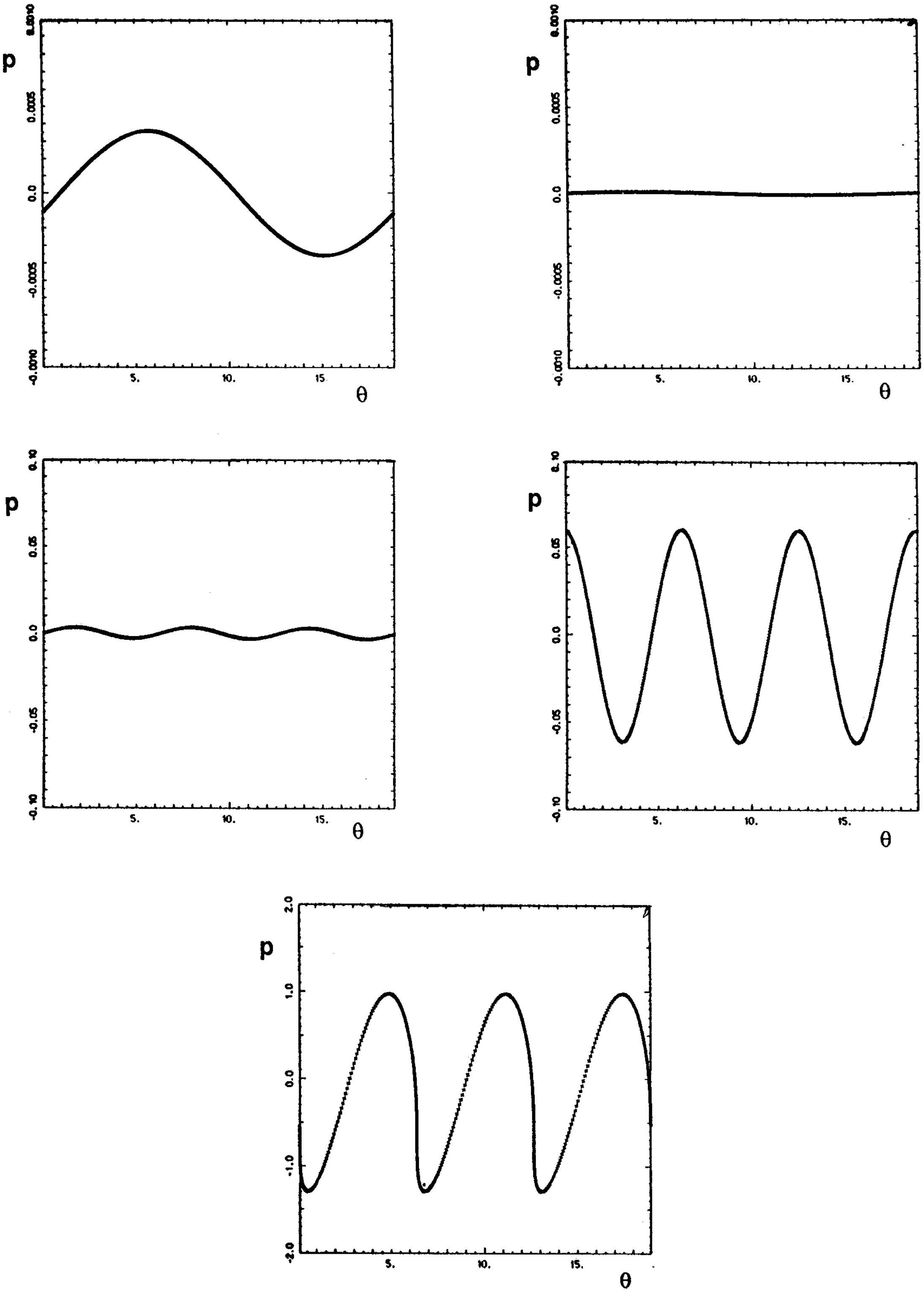

**Fig.20-a to 20-e** - Phase spaces for the third s=3 sub-harmonic case, traced at the end of the first wiggler period (a), at the end of the third wiggler period, where $N_S$=1 (b) and before saturation at the points $\bar{z}$= 30,34 and 38 (c-d-e respectivley).

## 3 - Some possible SHOK experiments

Although the applicability of the SHOK scheme covers the whole e.m. spectrum from the micro-waves up to the XUV rays, the availability in the near future of intense electron beams (some hundrets of A peak current) of high quality (rms normalized emittance in the range $1\div10\cdot10^{-6}$ m·rad) make feasible single pass high gain FEL's in the spectral region from 100 down to 5 nm of radiation wavelength (photon energy between 20 and 200 eV), where no coherent input signals are at present available. The full exploitation of the SHOK scheme lies therefore, in our opinion, within that spectral region, where the lacking of input signal can be overcome via the utilization of sub-harmonic input signals at higher wavelengths, to drive high gain FEL's in the X-VUV spectrum.

The recent developments of the frequency multiplication devices, applied to the high peak power Nd-YLF lasers, indicate that it will be possible to produce high peak power pulses in the VUV wavelength domain. A new laser system based on a mode locked ND-YLF frequency doubled laser produces 10 mJ pulses at a repetition rate of 1 kHz with a peak power of 200 MW over 50 ps, at a wavelength $\lambda$=532 nm. By means of a cascade of two 2-nd harmonic generator BBO crystals the green light is converted down to a wavelength of $\lambda$=133 nm with a total efficiency around the 10%. Laser puses in the VUV wavelength range at a peak power of 10 MW are in this way foreseen(16).

The anticipated availability, within the ARES project context, of high brightness electron beams gives us, as a natural choice, the opportunity to enlist in the following table the parameters of a typical "base" SHOK experiment, to be performed at the ARES facility: a further example for an "extended" SHOK experiment will be presented in the next section. The chosen sub-harmonic is the third one, s=3.

### Table 1 - Base SHOK experiment parameters

| | | | | |
|---|---|---|---|---|
| **Electron Beam** | T = 530 MeV | I = 400 A | $\varepsilon_n = 8\cdot10^{-6}$ m·rad | $\sigma_{beam}$=190µm |
| **Sub-harm. Laser** | | s = 3 | $\lambda_s$ = 133 nm | $Z_0$ = 1.7 m |
| **Wiggler** | $\lambda_w$ = 3 cm | $B_w$ = .75 T | $\rho$ = .0016 | $\lambda_r$ = 44 nm |

The radiated field power P at $\lambda_r$=44 nm is plotted as a function of the wiggler length in Fig.21. The saturation level is reached after 27 m of wiggler at 400 MW of peak power, starting without any input signal on the 44 nm wavelength field and with 10 MW of input signal on the 133 nm laser beam, which corresponds to a normalized sub-harmonic field intensity $|A_s^0|^2$ = .03. Since the rms beam radius within the wiggler is (in absence of ion focussing H=1) 190 µm, the radiated intensity, assuming an active optical guiding(18) of the electron beam on the radiated field, can be

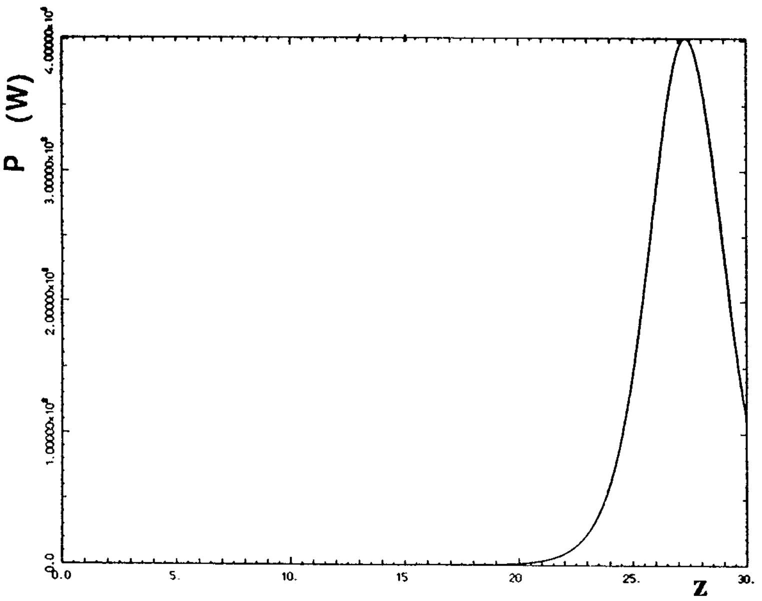

**Fig.21** - Exponetial growth of the radiation at $\lambda_r$=44 nm, driven by a third sub-harmonic laser beam of 10 MW peak power. See text for details.

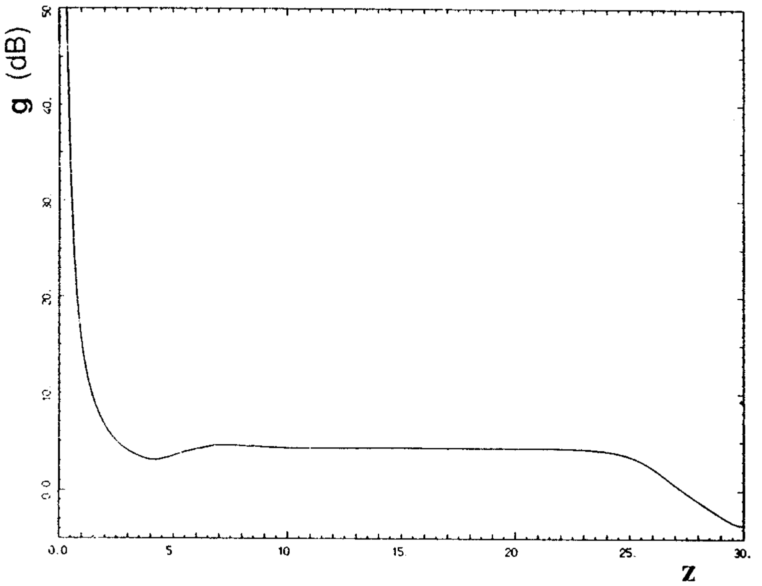

**Fig.22** - Incremental gain $g_{db}$ (in decibels) corresponding to the curve plotted in Fig.21. See text for details.

extimated at about $1 \cdot 10^{11}$ W/cm$^2$. The normalized beam emittance is in this case just compatible with the emittance threshold: the parameter $f_l=2\pi\varepsilon_n/(\lambda_r\gamma)$ comes out to be $f_l$=1.1. The final result is a frequency multiplication by a factor three of the ND-YLF laser beam together with an amplification by a factor 40 of its peak power. The incremental gain $g_{db}$, defined as dlog(P)/dz, is plotted in Fig.22: the plateau at 4 dB of the standard steady state exponential regime is anticipated by the large peak due to the driving effect of the sub-harmonic field. Since the electron bunches delivered by the ARES SC LINAC(17) are foreseen to be a few ps in time-length, a further compression of the 50 ps ND-YLF laser pulses could be envisaged, in order to push up the peak power of the sub-harmonic field at 133 nm. A 50 MW sub-harmonic signal will allow to reduce the wiggler length needed to reach saturation down to 23 m.

## 4 - Towards the "water window"

One of the main goal of the FEL facility under study at the ARES project is the generation of brigth coherent radiation at $\lambda_r$=5 nm, i.e. the construction of a device able to produce coherent soft X-rays at high peak power and within the so called "water window" at 50 Å (photon energy 248 eV).

A direct jump in frequency from the VUV light of the ND-YLF laser cited above up to the 50 Å X-ray radiation seems not feasibe via a simple SHOK scheme as presented in the past sections. At least one cascade with two or more jumps in frequency must be envisaged: a mixed scheme of SHOK + frequency multiplier appears to be mandatory.

Moreover, the electron beam must exhibits the best quality envisageable with the ARES SC LINAC under study: the parameters listed in the following table represent a typical set of values required to radiate at 5 nm. Note the low energy spread (made feasible by the low-frequency RF chosen for the SC LINAC), the high repetition rate and the respectable beam peak power $P_{beam}=3.28\cdot10^{11}$ W.

**Table 2 - Beam requirements to radiate at the "water window"**

| T [MeV] | I [A] | $\varepsilon_n$ [m rad] | $\Delta\gamma/\gamma$ [keV] | $\sigma_{bunch}$ (ps) | rep.rate (kHz) |
|---|---|---|---|---|---|
| 820 | 400 | $3\cdot10^{-6}$ | ± 250 | .5 | 0.1÷1. |

Since $\lambda_r$=5 nm is fairly the 25-th harmonics of $\lambda_r$=133 nm, a double jump in frequency by a factor 5 comes out to be the natural choice: however, as it has been illustrated in the past section, the efficiency of the SHOK scheme decreases with larger sub-harmonic orders s. Therefore a new "extended" SHOK scheme is necessary, as presented in the following, to assure the possibility to reach the water window without the need of extremely long wigglers. Such a new apparatus is based on two main properties of the SHOK scheme:

- The sub-harmonic laser beam is focussed in such a way to present a beam waist at the wiggler entrance: the defocussing part of the beam envelope inside the wiggler is the region of overlapping with the electron beam, where the sub-harmonic field induces a coherent energy spread to the beam.

- It has been shown that the total momentum transfer between the sub-harmonic optical field and the electron beam is negligible: the sub-harmonic field amplitude can be therefore assumed to be determined by the laser beam envelope behaviour, which is regulated by the laser optics in front of the wiggler.

In order to improve the efficiency of the sub-harmonic field in generating a coherent energy spread on the electron beam we can therefore envisage to add in front of the wiggler a few periods of what we call a "spreader", which is simply a wiggler whose period is scaled up by a factor s with respect to the period $\lambda_w$ of the main subsequent wiggler. The spreader is then a wiggler whose first harmonic equals the sub-harmonic optical field wave, whose wavelength is $s \cdot \lambda_r$. It will be shown that the number of spreader periods can be small, of the order of a few units, in order to maximize the performances of the whole system.

The main wiggler is tuned to radiate at a first harmonic of $\lambda_r$=25 nm: the simultaneous growth of the fifth harmonic at $\lambda_r$=5 nm causes the electron beam to be bunched also on this wavelength scale. The subsequent injection of the bunched beam, after some meters of the main wiggler, into a radiator tuned on the 5 nm wavelength makes possible to obtain high peak power radiation at the water window: a lay-out of the whole apparatus is shown in Fig.23. The system wiggler+radiator is discussed in details elsewhere(7).

A matching condition for the beam trajectory imposes a continuity condition on the transverse velocity at the interface between the spreader and the wiggler, i.e. the amplitude of the $\beta_T$'s in the spreader and in the wiggler must be equal: this requires that both have the same vector potential $a_w$. It follows that the peak magnetic field of the spreader $B_w^{sp}$ must be 1/s times the peak field of the wiggler.

The previous considerations suggest a typical set of parameters, for the extended SHOK device, as reported in the following table.

**Table 3 - Extended SHOK experiment parameters**

| | | | | | | |
|---|---|---|---|---|---|---|
| **Sub-harm. laser** | | s=5 | $P_{las}$=10 MW | | $\lambda_s$=125 nm | $Z_0$=.43 m |
| **Spreader** | $\lambda_w^{sp}$=20 cm | $B_w^{sp}$=.11 T | $a_w^{sp}$=1.48 | | $N_{period}=4$ | $\rho^{sp}$=.0034 |
| **Wiggler** | $\lambda_w$=4 cm | $B_w$=.56 T | $a_w$=1.48 | H=.5 | $\sigma_{beam}$=92 μm | $\rho$=.002 |
| **Radiator** | $\lambda_w^R$=2 cm | $B_w^R$=.41 T | $a_w^R$=.53 | $H^R$=.1 | $\sigma_{beam}^R$=50 μm | $\rho^R$=.001 |

The 1-d simulations have been performed integrating the SHOK equations 9) taking as initial conditions the output particles from the spreader, which is described via a set of standard FEL Compton equations whose first harmonic field is represented by the sub-harmonic laser beam. At the end of the main wiggler all the harmonics field intensities $|A_h|^2$ are set to zero, to reproduce the

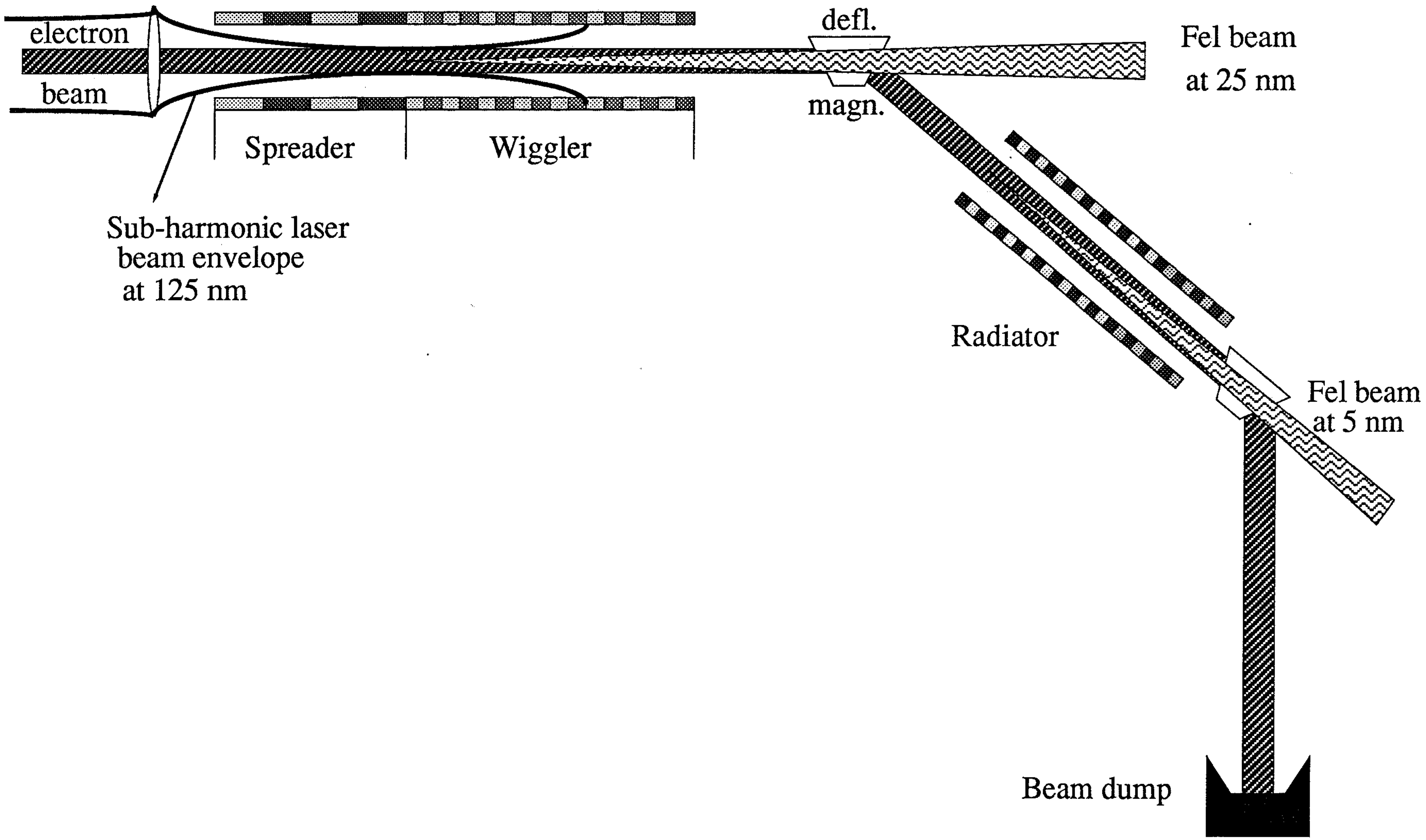

**Fig.23** - Extended SHOK apparatus

discarding of the radiation and the injection of only the electron beam into the radiator (as described elsewhere(7,19) in major details).

In Fig.24 the radiation field power P is plotted along the cumulative length z of the system spreader+wiggler+radiator: the negative part of the z-axis corresponds to the .8 m of the spreader length, while the wiggler extends from z=0 up to z=17 m. The power plotted up to the wiggler end corresponds to the first harmonic field of the wiggler, i.e. to the radiation at 25 nm: the entrance of the radiator corresponds to z=17 m (although this could not be the real disposition, i.e. the radiator can be far apart from the wiggler). The power of the radiation at $\lambda_r$=5 nm grows in the radiator and reaches saturation after still 10 m of radiator length, at a power level of 360 MW, which corresponds to an intensity of $4.6 \cdot 10^{12}$ W/cm$^2$. A slight ion focussing effect has been applied both to the wiggler (with a reduction by a factor H=.5 of the betatron wavelength) and to the radiator (with H=.1). The input sub-harmonic laser power has been taken $P_{las}$=10 MW, while no input field has been injected on the wiggler first harmonic at 25 nm. The logarithm of the amplitude of the bunching parameters on the first wiggler harmonic $|b_1|$ and on the fifth one $|b_5|$ are plotted (solid and dashed line respectively) in Fig.25 as funtions of the dimensionless $\bar{z}$ up to the wiggler end at $\bar{z}$ =10.5: for larger $\bar{z}$ the same parameters $|b_1^R|$ and $|b_5^R|$ correspond to the radiator (since the beam is injected from the wiggler into the radiator, the condition $|b_1^R| = |b_5|$ must hold at the interface). The strong driving effect of the sub-harmonic field is clearly visible in the first part of the wiggler, where the bunching grows very rapidly from the initial noise level.

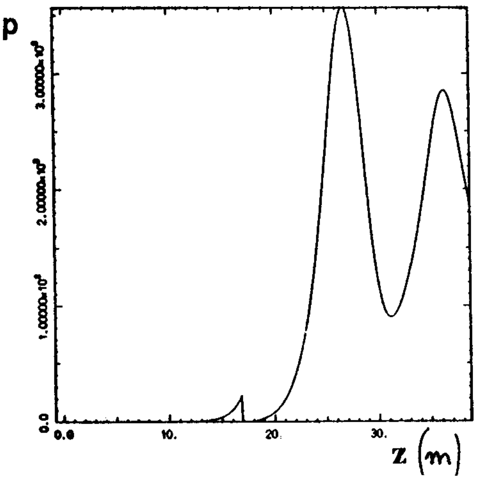

**Fig.24** - Exponential growth of the $\lambda_r$=5 nm radiation power within the "extended" SHOK scheme (spreader+wiggler+radiator). See text for details.

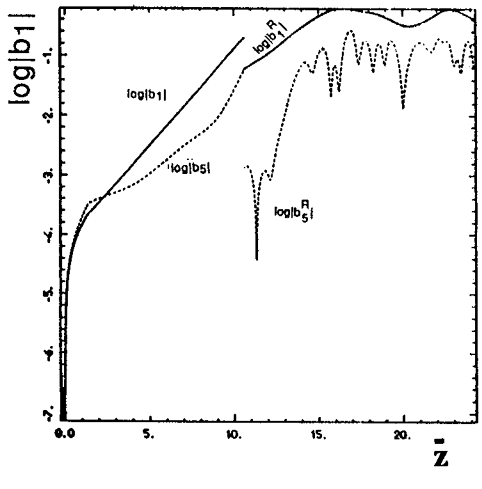

**Fig.25** - Logarithm of the first harmonic $|b_1|$ and fifth harmonic $|b_5|$ bunching amplitude along the wiggler ($\bar{z}$<10.5) and the radiator ($|b_1^R|$ and $|b_5^R|$).

The phase spaces are plotted in Fig.26a-f at some positions along the whole system: the energy spread induced by the 4 spreader periods is evident from the phase space traced at z=0 (wiggler entrance, Fig.26-a). The phase space extends over 5 buckets of the $\lambda_r$=25 nm radiation, since the sub-harmonic order is in this case s=5: the coherent spread is induced on the scale of the sub-harmonic wavelength. After 14 meters of wiggler length (Fig.26-b) the phase space still holds the energy modulation on the scale of the sub-harmonic wavelength, but the energy spread of the first harmonic at 25 nm sets up together with a slight modulation on the third harmonic at 8.3 nm, which further increases at the end of the wiggler (z=17 m, Fig.26-c, note the renormalization in the scale of p), until the sub-harmonic energy modulation is no more visible. The weak energy modulation on the wiggler third harmonic is still present at z=19 m (Fig.26-d), i.e. after 2 meters of radiator length, but at z=21.5 m (after 4.5 meters of radiator length, Fig.26-e) it has been overcome by the strong modulation in energy and phase given by the radiator first harmonic at 5 nm (wiggler fifth harmonic): note that the phase scale has been renormalized up to 25 buckets of the 5 nm wavelength, to take into account the jump in frequency from the wiggler to the radiator. Finally, at z=24 m after 7 meters of radiator length, the phase space traced in Fig.26-f just before saturation shows how the energy modulation has been converted completely into a phase modulation (i.e. a bunching) on the first harmonic of the radiator: 25 bunches can be counted all over the phase space, with a residual weak energy modulation on the scale of the 25 nm wavelength and a negligible modulation on the 125 nm wavelength scale.

## 5 - Conclusions

The results of this preliminary study on the coupling between an electron beam and a sub-harmonic field in a wiggler show that the energy modulation induced on the beam is adequate to start up an exponential gain regime in absence of any pre-bunching of the beam neither any coherent input signal on the wiggler first harmonic: such a scheme can be of great usefulness in all the single pass high gain FEL's which suffer for the lacking of an appropriate source of coherent input signals (in particular the X-VUV FEL's).

Further studies are in course on this subject, in order to explore the full potentiality of the SHOK scheme and to better understand the driving effect of the sub-harmonic optical field on the bunching and on the first harmonic field intensity: a collective variable description could clarify the role plaied by the sub-harmonic signal and its quasi-low-gain coupling with the electron beam.

3D simulations are also needed to investigate how the distributions in the transverse phase spaces of both the electron beam and the two radiation beams (the sub-harmonic and the first harmonic one) can affect the performances of the SHOK scheme.

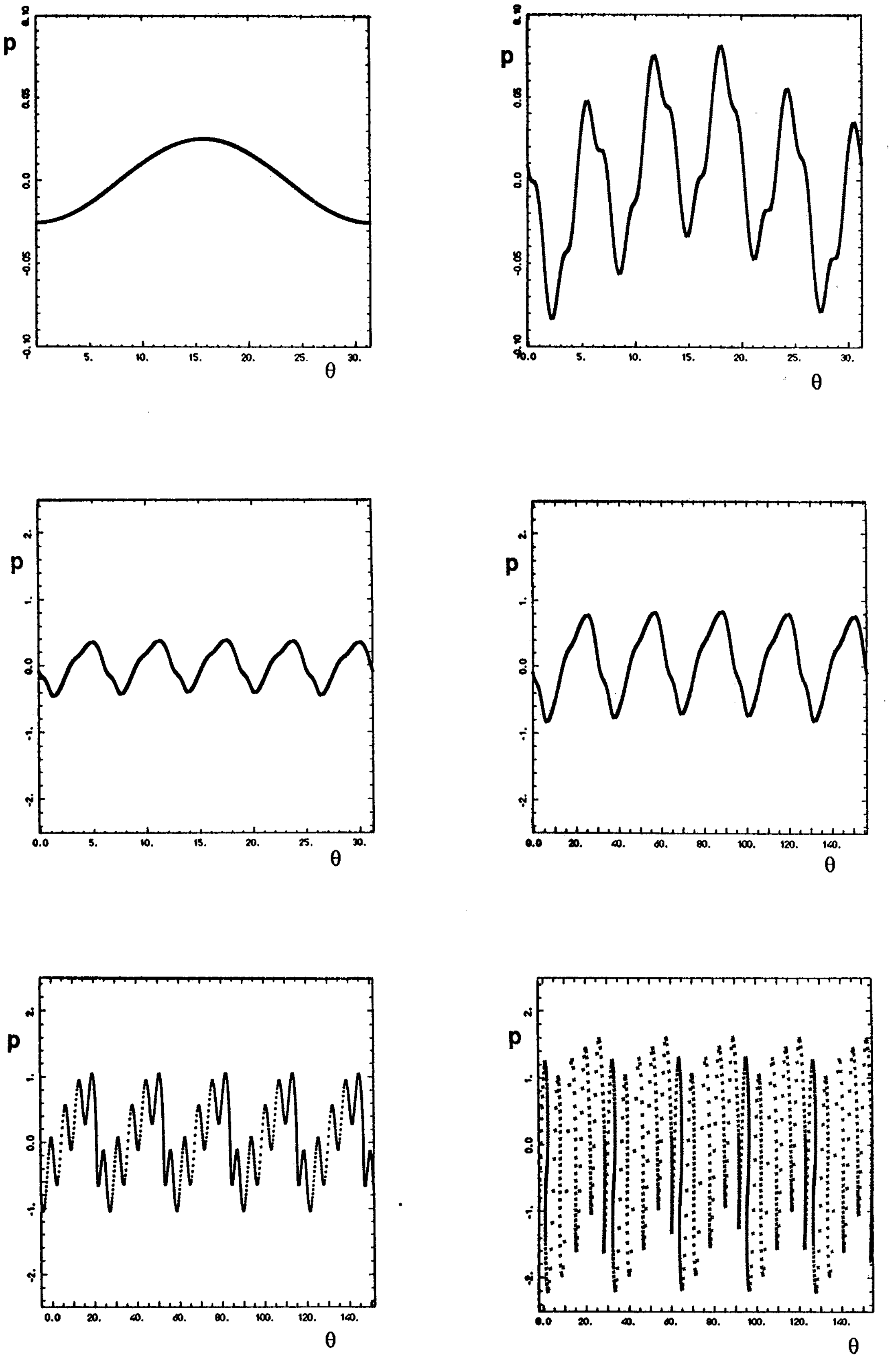

**Fig.26a-f** - Phase space plotted at some positions along the "extended" SHOK device (spreader+wiggler+radiator). See text for details.

## Acknowledgments

We are really very much indebted to G.Vignola and M.Castellano for all the claryfing discussions on the driving action of the sub-harmonic field. We would like to thank also A.Ghigo for all the useful informations about the new laser systems in the VUV range. Our gratitude is due to W.A.Barletta and A.M.Sessler for having stimulated our attention to the subject of XUV FEL and for their encouragement and support in proposing the XUV FEL experiments at the ARES SC LINAC facility.

## References

(1) J.C. Goldstein - Proc. ICFA Work. on low emittance $e^-e^+$ beams, Brookhaven, March 1987, p.180.

(2) C.Pellegrini - Proc. Int. Work. on coherent and coll. prop. in the interactions. of rel. electrons and e.m. rad., Como (Italy), Sept.1984, p.127.

(3) J.B. Murphy - Proc. ICFA Work. on low emittance $e^-e^+$ beams, Brookhaven, March 1987, p.197.

(4) R.Bonifacio et al. - Proc. of the INFN Int. School on Electromagnetic Radiation and Particle Beams Acceleration - Varenna (Italy), June 1988, p.35.

(5) R.Bonifacio et al. - Proc. of the INFN Int. School on Electromagnetic Radiation and Particle Beams Acceleration - Varenna (Italy), June 1988, p.259.

(6) R.Bonifacio, L.DeSalvoSouza, P.Pierini and E.T.Scharlemann - Proc. Int. FEL Conference 1989.

(7) L.Serafini et al., INFN rep. LNF-90/TC (R), March 1990.

(8) C.Pellegrini - NIM **A227** (1980) p.177.

(9) R.Coisson - Part. Accelerators, **11** (1981) p.245.

(10) D.F.Alferov and E.G.Bessonov - Sov. Phys. Tech. Phys. **24** (4) 1979, p.450.

(11) R.Bonifacio, C.Pellegrini and L.M.Narducci - Opt. Comm. **50** (1984) p.373.

(12) E.T.Scharlemann - "Wiggle plane focussing in a linear wiggler" - LLNL Report UCRL-92429.

(13) W.A.Barletta and A.M.Sessler - Proc. of the INFN Int. School on Electromagnetic Radiation and Particle Beams Acceleration - Varenna (Italy), June 1988, p.211-220.

(14) J.B.Murphy, C.Pellegrini and R.Bonifacio - Opt. Comm. **53** (1985) p.197.

(15) R.Bonifacio, F.Casagrande and C.Pellegrini - Opt. Comm. **61** (1987) p.55.

(16) A.Ghigo - Sistemi Laser per esperimenti FEL VUV - Memo ARES 35, Internal rep. LNF, Frascati, March 1990.

(17) "Ares Design Study (The Machine)" - Report LNF-90/005(R), January 17th 1990, Frascati.

(18) E.T.Scharlemann, A.M.Sessler and J.S.Wurtele, Proc. of Int. Work. on Coherent and Collective Prop. in the Int. of rel. electr.and e.m.Rad., Como, Italy, Sept. 1984.,p.29.

(19) M.Billardon, R.Coisson and Y.Lapierre - Appl. Phys. B39 (1986) 9.